AD-A048 175 CNR INC NEEDHAM MA F/G 17/2.1
MULTIPATH OVER LOS CHANNELS STUDY.(U)
NOV 77 P A BELLO, L PICKERING, C BOARDMAN F30602-76-C-0419
UNCLASSIFIED RADC-TR-77-355 NL

1 OF 3
ADA
048175

FG.

2

RADC-TR-77-355
Final Technical Report
November 1977

MULTIPATH OVER LOS CHANNELS STUDY

CNR, Incorporated

ROME AIR DEVELOPMENT CENTER
Air Force Systems Command
Griffiss Air Force Base, New York 13441

This report has been reviewed by the RADC Information Office (OI) and is releasable to the National Technical Information Service (NTIS). At NTIS it will be releasable to the general public, including foreign nations.

RADC-TR-77-355 has been reviewed and approved for publication.

APPROVED: Brian M Hendrickson

BRIAN M. HENDRICKSON
Project Engineer

APPROVED: Fred I Diamond

FRED I. DIAMOND, Technical Director
Communications and Control Division

FOR THE COMMANDER: John P. Huss

JOHN P. HUSS
Acting Chief, Plans Office

UNCLASSIFIED
SECURITY CLASSIFICATION OF THIS PAGE (When Data Entered)

(19) **REPORT DOCUMENTATION PAGE**		READ INSTRUCTIONS BEFORE COMPLETING FORM
1. REPORT NUMBER (18) RADC-TR-77-355	2. GOVT ACCESSION NO.	3. RECIPIENT'S CATALOG NUMBER
4. TITLE (and Subtitle) (6) MULTIPATH OVER LOS CHANNELS STUDY		5. TYPE OF REPORT & PERIOD COVERED (9) Final Technical Report, August 1976 - July 1977
		6. PERFORMING ORG. REPORT NUMBER N/A
7. AUTHOR(s) (10) Dr. P. A. Bello Dr. L. Pickering Mr. C. Boardman		8. CONTRACT OR GRANT NUMBER(s) (15) F30602-76-C-0419 NEW
9. PERFORMING ORGANIZATION NAME AND ADDRESS ✓ CNR, Incorporated 220 Reservoir Street Needham MA 02194		10. PROGRAM ELEMENT, PROJECT, TASK AREA & WORK UNIT NUMBERS (16) (17) 21 P.E. 62702F J.O. 45192107
11. CONTROLLING OFFICE NAME AND ADDRESS Rome Air Development Center (DCCT) Griffiss AFB NY 13441		12. REPORT DATE (11) November 1977
		13. NUMBER OF PAGES 253
14. MONITORING AGENCY NAME & ADDRESS (if different from Controlling Office) Same (12) 255p.		15. SECURITY CLASS. (of this report) UNCLASSIFIED
		15a. DECLASSIFICATION/DOWNGRADING SCHEDULE N/A

16. DISTRIBUTION STATEMENT (of this Report)

Approved for public release, distribution unlimited.

DDC
JAN 4 1978
E

17. DISTRIBUTION STATEMENT (of the abstract entered in Block 20, if different from Report)

Same

18. SUPPLEMENTARY NOTES

RADC Project Engineer: Brian M. Hendrickson (DCCT)

19. KEY WORDS (Continue on reverse side if necessary and identify by block number)

Communications Theory
Data Communications
Fading
Microwave
Frequency Selectivity
Multipath

20. ABSTRACT (Continue on reverse side if necessary and identify by block number)

A major source of propagation outages on microwave LOS links is multipath fading caused by steep negative refractive index gradients. The advent of high-speed digital transmission over the DCS microwave LOS links brings into concern the possible degrading effects of frequency-selective fading associated with such multipath. The present study extends previous results by CNR on channel modeling for multipath fading on LOS links and the consequent degrading effect of such distortion on digital modems and diversity combining. Two 2 bits/sec/Hz modems were examined. One technique used a baseband modem utilizing the

s/c 407852

LB

conventional radio with a frequency modulator and frequency discriminator in the receiver. The other technique used an IF modem and involved coherent receiver processing. While the theory developed is applicable to all the DCS links, two particularly difficult links were singled out for study: the Hohenstadt-Zugspitze link in Germany and the Swingate-Houtem link across the English Channel. Considerable SNR degradation was found to be possible for some propagation conditions. In addition, it is shown that conventional diversity switching can produce loss of bit count integrity, but a modified diversity switching plan can alleviate this problem.

TABLE OF CONTENTS

TABLE OF CONTENTS (Continued)

LIST OF ILLUSTRATIONS

LIST OF ILLUSTRATIONS (Continued)

LIST OF ILLUSTRATIONS (Continued)

LIST OF ILLUSTRATIONS (Continued)

LIST OF ILLUSTRATIONS (Continued)

LIST OF ILLUSTRATIONS (Continued)

LIST OF ILLUSTRATIONS (Continued)

LIST OF TABLES

EVALUATION

Current DoD plans indicate a continued transition from predominantly analog communications to digital communications. This has mandated a need to re-examine all channel models for accuracy when applied to digital communications signals.

In LOS microwave, fading is usually assumed flat. Availability calculations imply that if a channel is calculated to have, for example, a 40 dB fade margin, that it will be usable within 40 dB of the average received signal level. This program has demonstrated for the first time that group delay is its most severe at deep fades. If the microwave radio is not designed to handle large excursions in group delay, a high error rate will result several dB earlier than anticipated. There can thus be a wide variation between calculated and actual availability.

Most empirical data on multipath fading has been taken for link distances on the order of 30 miles or less. Links in the Defense Communication System at times exceed 100 miles. This program has documented, mathematically, conditions necessary for multipath fading to exist on long links.

Diversity switching on LOS microwave is usually accomplished by a selection switch. A question that always arises is "How far should the normal channel fade before the standby channel is switched in?" Results of this program demonstrated how group delay can cause losses in bit count integrity during diversity switching and proves that the best strategy is to switch to the best channel at all times.

Much work remains to be done in further examining the models developed in this program from a theoretical point of view and in developing additional experimental data to quantify system availability as the calculations apply to digital communications.

Brian M Hendrickson

BRIAN HENDRICKSON
Project Engineer

SECTION 1

SUMMARY

Continued evolution of the Defense Communication System (DCS) to an all digital communications network and previous indications that fading conditions on line-of-sight (LOS) microwave relay links may exhibit a high degree of frequency-selectivity have motivated the investigation reported here. The report describes the results of an investigation of frequency-selective fading on LOS links to determine the effect on digital communications performance. In the modeling effort and concurrent computation particular emphasis has been placed on updating and revising previous work to include diversity communications. In the effort aimed at determining modem performance the primary emphasis has been placed on determining the extra SNR degradation due to the frequency-selectivity of the multipath fading. Calculations have been performed for two modems, a baseband modem operating with conventional FM radios (DAU modem) and a narrow band phase-continuous FSK modem (IF modem). This section of the report provides a list of our conclusions (Section 1.1 below), a list of our recommendations for further work (Section 1.2), and a summary of the report contents (Section 1.3).

1.1 Conclusions

As a result of this study the following conclusions have been reached relative to the effects of frequency-selective fading on DCS microwave LOS links.

a) The largest group delay excursions occur during the deepest fades (Section 2.3.3). Consequently, diversity switching from one fading diversity channel to another channel with little or no fading on it can cause a sudden large discontinuity in group delay depending, among other things, on the fade depth threshold for switching. Because of the correspondence between the modem bit sync tracking behavior and the group delay (Section 4.2), and the fact that calculated discontinuities can be comparable to and exceed the symbol duration (Section 4.1), loss of bit count integrity will occur in some circumstances.

b) For diversity switching, use of the rule "switch to other channel if stronger than current channel," is recommended over use of other rules that postpone the switching until the signal fades to a prespecified threshold (Section 4.1).

c) According to the theoretical calculations frequency-selective fading on the 100-mile Hohenstadt-Zugspitze link is more extreme than on any other link we have encountered. Nevertheless, it is felt that some of the physical assumptions (e.g., regularity of layer structure over the path) may be near their limits of applicability for such a long link (Section 2.4.1). The intuitive notion that such an extreme geometry can lead to extreme fading is supported by the program of measurements described in [1.1] wherein it was reported that fading over the Hohenstadt-Zugspitze link path is greater than over any other tested in the DEB Stage I system.

d) Relative to our evaluation of SNR degradation of modem performance due to frequency-selective fading, performance losses vary widely with change of physical conditions. In all cases the SNR degradation increases as the fading on the link becomes more frequency-selective (as indicated by increased delay spreads of the interfering rays). Due to the pronounced frequency-selectivity of some fading situations complete degradation can occur in a 20 dB fade (see Tables 1-1 and 1-2 in Section 1.3.4).

e) SNR degradation losses, due to frequency-selective fading, were quite similar for the two modems considered (DAU modem and IF modem). During conditions of mild frequency-selectivity our calculations indicate that both modems perform well and under conditions of strong frequency-selectivity performance for both is severely degraded. In a narrow transition region, the IF modem has the superior edge (Section 3).

f) Whenever refractive multipath fading takes place on a link the most probable situation is that the fading is due to interference of no more than three rays (this is demonstrated in Section 2.2.4). In some of our computations, a fourth and fifth ray have appeared (see Section 2.4.2). These "extra" rays, which typically exist over only small intervals of layer height, are extremely close to one another in delay and are close also to the layer path that is greatest in delay. As a result, frequency-selectivity of the link still exhibits a three-path character.

g) There are no useful measurements of refractive index gradient taken in conjunction with measurements of signal distortion, i.e., the P-parameters (Section 2.3.2). Thus, a valid comparison of model calculations with experimental results is not possible. Relative to our propagation calculations, however, comparing the character of our calculated results with the character of experimental records indicates some striking similarities (see Section 2.5) and no discrepancies.

1.2 Recommendations for Further Work

To comprehensively determine the effects of frequency-selective multipath fading on estimates of system availability it is recommended that the following studies and experiments be carried out:

a) Model Augmentation

To increase the usefulness of the model the following tasks should be undertaken:

- As pointed out in Section 2.1.2 below, the effects of atmospheric turbulence, normally not a matter of serious concern, may be magnified in a refractive multipath fading condition. A study of this phenomena, to determine its effects on system performance, is recommended.

- Tilted atmospheric layers alter the polarization components of waves that interact with them, and for this reason, their effect on the performance of "frequency reuse" systems (those which use two orthogonally polarized waves to approximately double link capacity) should be determined.
- To increase the application of our model to a wider variety of physical situations, the "thin layer" case should be included. This is the case wherein the top and bottom of the atmospheric layer are both within the vertical region between the two terminals.
- Because of the sensitivity of multipath fading to some of the more important physical parameters (e.g., refractive index gradient and layer height) and the wide range of values these quantities can take on, statistical modeling of these quantities should be incorporated into the refractive multipath model.

b) Probability of Antenna Decoupling

Prolonged signal attenuation (antenna decoupling) not exhibiting the usual more rapid character of multipath fading has resulted in "blackouts" of some links in Germany. The analytical results of this report (and the companion computer programs) are singularly appropriate, for calculation of the relevant angles. For given or postulated antenna patterns we recommend a determination of the lapse rates required to cause antenna decoupling and hence the probability of its occurrence.

c) Diversity Design Study

Since the study results that have been traditionally used to determine diversity spacings are based on empirical data for a limited number of paths, the generalization to other paths, other frequencies, and other areas involves some degree of risk (as pointed out and summarized in [1.2]). A design study that takes into account all of the wide variety of parameters in a reasonable and consistent way should be undertaken. The following tasks and questions should be addressed:

- Further analysis of space diversity operation, with special emphasis on an analytical determination of optimal antenna spacing.

- All candidate diversity combining schemes should be evaluated—especially new schemes that, in addition to the standard fade level, use measurements of signal distortion in order to take into account the extra SNR degradation due to frequency-selective fadng and (when appropriate) the possible discontinuities during diversity switching.

- What effect does turbulence [see (a) above] have on the probability of simultaneous deep fading on diversity branches?

d) Availability Study

The probability that a link will be available is a basic parameter relating to link design. We recommend an extensive effort to calculate link availability via the three-step program outlined below.

- First, determine the probability that multipath fading will take place on a link. The results would initially take the form of bounds of various quantities, e.g., lapse rate of refractive index gradient and layer tilt. Based on available statistical measurements for these quantities (quite extensive in the case of lapse rate, the most important one) the results would yield the probability that multipath fading occurs on the link.

- Given the condition that multipath fading occurs, determine the probability that the P-parameter values (see Section 3) are such as to result in unacceptable error rate(determined through calculations of modem performance such as we describe in this report).

- In a diversity context, given the unacceptable performance of one diversity channel, determine the probability that performance of the other diversity channel is also unacceptable.

The three probabilities above, appropriately combined, yield the probability that the link will fail and, hence, the availability.

e) Channel Measurement

A carefully planned program of system function and distortion parameter measurement coupled with refractive index measurements is needed so that the relationship of the multipath and frequency-selective character of the link to the link parameters, geometry, and atmospheric conditions can be pinned down.

1.3 Summary of Report Contents

In this section we summarize the report contents.

1.3.1 Channel Model

A dependable model of the communication channel is a baseline requirement in any attempt to evaluate relative modem performance. The channel of interest here is the DCS LOS microwave relay channel. Because other causes of fading can be eliminated by simple design techniques, the modeling effort in this investigation centered on a phenomena known as refractive multipath. Loosely, it can be said that this phenomena derives from the fact that electromagnetic energy does not travel in straight lines in a medium characterized by a spatially varying refractive index. As it happens, the atmosphere in its usual condition is characterized by a slight, approximately linear decrease (or lapse) of refractive index with height. This slight lapse is not, in itself, enough to cause multipath fading. On occasion, however, there are regions of vertical extent characterized by a more rapid decline than usual, i.e., by a larger lapse rate. These regions are referred to as "layers" throughout this report. When there is the possibility that electromagnetic energy traversing a link may intersect with a layer, the equations of geometrical optics indicate that multiple ray paths may exist. In such a case the multiple paths interfere in the classical manner and result in multipath fading. The existence of this condition depends on the lapse rate of refractive index gradient, the path length, the transmitter and receiver elevations, the layer height, the layer thickness and the layer tilt. In terms of these parameters the equations of geometrical optics can be used to compute the number of paths, their relative delays, and their relative amplitudes, thus providing a complete characterization of the refractive multipath channel.

Calculation of the quantities required for this characterization are described in Section 2.2. Also described are two basic modifications of the model developed earlier at CNR [1.3]. One of these is the incorporation of layer tilt into the model (Section 2.2.3). The other is the inclusion of the physical situation illustrated in Fig. 1.1(b) wherein the layer is below the highest terminal, i.e., the highest terminal is immersed in the layer (Section 2.2.2). Both of these modifications were deemed necessary for the modeling of links that are extremely long and/or are characterized by an extremely large vertical separation of receiver and transmitter. The correctness of this conclusion is demonstrated in connection with the Hohenstadt-Zugspitze link in Section 2.4.1.

Though there are several layer parameters affecting the multipath character of fading on an LOS link it has long been recognized that the lapse rate of refractive index gradient plays a dominant role; measurements of this quantity have been made on a world-wide basis for many years. The primary data sources for probability distributions of this parameter are Bean and Dutton [1.4], [1.5], and Samson [1.6]. The latter is of particular use here in that it provides data for Stuttgart, Germany that can reasonably be applied to the Hohenstadt-Zugspitze link discussed in Section 2.4.1. Though the data referred to here constitutes the most comprehensive source, certain inadequacies in its collection could possibly lead to slightly erroneous conclusions (see Section 2.1.1).

Though large lapse rates are known to result in multipath fading there seems heretofore to have been no definitive statement about the relationship between lapse rate and the existence of multipath. We have determined (see Section 2.2.4) an existence condition for multipath due to refraction in a horizontal layer. This is given in terms of the inequality

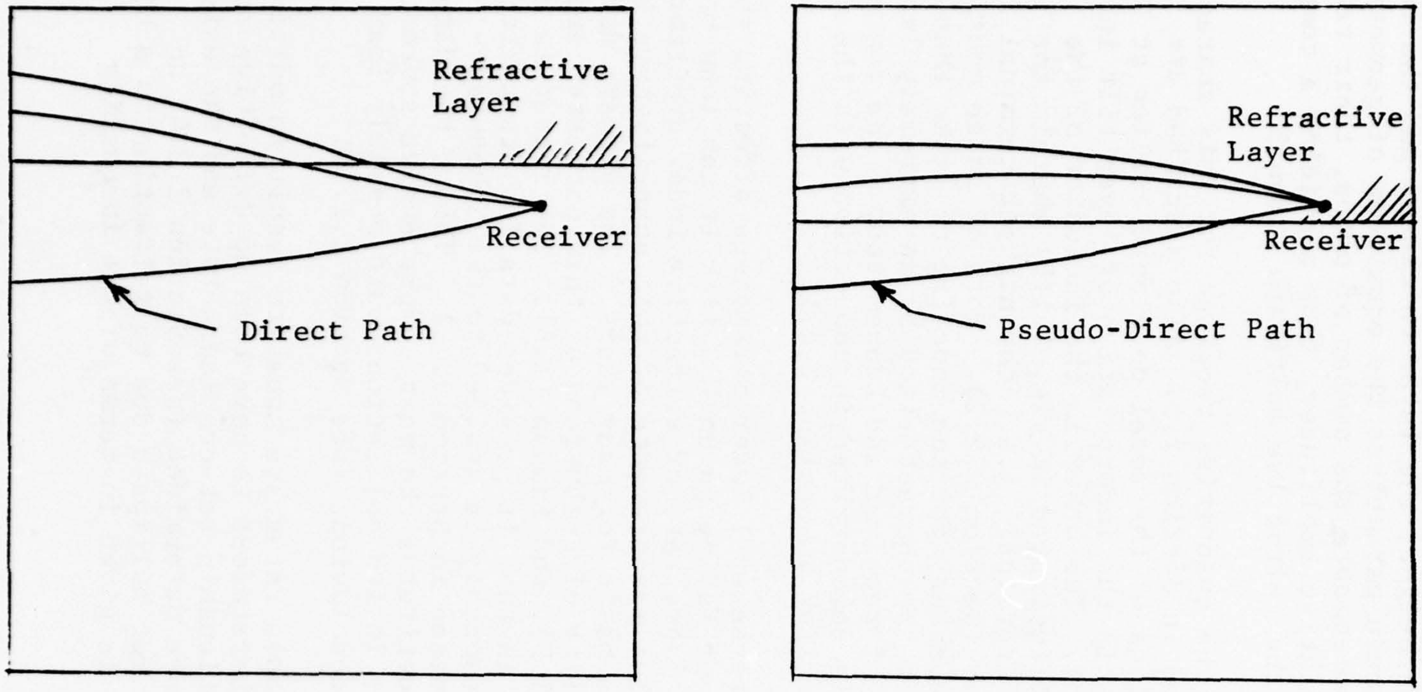

(a) Layer Above Receiver (Condition "A")

(b) Layer Below Receiver (Condition "B")

Figure 1.1 Layer-Receiver Geometry

$$\mathcal{L} \geq \frac{.62139 \times 10^6}{R_f \left[\sqrt{1 + \frac{L^2}{8R_f \Delta}} - 1 \right]} + 156.78 \qquad (1.1)$$

where $\mathcal{L}$ is the lapse rate of refractive index gradient, R_f is the radius of curvature of ray paths in the normal atmosphere (approximately 5300 feet), L is the link length and Δ is the height of the layer above the arithmetic mean of the transmitter and receiver heights. Thus, we see that the lapse rate must exceed some easily calculable value if multipath fading is to take place.

It should be pointed out that (1.1) holds only for condition "A" of Fig. 1.1. Time did not permit the determination of a similar inequality for condition "B".

Some simple observations can be made about the existence condition above. First, as the layer rises above the arithmetic mean of the receiver and transmitter heights a greater lapse rate is required in order to support multipath. Secondly, as the link length increases, less of a lapse rate is required in order to support multipath. These trends are evident in the graphical depiction provided in Fig. 1.2.

One of the most powerful applications of the existence condition in (1.1) is in the determination of the probability of multipath fading. Consider any particular link for which the right-hand side of (1.1) can be calculated. Designate this value $\mathcal{L}_0$. Then the probability that multipath fading exists on the link is just the probability that $\mathcal{L}$ exceeds $\mathcal{L}_0$. But, this probability is exactly that provided by the world-wide program of measurements described above. Hence, the probability of multipath fading on the link is quickly calculable.

As reiterated in our recommendations for future work the derivation of the existence condition applying to condition "B", so that an integrated view can be obtained, is strongly recommended. Such an analysis would provide upper bounds (i.e., worst-case indications) of the probability of outage.

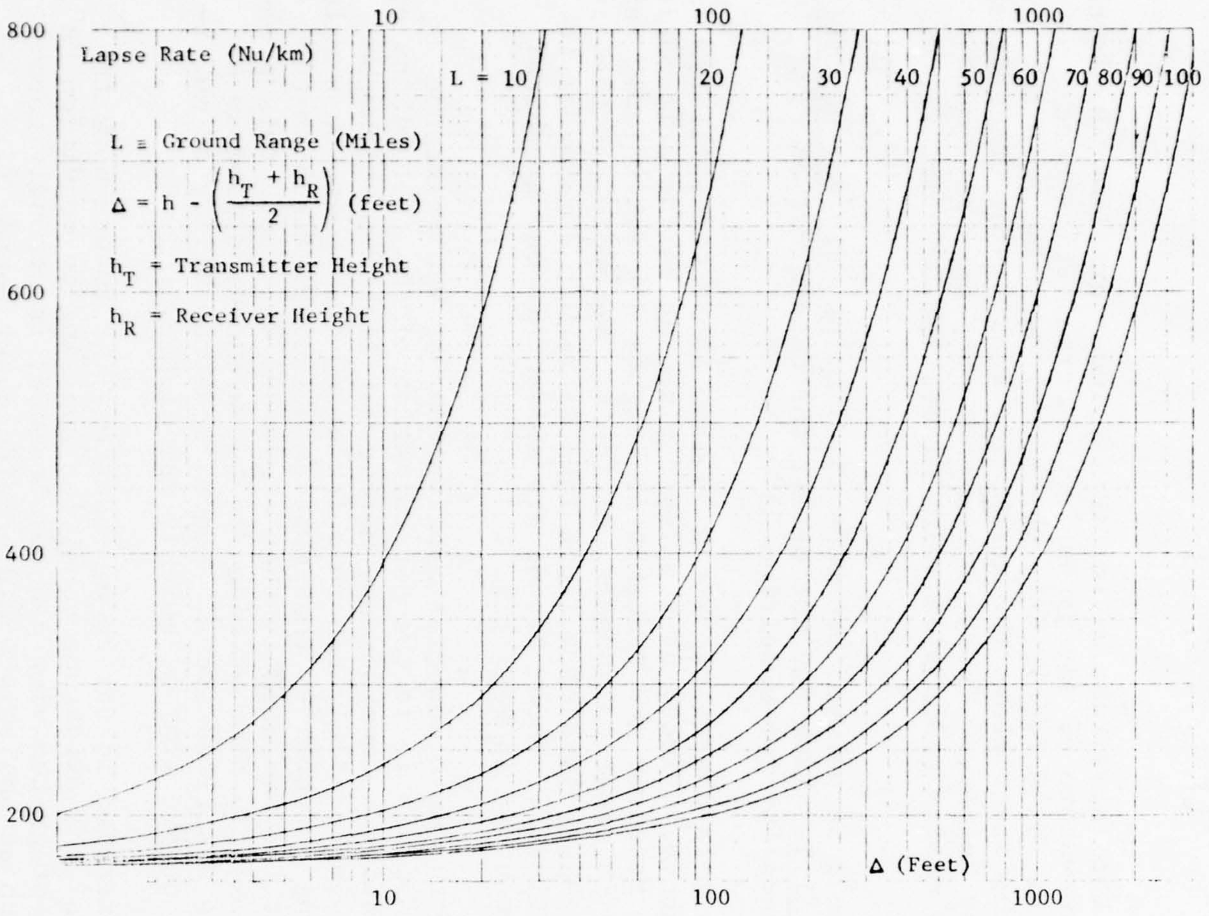

Figure 1.2 Lapse Rates Required for Existence of Refractive Multipath on LOS Links

From a physical point of view, the creation of atmospheric layers is a highly variable and complicated process, the study of which falls more within the bailiwick of meteorologists than engineers. Nevertheless, an understanding of the basic mechanisms resulting in layer formation is crucial to attainment of a complete computer model. For this reason a discussion of weather effects and layer formation is provided in Section 2.1.2 of this report. We have also provided in that section a graphic description of "heating from below", one of the more common causes of layer formation. The overall result of heating from below is the formation of three distinct atmospheric regions.

1) A narrow surface region near the ground characterized by strong gradients but slight turbulence (limited effect on communications, if any).

2) A thick central region characterized by <u>strong turbulence</u> due to rapid upward convection of air. This region constitutes a well-mixed homogeneous layer and is characterized by the standard lapse rate of refractive index gradient (about 40 Nu/km).

3) A stable upper layer characterized by larger than normal lapse rates.

The intermediate central region in this description is the region through which the direct or pseudo-direct path of Fig. 1.1 passes. The existence of turbulence in this region motivates consideration of adding to the phasor normally representing this path a small random phasor representing the turbulence.

1.3.2 Fading Characteristics Due to Refractive Multipath

That refractive multipath can occur with enough regularity to warrant concern is beyond dispute. The fact that it is inherently a frequency-selective phenomena seems to be less understood. The in-depth study described in this report indicates that the frequency-selectivity of multipath fading can be of profound importance. Some of the highlights of this report relative to the character of fading on microwave LOS links (diversity discussion is deferred until Section 1.3.3) are summarized below.

A first step on the road to obtaining an overview of refractive multipath fading is to examine its dependence on those parameters that are best defined probabilistically and retain as fixed parameters those quantities for which the probabilities are best known. Thus, one can reasonably ask "given a certain lapse rate for which the probabilities are relatively well known, what is the dependence of fade level on layer height and frequency?" The answer, to some degree, is provided by the contour plot of Fig. 1.3 which corresponds to a 30 mile link with the specific link geometry shown and an atmospheric layer with a relatively strong lapse rate of refractive index gradient (420 Nu/km). This figure was pieced together from 12 computer plots and constitutes a dual presentation of frequency-selectivity and spatial selectivity (operating frequency on the horizontal axis and layer height on the vertical axis). Essentially, it shows fade level as a surface over the height-frequency plane; each contour depicts the combination of layer height and frequency that will result in a fade to the depth with which each contour is designated.

In discussing contour plots it is helpful to refer to the regions inside the smallest contours (the 20 dB contours in Fig. 1.3) as the deep fade loci. It is clear from the contour diagrams that the deep fade loci are few and far between; in fact, only five of them appear in Fig. 1.3. Additionally, we note that the 10 dB fade contours extend over a few hundred MHz, whereas the 20 dB fade contours are much smaller. This is in keeping with experimental data pointed out by Kaylor [1.7] who has noted that the sharp deep fades occur during shallower fades that can extend over a band approximately 400 MHz wide.

Figure 1.3 was generated using operating frequencies in the 4 GHz band. It is of interest to compare these results with the results of calculations for the 8 GHz band which we provide in Fig. 1.4. One conclusion, borne out by analysis, is that the frequency spacings between the deep fade loci in the plots does not depend on the bands examined, i.e., given a layer height value the deep fade loci occur with the same frequency spacing in the 4 GHz band as they do in the 8 GHz band. In fact, we have derived an expression which, given a constant layer height h_L, yields the frequencies at which the deep fades will occur (see Section 2.3.3) and this expression indicates that at most two deep fades may occur every $|\Delta\tau(h_L)|^{-1}$ Hz, where $\Delta\tau$ is the delay difference between the two rays refracted in the layer.*

---

*Our arguments here relate to multipath interference between a total of three rays. It is demonstrated in Section 2.2.4 that the existence of a higher number of paths is considerably less probable an occurrence.

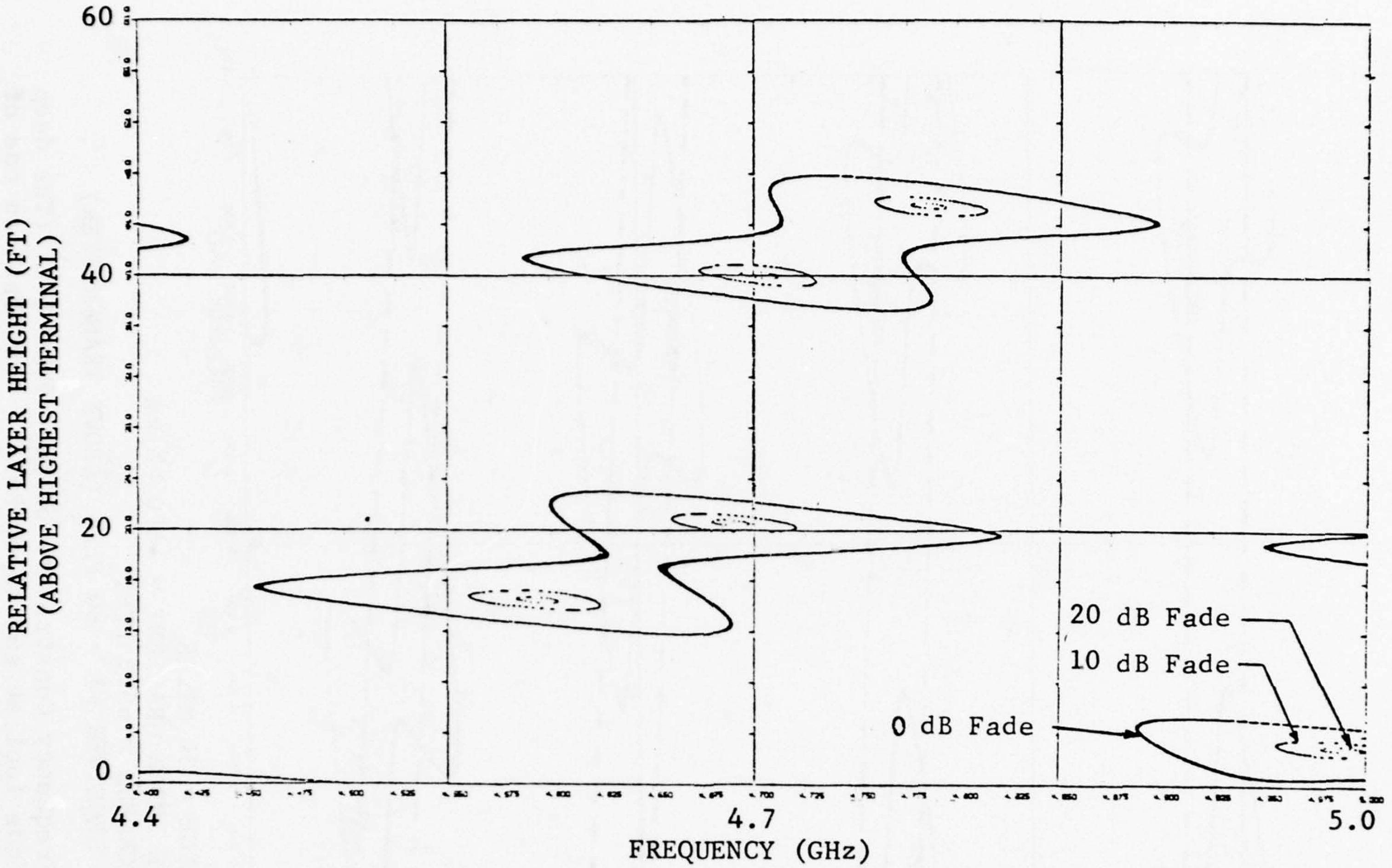

Figure 1.3 Deep Fade Loci Represented as Countour Plot

Receiver Height = 80 feet (above transmitter)
Refractive Index Gradient = -420 Nu/km
Ground Range = 30 miles
Layer Thickness > 62.6 feet

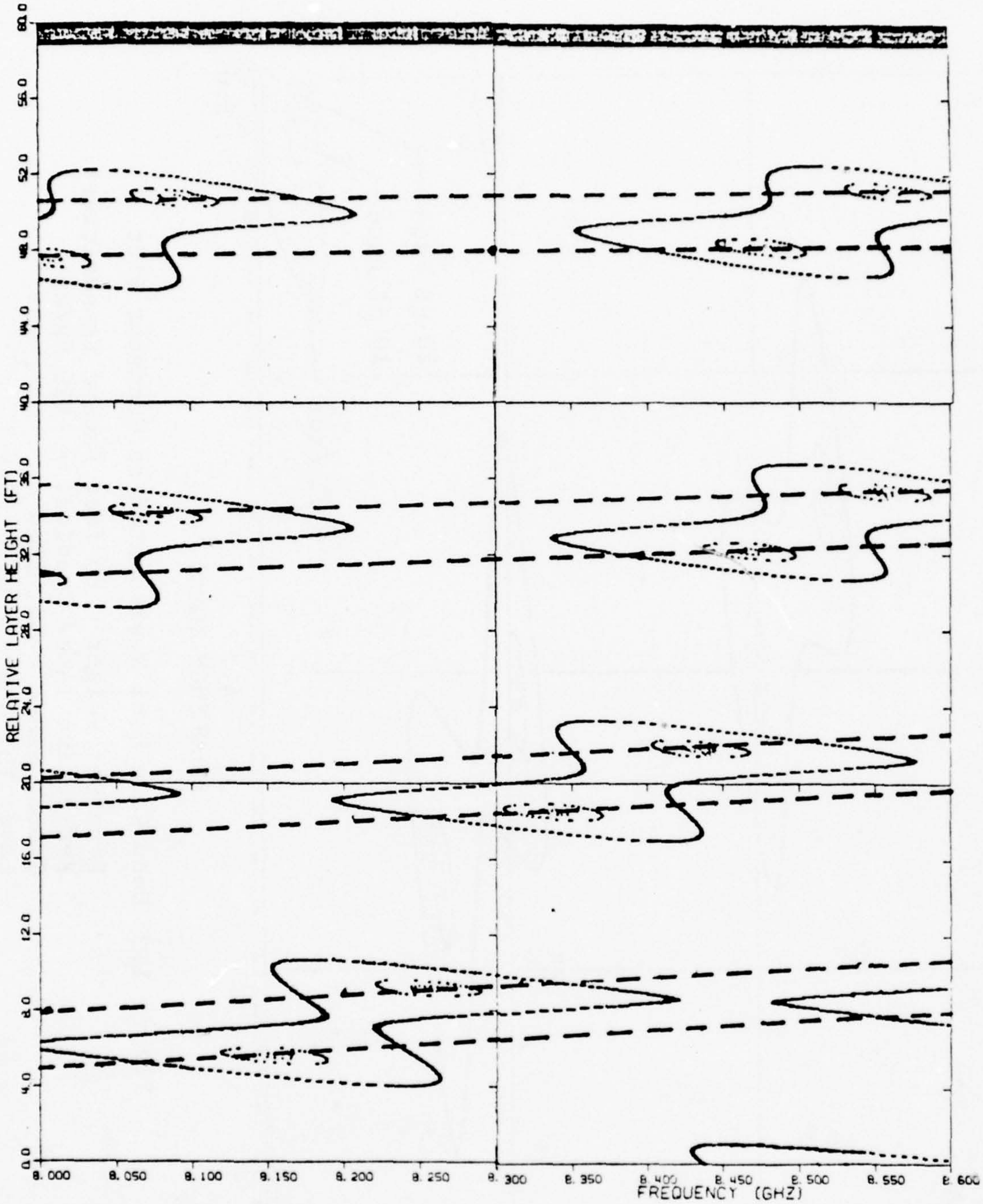

GROUND RANGE = 30 MILES
REFRACTIVE INDEX GRADIENT = -420 Nu/km
LAYER THICKNESS > 62.6 FEET
HEIGHT OF RECEIVER #1 = 80 FEET (ABOVE TRANSMITTER)

Figure 1.4 Frequency Constraints on Deep Fade Loci (The deep fade loci at any layer height must fall on one of the dotted lines.)

The expression referred to above [(2.156) in the text] has been used to generate the dotted lines in Fig. 1.4. Note that these lines pass directly through the deep fade loci, and hence result in a considerable reduction of effort in determining the deep fade loci which are the regions of greatest interest.

A second conclusion that can be made from a comparison of the two contour diagrams is that the relative occurrence vs. layer height of the deep fades does depend on the frequency band. Comparing Figs. 1.3 and 1.4 we see that the vertical separation of the deep fade loci in the 4 GHz band is approximately twice what it is in the 8 GHz band. This dependence can be demonstrated generally by appealing to the approximately linear dependence of $\Delta\tau(h_L)$ on layer height, (see Section 4.1). When this is done, we see that there can be at most two deep fades every $[f\Delta\tau(0)]^{-1}h_{max}$ feet, i.e., the layer height separation of the deep fade loci is inversely proportional to f. Thus, spatial selectivity becomes more important at the higher frequencies. If it can be assumed in the roughest sense that there is some regularity to the layer motion then one can conclude that fading will be more rapid in time at the higher frequencies.

It should be emphasized that the contour diagrams of Figs. 1.3 and 1.4 are really just "snapshots" of one particular physical situation. The actual situation is that the refractive index gradient and layer height have a complicated temporal interdependence; e.g., as layer height and/or refractive index change in time the contours of Fig. 1.4 change shape and the deep fade loci move. This motivates statistical modeling of the two basic physical parameters, layer height and refractive index gradient. A similar consideration should also be made of layer tilt (more important on the longer links).

Possible loss of bit count integrity during diversity switching (to be discussed in more detail in the following section), motivates consideration of the behavior of group delay during a fading condition. As it happens, IF modem bit synch tracking closely follows the center-of-band group delay, although small deviations occur. This point is illustrated in Fig. 1.5 which shows both group delay and bit synch tracking as the angle of the transfer function at the center of the band is varied over 360° (a discussion of the significance of this approach is provided in Section 3.2.1). The correspondence between group delay and modem tracking is even more pronounced in the case of the baseband modem.

Because of the correspondence cited above it is of interest to examine the behavior of the group delay in fading situations. This topic is discussed in detail in Section 2.3.3. Here, we

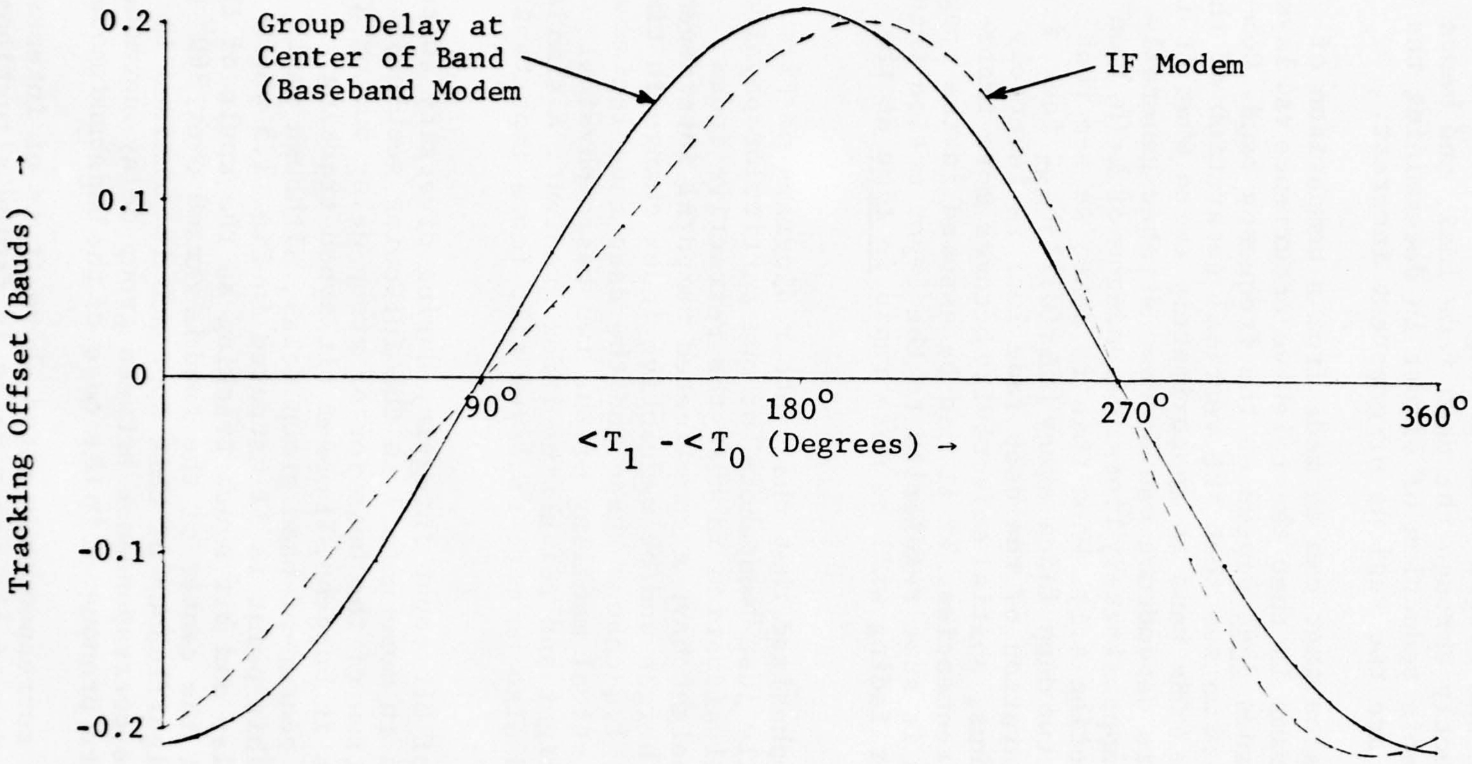

Refractive Index Gradient = -400 Nu/km
Layer Tilt Slope = 0.007
Fade Depth = 30 dB
Layer Height = 2270 Feet

Figure 1.5 Modem Tracking Behavior

merely point out that the group delay must in general satisfy the inequality

$$\tau_g \leq \frac{\sum_{i=1}^{N} \alpha_i |\tau_i|}{L} \tag{1.2}$$

where L is the center-of-band fade level, N is the number of interfering paths and α_i and τ_i are respectively the amplitude and delay on the i'th path. An important point in this connection is that the upper bound in (1.2) cannot be reached unless the frequency is such that the fade level is at a minimum. This indicates a close correspondence between the deep fade loci and the most extreme values of group delay—a correspondence that has been validated without exception in our plots of these quantities. Another point is that the group delay is unsubstantial when signal level is high, $L \gtrsim 1$. In such a situation most of the links we have studied (extremely long links excluded) indicate that the group delay magnitude remains below 10 ns. In a deep fade, however, the group delay can be extremely large (see Section 2.4 and Section 1.3.4 below) and often comes quite close to achieving the upper bound in (1.2).

1.3.3 Diversity Operation

The fading characteristics discussed above impact diversity operation simply by virtue of the fact that they differ from diversity channel to diversity channel. To get the full benefits of diversity operation one ideally would like to have the situation where there is always a strong, clear signal on the standby channel whenever the signal in the primary channel is unacceptably degraded. This situation corresponds to the case of non-overlapping deep fade loci when the contour diagrams for each diversity channel are superimposed. For the most part, a reasonable choice of diversity operating parameters results in just this condition. This is shown in Fig. 1.6 and consists of the 20 dB fade contour of Fig. 1.4 (diversity channel #1) with the 20 dB fade contours of a space diversity channel with receiving antenna located 30 feet below the primary receiving antenna. There is no overlap of the 20 dB fade contours; i.e., although some are close, as with the two pairs near 20 feet, simultaneous center-of-band fading below 20 dB will not take place. Note, however, for a carrier frequency (about 8.415 GHz) half way inbetween the two nodes at 22 feet, one space diversity channel may experience a 20 dB fade at the lower end of the band (14 MHz assumed) and the other may experience a 20 dB fade at the high end. One concludes, overall, however, that simultaneous center-of-band deep fading on both diversity channels is unlikely, as it should be.

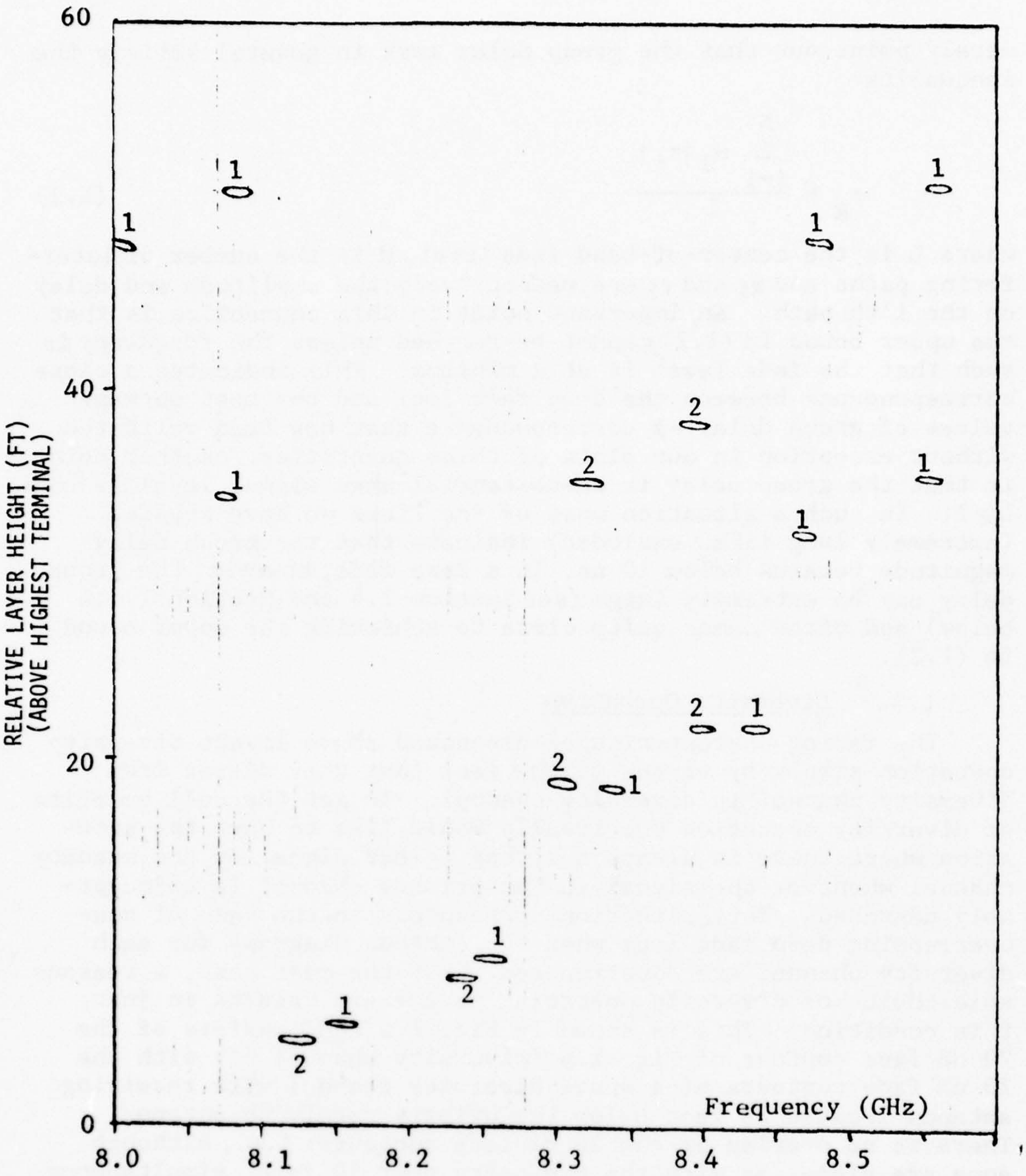

GROUND RANGE = 30 MILES
REFRACTIVE INDEX GRADIENT = -420 Nu/km
LAYER THICKNESS > 62.6 FEET

Figure 1.6 20-dB Fade Contours on Both Diversity Channels (Contours are numbered according to diversity channel) Receiver #1 is 80' above transmitter; Receiver #2 is 55' above transmitter

Space diversity operation is illustrated in Fig. 1.7 for a particular link of interest, the Swingate-Houtem link spanning the English Channel. The desired correspondence of nulls on one channel with high signal levels on the other is clear from the figure. A detailed discussion is provided in Section 4.

Relative to frequency diversity, simple rules, based for the most part on the expression that locates the deep fade frequencies (see Section 2.3.3), can be used to determine the "optimal" separation of carrier frequencies in specific situations. As a numerical example, our expressions indicate a frequency separation of 460 MHz for the physical situation used to generate the plot in Fig. 1.8. The plot, which illustrates the frequency selectivity across the whole band of permitted carrier frequencies on the Swingate-Houtem link, shows the reasonableness of this choice; the choice corresponds well with the distance between peak and null. To generate rules of general utility, statistical modeling is required.

With the purpose of examining a physical mechanism that in some circumstances will result in loss of bit count integrity, we now turn to a more microscopic view of the deep fade loci. Our concern here relates to the following question; what are the effects of diversity switching between space diversity channels as a layer moves through a deep fade locus?

We consider three simple diversity rules:

1. Switch to other channel if current channel fades to depth greater than 30 dB and other channel is stronger.
2. Switch to other channel if current channel fades to depth greater than 20 dB and other channel is stronger.
3. Switch to other channel if stronger than current channel.

Recall from our discussion of Section 1.3.2 that the largest excursions of group delay tend to occur during the deepest fades. This implies that diversity switching from a diversity channel with a deep fade on it to another channel with little or no fade is equivalent to switching from a channel with a large group delay to a channel with very small group delay. Because of the rapid switching on digital links, there can be a large sudden discontinuity in delay and hence a loss of bit count integrity.

For concreteness we look at the fade in Fig. 1.9 and assume upward layer motion* and initial operation of diversity channel #1. In Fig. 1.10 we have presented the group delay plot

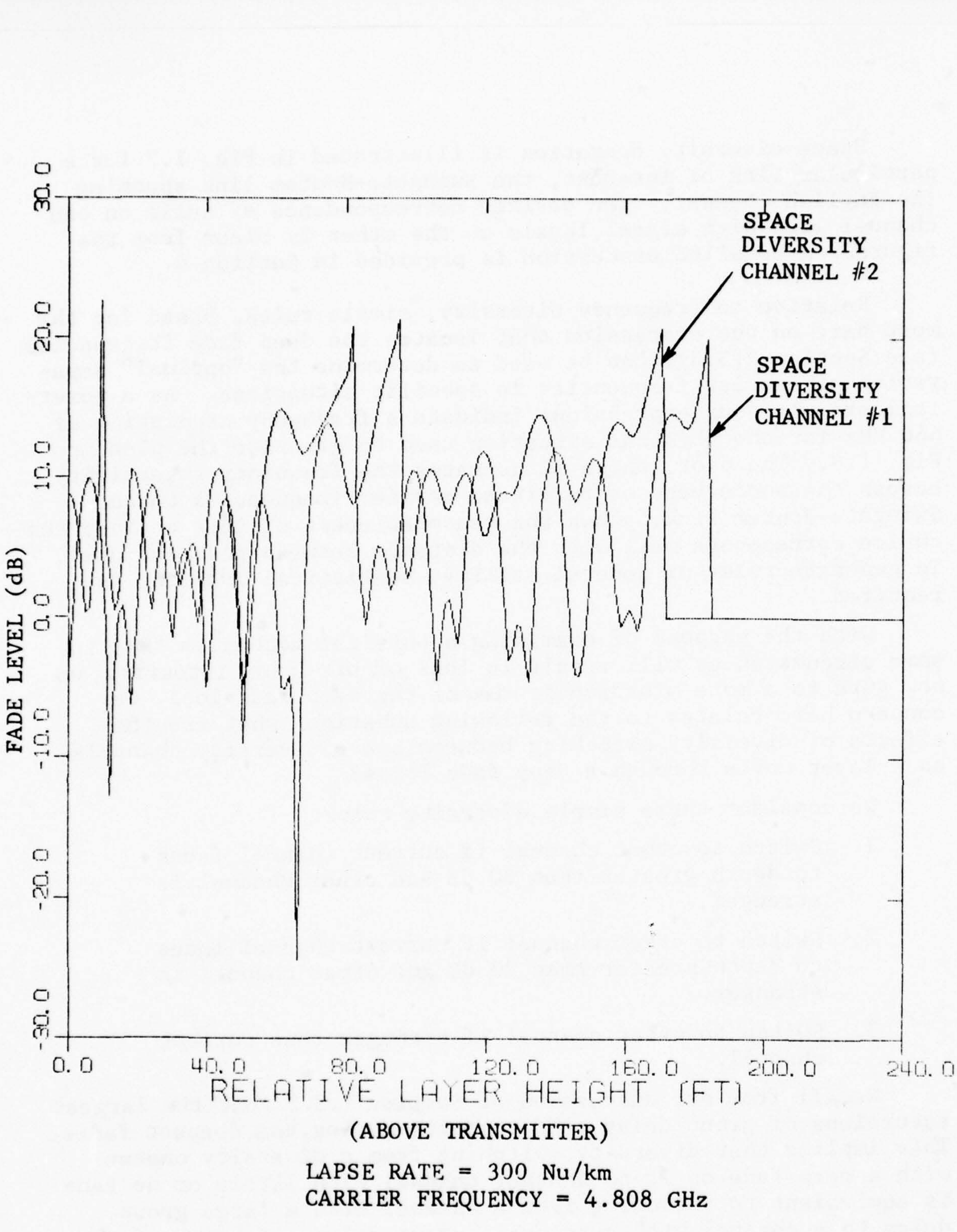

Figure 1.7 Theoretical Space Diversity Fade Record on Swingate-Houtem Link

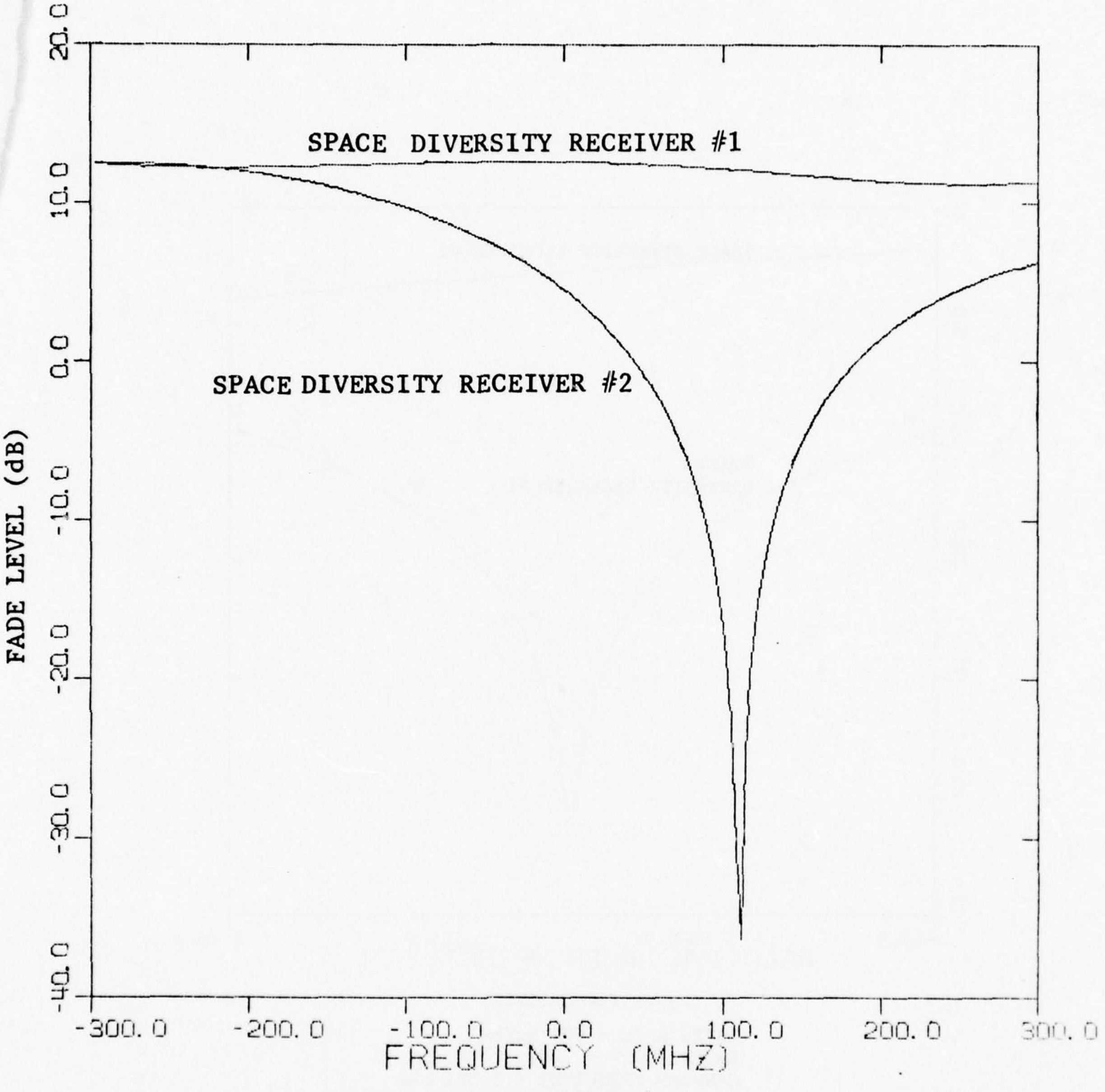

LAPSE RATE = 300 Nu/km
CENTER FREQUENCY = 4.7 GHz
LAYER HEIGHT = 65.9 FEET

Figure 1.8 Fade Level Vs. Frequency Over Total Band for Horizontal Layer on Swingate-Houtem Link

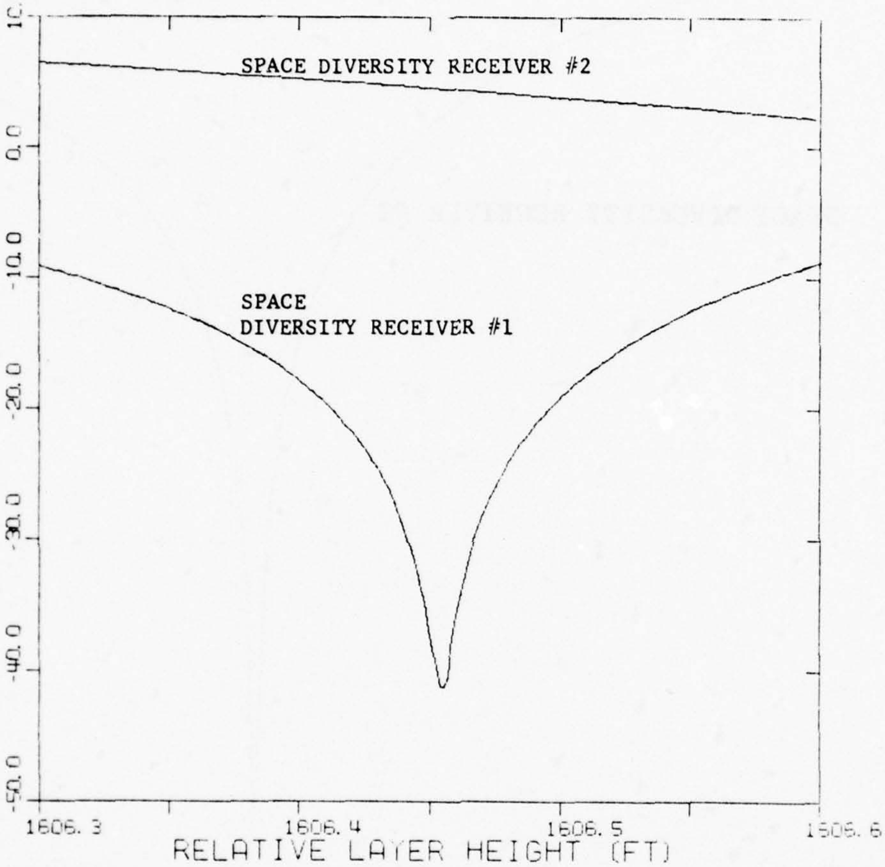

(ABOVE TRANSMITTER)

LAPSE RATE = 400 Nu/km
LAYER SLOPE = .009
CARRIER FREQUENCY = 8.301 GHz

Figure 1.9 Fade Depth Vs. Layer Height on Hohenstadt-Zugspitze Link

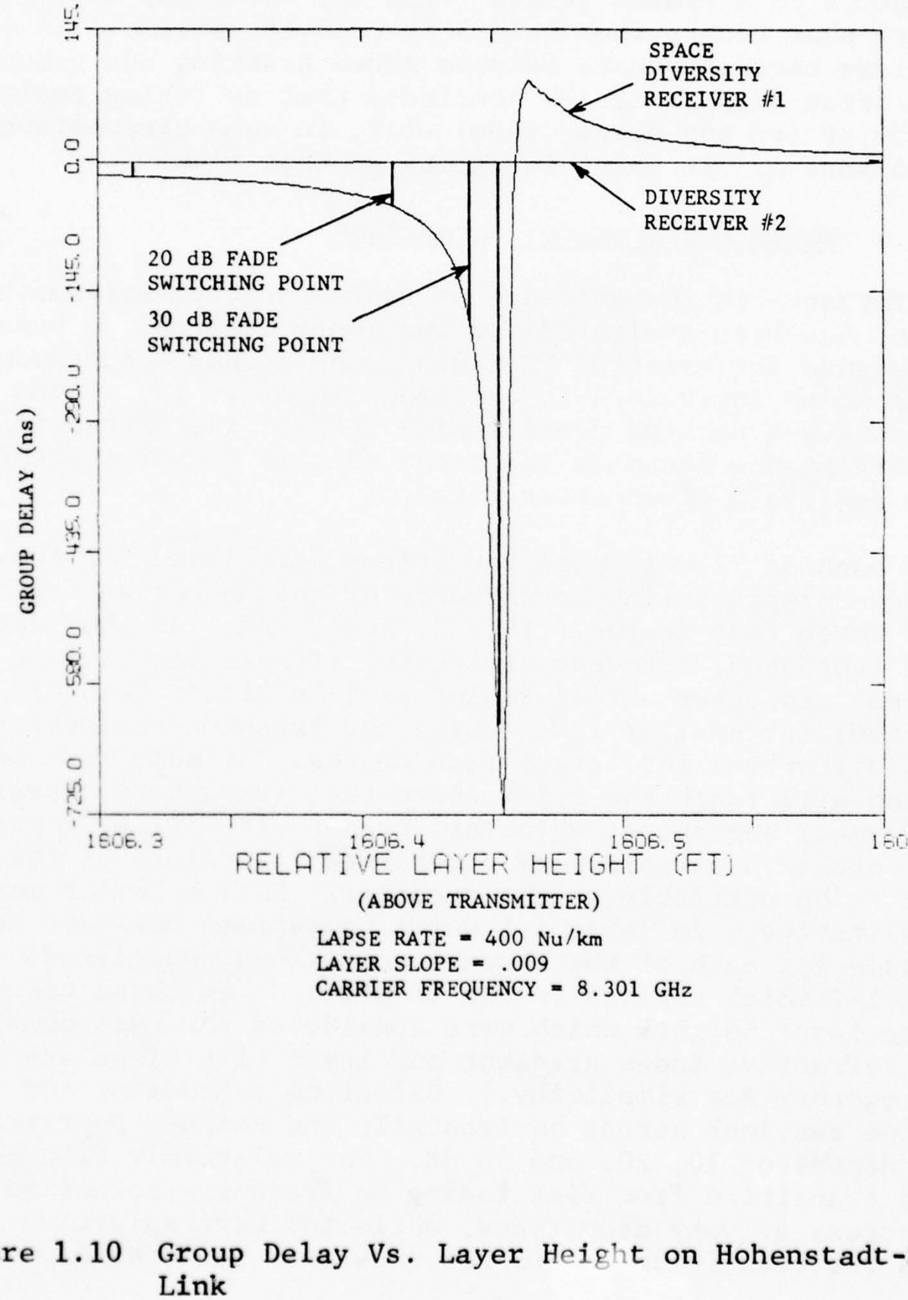

Figure 1.10 Group Delay Vs. Layer Height on Hohenstadt-Zugspitze Link

corresponding to Fig. 1.9 and marked off the points at which switching takes place according to the diversity rules listed above. For rule 1 we get a discontinuity of 177 ns. For rule 2 a 50 ns discontinuity occurs, whereas for rule 3 it can be shown on an expanded scale that the discontinuities are considerably less than 10 ns.

Relative to a symbol length (72.3 ns) the group delay discontinuity that occurs when rule 3 is used is extreme. In view of the close correspondence between modem tracking and group delay (Section 4.2) it can be concluded that switching during a fade to 30 dB (or any deeper fade) will, in some circumstances, result in loss of bit count integrity on this link.

1.3.4 Modem Performance Degradation

Performance in the presence of representative multipath conditions has been evaluated for two modem designs: a baseband modem designed for existing FM radios, and a phase-continuous FSK modem which interfaces to existing radios at IF. Both modems achieve a packing density of 2 Bps/Hz; the latter is a higher performance modem in the sense that it requires a smaller E_b/N_0 to achieve a given error rate.

For each of 27 multipath conditions calculated for the Hohenstadt-Zugspitze link performance of the modems was calculated at three fade depths: 10, 20, and 30 dB. As the depth of the fade increases, frequency-selective effects become more pronounced. In other words, fading will be "flat" (that is undistorted) for smaller fade depths and frequency-selective (that is distorted) for larger fade depths. At some fade depth distortion will reach the point where the eye-pattern closes for certain symbol sequences; when this happens it will be impossible to obtain a satisfactory error rate regardless of the value of E_b/N_0 available to the receiver. This behavior may be seen qualitatively in Table 1-1 which summarizes baseband modem performance for each of the channel conditions considered, or in Table 1-2 which applies to the IF modem. (In these tables the three layer heights which were considered for each combination of refractive index gradient and layer tilt slope are lumped together for simplicity.) Selecting a gradient and slope, one can look across horizontally and compare performance at fade depths of 10, 20, and 30 dB. For relatively flat channels the transition from flat fading to frequency-selective fading occurs at very deep fades, while for more selective channels the transition occurs for shallower fade depths. Since

TABLE 1-1

QUALITATIVE FADING BEHAVIOR OF BASEBAND MODEM

Refractive Index Gradient (Nu/km)	Layer Tilt Slope	Layer Tilt Angle (Degrees)	Fade Depth		
			10 dB	20 dB	30 dB
-400	0.007	0.401	Flat	Flat	Nearly Flat (Fig. 3.6)
	0.008	0.458	Flat (Fig. 3.7)	Mixed (Fig. 3.8)	Completely Degraded
	0.009	0.516	Nearly Flat (Fig. 3.9)	Completely Degraded	Completely Degraded
	0.010	0.573	Mixed (Fig. 3.10)	Completely Degraded	Completely Degraded
-350	0.008	0.458	Flat	Flat	Nearly Flat (Fig. 3.11)
	0.009	0.516	Flat	Mixed (Fig. 3.12)	Completely Degraded
	0.010	0.573	Nearly Flat (Fig. 3.13)	Completely Degraded	Completely Degraded
-300	0.009	0.516	Flat	Flat	Flat (Fig. 3.14)
	0.010	0.573	Flat	Nearly Flat (Fig. 3.15)	Completely Degraded

(The term "completely degraded" indicates eye closure and an error rate exceeding 10^{-2} over the range of received E_b/N_0 considered.)

TABLE 1-2
QUALITATIVE FADING BEHAVIOR OF IF MODEM

Refractive Index Gradient (Nu/km)	Layer Tilt Slope	Layer Tilt Angle (Degrees)	Fade Depth		
			10 dB	20 dB	30 dB
-400	0.007	0.401	Flat	Flat	Nearly Flat (Fig. 3.16)
	0.008	0.458	Flat	Nearly Flat (Fig. 3.17)	Completely Degraded
	0.009	0.516	Nearly Flat (Fig.3.18)	Mixed (Fig. 3.19)	Completely Degraded
	0.010	0.573	Nearly Flat (Fig.3.20)	Completely Degraded	Completely Degraded
-350	0.008	0.458	Flat	Flat	Nearly Flat (Fig. 3.21)
	0.009	0.516	Flat	Nearly Flat (Fig. 3.22)	Completely Degraded
	0.010	0.573	Nearly Flat	Degraded (Fig. 3.23)	Completely Degraded
-300	0.009	0.516	Flat	Flat	Flat (Fig. 3.24)
	0.010	0.573	Flat	Nearly Flat (Fig. 3.25)	Degraded (Fig. 3.26)

(The term "completely degraded" indicates eye closure and an error rate exceeding 10^{-2} over the range of received E_b/N_0 considered.)

fade depth is quantized to 10 dB increments in this table, the transition from flat fading to complete degradation is usually abrupt. Individual performance curves on which the tables are based may be found in Section 3.2.

Summarizing, our evaluation of SNR degradation of modem performance due to frequency-selective fading reveals that the performance losses can vary widely with change of physical conditions. In all cases the SNR degradation increases as the fading on the link becomes more frequency-selective. Due to the increased frequency-selectivity of some physical situations (see Tables 1-1 and 1-2) complete degradation can occur in a 20 dB fade. Increased frequency-selectivity, of course, corresponds, to increased delay spreads of the ray paths, and the trend toward greater frequency-selectivity corresponds generally with increases in lapse rate of refractive index gradient and, ad-hoc, increases in layer tilt. (As an example we point out that layer slope variations from .007 to .010 in Table 1-1, corresponding to a refractive index gradient of 400 Nu/km, are accompanied by delay spreads of the layer rays ranging from about 2.4 ns to 4.4 ns.) The parallel trends of increased frequency-selectivity and increased SNR degradation due to signal distortion are clear from the tables. (See Section 3 for detailed discussion.)

Comparing Tables 1-1 and 1-2 it may be seen that the effects of multipath on the two modems are remarkably similar. However, a careful examination of the tables or of the figures in Section 3 (Figs. 3.6 through 3.26) shows that the FSK modem is somewhat less susceptible to multipath than the baseband modem.

SECTION 1

REFERENCES

[1.1] R. W. Hubbard and R. F. Linfield, "Wideband Channel Probe Measurements for the DEB (Stage I) Path Test Program," ITS Report, Boulder, Colorado, April 1976.

[1.2] GTE Lenkurt, Inc., Engineering Considerations for Microwave Communications Systems, 1972.

[1.3] "Line-of-Sight Techniques Investigation," Final Report by CNR, Inc., on RADC Contract No. F30602-73-C-0244, (AD-006104).

[1.4] Bean et al., "A World Atlas of Atmospheric Radio Refractivity," Essa Monograph No. 1, U.S. Government Printing Office, Washington, D.C., 1966.

[1.5] B. R. Bean and E. J. Dutton, Radio Meteorology, National Bureau of Standards Monograph 92, 1 March 1966.

[1.6] C. A. Samson, "Refractivity Gradients in the Northern Hemisphere," OT Report 75-59, U.S. Department of Commerce, April 1975.

[1.7] R. L. Kaylor, "A Statistical Study of Selective Fading of Super-High Frequency Radio Signals," Bell Systems Technical Journal, September 1958.

[1.8] P. A. Bello, "A Study of the Relationship Between Multipath Distortion and Wavenumber Spectrum of Refractive Index in Radio Links," Proc. of the IEEE, Vol. 59, No. 1, January 1971, pp. 47 - 75.

SECTION 2

CHANNEL MODELING

In this section we describe, analyze, and examine the causes and effects of frequency-selective fading due to refractive multipath on microwave line-of-sight links. A major goal of the effort described here is to determine the eventual effects on modem performance. Because of its separate importance, however, discussion of this topic is deferred until Section 3.

In Section 2.1 below we describe the propagation channel. The viewpoint in Section 2.1 is primarily a physical one. We discuss the effects of weather on the formation of layers and emphasize the importance of certain layer parameters.

In Section 2.2 we describe our analysis of the propagation channel. This includes:

1) A description of the link and the setting up of the problem.

2) Solution of the problem using geometrical optics with emphasis placed on analyzing the situation wherein the layer is below the highest terminal.

3) Inclusion of layer tilt into the model.

4) Lapse rate requirements for the support of multipath.

It is from the results of this analysis (yielding all of the ray path delays and amplitudes) that one can compute any of the system parameters of interest.

In Section 2.3 we describe the system parameters, fade depth and group delay, and present in general terms a discussion of the P and T parameters that play a pivotal role in both the representation of signal distortion and the modem performance calculations of Section 3. Additionally, we describe in this section a significant relation between the frequencies at which the fade depth and group delay extrema occur.

Two important communication channels of interest, the Hohenstadt-Zugspitze link and the Swingate-Houten link are analyzed in detail in Section 2.4. Fading characteristics of the channel are depicted via plots of the multipath delay and amplitude profiles and plots of fade depth and group delay vs. layer height and frequency. Discussion of diversity effects is deferred until Section 4.

Certain propagation parameters relating to the Hohenstadt-Zugspitze link have been used in the modem performance calculations presented later in Section 3. The way in which these parameters have been selected in order to reduce them to a manageably small set is described in Section 2.4.3.

In Section 2.5 we present a brief review of the literature. The emphasis here is on relating our computed results to the available data that has been accumulated by others.

2.1 Description of Propagation Channel

In this section we describe the physical character of the LOS propagation channel. The basic nature of multipath fading on LOS links is described in Section 2.1.1. Section 2.1.2 describes the effect of weather conditions and the physical mechanism governing the formation of layers. Section 2.1.3 addresses some questions related to layer height and layer thickness.

2.1.1 Morphology of Refractive Multipath

In this section we describe the mechanism of refractive multipath and the physical conditions which cause it.

Generally, it can be said that refractive multipath arises because of the bending of electromagnetic rays in an inhomogenous medium. The equations of geometric optics indicate that electromagnetic rays travel in straight lines in a perfectly uniform atmosphere. In the troposphere, however, the atmosphere is often not uniform; in fact, because of its sandwiched location between the earth and the stratosphere, there may be rapid changes in temperature, pressure, and vapor pressure with height. These gradients, in turn, give rise to a gradient in refractive index. In fact, an acceptable order of magnitude of the variation ΔN of the index of refraction is obtained from the formula,

$$\Delta N \approx \Delta P - \Delta T + 7\,\Delta r \tag{2.1}$$

where ΔP is the pressure variation in millibars, ΔT is the variation of the temperature in degrees Kelvin, and Δr is the variation of the mixing ratio, defined as the mass of water vapor (in grams) mixed with 1 kg of dry air [2.1]. Measurement of each of the constitutive parameters in (2.1) is sometimes used for indirect measurement of N. (See, for example, the description of radiosonde measurements in [2.2].)

In its most commonly occurring state, the troposphere is characterized by a mild refractive index gradient; the refractive index decreases by about 40 Nu/km. In such a case, we say that the lapse rate $\mathcal{L}$ is given by

$$\mathcal{L} = 40 \text{ Nu/km} \tag{2.2}$$

(This is the numerical value used for the "standard" or "direct path" atmosphere in the remainder of this report.*) On some occasions, however, anomalous weather conditions can exist which result in the formation of refractive layers.

---

*It will be recalled that N units are just the usual dimensional units of refractive index multiplied by 10^6 (see [2.3, p. 3-11]).

When this happens, there is the usual "standard" lapse of 40 Nu/km until some unpredictable height, referred to as the "layer height", is reached, at which point a much stronger lapse (e.g., 300 Nu/km) occurs until the "top" of the layer is reached. At this point the milder lapse characterizing the standard atmosphere takes over.

The vertical region, characterized by the larger lapse, is referred to as the "layer". The extent of this region is referred to as the "layer thickness". The vertical point (measured with respect to some convenient reference), at which the stronger larger lapse begins, is referred to as the "layer height".

There are many complications to the picture described above. Not the least of these is the abundance of layer parameters which have not been measured extensively. Discussion of this topic, because it impacts our computer model, is deferred until Section 2.1.3. Another complication arises because the troposphere may not separate in simple fashion into well-defined layers of constant lapse rate. Additionally, the troposphere may vary linearly and/or nonlinearly in the horizontal direction. Although the possibility of such conditions actually occurring can in no way be ruled out, construction of a model based on such considerations would be of little use in view of the all-important fact that there would be no available empirical inputs to the model. Additionally, the use of the refractive index gradient as a valid description of tropospheric propagation is widely accepted. In fact, the entire worldwide effort to measure refractive index gradient is predicated on the assumption that a linear or near-linear dependence of this parameter on height is a dominant influence on tropospherically-propagated waves. If this were not so, the vast array of data collected (see an example in Figure 2.2) would be of little use. The fact that the premise is supported by the stable geometry of large air masses and frontal inversions is discussed in Section 2.1.2.

The basic laws of electromagnetic wave propagation indicate the propagation of waves in curved paths when a refractive index gradient is present. In fact, when the gradient is a constant, the rays travel in circular arcs [2.4]. For point-to-point LOS propagation on the earth's surface, these arcs may be concave-upward or concave-downward depending, respectively, on whether the refractive index increases or decreases with height. A negative refractive index gradient is by far the more common; thus, a ray typically tends to travel in concave-downward arcs. This does not mean that the ray necessarily tends to bend back to earth; the ray, though concave-downward, may have less curvature than the earth's surface and effectively bend away from the earth. A point of importance in this connection is the following: even though a ray path may be concave-downward, as illustrated in Figure 2.1(a), a plot of ray height vs. distance x along the path may exhibit an upward concavity as illustrated in Figure 2.1(b). From an engineering point of view, this latter representation is the one of importance. Analytically, it is achieved via an "earth-flattening" coordinate transformation [2.3]. The path resulting from this transformation, like that in Figure 2.1(b), shall be called the virtual path. Using the convention that a negative radius indicates an upward concavity and a positive radius indicates a downward concavity, we have from [2.3] that the virtual radius in miles is given by

$$R = \frac{0.62139 \times 10^6}{\mathcal{L} - 156.78} \tag{2.3}$$

where $\mathcal{L}$ is the lapse rate of refractive index gradient in Nu/km, i.e., is the rate at which the refractive index decreases with height.

From the expression for virtual radius of curvature in (2.3), we have constructed Table 2-1. In this table we use the descriptive terms "subrefraction", "super-refraction", etc., that have been used extensively in the literature. Each category corresponds to a range of lapse rate, and we have conformed with [2.5] and [2.6] in our definitions ... with one exception. Because of a gap that would occur between $\mathcal{L} = 0$ and $\mathcal{L} = 100$, we have bestowed the title "normal-refractive" on layers having lapse rates in that range.

Our major concern in this report is with layers in the last category. These are the "ducting" layers that give rise to refractive multipath. Extensive programs of measurement of lapse rates which have been and are being carried out on a worldwide basis indicate that ducting layers can and do occur with sufficient frequency to warrant concern.

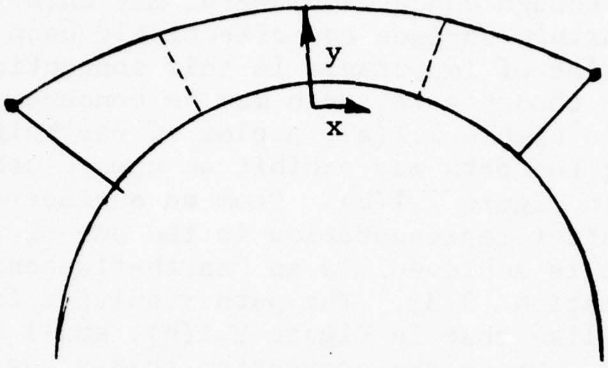

(a) Actual Path

Concave-downward Ray Path Above Earth

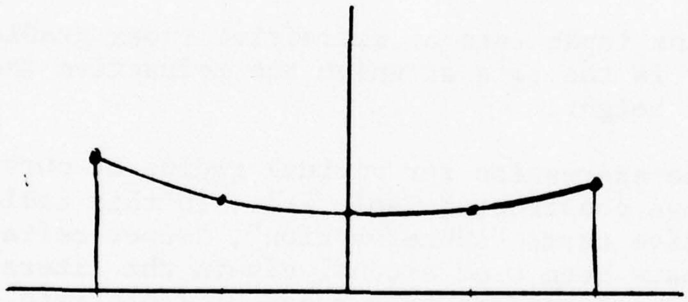

(b) Virtual Path

Plot of y vs. x, where
y ≡ height of ray path above earth
x ≡ distance along earth from
center point

Figure 2.1 Comparison of Actual Path and Virtual Path Geometries

TABLE 2-1

TYPES OF REFRACTIVE LAYERS

($\mathcal{L} \equiv$ lapse rate of refractive index gradient in Nu/km)

Type of Layer	Type of Lapse Rate	Ray Curvature on Actual Path	Ray Curvature on Virtual Path	Comments
1. Subrefractive	$\mathcal{L} \leq 0$	Concave upward (flat at $\mathcal{L} = 0$)	Concave upward	Reduces radio horizon; causes diffraction ("earth-bulge") fading
2. Normal-refractive	$0 < \mathcal{L} \leq 100$	Concave downward	Concave upward	No striking effects
3. Super-refractive	$100 < \mathcal{L} \leq 156.8$	Concave downward	Concave upward (flat at $\mathcal{L} = 156.8$)	Greatly extends service horizons; may cause interference between widely separated radio circuits operating on the same frequency
4. Ducting	$\mathcal{L} > 156.8$	Concave downward	Concave downward	Can cause serious multipath fading

This was clearly evident in the early comprehensive data of Bean, et al. [2.5] and from several measurement programs that have been described since [2.6], [2.7].

A wide-ranging collection of probability distributions is gathered together in [2.6]. One of particular interest, since it relates to our calculations on the Hohenstadt-Zugspitze link [see Section 2.4.1] is the data for Stuttgart, Germany, shown in Figure 2.2. This data shows that .2% of the observations made in Stuttgart indicated that the lapse rate exceeded 300 Nu/km. As pointed out in [2.8], this data is justifiable extrapolated to the Hohenstadt-Zugspitze link. Unfortunately, the information in Figure 2.2 does not constitute a comprehensive data source. The reason for this is that measurements were only taken two times a day (at the same time of day) for several months. If nothing more, the data certainly indicates the occasional occurrence of large lapse rate, whereas some places in the world never show lapse rates in excess of 150 Nu/km. (See data for Chita in the Soviet Union.) In such regions the phenomena of ducting rarely, if ever, occurs. In other regions, it appears to occur with substantial regularity.

2.1.2 Weather Effects and Formation of Layer

Refractive layers cannot occur unless there are gradients in pressure and/or temperature and/or moisture content of the atmosphere. From a consideration of all the available measurements, Craig, et al. [2.9] have adopted the following simple expression for numerical use:

$$(n - 1) \times 10^6 = \frac{c}{T}\left(p_d + e + \frac{be}{T}\right) = \frac{c}{T}\left(p + \frac{be}{T}\right) \qquad (2.4)$$

where

n = the index of refraction of moist air
c = 79°K/mb
b = 4800°K
T = temperature in °K
p = total pressure in mb
e = the partial pressure of water vapor in mb

When n is replaced by the modified refractive index, the left-hand side of (3.4) becomes a quantity that is called the refractive modulus M.

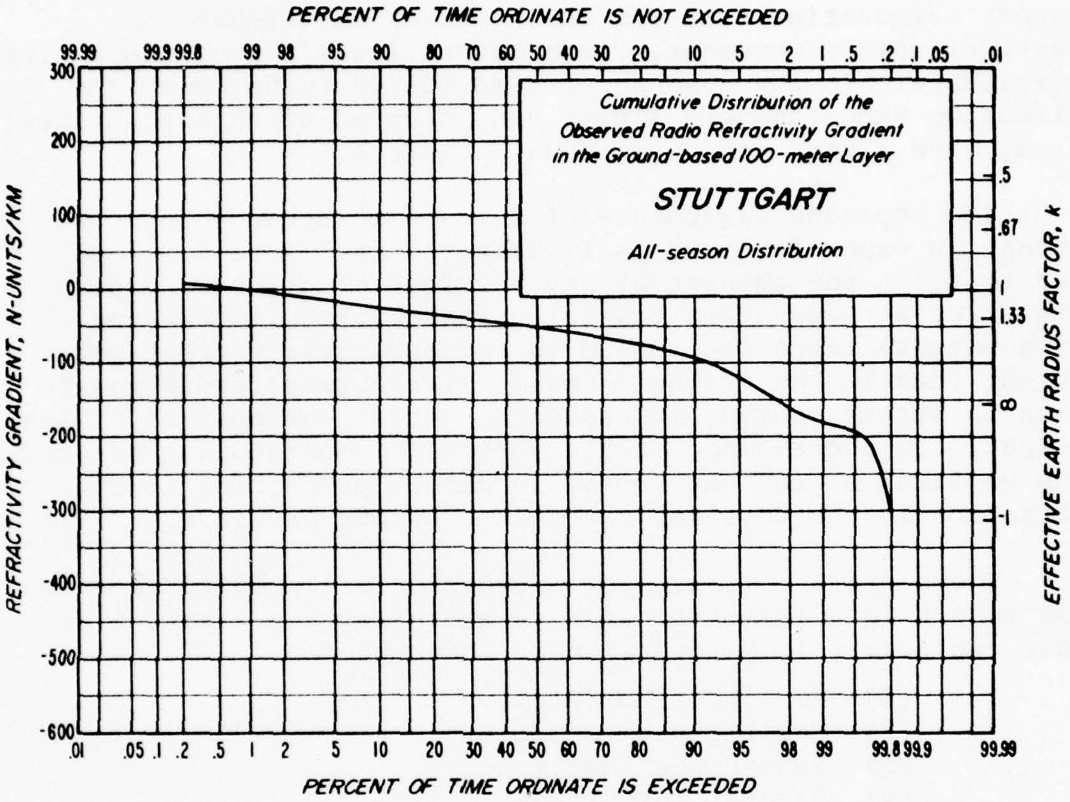

<u>Note</u>: k = -R/a where R is the radius of curvature in text and a is the earth's radius.

Figure 2.2 Distribution of Radiosonde Data for Stuttgart, Germany (Federal Republic) From [2.6]

Pressure varies so slowly with height that its contribution to (2.4) can be discounted. On the other hand, the humidity variation is an important part of ΔM. The water vapor, evaporating from the earth, tends to diffuse in a vertical upward movement, distributing iteself over the entire atmosphere. In the absence of atmospheric turbulence, the diffusion proceeds very slowly and, because of this stability, e may have a very strong vertical gradient.

The separate dependence of M on temperature change and change in vapor pressure is illustrated in Figure 2.3. We see that, in the absence of any vertical gradient of vapor pressure, a temperature inversion (temperature increasing with height) tends to cause M to increase less rapidly with height than in the standard case. If the temperature inversion is strong enough, it causes an actual decrease of M with height. In the absence of any vertical temperature gradient, the vertical M gradient varies in direct proportion to the variation in the vertical gradient of vapor pressure.

There are a multitude of meteorological conditions that can result in a formation of a super-refracting layer, i.e., that can result in M inversions. These are:

(1) Heating from below
(2) Cooling from below
(3) Subsidence inversions
(4) Frontal inversions

Craig and Montgomery [2.10] have presented a graphic description of "heating from below", one of the more common causes of layer formation. Following their scenario, we examine the sequence of events occurring on a calm clear morning as a result of the ground being warmed by solar radiation. Near the initially cold ground there is an initially stable air mass but, as the ground heats up, packets of air warmed by contact with the ground begin to rise convectively. These packets accelerate at first and then begin to declerate at a level that is well-defined from thermodynamic considerations, i.e., "there is a definite top to the convection". The overall result of heating from below is the formation of three layers:

(1) A narrow surface layer near the ground characterized by strong gradients but slight turbulence (air packets are just starting their acceleration)

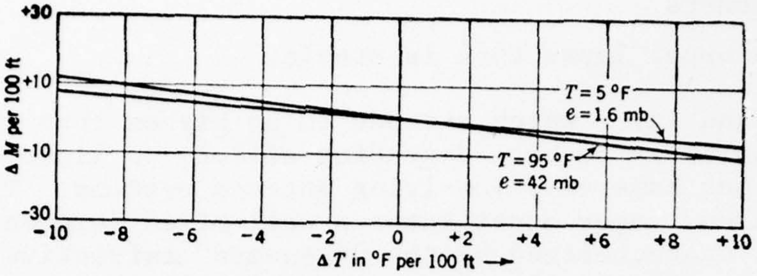

(a) M-Gradient vs. Temperature

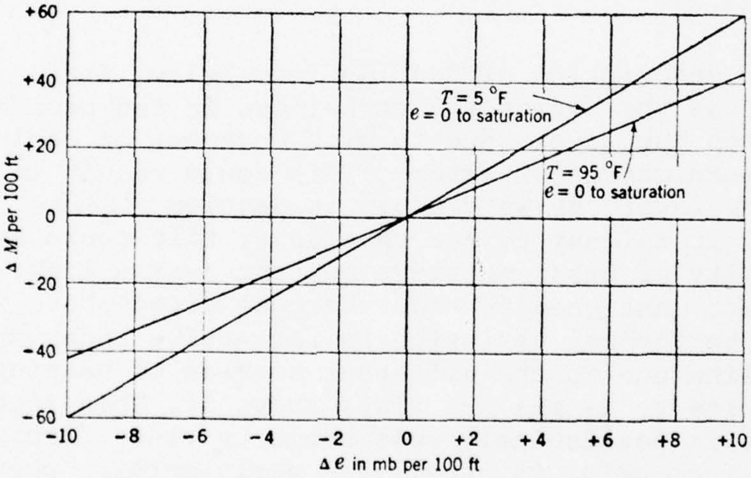

(b) M-Gradient vs. Vapor Pressure

Figure 2.3 M-Gradients Produced by Gradients of Temperature and Vapor Pressure (from [2.9])

(2) A thick central layer characterized by strong turbulence due to rapid convection of the air packets

(3) An upper layer that is stable.

The ground layer which extends to no higher than about 50 feet is unlikely to have degrading effects on links other than those that have very low-lying antenna systems. The second turbulent layer constitutes a well-mixed homogenous layer and is characterized by the "standard" refractive index gradient (about -40 Nu/km). The highest layer is stable, but is commonly characterized by a lapse of water vapor concentration. To quote Craig and Montgomery [2.10] "The stable layer is therefore usually superstandard."* This observation derives from the data of Figure 2.3(b).

The features that the above description have in common with our computer model illustrated later in Figure 2.5 – 2.7 should be apparent.

In their description of heating from below, the authors go on to discuss the horizontal variations in the boundary heights between the layers due to wind movement of cool air masses over warm masses of water. This could result in tilting of the layer, as we discuss in Section 2.2.3. Additionally, it is easy to see that layer tilt could arise from variability of earth moisture content over a link. A possibility not mentioned in the reference cited above would be a regular horizontal variation in refractive index profile over a long link due to the different degrees of heating that the link submits to as the sun rises above it. This mechanism of layer tilt is particularly reasonable in view of the fact that heating from below is usually an early morning phenomenon.

One interesting feature of the scenario discussed above is the "fully-developed turbulence" in the intermediate homogenous layer. This layer, which is called the "direct

---

*Meteorologists, for purposes of easy reference, often break down the several situations we have categorized in Table 2-1 into standard, substandard, and superstandard. By "substandard" they refer to the condition wherein the refractive index increases more rapidly with height than in the standard case. By superstandard they refer to a greater rate of decrease.

path" or "pseudo-direct path" in our model (see Section 2.2.1) has not been investigated as a turbulent (scintillating) channel. As mentioned above, the region below the stable layers causing refractive multipath, though characterized on the average by the lapse rate for the "standard" atmosphere, may exhibit strong turbulence. Turbulence, or randomness of the refractive index, has long been a topic of interest for experts on atmospheric propagation. The general consensus, however, is that the rms values of amplitude fluctuations are so small as to not warrant undue consideration as far as communication system performance is concerned; typical estimates [2.3] are that the rms value of the randomly fluctuating phasor representing the turbulence is 20 dB down from the direct path. Consider the implications of this report, however; classical interference of multipath rays can, with a high enough probability to warrant concern, yield a resultant phasor (signal level) that is 20 dB down from the direct path signal level. Now, consider a random phasor (rms value 20 dB down from the direct path) that is added to the phasor representing the direct path. By superposition this phasor can be added to the resultant phasor of the classical multipath interference. We find ourselves in the position of adding a random phasor with rms value 20 dB down from the direct path to a small "deterministic" phasor of approximately the same amplitude. The effects can be dramatic. Whereas, turbulence can normally be neglected, a deep fade condition due to refractive multipath can greatly magnify its effects. It is recommended that this condition, probable in a meteorological context, be investigated more fully.

The phenomenon of subsidence is also known to be a cause of superstandard refractive conditions; this phenomenon is the sinking or lowering of large masses of air from high to low levels. For reasons described by Craig [2.11], this condition tends to result in stable layers below which exists a region wherein air is mixed by turbulence or convection. The base of the layer (subsidence) is often characterized by a subsidence inversion wherein the humidity rapidly decreases with height; this latter situation arises because the air above the inversion, having descended from higher levels, is usually very dry. Because of the temperature increase, which is always present, and the humidity decrease, which is frequently present, there is practically always a superstandard M gradient in a subsidence inversion.

Fronts can have important effects on temperature, humidity, and M profile, but because their effects are more variable than those of subsidence, meteorologists are reluctant to make general statements about the effects they will have on propagation. A front (or frontal surface) is the boundary between two large air masses and, because the overriding air mass is the warmer one, there is always a stable layer and often a temperature inversion. Unlike the interaction between two large air masses in a subsidence inversion, the overriding air is moist. Some information is available on slopes of frontal surfaces, however (see Section 2.2.3 below). The same physical mechanisms governing the tilt of fronts govern the tilt of subsidence boundaries as well and, in lieu of more definitive data, have been used in our computer model.

2.1.3 Additional Layer Parameters

In this section we discuss two additional layer parameters, the layer thickness, and the layer height.

Dependence of multipath fading on layer thickness has an "on or off" character to it. A layer is either thick enough to trap a given ray or is so thin that the ray escapes from the top of the layer and bends away from the earth. A record of fade level vs. layer thickness (all other parameters constant) would display sharp discontinuities due to this phenomenon.

Some measurements of layer thickness have been made. Statistical distributions of layer thickness, based on measurements over a three-year period in the Arctic (Fairbanks, Alaska), in a temperature climate (Washington, DC), and in a tropical maritime climate (Swan Island), are reported by Bean and Dutton [2.2]. This data is reproduced in Figure 2.4. Note that one can make the rough conclusion from this figure that layers with thickness in excess of 280 meters were observed 2% of the time in the temperature region.

Beckmann and Spizzichino [2.1] have also presented data on layer thicknesses. Their rough deductions from measurement of the cutoff wavelength indicate that layers with thicknesses in excess of 100 m may be present more than 10% of the time.

Unfortunately, there does not seem to be data available on the joint statistics of layer thickness and refractive index gradient; i.e., we cannot gain any insight into the frequency of occurrence of thick layers with large lapse rates.

Layer height is another parameter for which the data is very limited. In fact, because there seems to be no useful data available for layer heights, we have tended to view this parameter as an independent variable against which to plot the results of our calculations. There are reasons to suspect that the height of the layer is a highly variable dynamic quantity. In fact, Bullington [2.12] has come up with estimates of vertical velocity for layers (a few feet per minute).

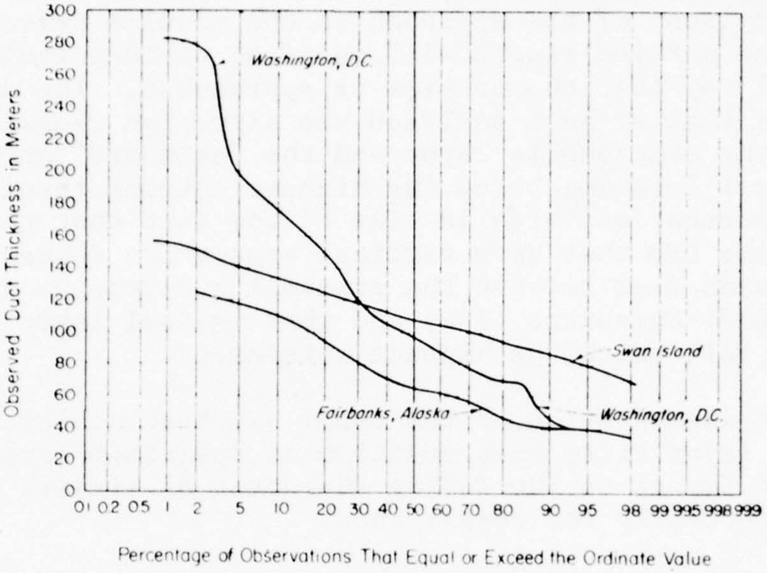

Figure 2.4 Statistical Distribution of Layer Thickness (from [2.2])

2.2 Analysis of Propagation Channel

In this section we describe our analysis of refractive multipath on LOS links. The analysis, of course, draws on earlier analytical approaches presented in a previous CNR report [2.13]. Comparisons of the approach to the problem presented here and in the earlier report will manifest obvious similarities in the general way that the problem is approached. The difference, here, is that we have analyzed the situation wherein the interface of the atmospheric layer and the "standard" atmosphere is at a vertical location below the highest antenna terminal. This is an important addition in view of the fact that there are links in the DEB that have vertical separation distances of a few thousand feet between the transmit and receive antennas (e.g., Hohenstadt-Zugspitze link) and that typical layer heights on such links fall below the highest antenna.

A further augmentation of the model has been achieved by incorporating layer tilt; this addition as described earlier can have great impact on the fading character of signals on some links, especially the longer ones.

The link model is set up and described in Section 2.2.1. The solution of the problem, including calculation of direct path and multipath quantities, is described in Section 2.2.2. The manner in which the model is adapted to include layer tilt is described in Section 2.2.3. In Section 2.2.4 we show how the analytical results can be used to determine bounds on refractive index gradient, i.e., we determine how large a lapse rate of this all-important parameter is required in order that multipath be supported on a given link.

The analysis described in this section is the mathematical framework for the CNR software that has been used to generate all of the fading characteristics of the channel presented in this report and the propagation parameters (ray path delays and amplitudes) used as input values to the modem performance software described in Section 3.

2.2.1 Description of Link

The manner in which refractive layers are generated by atmospheric conditions was described in Section 2.1.2. Throughout the remainder of this report, it is assumed that there exists a stable layer of finite thickness at the link location. The bottom interface of this layer can lie above or below the highest terminal, as illustrated in Figure 2.5. In Figure 2.5(a) we see the situation wherein the layer interface is above the highest receiver; this is subsequently referred to as condition "A". It will be recalled that this situation has been analyzed before with some computations appearing in [2.3] and [2.13]. Because of limitations in application to links with extreme geometries (like some of those in the DEB), it was deemed necessary, however, to perform an analysis of the situation shown in Figure 2.5(b). In this figure we see the lower layer interface positioned below the receiver. We call this condition "B". The difference between this situation and the previous model developed at CNR is that the receiver is located within the layer.

Expanded views of the situations illustrated in Figure 2.5 are shown in Figures 2.6 and 2.7. The first of these, which appeared in an earlier report [2.13], illustrates condition "A"; the layer interface is above the receiver. The second illustrates condition "B" which will be given a detailed treatment in Sections 2.2.2 and 2.2.3.

The primary difficulty in the analysis (as with the previous analysis) relates to determining the ray transmit and receive angles, θ_0^T and θ_0^R, respectively. The nature of the medium is such (constant refractive index gradient) that once these two angles are determined, the single corresponding multipath ray path is completely defined; the associated delay and power loss can then be quickly computed. A multiplicity of ray paths is possible because of the multiplicity of solution pairs θ_T and θ_R and because of the variable number n of L_2 segments*. Unfortunately, the fact that the current model (condition "B") places the receiver in a region characterized

---

*The usual case of interest is $n = 0$. For any given link geometry, the case $n > 0$ requires a more extreme refractive condition of the layer than the $n = 0$ case.

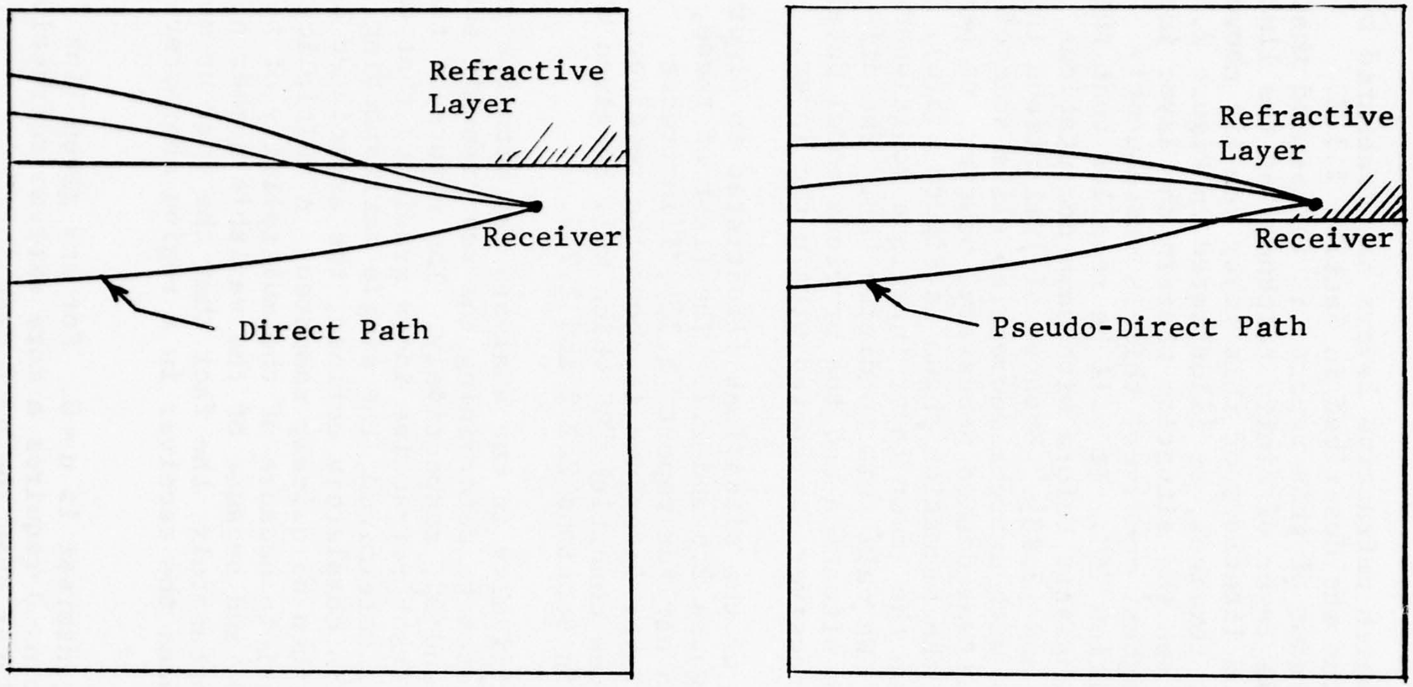

(a) Layer Above Receiver (Condition "A")

(b) Layer Below Receiver (Condition "B")

Figure 2.5 Layer-Receiver Geometry

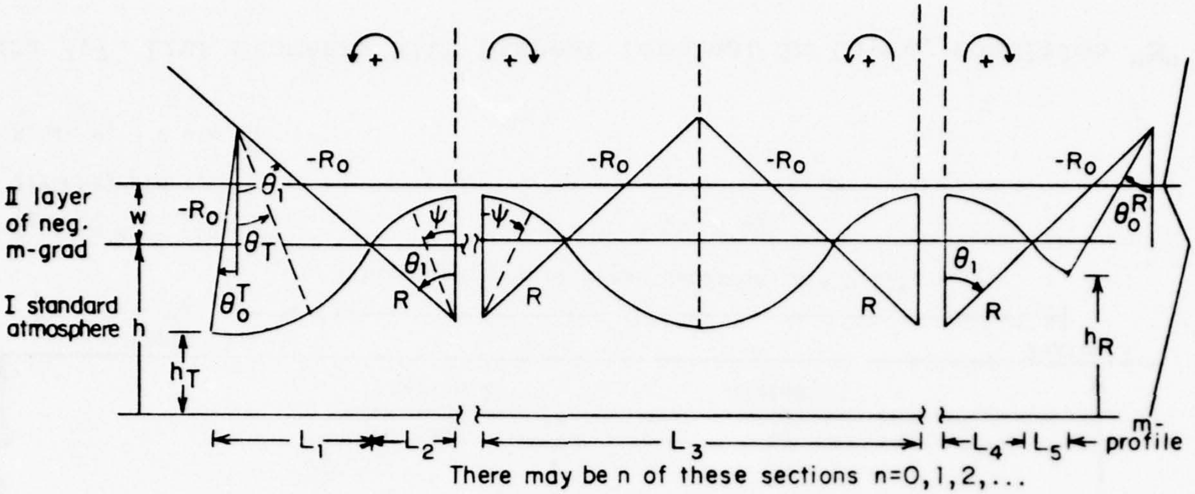

$L_1 = R_o(\sin\,\theta_o^T - \sin\,\theta_1)$

$L_2 = R\,\sin\theta_1$

$L_3 = 2(R-R_o)\,\sin\,\theta_1$

$L_4 = R\,\sin\,\theta_1$

$L_5 = R_o(\sin\,\theta_o^R - \sin\,\theta_1)$

Figure 2.6 Geometry of Single Stratified Layer Above Terminals, Condition "A" From [2.13]

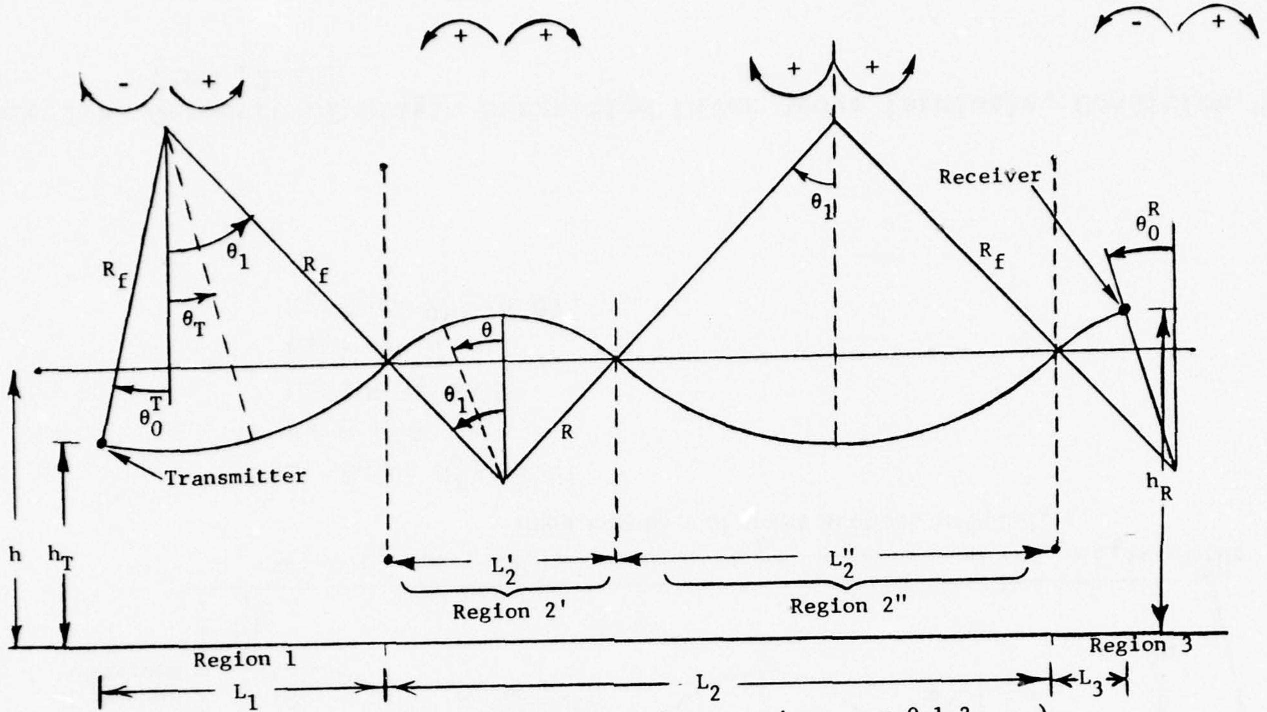

(There may be n of these sections, n = 0,1,2, ...)

$L_1 = R_f (\sin \theta_1 - \sin \theta_0^T)$

$L_2 = 2(R + Rf) \sin \theta_1$

$L_3 = R \sin \theta_1 + R \sin \theta_0^R$

$L = L_1 + nL_2 + L_3$

Figure 2.7 Link Geometry With Highest Terminal in Layer, Condition "B" by a different refractive index than that characterizing the region surrounding the transmitter results in some complications of the analysis. We have been able to solve the problem exactly, however; the details of the solution are provided in Section 2.2.2.

In terms of the parameters and geometries illustrated in Figure 2.7, it can be simply stated that the CNR software, based on analytical results presented in this section, computes the amplitude and delay for each of the ray paths supported by the propagation channel. It is in terms of these, of course, that complete characterization of the communication channel is achieved.

Before proceeding with the analysis, it is important to separate and identify the input parameters. This is required because of the wide variety of different results obtainable with different input parameters and the importance of carefully selecting the input parameters in accordance with available measurements. The list of input parameters is provided in Table 2-2; we have categorized the parameters according to whether they are link design parameters (man-made) or layer-related parameters. We have also categorized them according to whether they are dynamic or static.

The initial analytical treatment assumes a perfectly horizontal refractive layer; the tilted layer case can be converted to this simpler problem via the coordinate transformation discussed in Section 2.2.3. Thus, results in this section will not depend on layer slope S.

Additionally, it will be noted that there are no frequency variables in Table 2-2. Frequency is totally a system parameter (see Section 2.3) and, even though all the system distortion parameters have a strong dependence on frequency, it plays no role in the determination of the ray path delays and amplitudes.

2.2.2 Solution of Problem Using Geometrical Optics

The equations of geometrical optics are perfectly suited for use in determining the delays and amplitudes characterizing LOS links. It will be recalled from electromagnetic theory that wave propagation is governed by the equation of

TABLE 2-2

PROPAGATION INPUT PARAMETERS

Parameter	Definition	Dynamic Nature of Parameter	Comments
L	Ground Range	Static	Range considered 10 - 100 miles Some specific links studied more intensively
h_T	Transmitter Height	Static	
h_R	Receiver Height	Static	
h_L	Layer Height	Dynamic	Complicated combined changes in all of these quantities are the cause of the time variability of fading; h_L and G are thought to be more dynamic than the others
w	Layer Thickness	Dynamic	
S	Layer Slope	Dynamic	
G	Refractive Index Gradient of Layer	Dynamic	It is sometimes more convenient to use "lapse rate" which, algebraically, is just the negative of G

Some basic constants assumed throughout:

$c_0 = 186{,}000$ mi/sec

$R_0 = -5280$ mi.

the eikonal (geometrical optics limit) when two basic conditions hold:

(1) The index of refraction does not change appreciably in a distance equal to the wavelengths of radiation.

(2) In a distance equal to the wavelength of radiation, the fractional change in the spacing between adjacent rays must be small compared to unity.

Clearly, geometrical optics becomes more applicable as one goes to higher frequencies. On the basis of condition (1), a LOS link operating at a carrier frequency $f_c = 1$ GHz was judged to be safely modelable using the geometrical optics approximation [2.3]. On this basis it is deemed thoroughly applicable to the 4- and 8-GHz links treated in this report.

It is not as easy to determine whether geometrical optics applies using condition (2). Work done by Wong [2.14], however, indicates that in the presence of atmospheric layers the rays travel in well-defined bundles. Within each of these bundles, condition (2) is satisfied at all but a finite number of caustic points. At these caustics, which are formed by the intersection of adjacent rays, the ray theory can be slightly modified [2.15], [2.16] to provide approximate field intensity. In the other regions where the separate ray bundles intersect, the relative amplitudes and phases of each bundle can be calculated from ray theory, since each satisfied condition (2). These regions are known as multipath regions, interference regions, and radio anti-holes.

The use of ray techniques has long been a commonly-accepted practice for analysis of microwave line-of-sight links and is used throughout this report without further discussion.

Before commencing with the analysis, it is instructive to note two interesting and important features of the geometrical approach:

(1) The time it takes a wavefront to pass from point a to b along a path is proportional to the integral of refractive index along the path between the points; i.e.,

$$\tau = \frac{1}{c_0} \int_a^b n \, d\sigma \qquad (2.5)$$

where n is the refractive index and c_0 is the free space speed of light.

(b) When the refractive index of a medium changes linearly, i.e., when its gradient $G = \nabla n$ is a constant, the radius of curvature of each ray path in the medium is given by:

$$|R| \approx \left|\frac{1}{G}\right| \qquad (2.6)$$

Equation (2.5), representing delay as a path integral, is the basic means whereby the path delays on LOS links are calculated. One need only know the refractive index and the path geometry. If G is a constant, the value of n at any point is determined from knowledge of h_L and G in Table 2-2. Determination of the ray path geometry is a more difficult task, however, and is a main focus in the remainder of this section. We simply point out here that (2.6) is a crucial aid in determining the path geometry; it indicates that the radius of curvature, like the gradient, is a constant. Hence, the ray paths are segments of circles, an important simplifying feature.

The analytical approach to this problem can be logically divided into two efforts: one is directed at determining delays and amplitudes on the direct path; the other is directed at determining delays and amplitudes of the multipath rays. The distinction between the direct path and the multipath rays is important. The direct path is that path that exists between transmitter and receiver when there is no refractive layer present. A normal, or "average", atmosphere is assumed. This path can alternatively be called the "free-space" or "clear atmosphere" path, but we make no use of such nomenclature. The multipath rays, of course, are those rays that are refracted by the atmospheric layer. Fortunately, the direct path yields simple analytical expressions for delay and amplitude, and is always used as a reference in this report. Thus, rather than referring to a multipath ray with delay 500,002 ns, vis-a-vis a direct path with delay 500,000 ns, we refer to the multipath ray as having delay 2 ns. A similar statement can be made regarding the amplitude. Summarizing, we merely state that henceforth in this report the path amplitude α and path delay ξ of a multipath ray refer to the relative quantities defined below. For the j^{th} ray (out of a total of N rays),

$$\alpha_j^{Rel} = \alpha_j^{abs} / \alpha_1^{abs} \tag{2.7}$$

$$j = 1, \ldots, N$$

$$\xi_j^{Rel} = \xi_j^{abs} - \xi_1^{abs} \tag{2.8}$$

where the direct path is taken, as always, to be path #1. Since we are using α and ξ without the superscripts to denote the relative quantities, we have $\alpha_1 = 1$ and $\xi_1 = 0$ for the direct path. The reader will note that this convention is exactly the same as considering the overall channel transfer function and normalizing with the direct path channel transfer function.

The normalization described above will be used independently of whether or not a direct path between transmitter and receiver exists. That both cases can hold should be obvious from Figure 2.5. In part (a) of the figure, a direct path to the receiver always exists. In part (b) of the figure, there is no direct path. In either case, however, all quantities will be referenced to the direct path.

All of the calculations in this report make use of the earth-flattening coordinate transformation described in 2,13, p.2-14]. From the cited reference we have taken Figure 2.8 which summarizes the effects of the transformation. From the figure it will be noted that a ray whose curvature exactly matches that of the earth has an infinite radius of curvature in the flattened-earth coordinate system, whereas a perfectly straight ray appears as a circular segment with concave side upwards in the flattened earth coordinate system.

For the direct path, the atmosphere is assumed to have its standard value $G = -39$ Nu/km. In the flattened earth coordinate system, this corresponds to a concave-upward circular segment with radius of magnitude $R_f = 5280$ miles. Generally, the radius of curvature is related to the gradient via the relation

R = actual radius of curvature
R_{mod} = modified radius of curvature
a = radius of earth

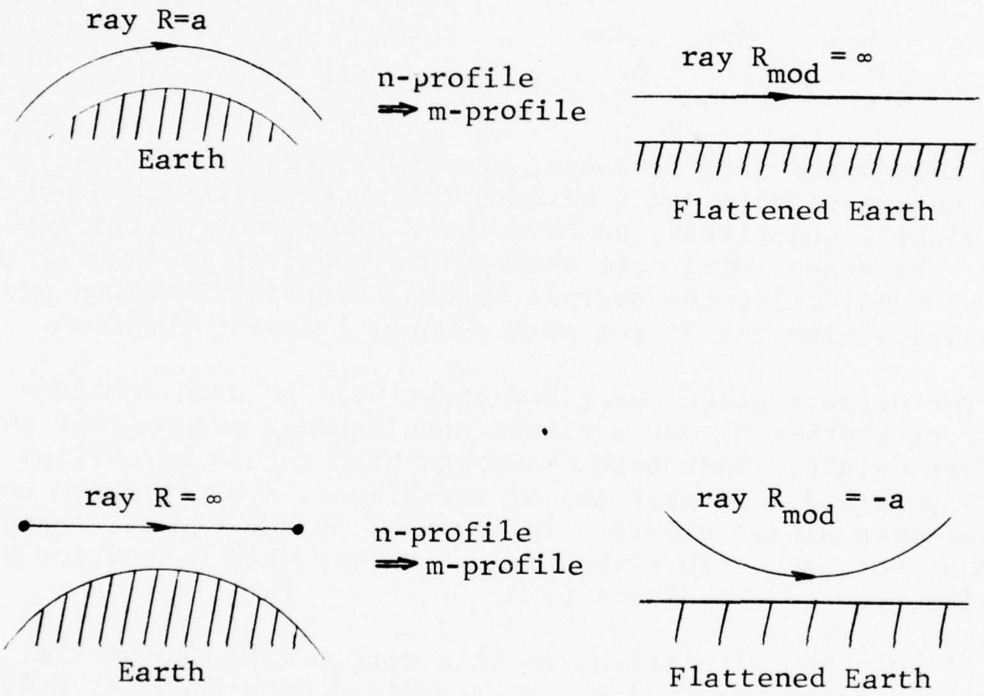

$m = n + z/a$
$M = N + z/a$

Figure 2.8 Effect of Earth-Flattening Coordinate Transformation of Ray Trajectories (From [2.13])

$$R = \frac{-\ 0.62139 \times 10^6}{G + 156.78} \tag{2.9}$$

It will be noted that this expression yields an infinite radius and a change of sign at the transition point:

$$G = -156.78 \tag{2.10}$$

It is convenient to describe this behavior in terms of the lapse rate of refractive index gradient, which is just the algebraic negative of G. Were the lapse rate to rise from its "standard-atmosphere" value of 39 Nu/km to some large but realizable value (e.g., 300 Nu/km), the ray path would first be concave-upward, reach a point at approximately 157 Nu/km where it becomes perfectly flat, and then become concave-downward bending the rays back toward the earth.

The earth-flattening coordinate transformation has the effect of modifying the refractive index n, resulting in the "modified refractive index" m. The relationship between the two quantities is given in Figure 2.8, and is discussed at length in [2.13, Section 2.1.1.2].

2.2.2.1 Calculation of Direct Path Quantities

Like the refractive index, the modified refractive index varies linearly with height and can be simply represented as

$$m(z) = m_0 + g_0 z \tag{2.11}$$

where z is the height above some conveniently chosen zero point, m_0 is the value of the modified refractive index at that point, and g_0 is the direct path gradient of the modified refractive index. The radius of curvature is given by

$$\begin{aligned} R_0 &= -\left(\frac{\partial m}{\partial z}\right)^{-1} \\ &= \frac{1}{g_0} \end{aligned} \tag{2.12}$$

Thus, from our standard atmosphere assumption for the direct path ($G_0 = -39$ Nu/km), g_0 and R_0 are immediately determinable via (2.9) and (2.12).

The direct path geometry is illustrated in Figure 2.9; the ray path curvature has been grossly exaggerated to make it visible. From the geometry, we see that any point along the ray path positioned such that its radius arm is at an angle α with the vertical is at a height z given by

$$z = h_T - (R_f \cos\alpha - R_f \cos\alpha_T) \tag{2.13}$$

Substituting in (2.11),

$$m = m_0 + g_0 h_T + \cos\alpha_T - \cos\alpha \tag{2.14}$$

The time delay is proportional to the integral of m over the path, i.e., over the circular arc. The differential arc length is given by

$$d\sigma = R_f \, d\alpha \tag{2.15}$$

and $\quad m_0 + g_0 h_T \approx 1$

Performing the simple integral and dividing by c, the speed of light in vacuo, we obtain

$$\xi_1(\alpha_T, \alpha_R) = \frac{R_f}{c}\left[(\sin\alpha_T + \sin\alpha_R) - (1 + \cos\alpha_T)(\alpha_T + \alpha_R)\right] \tag{2.16}$$

A companion expression for (2.16) represents power on the path as a function of the angles α_T and α_R. This can be derived by following exactly the same procedure described in [2.3] and [2.13] but omitting the simplifying assumption that sets $\cos\alpha_T = 1$. As a result, we get the power factor*

---

*The square root of this quantity is the ray path amplitude that we have repeatedly referred to.

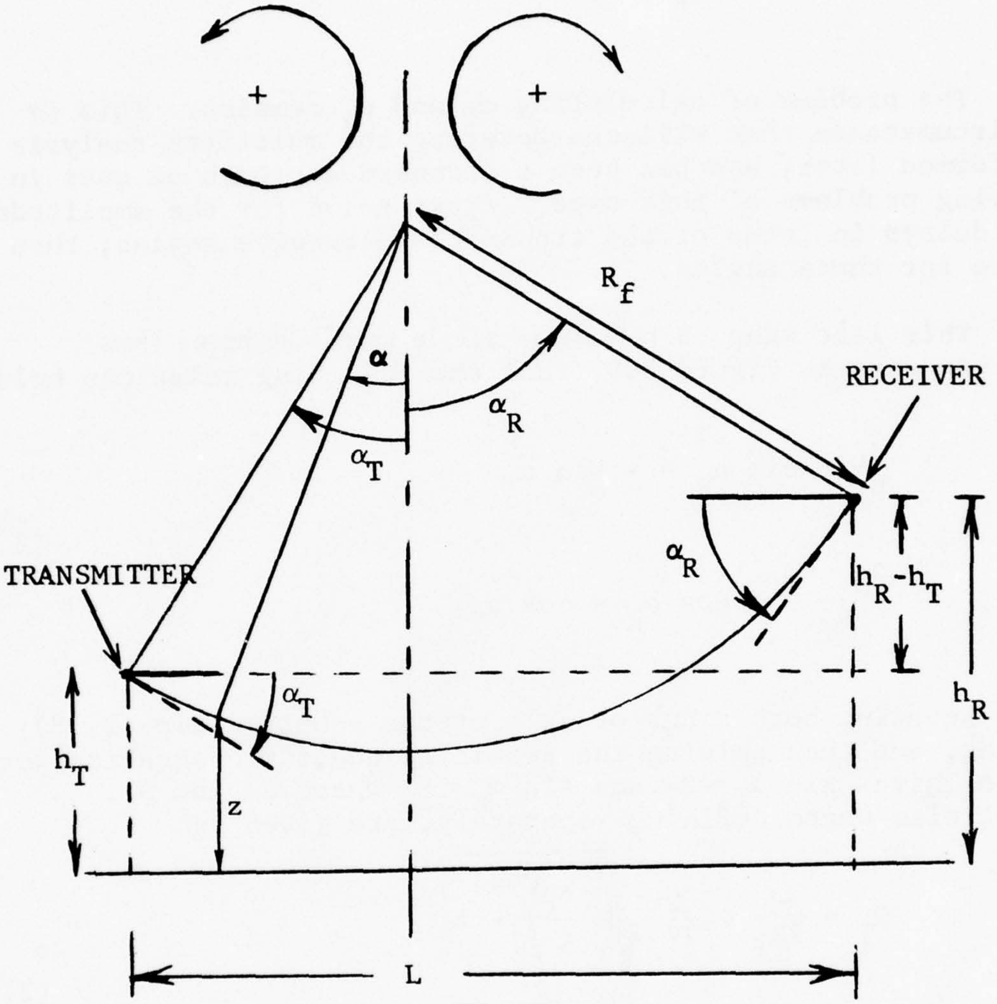

Figure 2.9 Direct Path Geometry for LOS Link ($R_f = -R_0$)

$$\vartheta = \frac{1}{L \sin \alpha_R} \frac{d}{dL} (\sin \alpha_T) \tag{2.17}$$

The problem of calculating α_T and α_R remains. This is a circumstance that will characterize the multipath analysis performed later, and has been a standard approach of ours in solving problems of this type: first solve for the amplitudes and delays in terms of the transmit and receive angles; then solve for those angles.

This last step is relatively simple here. We note, from the geometry in Figure 2.9, that the following relations hold:

$$\begin{aligned} \frac{L}{R_f} + \sin \alpha_R &= - \sin \alpha_T \\ \frac{h_R - h_T}{R_f} + \cos \alpha_R &= \cos \alpha_T \end{aligned} \tag{2.18}$$

Squaring both sides of each of the equations in (2.18), adding, and then solving the resulting quadratic equation for $\sin \alpha_R$ gives $\sin \alpha_T = S_T$ and $\sin \alpha_R = S_R$ where S_T and S_R, quantities worth defining separately, are given by

$$\begin{aligned} S_T &= \frac{-L}{2R_f} + \frac{\Delta h}{2R_f} \sqrt{\left(\frac{2R_f}{r}\right)^2 - 1} \\ S_R &= \frac{-L}{2R_f} - \frac{\Delta h}{2R_f} \sqrt{\left(\frac{2R_f}{r}\right)^2 - 1} \end{aligned} \tag{2.19}$$

where r is the slant range,

$$r = \sqrt{L^2 + (\Delta h)^2} \tag{2.20}$$

and Δh is the vertical terminal difference,

$$\Delta h = h_R - h_T \tag{2.21}$$

In terms of these quantities, we have the direct path delay and amplitude given, respectively, by

$$\begin{aligned} \xi_1 &= -\frac{L}{c} - \frac{R_f}{c}\left[1 + \sqrt{1 - S_T^2}\right]\left[\sin^{-1}(S_T) + \sin^{-1}(S_R)\right] \\ \alpha_1 &= \sqrt{\frac{1}{L\,S_R}\,\frac{d\,S_T}{d\,L}} \end{aligned} \tag{2.22}$$

The amplitude can be determined directly in terms of the geometrical parameters, h_T, h_R, etc. Substituting the expression for S_T and S_R into the expression for α_1, we obtain, after some manipulation, the result

$$\alpha_1 = \frac{1}{r}\left[\frac{1 + \left(\frac{r}{2R_f}\right)\frac{r^2}{L\,\Delta h}\sqrt{1 - \left(\frac{r}{2R_f}\right)^2}}{1 - \left(\frac{r}{2R_f}\right)^2 + \left(\frac{r}{2R_f}\right)\frac{L^2}{L\,\Delta h}\sqrt{1 - \left(\frac{r}{2R_f}\right)^2}}\right]^{\frac{1}{2}} \tag{2.23}$$

This is quite reasonably approximated by the expression,

$$\alpha_1 \approx \frac{1}{r}\left[\frac{1 + \left(\frac{r}{2R_f}\right)\frac{r^2}{L\,\Delta h}}{1 + \left(\frac{r}{2R_f}\right)\frac{L^2}{L\,\Delta h}}\right]^{\frac{1}{2}} \tag{2.24}$$

which is the expression we have used in our programs.

It should be pointed out that (2.24) takes into account larger values of Δh than the expression used to generate results in an earlier report under another contract. The earlier approximation, $\alpha_1 \approx L^{-1}$, which was appropriate for earlier applications, is inappropriate for the extreme geometries of the links encountered in the current study.

2.2.2.2 Calculation of Multipath Quantities

Since the direct path delays and amplitudes are directly calculable from the expressions just derived, we now take the second step toward determining the relative multipath delays and amplitudes in (2.7) and (2.8); we now calculate the delays and amplitudes of the rays refracted by the atmospheric layer. As discussed before, we are interested in both of the situations illustrated in Figure 2.5. Condition "A" in the figure, which is illustrated in more detail in Figure 2.6, has been treated in earlier reports. We will treat it briefly at a later point in this section, but our treatment will be limited to presenting (not rederiving) the earlier results in the formalism adopted here and to a few comments on the advantages of looking at the problem in this new way. Of particular interest in this regard is an inquality that we generate in Section 2.3.3 which demonstrates the limitations of the condition "A" results when trying to apply them to links with a large vertical separation between transmitter and receiver, e.g., the Hohenstadt-Zugspitze link in Germany.

Our primary interest here is in condition "B" of Figure 2.5 which is illustrated in much more detail in Figure 5.7. This is the case wherein one of the terminals is in the layer, a likely situation if there is a significant difference in the terminal heights.

To analyze this case, we refer to the geometry and nomenclature of Figure 2.7. The problem is primarily one of analyzing the system geometry to determine path delays and power loss in terms of the transmit and receive angles θ_0^T and θ_0^R or, equivalently, in terms of the normalized parameters k_T and k_R, which are defined according to

$$\sin \theta_0^R = \frac{k_R L}{2R} \tag{2.25}$$

$$\sin \theta_0^T = - \frac{k_T L}{2R_f} \tag{2.26}$$

where L is the ground range between transmitter and receiver, R is the radius of curvature of the ray in the layer, and R_f is the radius of curvature of the ray in free space. The radii are related to the modified refractive index gradients g_0 of the free space below the layer and g_1 of the layer through

$$g_0 = \frac{1}{R_f} \tag{2.27}$$

and

$$g_1 = -\frac{1}{R} \tag{2.28}$$

They are related to the unmodified refractive index gradients through the earlier expression in Figure 2.8. In terms of g_0 and g_1 and the reference level refractive index, m_0, it is helpful to define a free space index:

$$M_F = m_0 + g_0 z \tag{2.29}$$

and an index applicable to the layer given by,

$$M_L = m_0 + g_0 h_L + g_1(z - h_L) \tag{2.30}$$

We now turn to the geometry of Figure 2.7. A simple examination gives the following results:

$$L_1 = R_f \sin \theta_1 - R_f \sin \theta^T \tag{2.31}$$

$$L_2 = 2(R + R_f) \sin \theta_1 \tag{2.32}$$

$$L_3 = R \sin \theta_1 + R \sin \theta_0^R \tag{2.33}$$

The section L_2 can be repeated n times, resulting in a total ground range,

$$L = L_1 + n L_2 + L_3 \tag{2.34}$$

Keeping in mind our goal of expressing all quantities in terms of θ_0^T and θ_0^R, it is easy to determine from (2.31) and (2.34) that

$$\sin \theta_1 = \frac{L - R \sin \theta_0^R + R_f \sin \theta_0^T}{(2n+1)(R+R_f)} \tag{2.35}$$

Examination of Figure 2.7 also yields two relations that will be essential in the later development. These are:

$$h_L = h_T + R_f \cos \theta_0^T - R_f \cos \theta_1 \tag{2.36}$$

and

$$h_L = h_R - \left(R \cos \theta_0^R - R \cos \theta_1\right) \tag{2.37}$$

We recall that the delay for each multipath ray is found simply by performing the integral of refractive index along the path. The calculation is facilitated by noting the useful relations listed below which give the variable height z of any point along the path.

- <u>In Region 1</u>:

$$z = h_T + R_f \cos \theta_0^T - R_f \cos \theta_T \tag{2.38}$$

- <u>In Region 2'</u>:

$$z = h_L + R(\cos \theta - \cos \theta_1) \tag{2.39}$$

- <u>In Region 2"</u>:

$$z = h_T + R_f\left(\cos \theta_0^T - \cos \theta\right) \tag{2.40}$$

- In Region 3:

$$z = h_R - (R \cos \theta_0^R - R \cos \theta) \tag{2.41}$$

Substituting these expression in (2.29) and (2.30) and then performing the angular path integrations of refractive index over each of the ray segments in Figure 2.5 and dividing by c, we obtain

$$\tau = \frac{R}{c}\left(M_{F0}\,\theta_0^R - \sin \theta_0^R\right) - \frac{R_f}{c}\left(M_{F0}\,\theta_0^T - \sin \theta_0^T\right) + (2n+1)\,\frac{(R+R_f)}{c}\left(M_{F0}\,\theta_1 - \sin \theta_1\right) \tag{2.42}$$

where M_{F0} is defined as,

$$M_{F0} = m_0 + g_0 h_T + \cos \theta_0^T \tag{2.43}$$

Thus, from (2.35), (2.42), and (2.43), we see that the delay to be associated with any multipath ray depends on the transmit and receive angles θ_0^T and θ_0^R, respectively.

Having determined delay as a function of θ_0^T and θ_0^R, we now turn to the calculation of power. This result is obtained by considering the fundamental intensity law for ray optics as described earlier. The result is given by

$$\mathcal{P} = \frac{\cos \theta_0^T}{L \sin \theta_0^R}\,\frac{d\,\theta_0^T}{d\,L} \tag{2.44}$$

where $\mathcal{P}$ is the power factor, i.e., the ratio of received to transmitted power.

This completes the representation of delay and power factors as functions of transmit and receive angles. Before writing these results in terms of the more useful dimensionless parameters in (2.25) and (2.26), we note that $g_0 h_T$ in (2.43) is is an extremely small quantity. In fact, examination of (2.42) and (2.43) reveals that we can replace $m_0 + g_0 h_T$ with unity without incurring error. Thus, using

$$M_{F0} = 1 + \cos \theta_0^T \tag{2.45}$$

and (2.35) in (2.42), and (2.25) and (2.26) in (2.42) and (2.44), we obtain

$$\mathscr{P}(k_T, k_R) = -\left(\frac{R}{R_f}\right)\left(\frac{1}{k_R L}\right)\left(\frac{\partial k_T}{\partial L} + \frac{k_T}{L}\right) \tag{2.46}$$

for the power factor, and

$$\begin{aligned}\tau(k_T, k_R) = {} & \frac{R}{c}\left\{\sin^{-1}\left(\frac{k_R L}{2R}\right)\left[1 + \sqrt{1 - \left(\frac{k_T L}{2R_f}\right)^2}\,\right] - \frac{k_R L}{2R}\right\} \\ & - \frac{R_f}{c}\left\{\sin^{-1}\left(\frac{-k_T L}{2R_f}\right)\left[1 + \sqrt{1 - \left(\frac{k_T L}{2R_f}\right)^2}\,\right] + \frac{k_T L}{2R_f}\right\} \\ & + (2n+1)\left(\frac{R + R_f}{c}\right)\left\{\sin^{-1}\left[f_1(k_T, k_R)\right]\left[1 + \sqrt{1 - \left(\frac{k_T L}{2R_f}\right)^2}\,\right]\right. \\ & \left. \qquad - f_1(k_T, k_R)\right\}\end{aligned} \tag{2.47}$$

for the delay. In this expression,

$$f_1(k_T, k_R) = \frac{L}{(2n+1)(R + R_f)}\left(1 - \frac{k_T + k_R}{2}\right) \tag{2.48}$$

is just $\sin \theta_1$ in (2.35).

We have now arrived at the same point in the multipath analysis that we were at in the direct path analysis after (2.16) and (2.17). It remains to determine the transmit and

and receive angles (equivalent to determining k_T and k_R). This was quite simple for the direct path, but is more complicated here. As in the earlier case, however, we start by appealing to the geometry.

From (2.36) and (2.37) we have the constraining equations,

$$h_L = h_T - R_f\left(\cos\theta_1 - \cos\theta_0^T\right) \tag{2.49}$$

$$h_L = h_R + R\left(\cos\theta_1 - \cos\theta_0^R\right) \tag{2.50}$$

which must be solved simultaneously for θ_0^T and θ_0^R, i.e., for k_T and k_R. The solution is facilitated by using the expansion

$$\cos\theta_1 - \cos\theta_0 = \frac{1}{2}\left(\sin^2\theta_0 - \sin^2\theta_1\right) + \frac{1}{8}\left(\sin^4\theta_1 - \sin^4\theta_0\right) + \ldots \tag{2.51}$$

In this expansion we note that the ratio of the magnitudes (last term to first) is given by

$$\frac{1}{4}\left(\sin^2\theta_0 + \sin^2\theta_1\right) \tag{2.52}$$

which will be entirely negligible for the small angles occurring on LOS links. Consequently, we can drop all terms but the first, getting

$$h_L = h_T - \frac{R_f}{2}\left(\sin^2\theta_0^T - \sin^2\theta_1\right) \tag{2.53}$$

$$h_L = h_R + \frac{R}{2}\left(\sin^2\theta_0^R - \sin^2\theta_1\right) \tag{2.54}$$

Substituting from (2.25) and (2.26), and using (2.35), we obtain, after some manipulation, the two equations

$$k_R^2\rho^2 - k_T^2 = A \tag{2.55}$$

$$k_R^2\rho^2 - (\bar{k} - 1)^2 \frac{8}{B_n} + k_T^2 = -S \tag{2.56}$$

where

$$\rho = \frac{R_f}{R} \tag{2.57}$$

$$\bar{k} = \frac{k_T + k_R}{2} \tag{2.58}$$

$$A = \left[(h_L - h_T) - \rho(h_R - h_L)\right] \frac{8R_f}{L^2} \tag{2.59}$$

$$S = \left[(h_L - h_T) + \rho(h_R - h_L)\right] \frac{8R_f}{L^2} \tag{2.60}$$

and

$$B_n = \frac{1}{R_f^2} (2n+1)^2 \; (R + R_f)^2 \tag{2.61}$$

Tedious manipulation of (2.55) - (2.61) indicates that the set of solutions to (2.55) and (2.56) can be found by solving a quartic equation for y and then using either (2.55) or (2.56) to determine x. The quartic equation is given by

$$y^4 + ay^3 + by^2 + cy + d = 0 \tag{2.62}$$

where

$$\begin{aligned}
a &= 4(1 + \rho^2 G) \,/\, (\rho^2 G^2 - 1) \\
b &= \left[4G(\rho^2 - 1) - 2\rho^2 G^2 (P + 2) + (P - Q)\right] \Big/ \left[G(\rho^2 G^2 - 1)\right] \\
c &= 4\left[(Q - P) - \rho^2 G(P + 2)\right] \Big/ \left[G(\rho^2 G^2 - 1)\right] \\
d &= \left[\rho^2 G(P + 2)^2 + 4(P - Q)\right] \Big/ \left[G(\rho^2 G^2 - 1)\right]
\end{aligned} \tag{2.63}$$

and

$$P = \frac{A}{2\rho^2} - \frac{B_n(A+S)}{4}$$

$$Q = \frac{B_n(A-S)}{4} - \frac{A}{2} \qquad (2.64)$$

$$G = \frac{\rho^2(B_n - 1) - 1}{2\rho^2}$$

As it happens, quartic equations are the highest-order equations for which general solution formulas exist. The existence of these formulas indicate that the problem is, in essence, completely solved by (2.57) - (2.63), and does not require recourse to iterative numerical procedures. Additionally, it provides us with a means (by putting constraints on the coefficients) of determining inequalities which govern the existence of multipath on any given link. This topic is discussed in Section 2.2.4.

It is of interest to examine the dependence of (2.61) on n. Recall from Figure 2.7 that n can be thought of roughly as the number of times the ray reenters the layer after its initial entry. For any given link, some consideration of Figure 2.7 reveals that increases in n require greater bending properties of the layer, i.e., larger lapse rates of the refractive index gradient. From our earlier discussion in Section 2.1, we know that the larger lapse rates are less likely to occur in nature. In fact, it has been our experience in examining several links that large lapse rates are required in order to produce multipath in the minimal reentry case when $n = 0$. Thus, we are already at the low end of the probability scale when we consider the $n = 0$ case for practically all links of interest.

It should be pointed out that there are some situations, themselves improbable, where $n > 0$ could be of importance. This situation arises when the layer is so configured that the receiving and transmitting terminals are both very close to the layer interface. A limiting case occurs when the layer interface coincides exactly with receiver and transmitter. In this case, the ray can skip in and out of the layer an unlimited number of times with negligible bending provided by the layer. This is a zero probability circumstance, of course.

It is a simple matter to determine from (2.61) and (2.64) that $G = \rho^{-1}$ when $n = 0$. In such a case, the division by ρ^2G^2-1 in (2.63) is not allowed and the equation to solve is a cubic

$$y^3 + b_2y^2 + b_1y + b_0 = 0 \tag{2.65}$$

where

$$b_2 = \frac{4(\rho^2 - 1) - \rho(Q + P + 4)}{4(\rho + 1)}$$

$$b_1 = \frac{4[\rho(Q - P) - \rho^2(P + 2)]}{4(\rho + 1)} \tag{2.66}$$

and

$$b_0 = \frac{\rho^2(P + 2)^2 + 4\rho(P - Q)}{4(\rho + 1)}$$

Formulas for solving (2.62) and (2.65) are given in [2.].

Note that the existence of the two simultaneous equations, (2.55) and (2.56), which relate k_T and k_R, can now be used to derive an analytical expression for the power factor ϑ in (2.46) by allowing evaluation of the derivative. Manipulating (2.55) and (2.56), we obtain

$$\frac{\partial k_T}{\partial L} = \frac{B_n\left(\frac{\rho^2 k_R}{2}\right)(A + S) - 2LA(\bar{k} - 1)}{k_T B_n \rho^2 k_R - Q_0} \tag{2.67}$$

where

$$Q_0 = (\rho^2 + 1)k_R k_T + \left(\rho^2 k_R^2 + k_T^2\right) - 2\left(k_T + \rho^2 k_R\right) \tag{2.68}$$

and

$$\bar{k} = \frac{k_T + k_R}{2} \tag{2.69}$$

The analytical development is now complete. The transmit and receive angles can be determined by solving the quartic (2.62) or the cubic equation (2.65); and by substituting the solution back into the constraining simultaneous equations (2.55) and (2.56). With a set of values so determined, the amplitude and the delay for the corresponding path can then be calculated from (2.46) and (2.47).

2.2.3 Inclusion of Layer Tilt into Model

The analytical results presented in the previous sections correspond to the physical situation wherein the refractive layer is perfectly horizontal with respect to the ground. This is not always the case. That layers are subject to tilting has been reported in the literature. The experimental data is limited, but these limitations are not due to absence of the phenomena; they exist primarily because of the difficulty in measuring layer tilt. It is clear that, if measurements of layer tilt with concurrent measurements of refractive index gradient are to be made, one must have the services of at least three neighboring radiosonde stations working in close conjunction with one another. Because of this, data on layer tilt is extremely sparse. Gossard [2.17] has presented some limited estimates that derive from his study of refractive layers perturbed by waves. Because of the indirect manner in which these estimates were derived, they have not been deemed suitable for inclusion here. If one is willing to make the assumption that the refractive layers derive entirely from frontal inversions*, one can use the data of Kerr [2.18] who

---

*Frontal inversions are known to be a causative mechanism, but are not thought to be the sole mechanism (see Section 2.1.2).

has pointed out that wave fronts have tilt slopes ranging between 0.0033 and 0.010, corresponding to an angular range of 0.190 to 0.573 degrees. For lack of more definitive data, this is the data that we have used in our calculation when deemed appropriate.

Layer tilt is less important on the shorter links than on the longer links. Recollection of results (condition "A" only) presented in an earlier report [2.13] and some simple geometrical reasoning indicates why this is so. Earlier results indicated that multipath was only important when the layer was in close proximity with both terminals. When the layer moved away from one terminal or the other, the multipath spread would decrease. For our purposes here, we simply note that the multipath condition depends sensitively on the position of the layer relative to both terminals. Tilt of a refractive layer over a short link does little to change these relative positions. Over a long link, however, the effect can be dramatic. For more details, the reader is referred to our coverage of the 100-mile Hohenstadt-Zugspitze link discussed in Section 2.4.1.

The basic work on determination of delays and amplitudes has already been done, and the phenomenon of layer tilt has been incorporated into our model via some straightforward coordinate transformations. For the most part, these coordinate transformations reflect the changes in relative positioning of the terminals and layer interface due to layer tilt, as discussed in the previous paragraph.

The tilted layer configuration is illustrated in Figure 2.10. Were the tilted planar interface to stretch to the ground, the line of intersection between it and the ground plane would be perpendicular to the vertical plane containing the transmitter and receiver. (Consideration of a more complicated geometry at this time would only confuse the issues.) The layer is seen to tilt at an angle θ relative to the earth. It is reasonable to assume that the tilt applies to the refractive index profile just below the layer interface as well as it does to the layer proper. As a consequence of this, one is able to effect a coordinate transformation that ultimately enables computation of the multipath profiles for various values of layer height h_L, refractive index gradient G, and layer tilt slope S. As inputs to the called subroutines, however, one uses the transformed quantities

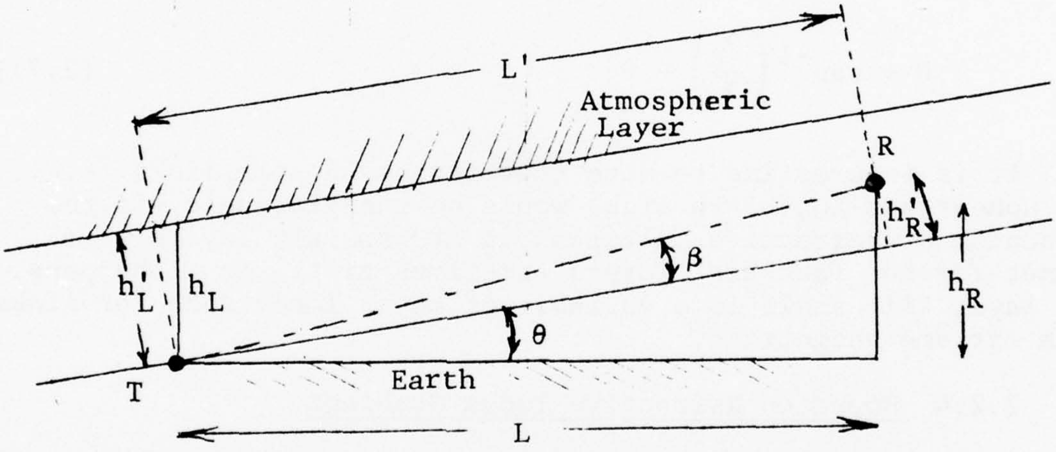

Figure 2.10 Geometry of Layer Tilt

$$h_L' = h_L \cos \theta$$

$$h_R' = r_s \sin \beta \tag{2.70}$$

$$L' = r_s \cos \beta$$

where

$$r_s = \sqrt{L^2 + h_R^2}$$

and

$$\beta = \tan^{-1}\left(\frac{h_R}{L}\right) - \theta \tag{2.71}$$

It is interesting to note that fading on some links (e.g., the Hohenstadt-Zugspitze link) would be unexplainable via the mechanism of refractive multipath in atmospheric layers were it not for the fact that layers sometimes tilt. As it happens, the layer tilt angle is a variable of major importance for links with extreme geometries.

2.2.4 Bound on Refractive Index Gradient

To determine the appropriateness of utilizing the condition "A" results derived under an earlier contract [2.13], it was decided early on in this program to find out if the geometry of longer links (with a large vertical separation between transmitter and receiver terminals) implied a requirement of extremely large lapse rate in order for multipath to be supported on the link. As we demonstrate below, this turned out to be the case, a fact that was the prime motive for developing a set of equations that governed condition "B". Because of time limitations, our investigation was limited to the case wherein the layer is horizontally situated relative to the earth.

The current development has the advantage of providing a method of approaching the governing simultaneous equations in such a way as to determine the realness (or complexness) of the roots to the system. Realness of roots is required, of course, in order to have multipath. The conditions governing the realness of the roots are identical to the conditions which indicate whether or not multipath exists on the link. It is felt that a powerful approach is available here for determining the ranges of parameter values which allow multipath on the link. Unfortunately, we have not been able to pursue this question in depth. The development here is limited to determining the bounds on lapse rate under condition "A"; this course was pursued for the reasons stated above. One germane conclusion here is that lapse rates exceeding those occurring in nature are required if multipath (under condition "A") is to be supported on some of the "extreme" geometry links, e.g., the Hohenstadt-Zugspitze link.

Our development is initiated by applying a change of variables (that preserves the realness or complexness of the roots) to the set of simultaneous quadratic equations governing propagation under condition "A". We apply the change of variables

$$u = \frac{x+y}{2} \qquad v = \frac{x-y}{2} \tag{2.72}$$

to the system of equations (see [2.13, p. C-1])

$$x^2 - y^2 = A \tag{2.73}$$

$$x^2 - \frac{2}{B_n}\left(\frac{x+y}{2} - 1\right)^2 + y^2 = -S \tag{2.74}$$

to get

$$uv = \frac{A}{4} \tag{2.75}$$

$$(u+v)^2 - \frac{2}{B_n}(u-1)^2 + (u-v)^2 = -S \tag{2.76}$$

In these expressions we have used thc condition "A" definitions:

$$B_n = (n+1)^2 \left(1 + \frac{R}{R_f}\right)^2 \tag{2.77}$$

$$A = 8\,R_f\,(h_R - h_T)/L^2 \tag{2.78}$$

$$S = 16\,R_f\,(h - \bar{h})/L^2 \tag{2.79}$$

where R_f is the radius of curvature below the layer, h is the layer height, and $\bar{h}$ is the arithmetic average of receiver height h_R and transmitter height h_T.

We are interested in the conditions that must be met in order that there be a pair or real roots, x and y, i.e., a pair of real roots, u and v. Assuming a real solution for v, we must also have a real solution for u. Evaluating the discriminant of (2.76), we obtain the inequality

$$B_n\left(v^2 + \frac{S}{2}\right) - 1 \leq \frac{1}{B_n - 1} \tag{2.80}$$

With the aid of the trivial inequalities

$$\begin{aligned} v^2 &\geq 0 \\ B_n &\geq 1 \end{aligned} \tag{2.81}$$

we get

$$B_n\left(\frac{S}{2}\right) - 1 \leq \frac{1}{B_n - 1} \tag{2.82}$$

which, after more manipulation, yields

$$B_n \leq \frac{2}{S} + 1 \tag{2.83}$$

Substituting (2.77) and (2.79) into this expression, some further manipulation gives

$$n \le \frac{1}{\left(1 + \frac{R}{R_f}\right)} \sqrt{1 + \frac{L^2}{8 R_f (h - \bar{h})}} - 1 \tag{2.84}$$

Thus, in terms of the geometrical parameters of the link (L and $\bar{h}$) and the physical parameters of the direct path atmosphere (R_f) and the layer (R and h), we have determined a bound on n, the number of excess passages through the layer (see Figure 2.6).

In order for multipath to exist on the link at all, the right-hand side of (2.84) must be equal to or exceed zero. We get, after some manipulation, the inequality

$$Q(R) \le 0 \tag{2.85}$$

where

$$Q(R) = 8\left(\frac{\Delta}{R_f}\right)R^2 + (16\Delta)R - L^2 \tag{2.86}$$

and $\Delta = h - \bar{h}$. This expression increases monotonically with R. Thus, for a positive root R_+ of the quadratic equation $Q(R) = 0$, the inequality

$$R \le R_+ \tag{2.87}$$

must hold if the inequality (2.85) is to hold (which it must if multipath is to exist on the link); the inequalities (2.83), (2.84), (2.85), and (2.87) are all inequalities that must be satisfied for multipath to exist on the link. Thus, (2.87) provides us with the upper bound on R, the radius of curvature of the ray in the layer. Solving for the positive root of (2.86), we get

$$R \leq R_{max} \tag{2.88}$$

where

$$R_{max} = R_f \left[\sqrt{1 + \frac{L^2}{8 R_f \Delta}} - 1 \right] \tag{2.89}$$

The ray cannot curve in an arc to less a degree than indicated by (2.88) and (2.89) if multipath is to exist on the link. Thus, the bending requirement of the layer, if it is to support multipath, is firmly established. The reader will note that this puts a bound on refractive index gradient; i.e., the lapse rate of the layer must exceed some value corresponding to (2.89) if multipath is to exist on the link. The relationship betwen R and the lapse rate $\mathcal{L}$ is given by

$$R = \frac{.62139 \times 10^6}{\mathcal{L} - 156.78} \tag{2.90}$$

where R is in miles and $\mathcal{L}$ is in Nu/km. When $\mathcal{L}$ is in excess of 156.78 Nu/km, it is clear from this relation that R decreases with increasing lapse rate. From (2.88) we see that R obtains a value small enough to support multipath on the link when the inequality

$$\mathcal{L} \geq \frac{.62139 \times 10^6}{R_f \left[\sqrt{1 + \frac{L^2}{8 R_f \Delta}} - 1 \right]} + 156.78 \tag{2.91}$$

is satisfied.

Curves illustrating the lapse rates required to allow multipath on different links are shown in Figure 2.11. We see that the lapse rate requirement rises sharply as Δ increases, i.e., as the layer rises.

The curves in Figure 2.11 have important implications relative to the limitations of the condition "A" model. Recall that the model requires that the layer be above the highest

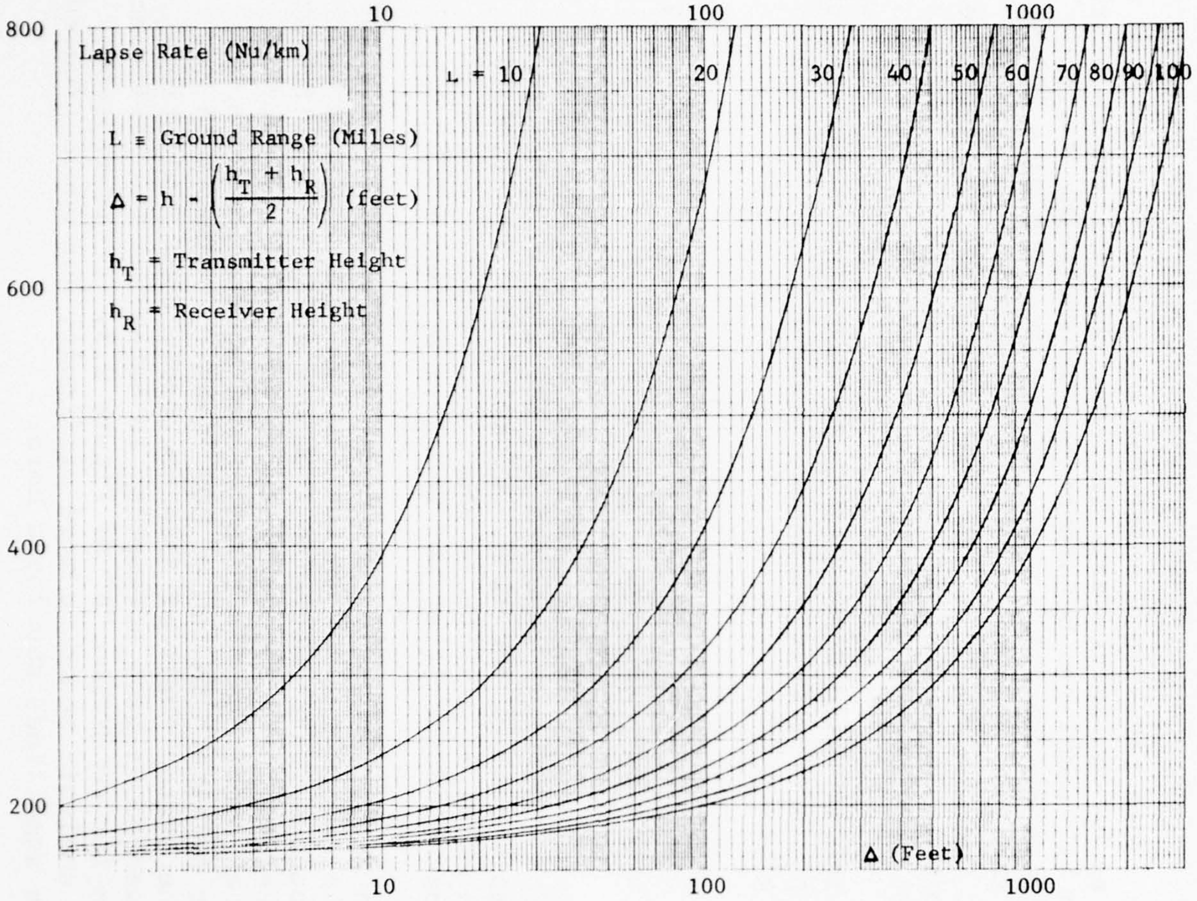

Figure 2.11 Lapse Rates Required for Existence of Refractive Multipath on LOS Links

terminal (chosen without loss of generality to be the receiver). Hence,

$$\Delta = h - \frac{h_T + h_R}{2} \geq h_R - \frac{h_T + h_R}{2} = \frac{h_R - h_T}{2} \qquad (2.92)$$

Thus, the lapse rate requirement for any given link is seen to increase as $h_R - h_T$ increases. In fact, the limitations of the condition "A" model can be determined by replacing Δ with $(h_R - h_T)/2$ in Figure 2.11, e.g., for $h_R - h_T = 200$ on a 200-mile link, we see that a lapse rate of 680 Nu/km is required in order for the condition "A" LOS multipath model to give rise to multipath. In view of data in [2.] and [2.], this is an extreme requirement.

For the 100-mile Hohenstadt-Zugspitze link in Europe, the requirement is even more extreme. Examination of the link geometry gives

$$\frac{h_R - h_T}{2} = 3511.16 \text{ feet} \qquad (2.93)$$

which, when used in (2.91), indicates that a lapse rate in excess of 872 Nu/km is required for the earlier model to produce multipath on the link. Clearly, the condition "A" multipath model is unsuitable where such extreme vertical separations of transmitter and receiver are encountered.

On a worldwide basis, the measurement of refractive index lapse rate has been going on for several years. As far as we have been able to determine from our study of the literature, the inequality in (2.91) constitutes the first and only "existence" condition (in terms of refractive index lapse rate) for multipath fading on LOS links.* Since it is not one of the stated goals of this contract, time limitations have prevented us from attempting to determine the "existence" condition for condition "B" of Figure 2.5. It is expected that the analysis would be more difficult, but would proceed along the same lines developed here.

---

*Other "existence" conditions related to different quantities, e.g., path length, layer thickness, have been presented in earlier CNR reports [2.13].

It is of interest to determine the lapse rate requirement when n, the number of excess passages through the layer, exceeds zero. Such a condition corresponds exactly with the condition that the total number of ray paths is greater than three, as discussed in connection with (2.62) through (2.65). An analysis similar to that described above indicates that the lapse rate required to result in n excess passages is given by

$$\mathcal{L} \geq \frac{.62139 \times 10^6}{\frac{R_f}{n}\left[\sqrt{1 + \frac{L^2}{8R_f\Delta}} - (n+1)\right]} + 156.78 \qquad n \geq 1$$

Since the right-hand side of this expression must always exceed 156.78 (if multipath is to exist at all) we see that a larger lapse rate is required if extra passages, and hence extra ray paths, are to exist. Since large lapse rates are invariably less probable than small ones, we conclude that the existence of more than three paths is less probable than the existence of just three. In all but a few anomalous situations the difference in probabilities will be substantial.

2.3 System Parameters

In this section we categorize and describe the various system parameters of importance under this study. All of these parameters derive from the time-varying channel transfer function $T(f,t)$ and serve to bridge the gap between the physical parameters describing the propagation channel and the quantitative measures of system performance. Theoretically, one need only know $T(f,t)$ to evaluate system performance. In practice, one (or both) of two conditions obtain:

(1) Not enough information about the propagation channel is available to precisely reconstruct $T(f,t)$;

(2) In the event $T(f,t)$ is available, it is difficult to use it in its unmodified state.

One is forced to consider finite parameter characterizations of the channel. The whole topic of models for random time-varying channels (including reductions to finite parameter models) has been discussed comprehensively by Bello [2.19]. In this report we represent signal degradation in terms of the T-parameters and P-parameters, a development motivated primarily by condition (2) above. The T-parameter representation is of a general nature, whereas the P-parameter characterization arises because of the emphasis here on angle modulation.

Two of the parameters mentioned above, because they have classically played a dominant role in providing a physical description of the channel and/or in providing a means whereby one can gauge system performance, are given a separate treatment in Section 2.3.1. These are T_0 and P_1; the magnitude of T_0 is known classically as the fade level (at band center) and the negative of P_1 is known as the group delay (at band center).

Because characterization of frequency-selective fading generally requires a greater number of parameters than the two mentioned above, Section 2.3.2 is devoted to a general discussion of the T- and P-parameters. Their importance relative to the distortion of angle-modulated signals is emphasized.

In Section 2.3.3 we return to a closer look at fade depth and group delay; we use the accepted form for the channel transfer function on LOS refractive multipath links [see (9)] and examine the joint behavior of these parameters during a deep fade. We make the important observation that the largest excursions in group delay can only occur during a deep fade ... an observation that will take on much greater importance when we later consider diversity switching in Section 4. Additionally, we derive an expression whereby one can determine those frequencies at which the deepest fades occur.

2.3.1 Fade Depth and Group Delay

A time-varying communication channel can, in general, be represented by a transfer function T(f,t) which provides a joint depiction of the frequency-selective and time-selective behavior of the channel. In this section we discuss two of the most important parameters associated with T(f,t). These are: (1) the fade level which is just the magnitude of T(f,t); and (2) the group delay which is the frequency derivative of the phase of T(f,t). The quantity |T(f,t)|, when evaluated at one particular frequency (e.g., the carrier frequency), is the commonly referred-to fade record, a function of time giving rise to variations in the received signal level. When evaluated at one particular time instant, a "snapshot" of the frequency transfer function is obtained. In this section we are interested in characterizing the frequency-selective behavior of the channel and, for that reason, will concentrate on the latter point of view.

For our purposes, it is of interest to consider the channel transfer function written in the general form,

$$T(f,t) = A(f,t)\, e^{j\theta(f,t)} \tag{2.94}$$

At a particular frequency and time, we refer to the fade level

$$L(f,t) = |T(f,t)| \tag{2.95}$$

which is just the channel transfer function magnitude. In dB, this is given by

$$L_{dB}(f,t) = 20 \log_{10}|T(f,t)| \tag{2.96}$$

AD-A048 175 CNR INC NEEDHAM MA F/G 17/2.1
MULTIPATH OVER LOS CHANNELS STUDY.(U)
NOV 77 P A BELLO, L PICKERING, C BOARDMAN F30602-76-C-0419
UNCLASSIFIED RADC-TR-77-355 NL

3 OF 3
ADA
048175

END
DATE
FILMED
1-78
DDC

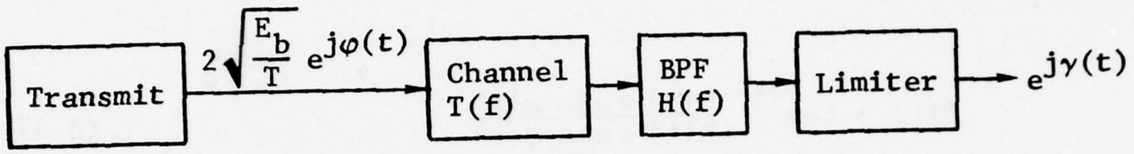

a) Actual System Configuration

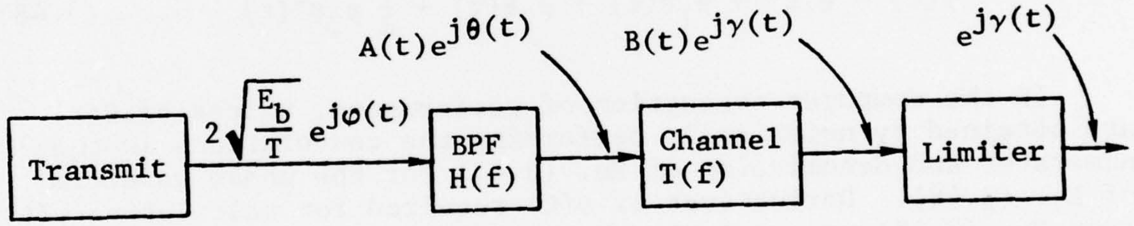

b) Equivalent System

Figure 3.3 Block Diagram Showing Signal Processing Elements

$$\varphi(t) = \varphi_0' + \frac{\pi}{8}(2i - 3)\frac{t}{T} \qquad (3.46)$$

As the conversion between reference frames is always a known phase shift, this apparent source of confusion should cause no conceptual difficulties. Thus we let $\theta(t)$ denote the (phase) response of the BPF to the transmitted phase $\varphi(t)$. The relationship between these quantities is

$$\theta(t) = \tan^{-1} \frac{h(t) * \sin \varphi(t)}{h(t) * \cos \varphi(t)} \qquad (3.47)$$

where $h(t)$ is the low pass equivalent impulse response of the BPE (This is valid under the assumption that $h(t)$ is real, corresponding to a symmetric bandpass filter.) The (phase) response of the channel $\gamma(t)$ may in turn be written in terms of $\theta(t)$ using the p series discussed earlier:

$$\gamma(t) = \theta(t) + p_1\dot{\theta}(t) + p_2\ddot{\theta}(t) + \frac{1}{2} p_3\dot{\theta}^2(t) \qquad (3.48)$$

In the computer evaluation of performance, values of $\theta(t)$ are obtained by numerically performing the convolutions in the numerator and denominator of Eq. (3.47) for the phase waveform of Eq. (3.46). Derivatives of $\theta(t)$ required for calculating $\gamma(t)$ from Eq. (3.48) are evaluated by standard numerical procedures. That is,

$$\dot{\theta}(t) = \frac{\theta(t + \Delta) - \theta(t - \Delta)}{2\Delta} \qquad (3.49)$$

$$\ddot{\theta}(t) = \frac{\theta(t + \Delta) - 2\theta(t) + \theta(t - \Delta)}{\Delta^2} \qquad (3.50)$$

If multipath had no effect on the extraction of reference by the receiver, the relationships presented so far would be sufficient to calculate modem performance. However, this is not the case and we must investigate the effect of multipath on both the derived phase reference and the derived symbol clock.

The PLL's shown in Fig. 3.3 function as narrow band filters which pass only a discrete component at the appropriate frequency. Since the bandwidths of these loops are usually very much narrower than the system bandwidth, we will neglect all noise effects and model them as having zero-bandwidth. Thus we have the following transfer functions for the zonal filters at $8f_0$ and $8f_1$

$$H_0(f) = \delta(f - 8f_0) \tag{3.51}$$

$$H_1(f) = \delta(f - 8f_1) \tag{3.52}$$

Here we are assuming a center frequency $8f_c$. The only component in the output of the eighth law device which will have any effect is also that at $8f_c$. Neglecting gain factors, this component will have complex envelope

$$z(t) = e^{j8\gamma(t)} \tag{3.53}$$

Proceeding in a straightforward manner, the respective filter outputs become

$$\left\{ \int_{-\infty}^{\infty} e^{j[8\gamma(\tau) - 2\pi 8f_0\tau]} \, d\tau \right\} e^{j2\pi 8f\text{[illegible]}} \tag{3.54}$$

and

$$\left\{ \int_{-\infty}^{\infty} e^{j[8\gamma(\tau) - 2\pi 8f_1\tau]} \, d\tau \right\} e^{j2\pi 8f_1 t} \tag{3.55}$$

Since no amplitude effects are retained by the PLL, these expressions may be further simplified to

$$e^{j2\pi 8f_0 t + \Psi_0} \tag{3.56}$$

and

$$e^{j2\pi 8f_1 t + \Psi_1} \tag{3.57}$$

where the phase shifts are given by

$$\Psi_0 = \tan^{-1} \frac{\int_{-\infty}^{\infty} \sin\,[8\gamma(\tau) - 2\pi 8f_0\tau]\, d\tau}{\int_{-\infty}^{\infty} \cos\,[8\gamma(\tau) - 2\pi 8f_0\tau]\, d\tau} \tag{3.58}$$

$$\Psi_1 = \tan^{-1} \frac{\int_{-\infty}^{\infty} \sin\,[8\gamma(\tau) - 2\pi 8f_1\tau]\, d\tau}{\int_{-\infty}^{\infty} \cos\,[8\gamma(\tau) - 2\pi 8f_1\tau]\, d\tau} \tag{3.59}$$

Now we must describe how the four integrals appearing in Eqs. (3.58) and (3.59) may be computed numerically. For concreteness, we consider that in the numerator of Eq. (3.57), although all four are handled in an identical manner. First, we break the interval of integration into one baud intervals:

$$\int_{-\infty}^{\infty} \cos\,[8\gamma(t) - 2\pi 8f_1 t]\, dt = \sum_k \int_{kT - \frac{T}{2} + \tau_g}^{kT + \frac{T}{2} + \tau_g} \cos\,[8\gamma(t) - 2\pi 8f_0 t]\, dt \tag{3.60}$$

where τ_g is the group delay of the receiver bandpass filter $H(\omega)$. This filter is designed with minimal distortion; in particular, over the interval $(kT - \frac{T}{2} + \tau_g,\ kT + \frac{T}{2} + \tau_g)$ the filter output phase waveform will depend only on the pair of frequencies transmitted during the intervals $(kT - T, kT)$ and $(kT, kT + T)$ and the transmitted phase at time kT. It can easily be shown that all of the eight equally spaced phases allowed at kT give the same value for the integrand in question. Thus, the integral in Eq. (3.60) will take on exactly 16 distinct values corresponding to the 16 possible combinations of preceding and succeeding frequencies. In considering Eq. (3.60) we must recall that the summation over an infinite number of T sec intervals is a mathematical fiction arising from the fact that we have assumed zero bandwidth for PLL. In fact, the summation will include a finite but very large number of T sec integrals. In this summation, each of the 16 distinct values for the T sec integral will occur with equal probability, assuming a random data sequence. The number of terms in the summation will be large enough that we may neglect variations of the number of each distinct type about its expected value. Thus the final value of the summation will be proportional to the average of the 16 possible values for the basic T sec integral. Thus, in calculating Eq. (3.60) we will simply calculate and sum the 16 distinct values taken on by the integral appearing on the right-hand side. This involves, of course, calculating the actual value of $\gamma(t)$ in the presence of multipath using Eqs. (3.46), (3.47) and (3.48) for each of the 16 frequency combinations. In this manner the integrals appearing in Eqs. (3.58) and (3.59) are numerically evaluated (to within a proportionality constant) and Ψ_0 and Ψ_1 are calculated.

Having obtained Ψ_0 and Ψ_1, we note that phase error in the symbol reference is $\Psi_0 - \Psi_1$, so that the actual sampling instant is given by

$$t_s = \frac{\Psi_0 - \Psi_1}{2\pi} T \tag{3.61}$$

Thus, due to the timing error, $\gamma(0)$ in Eqs. (3.41) and (3.44) must be replaced by $\gamma(t_s)$ in calculating the error probability. However, an additional term arises from the derived phase reference:

$$e^{j2\pi f_0 t + \Psi_0} \tag{3.62}$$

where Ψ_0 is simply $\Psi_0/8$. Replacing t by t_s [from Eq. (3.61)] and f_0 by its value - 3/16T gives the phase of the reference at the sampling instant:

$$\varphi_{ref} = \frac{\Psi_0 - 3\Psi_1}{16} \tag{3.63}$$

Now we may rewrite Eqs. (3.41) and (3.44) to include the effect of the derived phase and symbol references:

$$P_A(j,k) = 1 - \Phi\left[\frac{\frac{\pi}{8} + (k-j-1)\theta_0 - \gamma(t_s) + \varphi_{ref}}{\sigma}\right] \tag{3.64}$$

$$P_B(j,k) = 1 - \Phi\left[\frac{\gamma(t_s) - \varphi_{ref} + \frac{\pi}{8} - (k-j+1)\theta_0}{\sigma}\right] \tag{3.65}$$

Actual error rates are calculated from (3.45) as before.

3.2 Receiver Performance Over Multipath Channels

3.2.1 Channel Selection

Section 3.1 above has described the analytical basis for the computer software which has been developed to calculate performance of the two modems of interest in the presence of multipath. In this section we present results obtained with this software for the Hohenstadt-Zugspitze link. In obtaining this data, it was desired to consider a wide range of multipath conditions which could exist on this link. This has involved two processes of selection which will be described before proceeding to the actual performance results. The first selection process is that of selecting a set of physical channel parameters for which to calculate the path structure. Given the path structure, in the form of amplitudes and relative delays, one must then calculate the parameters which characterize the communication channel at various fade depths.

The multipath structure of the Hohenstadt-Zugspitze has been discussed in detail in Section 2.4. In selecting channel conditions, we have taken sample points from each of the multipath profiles illustrated in Figs. 2.16 to 2.18. The layer height samples are given approximately by

$$h_L = h_{min} + n\left(\frac{h_{max} - h_{min}}{4}\right) \qquad n = 1,2,3 \tag{3.66}$$

where h_{min} is the smallest layer height resulting in multipath for a given layer tilt and h_{max} is the largest. This scheme is illustrated in Fig. 3.4 where we have numbered the cuts according to the value of n in (3.66). This numbering, accompanied by the exact layer heights involved, also appears on the error rate curves to be presented later in this report. For the refractive index gradient the values -400, -350, and -300 Nu/km are used; these are in reasonable accord with relevant data [2.6]. For each value of refractive index gradient the layer slopes given in Table 3-1 have been used in the calculations. Not all combinations of refractive index gradient and layer slope result in multipath, however. All of the multipath profiles resulting from those combinations that do support multipath have been illustrated earlier in this report and have been sampled in the manner illustrated in Fig. 3.4. This results in consideration of 27 distinct channel conditions. This approach via the propagation software provides us with the discrete set of amplitudes and delays that have been used in the simulations described below.

Given a set of path delays and amplitudes obtained in the manner described above, phases must be determined for each path which will result in a deep fade. Referring to Section 2.3.2, it has been shown that for a set of N amplitudes (α_i) and delays (ξ_i) the first three terms in the frequency power series model for the channel transfer function are given by

$$T_0 = \sum_{i=1}^{N} \beta_i \tag{3.67}$$

$$T_1 = \sum_{i=1}^{N} \beta_i \eta_i \tag{3.68}$$

$$T_2 = \frac{1}{2} \sum_{i=1}^{N} \beta_i \eta_i^2 \tag{3.69}$$

where β_i is the complex amplitude

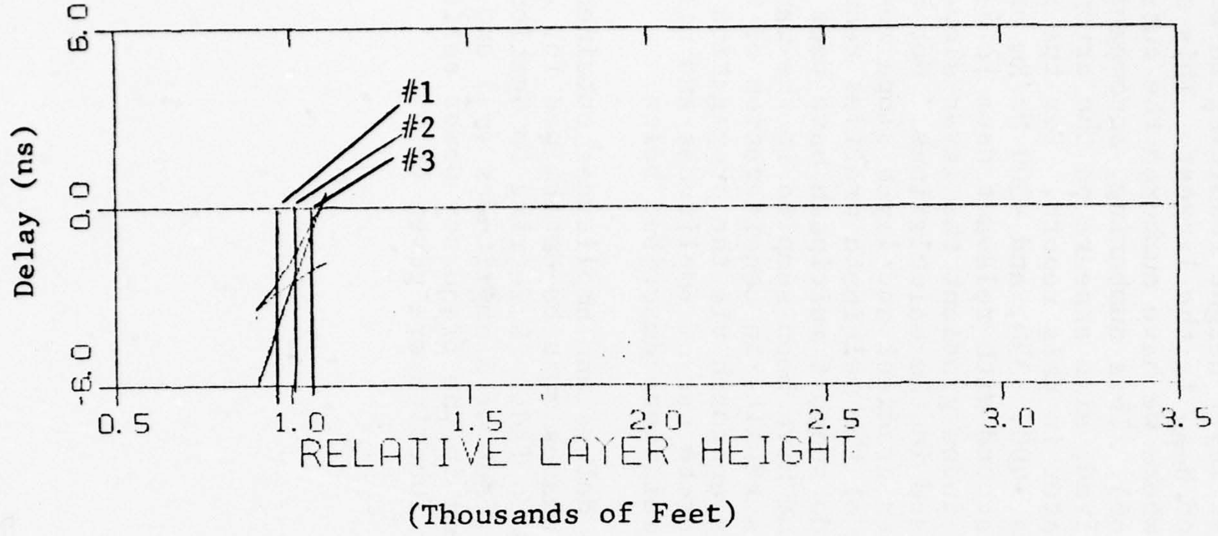

Figure 3.4 Layer Height Sample Points of Diversity Receiver No. 1 on the Hohenstadt-to-Zugspitze Link

TABLE 3-1

VALUES OF LAYER SLOPE USED IN CALCULATIONS AND CORRESPONDING LAYER TILT ANGLES

Layer Slopes	Layer Tilt Angle (Degrees)
.003	.172
.004	.229
.005	.286
.006	.344
.007	.401
.008	.458
.009	.5156
.010	.573

$$\beta_i = \alpha_i e^{-j2\pi f \xi_i} = \alpha_i e^{j\theta_i} \qquad (3.70)$$

and η_i is the delay after subtraction of the mean delay

$$\eta_i = \xi_i - \xi_0 \qquad (3.71)$$

The value of T_0 gives the fade depth at the center of the frequency band. For a deep fade the value of T_0 will be quite small compared to the magnitude of the vectors β_i. This situation is illustrated in Fig. 3.5 for the case $N = 3$ which is of interest here. From this figure it is clear that when T_0 is small, small variations in either the magnitude or angle of the β_i's can produce significant variation in both the magnitude and angle of T_0. On the other hand, these small variations in the β_i's will not greatly affect T_1 and T_2 as given by Eqs. (3.68) and (3.69). Based on these considerations, the following procedure has been used in calculating T_0, T_1, and T_2 for a set of gains and delays:

1) Find the values of θ_i which give

$$T_0 = 0.$$

2) Use these values of θ_i to calculate T_1 and T_2.

3) Select the magnitude of T_0 to give the desired fade depth.

4) Allow the angle of T_0 to vary over the range $(0, 2\pi)$. For each value in this range the coefficients p_1, p_2, and p_3 may be calculated and the software used to evaluate error probability. The error probabilities obtained in this way are then averaged.

3.2.2 Baseband Modem Performance

For each of the 27 multipath conditions performance of the baseband modem was calculated at three fade depths: 10, 20, and 30 dB. As the depth of the fade increases, frequency-selective

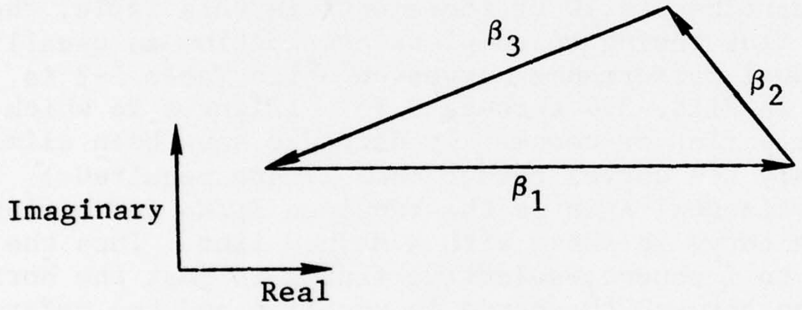

Figure 3.5 Example of Alignment of Path Vectors Producing Deep Fade

effects become more pronounced. In other words, fading will be "flat" (that is undistorted) for smaller fade depths and frequency-selective (that is distorted) for larger fade depths. At some fade depth distortion will reach the point where the eye-pattern closes for certain symbol sequences; when this happens it will be impossible to obtain a satisfactory error rate regardless of the value of E_b/N_0 available to the receiver. This behavior may be seen qualitatively in Table 3-2 which summarizes modem performance for each of the channel conditions considered. (In this table the three layer heights which were considered for each combination of refractive index gradient and layer tilt slope are lumped together for simplicity.) Selecting a gradient and slope, one can look across horizontally and compare performance at fade depths of 10, 20, and 30 dB. For relatively flat channels the transition from flat fading to frequency-selective fading occurs at very deep fades, while for more selective channels the transition occurs for shallower fade depths. Since fade depth is quantized to 10 dB increments in this table, the transition from flat fading to complete degradation is usually abrupt. Individual performance curves on which Table 3-2 is based are shown in Figs. 3.6 through 3.15. (Figures in which fading is entirely flat or completely degraded have been eliminated, so that only ten curves rather than 27 are required.) In each case the horizontal axis is the received E_b/N_0 and a flat fading reference curve is shown with a dashed line. Thus the degradation due to frequency-selective fading is just the horizontal separation between the curve in question and the reference curve.

3.2.3 IF Modem Performance

The performance of the phase-continuous FSK modem was evaluated for the same set of conditions for which the baseband modem was evaluated. In making these calculations a bit rate of 27.648 Mb/s was assumed for equivalence with the baseband modem, although the breadboard of the IF modem actually operates at a bit rate of 27.275 Mb/s. As before, flat fading performance is shown with a dashed line. In this way the loss in performance due to frequency-selective fading may be compared between modems even though the absolute performance of the two modems (in flat fading) is considerably different. Table 3-3 presents a summary of performance of the IF modem which may be compared with the earlier table for the baseband modem. On the whole, the effects of multipath on the two modems are remarkably similar. However, a careful examination of the tables or of the accompanying figures (3.16 - 3.26) shows that the FSK modem is somewhat less susceptible to multipath than the baseband modem. As an example, Fig. 3.17 shows less degradation than Fig. 3.8; both apply to the same channel.

TABLE 3-2

QUALITATIVE FADING BEHAVIOR OF BASEBAND MODEM

Refractive Index Gradient (Nu/km)	Layer Tilt Slope	Layer Tilt Angle (Degrees)	Fade Depth		
			10 dB	20 dB	30 dB
-400	0.007	0.401	Flat	Flat	Nearly Flat (Fig. 3.6)
	0.008	0.458	Flat (Fig. 3.7)	Mixed (Fig. 3.8)	Completely Degraded
	0.009	0.516	Nearly Flat (Fig. 3.9)	Completely Degraded	Completely Degraded
	0.010	0.573	Mixed (Fig. 3.10)	Completely Degraded	Completely Degraded
-350	0.008	0.458	Flat	Flat	Nearly Flat (Fig. 3.11)
	0.009	0.516	Flat	Mixed (Fig. 3.12)	Completely Degraded
	0.010	0.573	Nearly Flat (Fig. 3.13)	Completely Degraded	Completely Degraded
-300	0.009	0.516	Flat	Flat	Flat (Fig. 3.14)
	0.010	0.573	Flat	Nearly Flat (Fig. 3.15)	Completely Degraded

(The term "completely degraded" indicates eye closure and an error rate exceeding 10^{-2} over the range of received E_b/N_0 considered.)

TABLE 3-3

QUALITATIVE FADING BEHAVIOR OF IF MODEM

Refractive Index Gradient (Nu/km)	Layer Tilt Slope	Layer Tilt Angle (Degrees)	Fade Depth		
			10 dB	20 dB	30 dB
-400	0.007	0.401	Flat	Flat	Nearly Flat (Fig. 3.16)
	0.008	0.458	Flat	Nearly Flat (Fig. 3.17)	Completely Degraded
	0.009	0.516	Nearly Flat (Fig. 3.18)	Mixed (Fig. 3.19)	Completely Degraded
	0.010	0.573	Nearly Flat (Fig. 3.20)	Completely Degraded	Completely Degraded
-350	0.008	0.458	Flat	Flat	Nearly Flat (Fig. 3.21)
	0.009	0.516	Flat	Nearly Flat (Fig. 3.22)	Completely Degraded
	0.010	0.573	Nearly Flat	Degraded (Fig. 3.23)	Completely Degraded
-300	0.009	0.516	Flat	Flat	Flat (Fig. 3.24)
	0.010	0.573	Flat	Nearly Flat (Fig. 3.25)	Degraded (Fig. 3.26)

(The term "completely degraded" indicates eye closure and an error rate exceeding 10^{-2} over the range of received E_b/N_0 considered.)

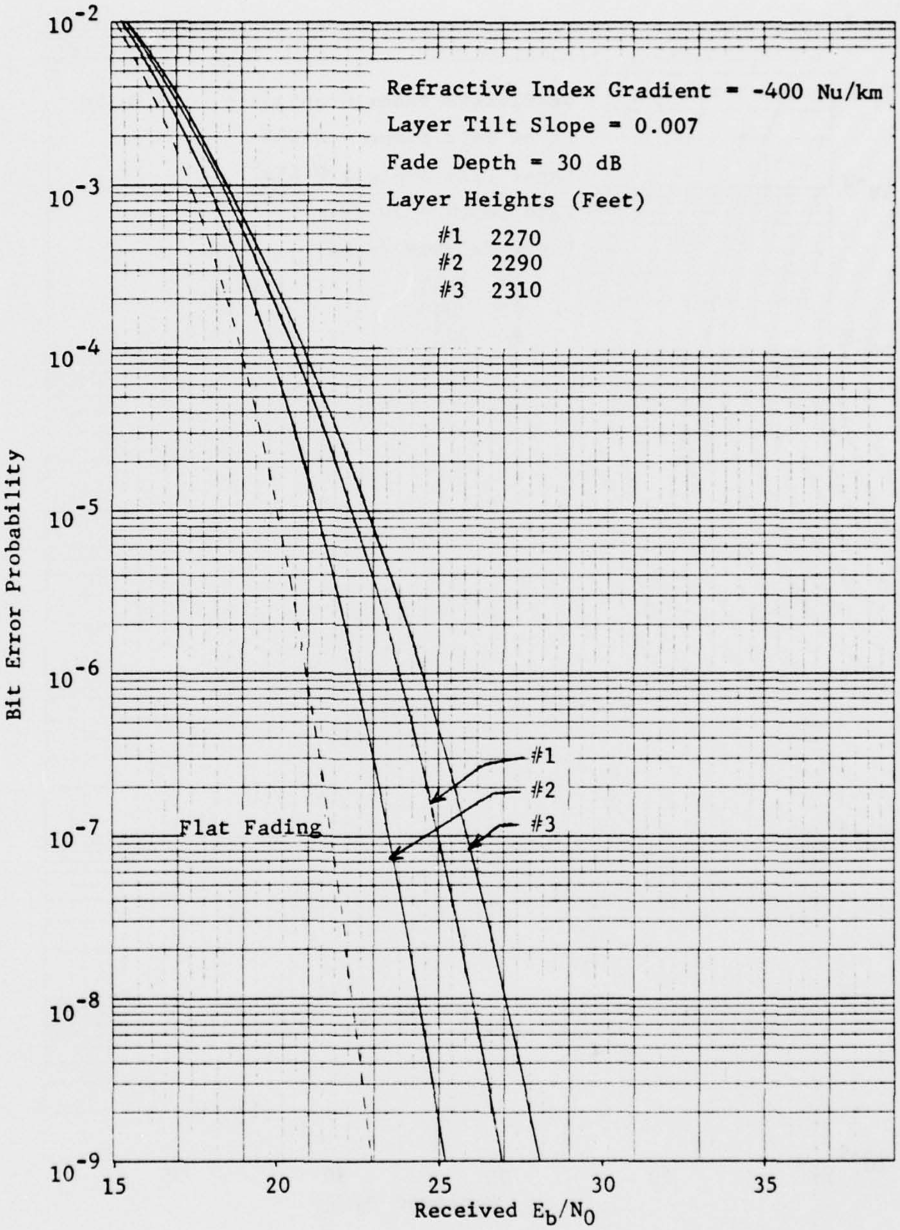

Figure 3.6 Simulated Performance of DAU Modem

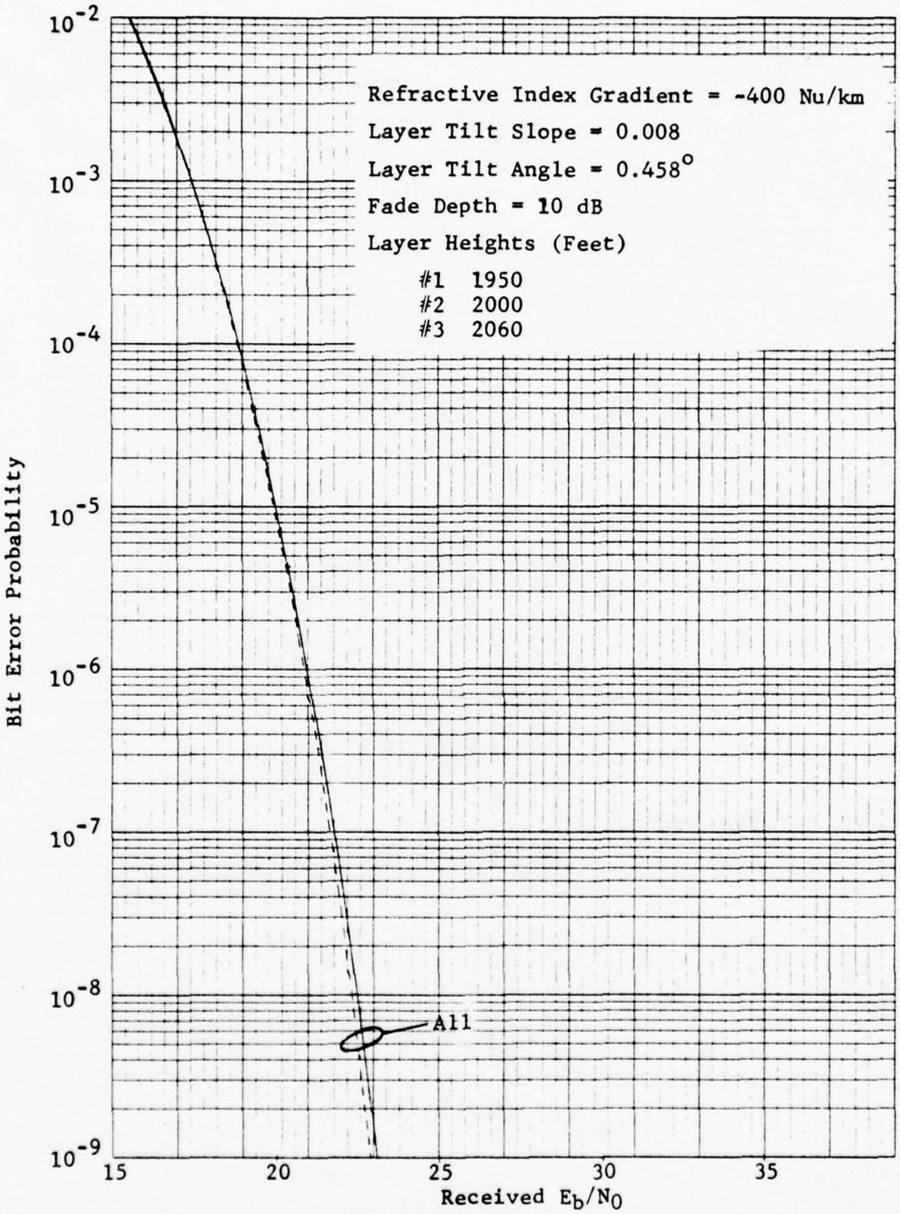

Figure 3.7 Simulated Performance of DAU Modem

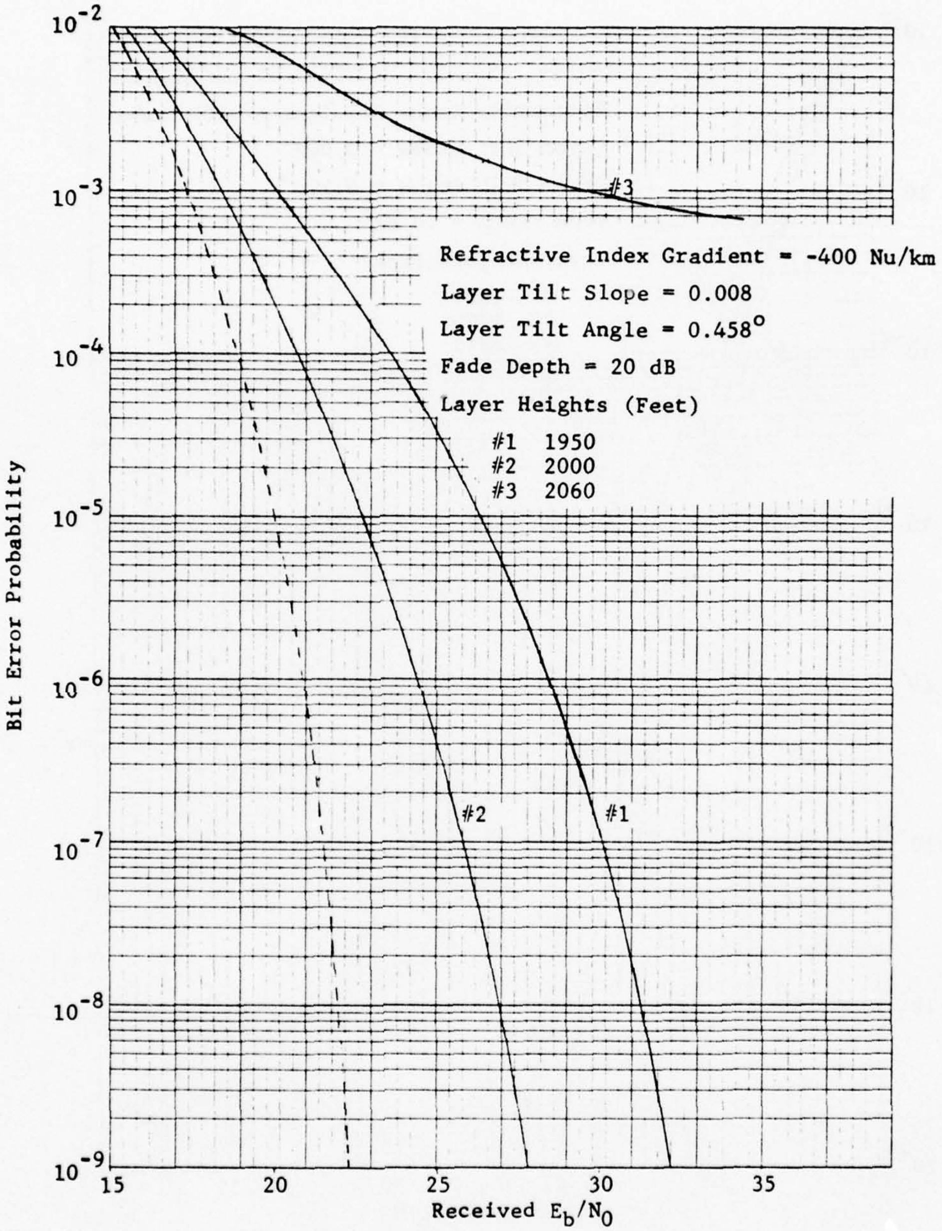

Figure 3.8 Simulated Performance of DAU Modem

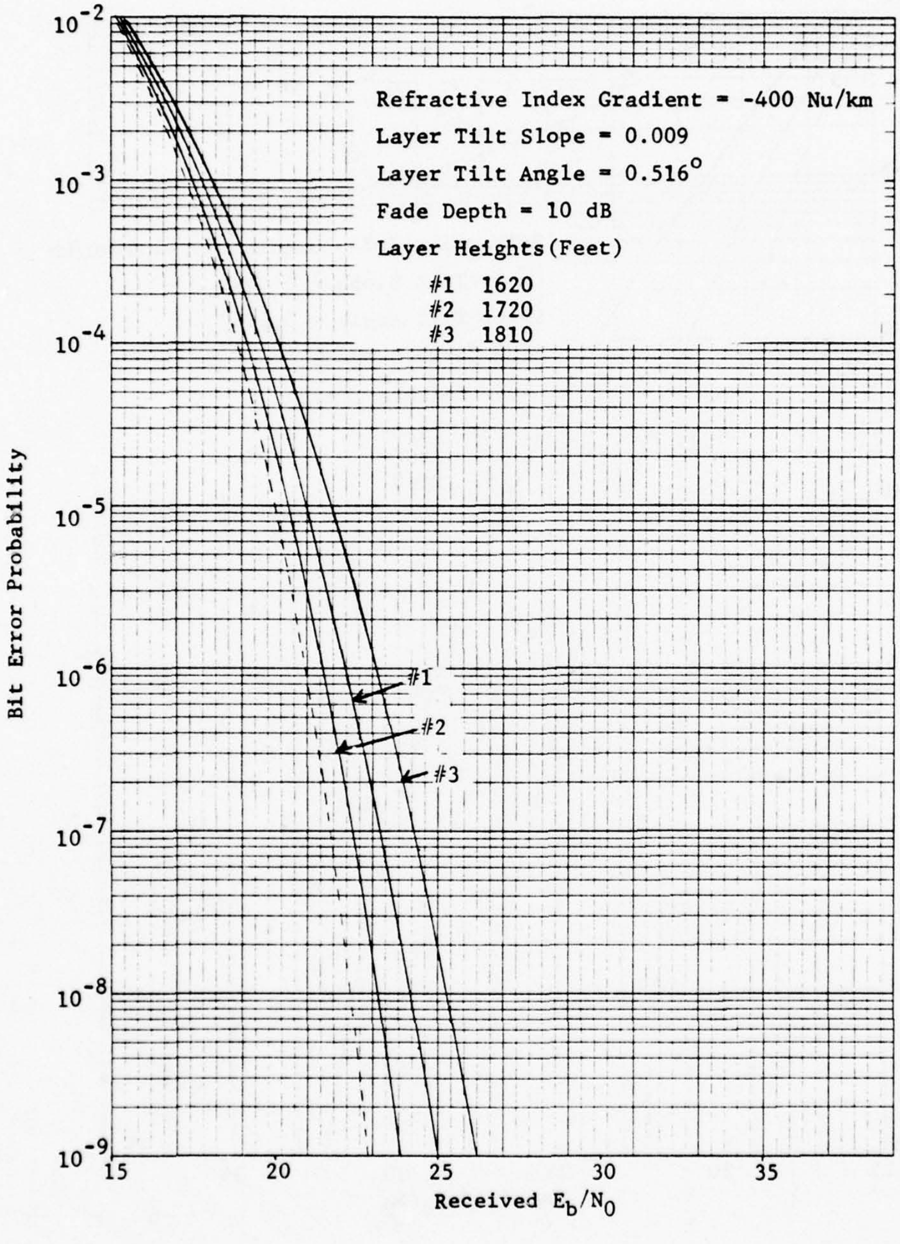

Figure 3.9 Simulated Performance of DAU Modem

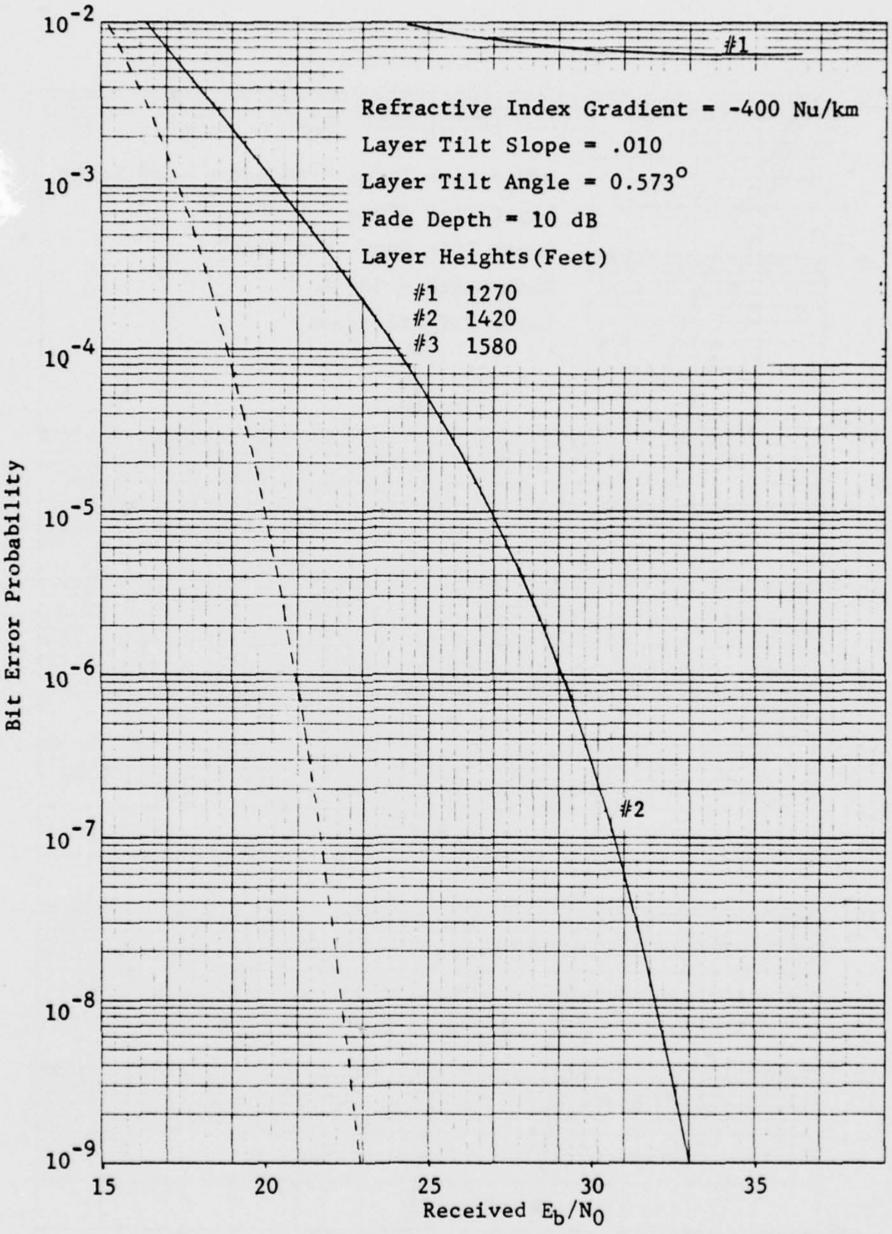

Figure 3.10 Simulated Performance of DAU Modem

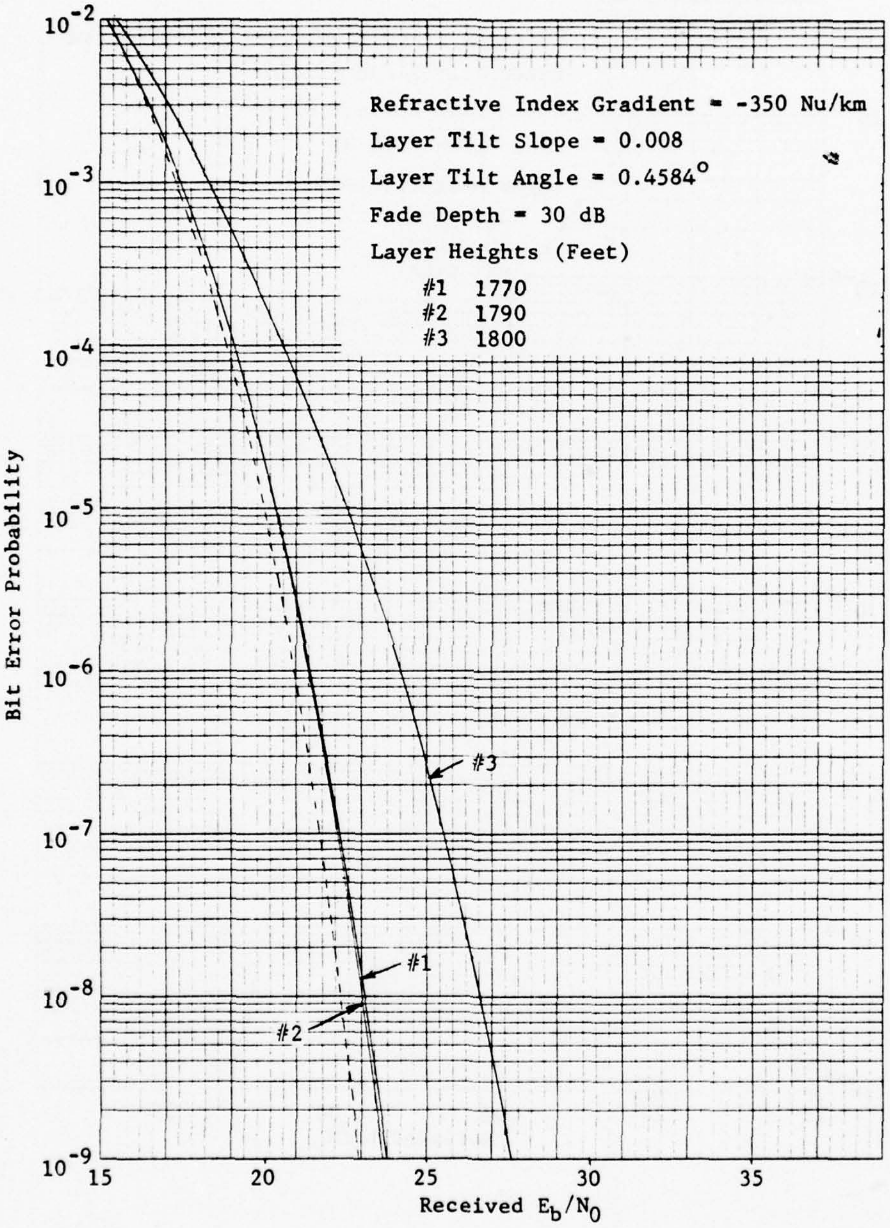

Figure 3.11 Simulated Performance of DAU Modem

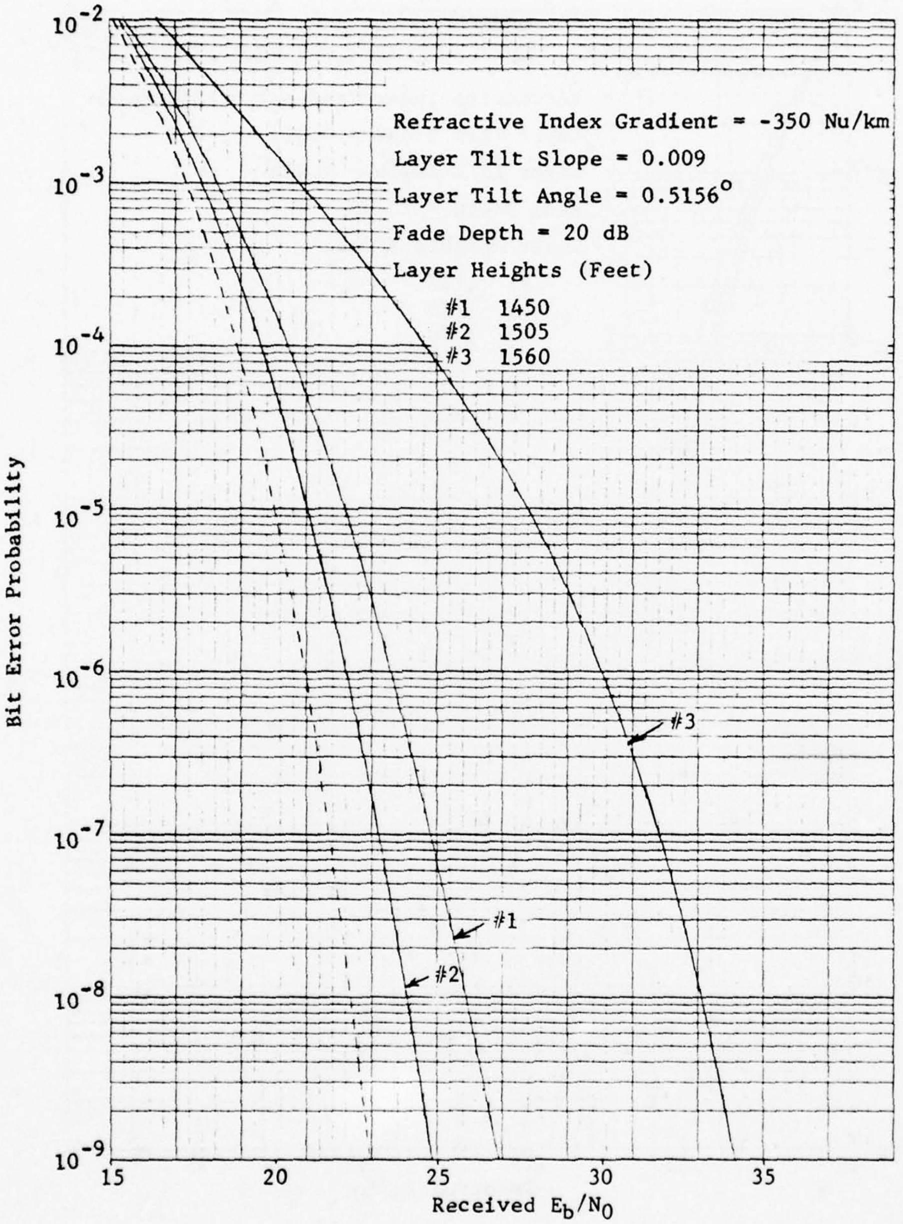

Figure 3.12 Simulated Performance of DAU Modem

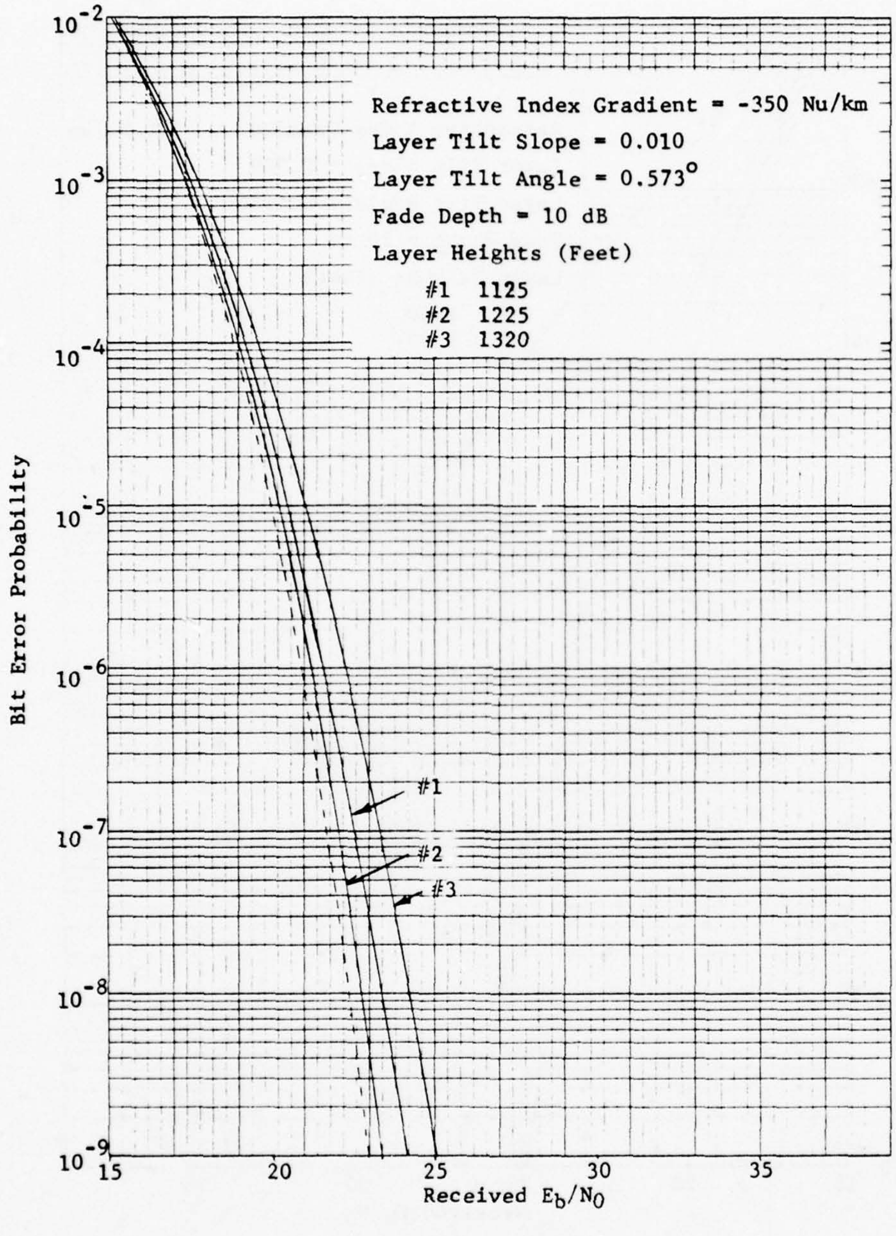

Figure 3.13 Simulated Performance of DAU Modem

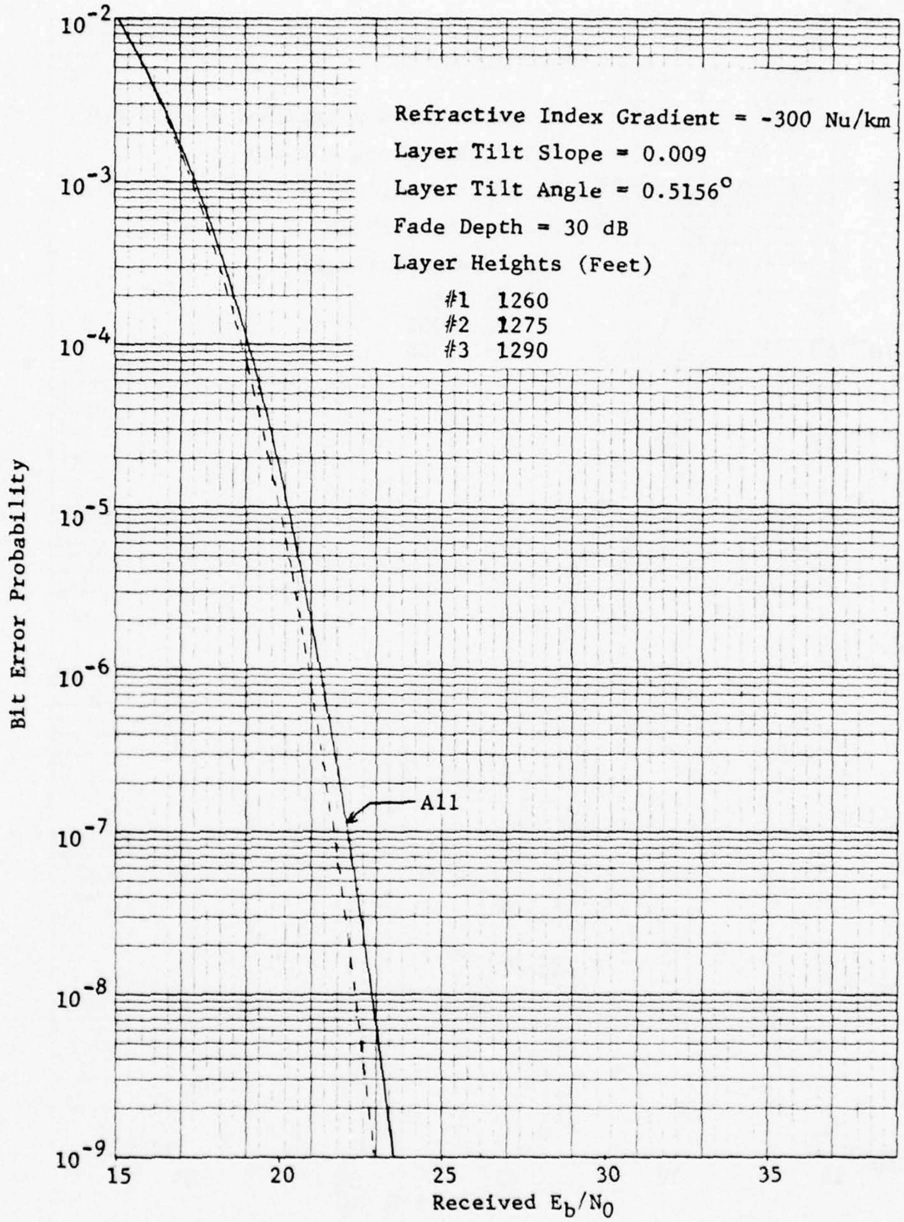

Figure 3.14 Simulated Performance of DAU Modem

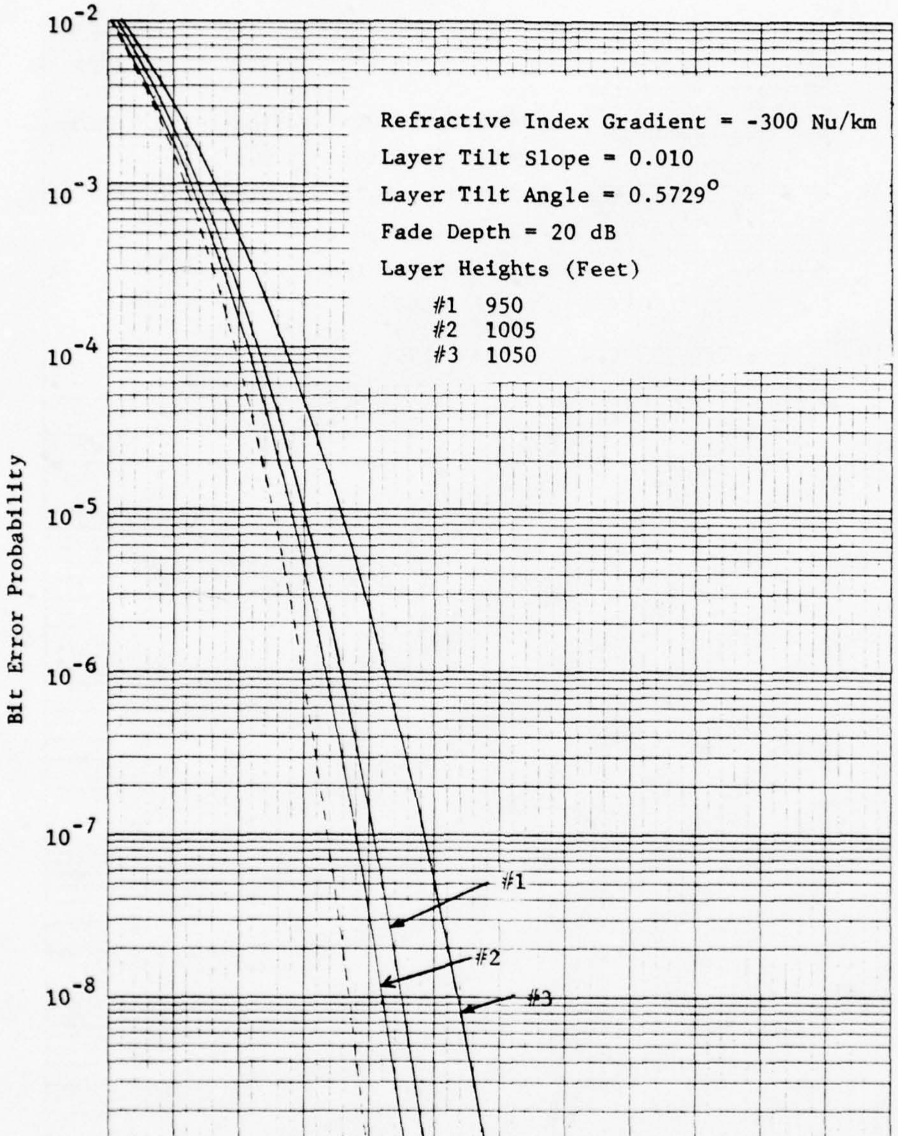

Figure 3.15 Simulated Performance of DAU Modem

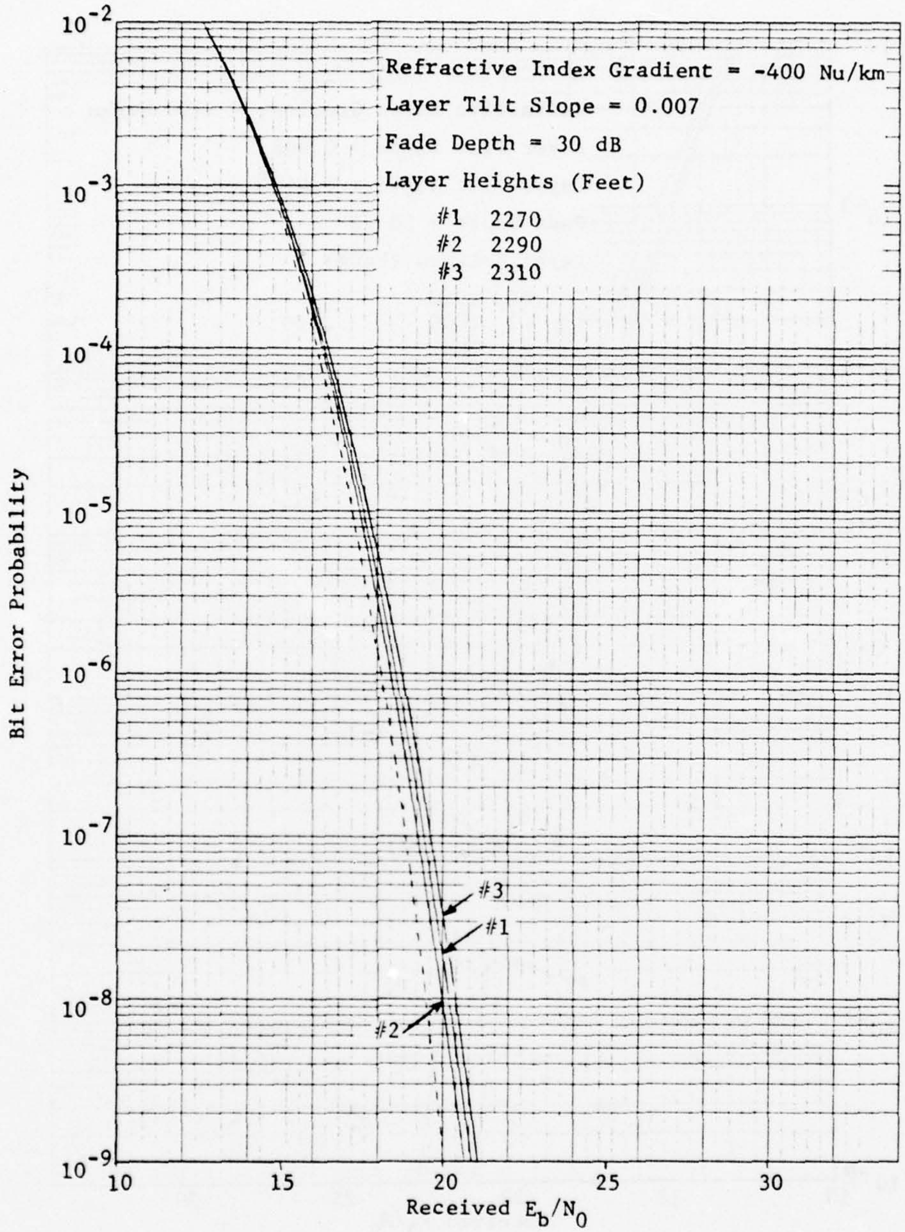

Figure 3.16 Simulated Performance of IF Modem

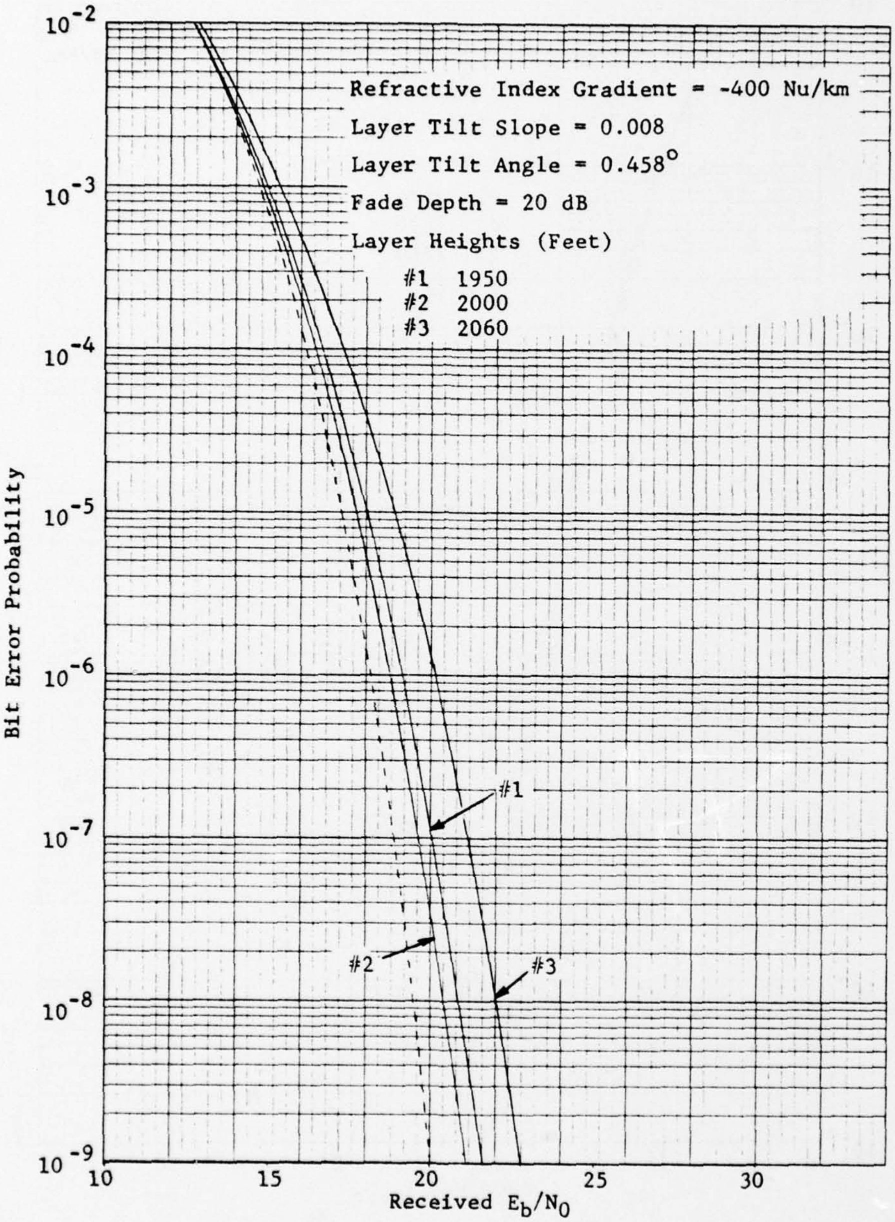

Figure 3.17 Simulated Performance of IF Modem

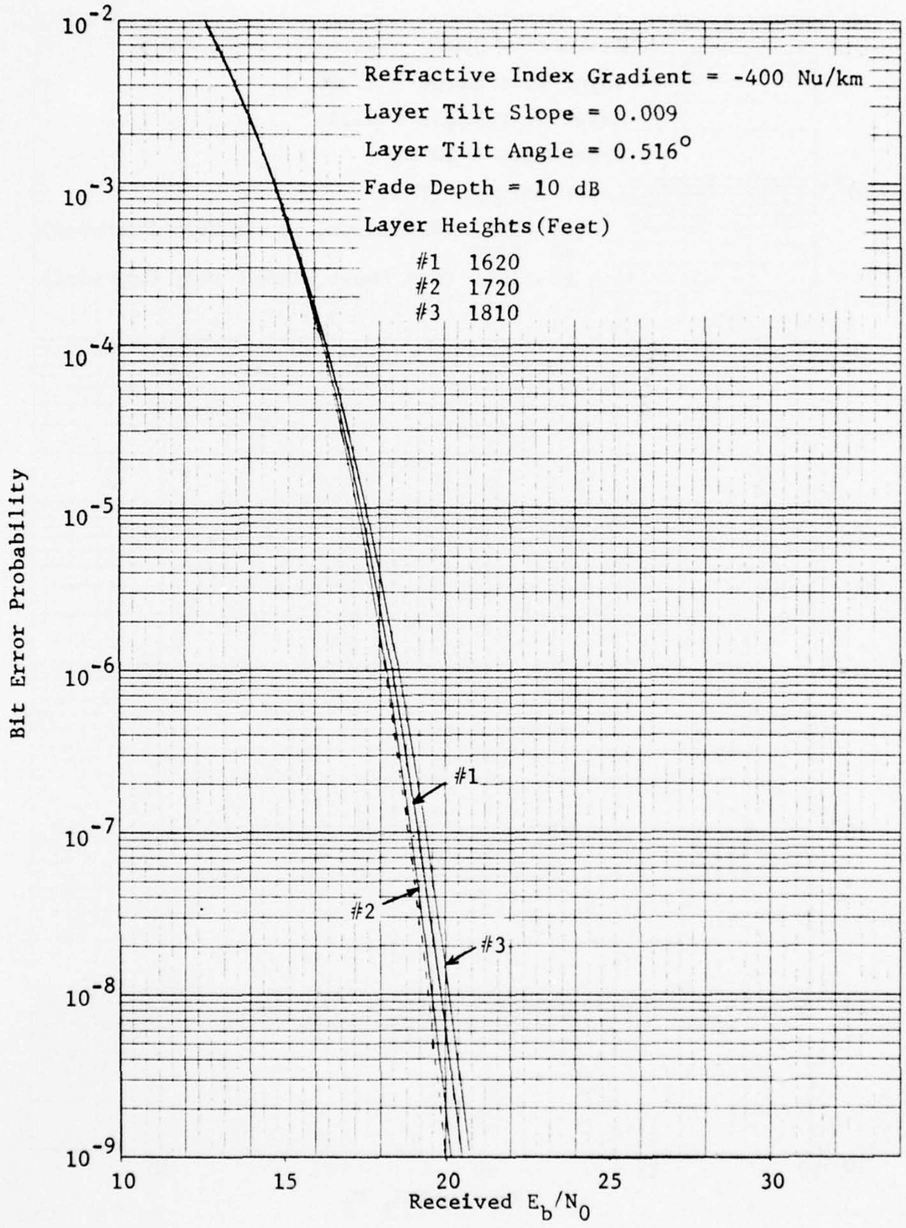

Figure 3.18 Simulated Performance of IF Modem

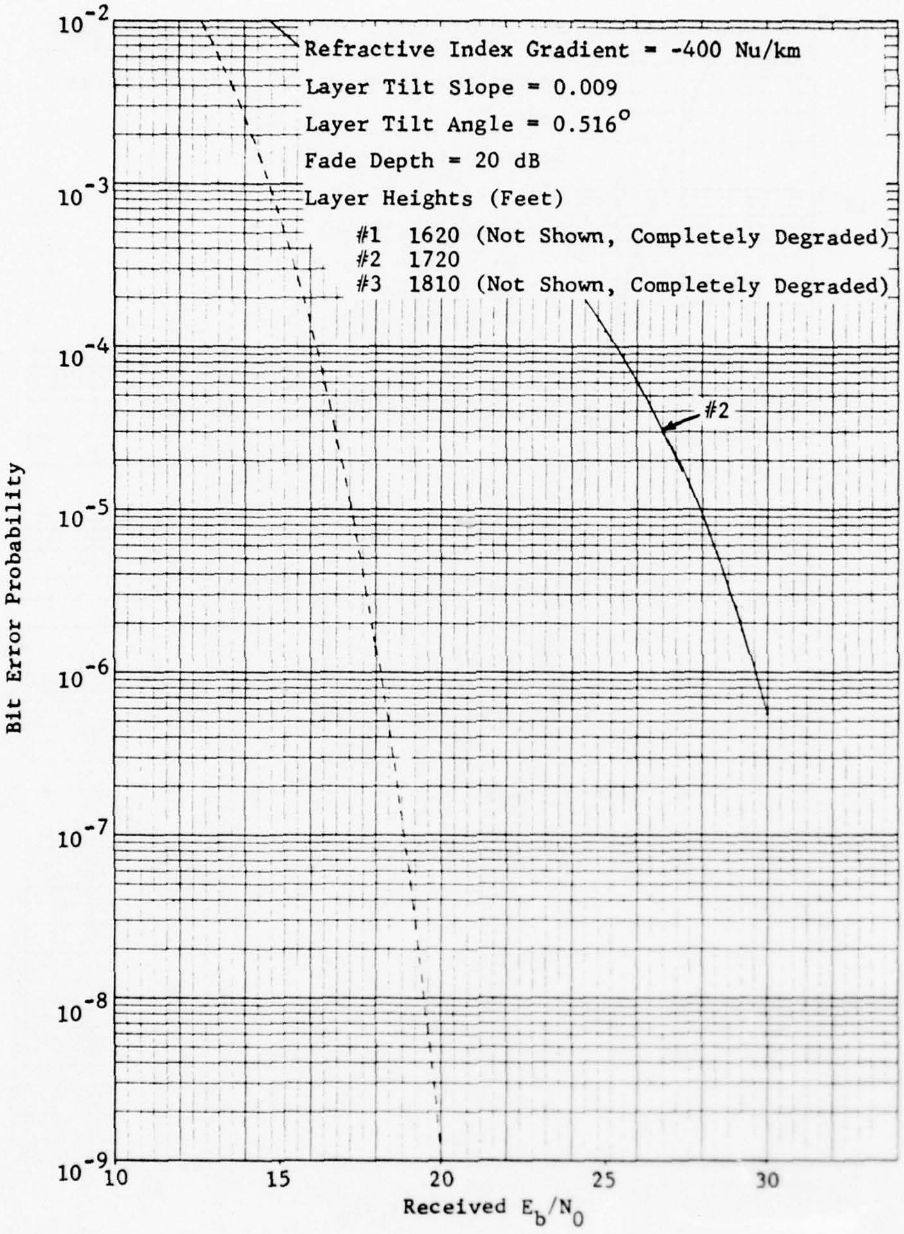

Figure 3.19 Simulated Performance of IF Modem

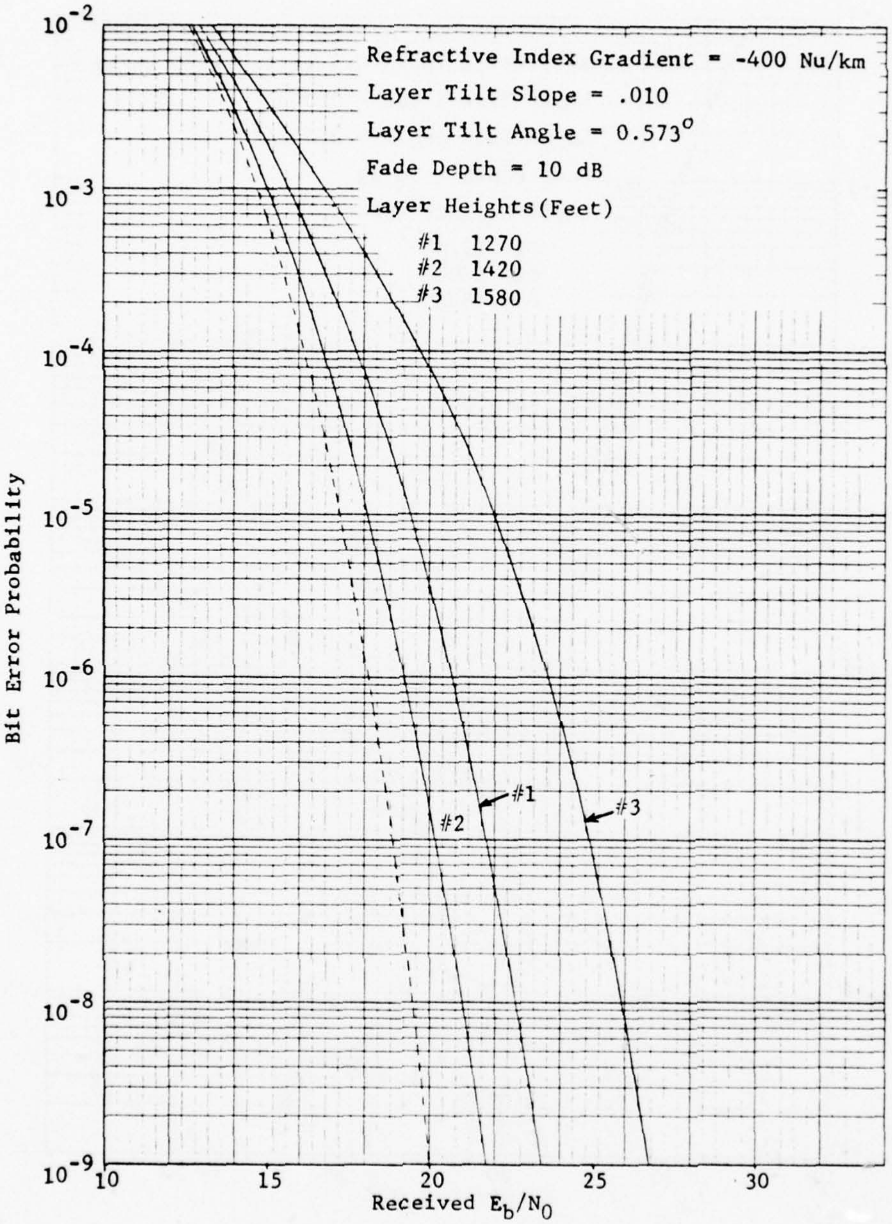

Figure 3.20 Simulated Performance of IF Modem

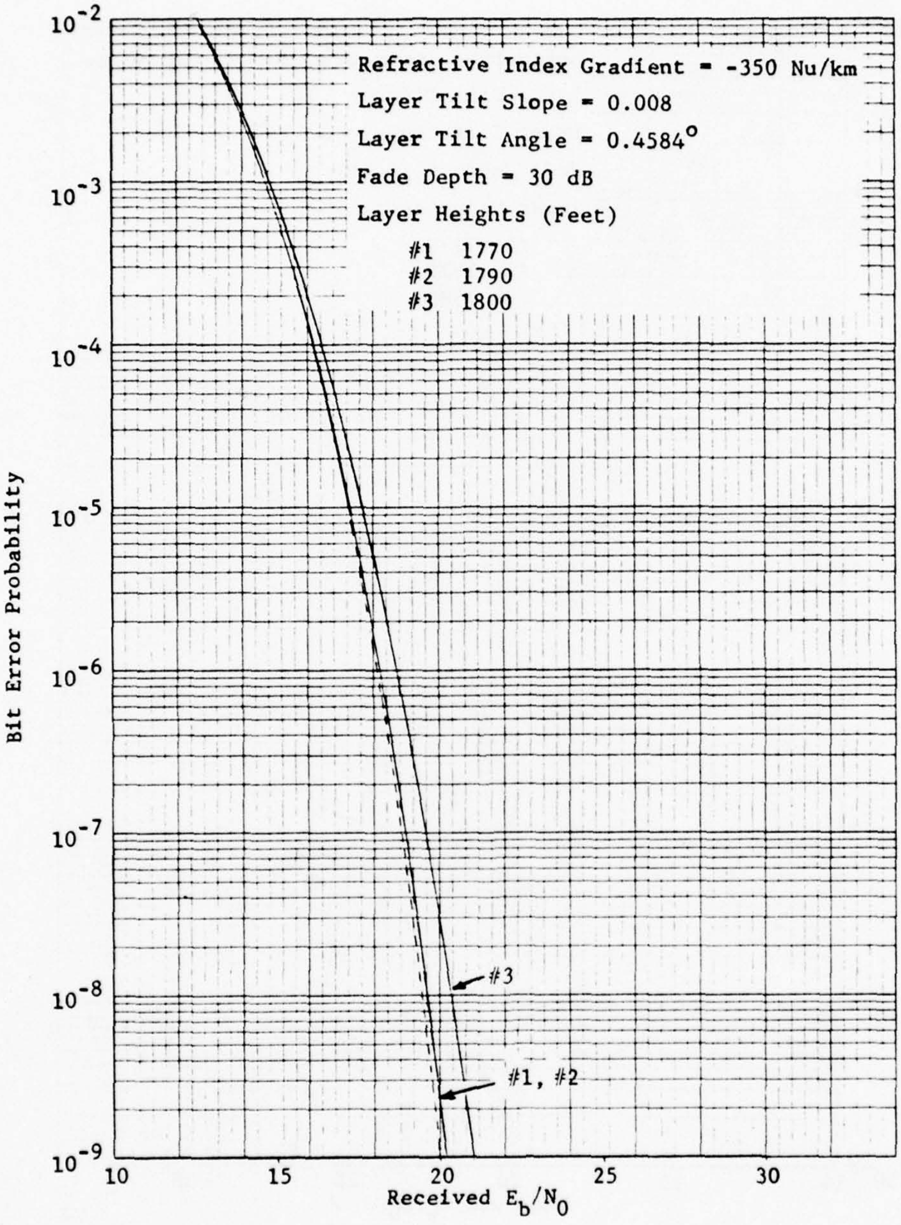

Figure 3.21 Simulated Performance of IF Modem

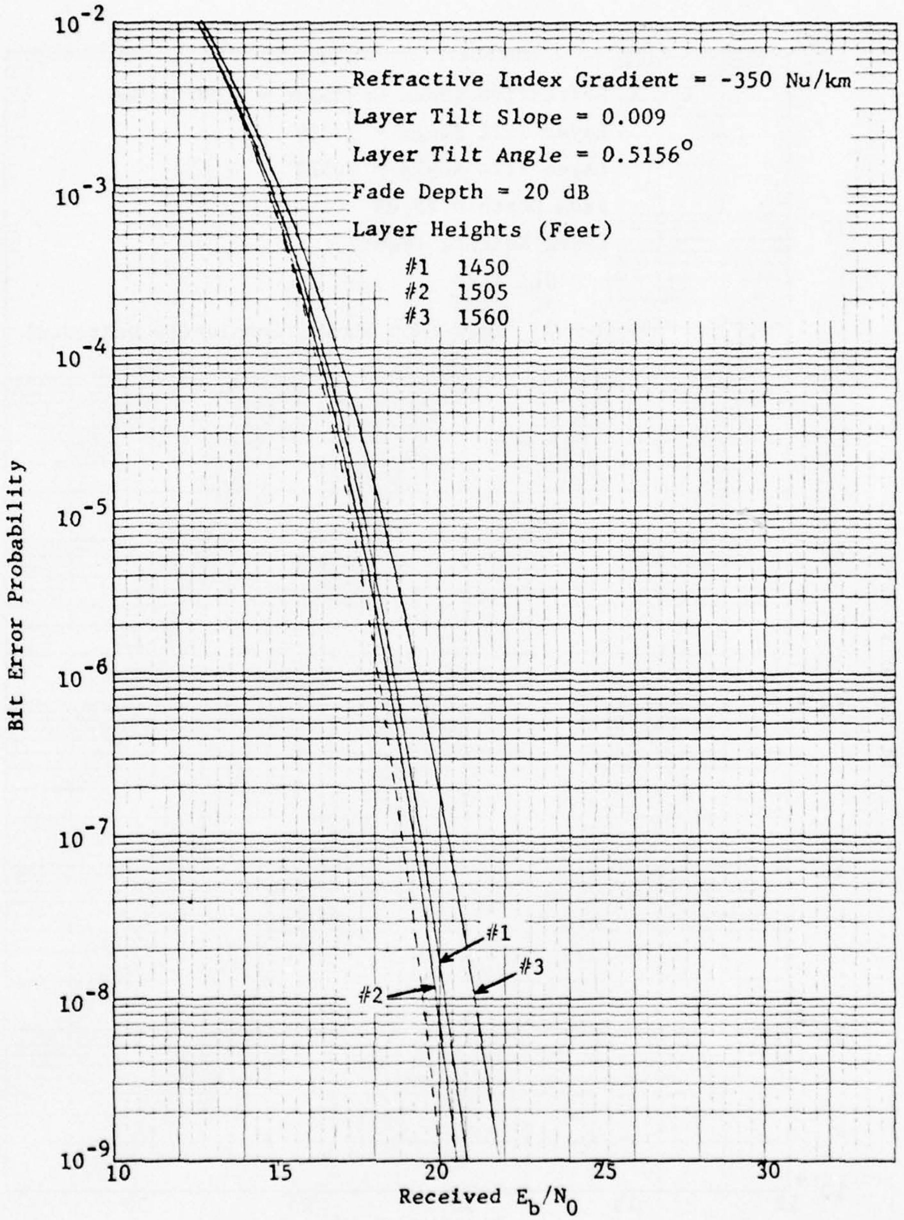

Figure 3.22 Simulated Performance of IF Modem

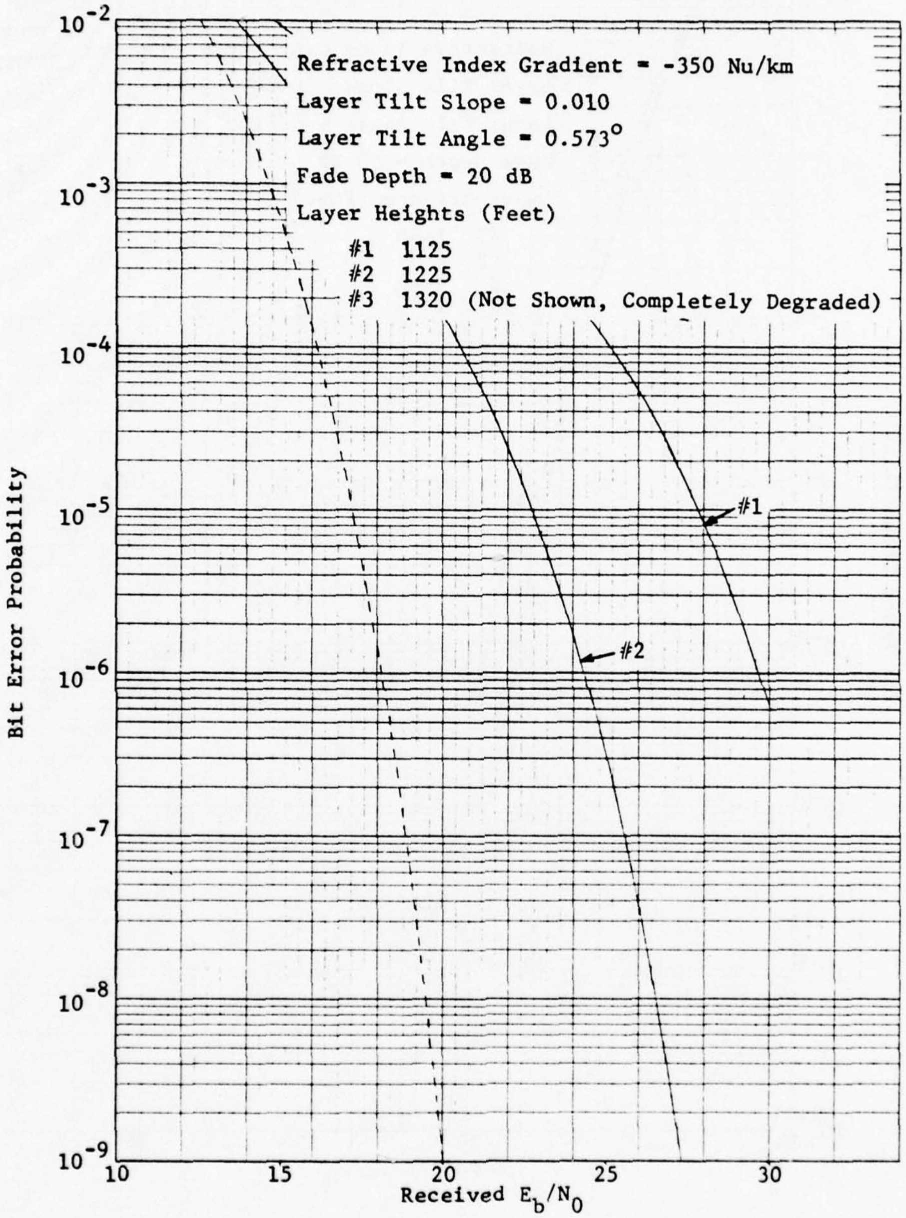

Figure 3.23 Simulated Performance of IF Modem

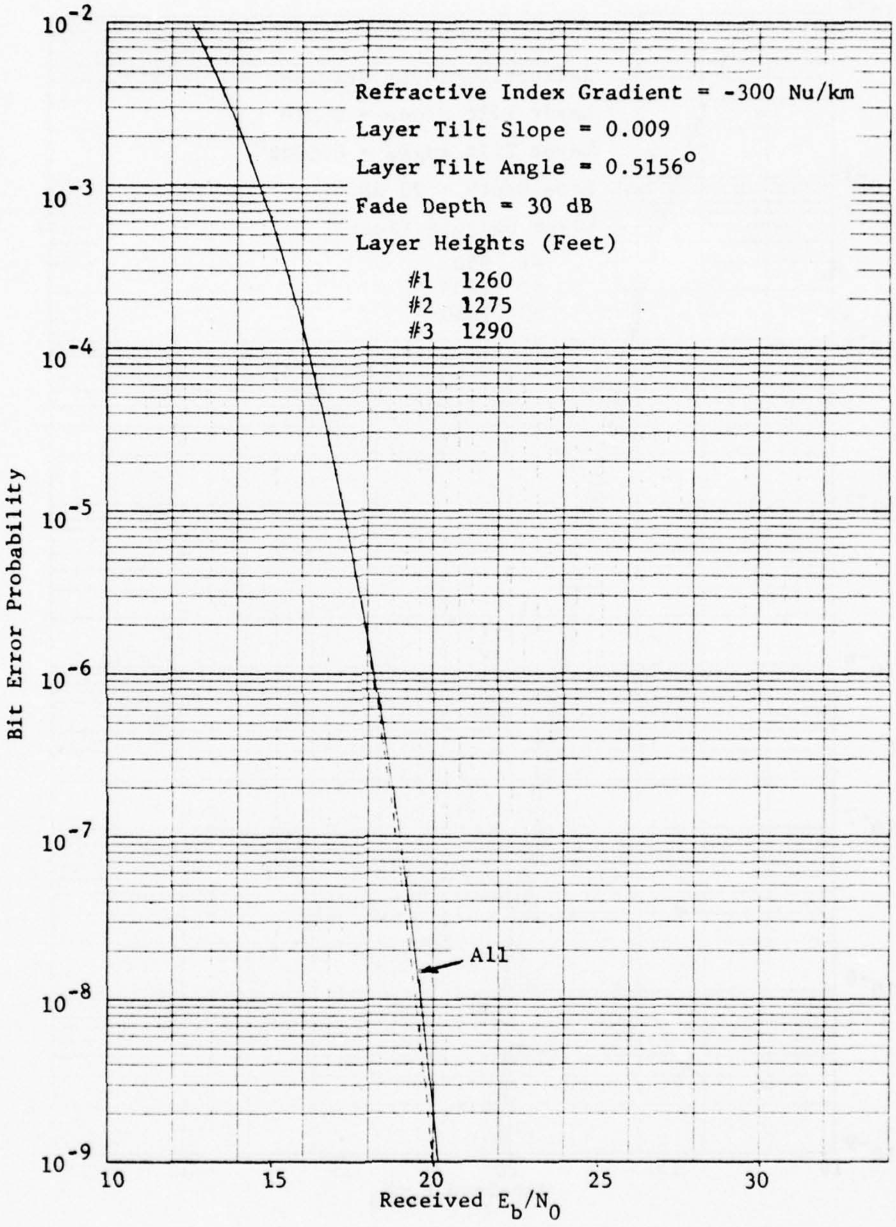

Figure 3.24 Simulated Performance of IF Modem

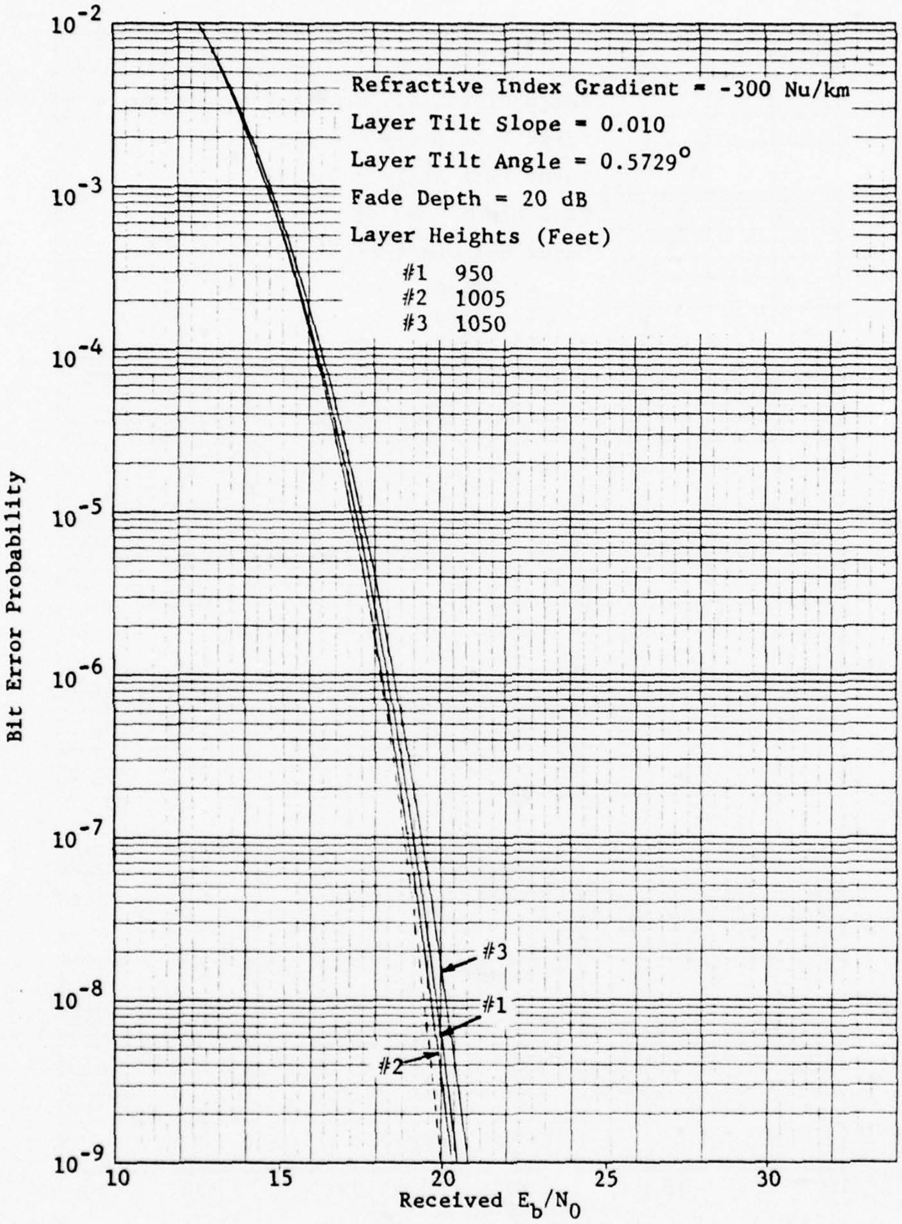

3.25 Simulated Performance of IF Modem

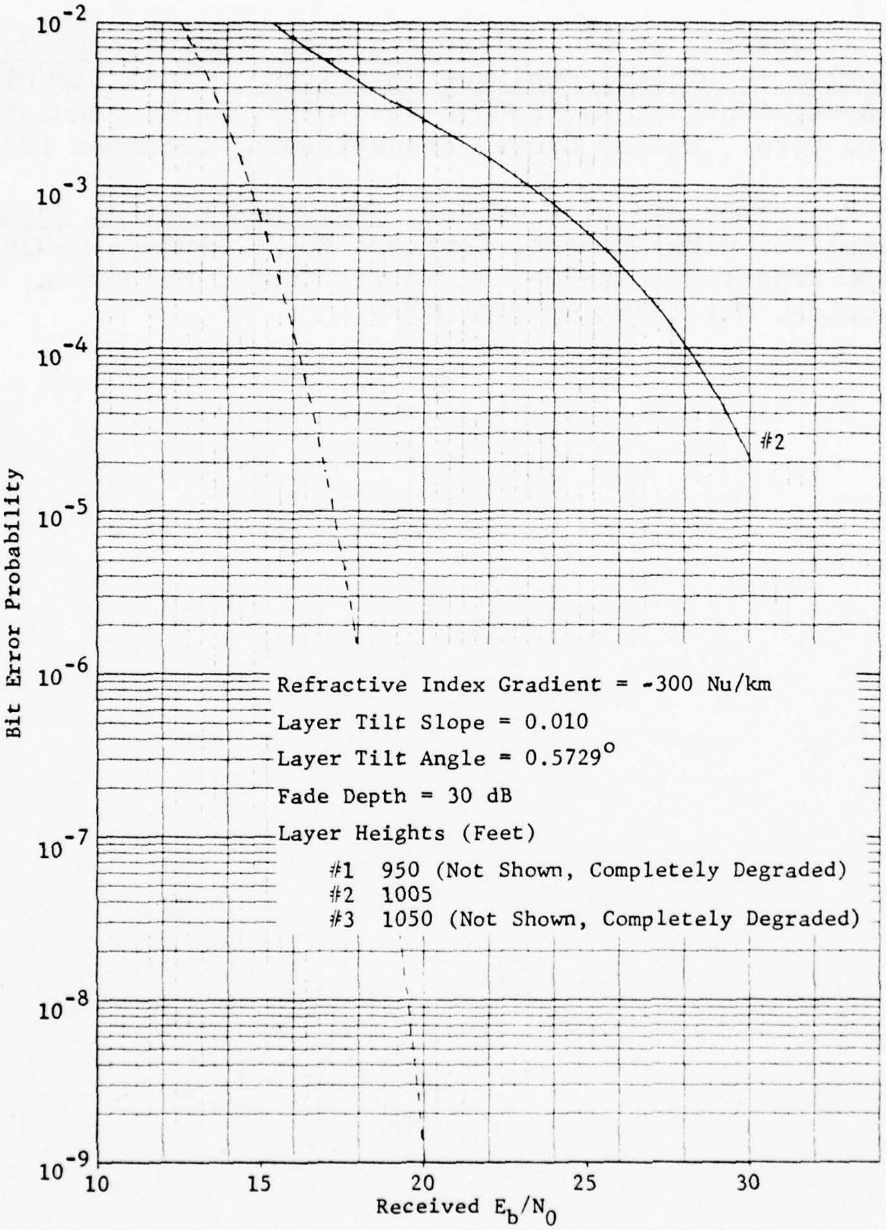

Figure 3.26 Simulated Performance of IF Modem

SECTION 3

REFERENCES

[3.1] F. A. Jessen, et al., Microwave Data Transmission Test Program -- Digital Applique Unit (DAU), Final Technical Report, Contract No. F30602-73-C-0203, RADC, Aeronutronic Ford Corp., Willow Grove, Pennsylvania, December 1975.

[3.2] T. R. Losson and D. D. McRae, Broadband Digital Modem, Final Technical Report, Contract No. F30602-74-C-0263, RADC Report No. TR-76-117, Harris Corp., Melbourne, Florida, May 1976 , AD# A025 399.

SECTION 4

EFFECT OF FREQUENCY-SELECTIVE FADING ON DIVERSITY COMBINING

This section is devoted to an examination of frequency-selective fading in a diversity context. In Section 4.1, the propagation aspects are discussed. The emphasis is primarily on space diversity, but some discussion of frequency diversity (including a rough rule of thumb for choosing the frequency separation) is provided. A series of plots provides a graphic view of diversity operation in a refractive multipath environment and some interesting conclusions about the advisability of certain diversity combining options.

Certain aspects of the tracking performance of modems during diversity operation are discussed in Section 4.2.

4.1 Propagation Effects in Diversity Operation

In this section we present the results of exercising the LOS software developed at CNR to determine the effects on diversity operation of the frequency-selective behavior of refractive multipath. In view of the complicated dependence of refractive multipath on several parameters (compounded in a diversity context), this is a task of considerable scope. Nevertheless, we have been able to generate, through a series of plots, an information overview of diversity operation in a refractive multipath environment and reach some important conclusions about the advisability of choosing certain options for diversity switching rules.

A first step on the road to obtaining the desired overview is to develop a more general view of refractive multipath on a single diversity channel. This was achieved early in this program via the fade level contour diagram illustrated in Figure 4.1. This figure was pieced together from 12 computer plots and constitutes a dual presentation of frequency and spatial selectivity (operating frequency on the horizontal axis and layer height on the vertical axis). The layer height on the vertical axis is, here, unlike our earlier plots, measured relative to highest terminal (receiver). The reason for this is that our contour plots were computed before the model modification of Figure 2.5(b) which takes into account layer

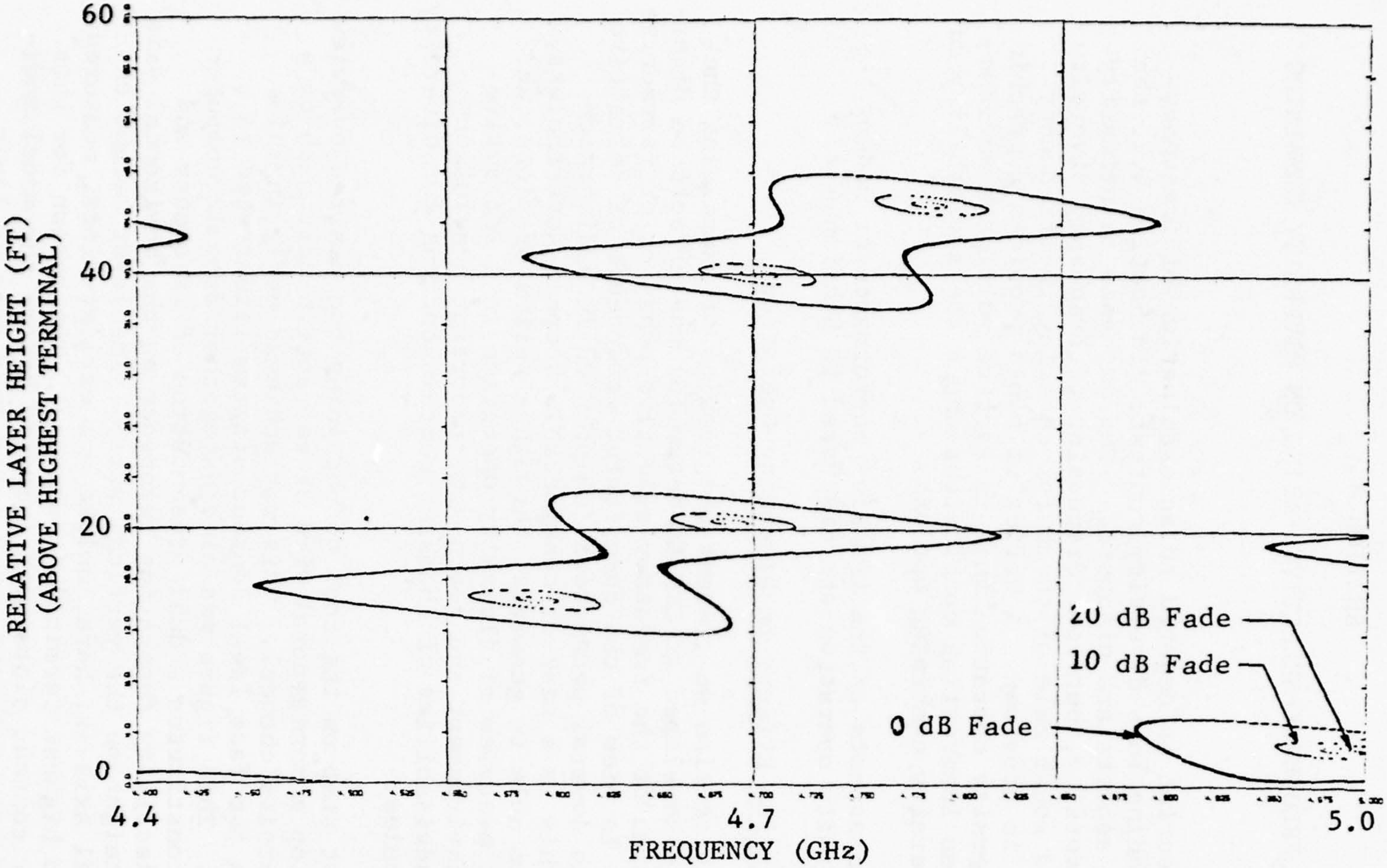

Figure 4.1 Deep Fade Loci Represented as Countour Plot

Receiver Height = 80 feet (above transmitter)
Refractive Index Gradient = -420 Nu/km
Ground Range = 30 miles
Layer Thickness > 62.6 feet

positions below the highest terminal. Thus, there is a gap of 80' in considered layer heights corresponding to the vertical region between transmitter and receiver.

For the situation described by the specified parameters below the figure caption, each contour in Figure 4.1 depicts the combination of layer heights and frequencies that will result in a fade to the depth with which each contour is designated. In our initial investigations under this program, the software leading to Figure 4.1 was generated in order to allow searches for deep fade loci over extensive areas in layer height and frequency space. As we can see, the deep fade loci are few and far between; in fact, there are only five of them appearing in Figure 4.1. Additionally, we note that the 10-dB fade contours extend over a few hundred MHz, whereas the 20-dB fade contours are much smaller. This is in keeping with experimental data pointed out by Kaylor [4.1] who has noted that the sharp deep fades occur during shallower fades that can extend over a band approximately 400 MHz wide.

Figure 4.1 was generated using operating frequencies in the 4-GHz band. We have performed similar computations for the 8-GHz band because of the importance of the latter on military links. The results are illustrated in Figure 4.2 for diversity receiver #1 (80 feet above transmitter), and in Figure 4.3 for diversity receiver #2 (55 feet above the transmitter).

An overlay of the two figures results in Figure 4.4 where we show the 20-dB fade only. We see that there is no overlap of the 20-dB fade contours. Although some are close, as with the two pairs near 20 feet, there will not be simultaneous center-of-the-band fading below 20 dB on the two diversity channels. It is interesting to note, however, that the nodes at 22 feet are separated approximately by 15 MHz; for a carrier frequency half way inbetween (≈ 8.415 MHz), one space diversity channel may experience a 20-dB fade at the lower end of the band, and the other a 20-dB fade at the upper end of the band. For the current configuration, the effect on a 14-MHz bandwidth signal could be marginal. At greater bandwidths, it would become important.

The overall impression of examining plots like those presented above is that the likelihood of simultaneous fades on both diversity channels is very small (as it should be).

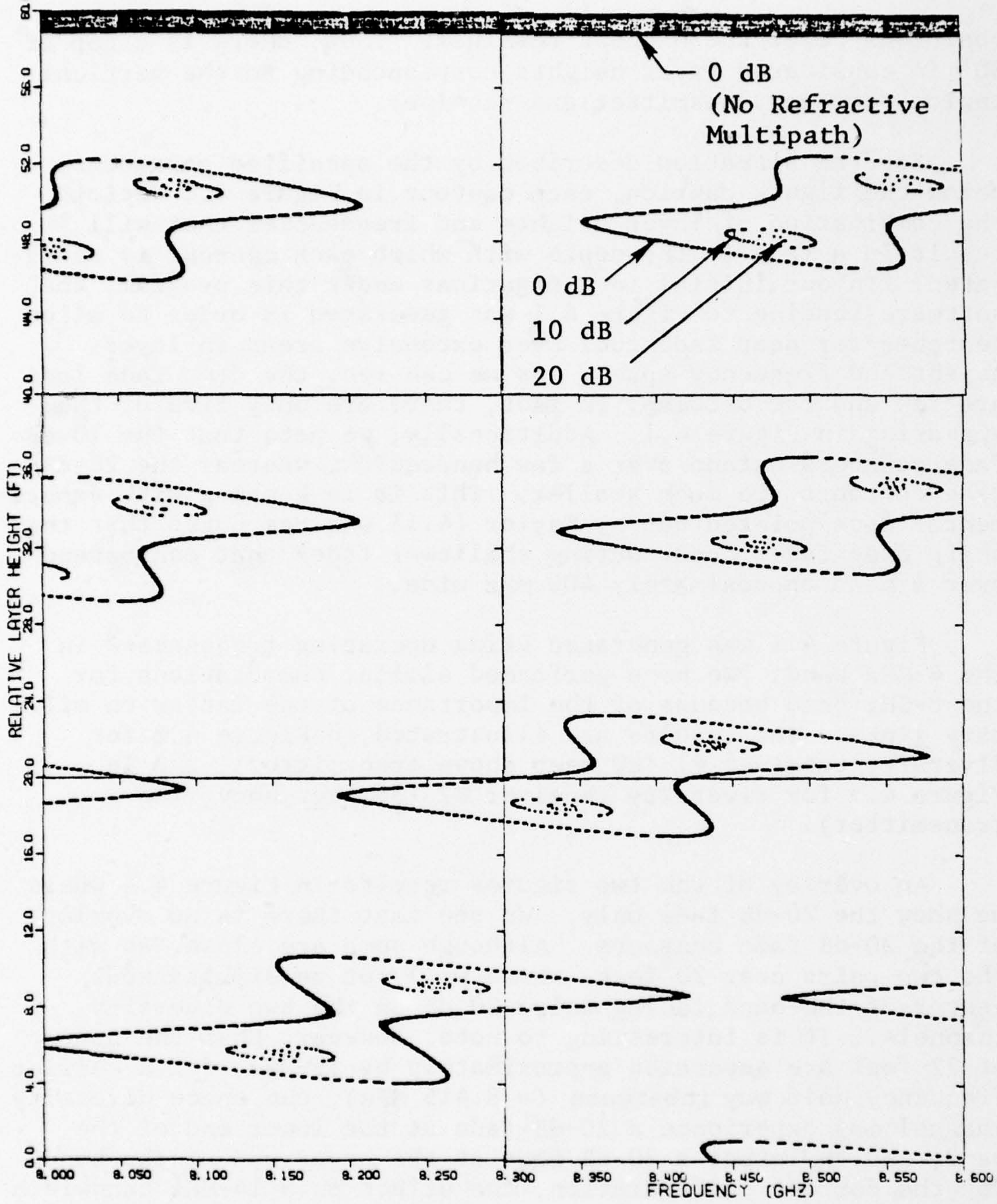

GROUND RANGE = 30 MILES
REFRACTIVE INDEX GRADIENT = -420 Nu/km
LAYER THICKNESS > 62.6 FEET
HEIGHT OF RECEIVER #1 = 80 FEET (ABOVE TRANSMITTER)

Figure 4.2 Deep Fade Loci in 8-GHz Band (Receiver #1)

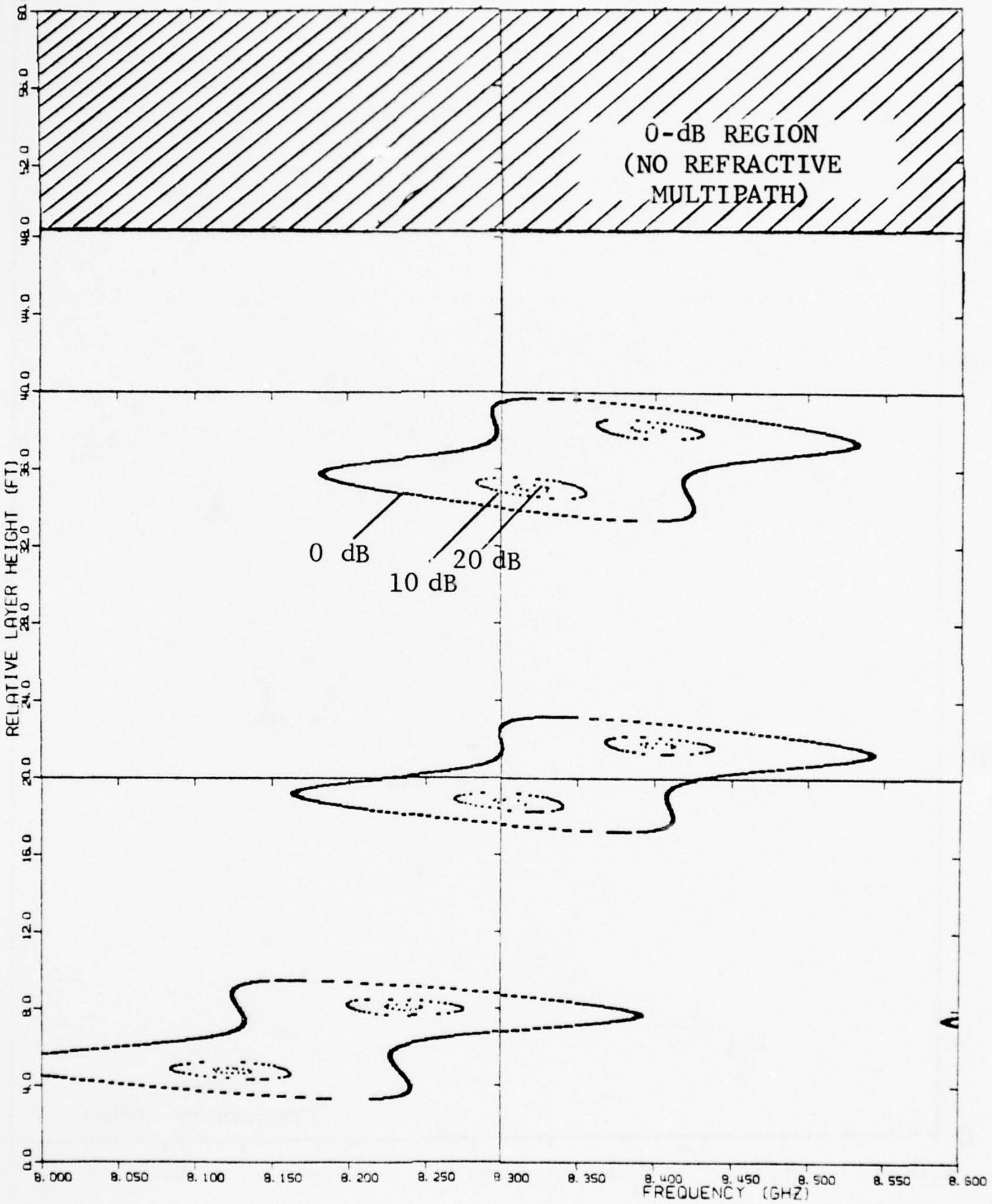

GROUND RANGE = 30 MILES
REFRACTIVE INDEX GRADIENT = -420 Nu/km
LAYER THICKNESS > 62.6 FEET
HEIGHT OF RECEIVER #2 = 55 FEET (ABOVE TRANSMITTER)

Figure 4.3 Deep Fade Loci in 8-GHz Band (Receiver #2)

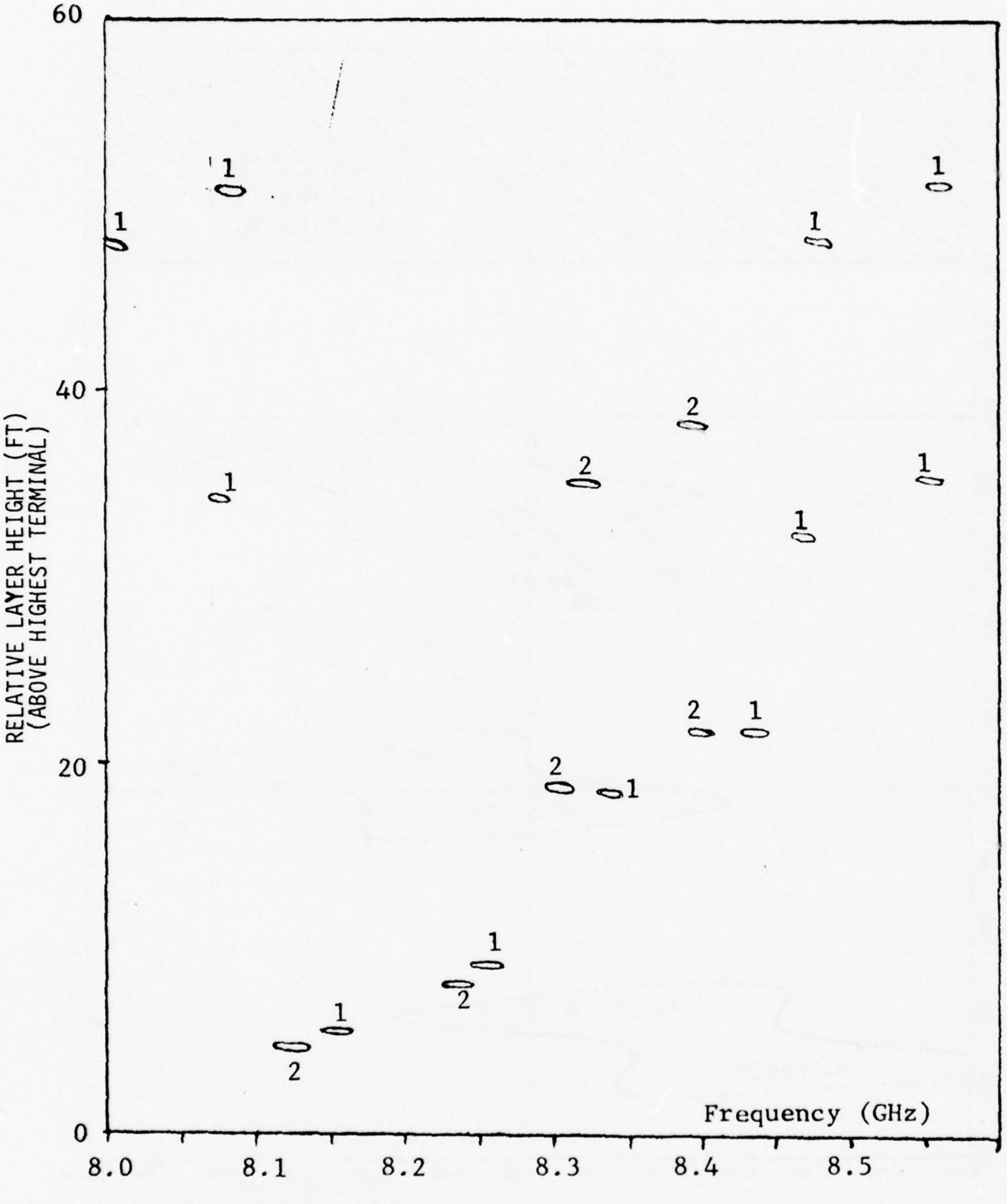

GROUND RANGE = 30 MILES
REFRACTIVE INDEX GRADIENT = -420 Nu/km
LAYER THICKNESS > 62.6 FEET

Figure 4.4 20-dB Fade Contours on Both Diversity Channels (Contours are numbered according to diversity channel) Receiver #1 is 80' above transmitter; Receiver #2 is 55' above transmitter

In the earlier part of this program, we computed plots of fade depth vs. layer height, fade depth vs. frequency, group delay vs. layer height, etc., for the physical situation used to generate Figures 4.1 through 4.4. These were presented in the monthly reports. Because an extremely large number of computational results can be generated for any particular link, we have, in our attempt to limit the number of curves presented here, limited our calculations to the Swingate-Houten link spanning the English Channel and the Hohenstadt-Zugspitze link in Germany. The curves presented below, however, are further reductions in that they represent "cuts" of the contour plots presented above (constant frequency, variable layer height or constant layer height, variable frequency curves). Such curves were presented earlier in Section 2, but are examined here in the context of diversity operation on the links.

One of the reasons for the reduction described above is that generation of the contour plots presented above is a relatively time-consuming and expensive procedure for locating the deep fade loci. The other is that we have been able to devise analytical techniques for reducing the amount of effort in finding the deep fade loci. The main analytical result in this context is that given earlier in (2.156). This result states simply that, given the amplitudes and delays for any probable multipath situation, one can determine the frequencies at which the deep fades occur. Thus, one is able to determine the <u>lines</u> in the two-dimensional layer height-frequency space along which the deep fade loci lie. These lines, as determined from (2.156), are presented as dotted lines in Figure 4.5. They are seen to pass exactly through the deep fade loci.

It is of interest to examine a simplification of (2.156) that is suggested by the approximate linearity of all the multipath delay profiles we have computed under this program; whenever three paths are present, the delay difference $\Delta\tau = \tau_3 - \tau_2$ between the multipath rays follows an approximate linear dependence on layer height. To make use of this, we reproduce (2.156) here for convenience:

$$f = \frac{\pm \cos\left[\dfrac{\alpha_1^2 - \left(\alpha_2^2 + \alpha_3^2\right)}{2\alpha_2\alpha_3}\right]}{2\pi\,\Delta\tau} + \frac{n}{\Delta\tau} \qquad n = 0, \pm 1, \pm 2, \ldots \qquad (4.1)$$

This expression gives, for any layer height, the frequencies at which the deep fade loci appear. We have already seen in

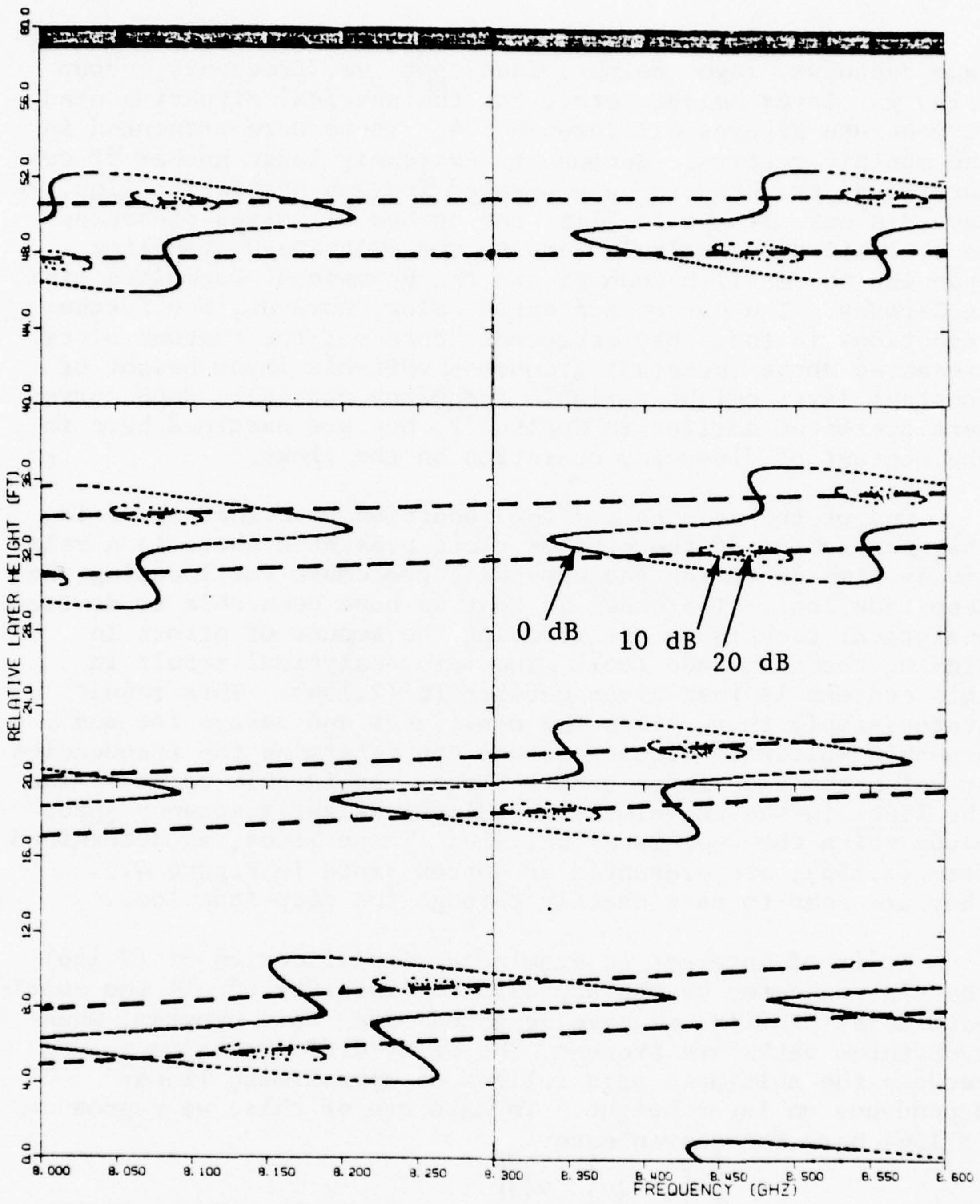

GROUND RANGE = 30 MILES
REFRACTIVE INDEX GRADIENT = -420 Nu/km
LAYER THICKNESS > 62.6 FEET
HEIGHT OF RECEIVER #1 = 80 FEET (ABOVE TRANSMITTER)

Figure 4.5 Frequency Constraints on Deep Fade Loci (The deep fade loci at any layer height must fall on one of the dotted lines.)

the contour plots, e.g., Figure 4.5, that the deep fade loci tend to cluster in groups of two. These clusters correspond to the choice of n in (4.1) above. We now show, using the linearity of the multipath delay profiles, that the frequency separation of the clusters at any layer height can be represented in terms of two parameters $\Delta\tau(0)$, the delay separation at some convenient reference layer height, and h_{max}, the maximum layer height supporting multipath. After examination of the multipath delay profiles (e.g., Figure 2.41), it is a simple matter to determine that

$$\Delta\tau(h_L) = \frac{\Delta\tau(0)}{h_{max}}\left(h_{max} - h_L\right) \qquad 0 \le h_L \le h_{max} \qquad (4.2)$$

Thus, the clusters occur every Δf Hz where

$$\Delta f = \left(\frac{h_{max}}{h_{max} - h_L}\right)\frac{1}{\Delta\tau(0)} \qquad (4.3)$$

For the data used to generated Figure 4.2[*], $\Delta\tau \approx 0.4$ ns and $h_{max} = 59$. So, at $h_L = 50'$ the deep fade loci are 16.4 GHz apart. The smallest value is at $h_L = 0$. There the loci are 2.5 GHz apart.

For this example, the implication is clear; a plot of fade level vs. frequency (constant layer height) will show deep fades only once in extremely wide bands.

It is of more interest to examine the frequency width of the fade contours in the context of our above discussion. Consider a physical situation wherein the maximum layer height supporting multipath is given by h_1 and the reference height delay difference is $\Delta\tau_1(0)$; compare this with another physical condition of the link that is characterized by corresponding values h_2 and $\Delta\tau_2(0)$. If we make the reasonable (but rough) assumption that the fade contour widths in frequency are in the same proportion as the frequency separation between the deep fade loci, we have

---

[*] Recall that the zero reference is at the receiver height.

$$\frac{w_2(h_L)}{w_1(h_L)} = \frac{h_2}{h_1}\left(\frac{h_1 - h_L}{h_2 - h_L}\right)\frac{\Delta\tau_1(0)}{\Delta\tau_2(0)} \tag{4.4}$$

where w_1 and w_2 are the contour widths. Thus, of course, is a measure of the relative frequency selectivity in each of the fading conditions. Note that if we constrain ourselves to the region $h_{L_1} = h_{L_2} = h_L \gtrsim 0$ where, as pointed out above, the frequency selectivity is greatest, we have simply

$$\frac{w_2(0)}{w_1(0)} = \frac{\Delta\tau_1(0)}{\Delta\tau_2(0)} \tag{4.5}$$

Thus, we see that there is an important dependence between the frequency selectivity of fades and the delay width and layer height extent of the multipath delay profiles. Examination of the great variety of multipath delay profiles presented in Section 2 indicates that there can be a wide variety of frequency-selective fading on LOS links.

Before proceeding with presentation of our calculated curves for two special links of interest, we point out two observations about the contour plots above that, though simple, deserve comment.

First, the frequency separations between the deep fade loci in the plots does not depend on the band examined, i.e., the deep fade loci occur with the same frequency spacing in the 4-GHz band as they do in the 8-GHz band.

Secondly, the relative occurrence vs. layer height of the deep fades does depend on the frequency band. Comparing Figure 4.1 and Figure 4.2, we see that the vertical separation of the deep fade loci in Figure 4.1 (4-GHz band) is approximately twice what it is in Figure 4.2 (8-GHz band). This dependence can be demonstrated in a more general sense by appealing to the approximate linearity of the multipath delay profiles that were previously used to generate (4.2). Substituting (4.2) in (2.155), we obtain an expression analogous to (2.156) that yields the layer height separation of the deep fade loci. Their location within the layer height band allowing multipath is governed by

$$\frac{h_{max} - h_L}{h_{max}} = \frac{\pm \cos^{-1}\left[\dfrac{\alpha_1^2 - \left(\alpha_2^2 + \alpha_3^2\right)}{2\alpha_2\alpha_3}\right]}{2\pi f \tau(0)} + \frac{n}{f \Delta\tau(0)} \qquad (4.6)$$

wherein we see that the layer height separation of the deep fade loci is inversely proportional to f. Thus, spatial selectivity becomes more important at the higher frequencies.

We now present the results of computations that we have done for two links of interest: the Swingate-Houtem link over the English Channel, and the Hohenstadt-Zugspitze link in Germany. We start with the Swingate-Houtem link. This link, as depicted in Figure 4.6, consists of several possible diversity channels. Because of time limitations, we have only done calculations for the two emphasized in Figure 2.35. These consist of one transmitter and two diversity receivers separated by 30 feet. The first is located 47 feet above the transmitter, the second, 17 feet above the transmitter. In Figure 4.6 we illustrate diversity operation on this link when the lapse rate is 300 Nu/km and the carrier frequency is 4.4465 GHz. This carrier, one of the operating carriers on the link, was not chosen with any particular interest in getting deep fades. It is clear from the figure that the choice of diversity separation has resulted in anti-positioning of the deep fades, i.e., one can very roughly say that the deeper fades on one channel are positioned against high signal levels on the other. The multipath delay profile corresponding to this physical situation was illustrated earlier in Figure 2.37. Comparing the two, it can be seen that the cutoff points correspond and that signal enhancement occurs at the points where the ray paths merge.

Similar dependencies are evident when a different carrier frequency is chosen, as shown in Figure 4.7 for a carrier frequency of 4.808 GHz. This plot shows a fade to less than -20 dB at 65.9 feet (as a computer printout of the numerical values shows).

In order to get some insight into frequency diversity operation, we have plotted the frequency dependence of fade depth and group delay for the layer height of 65.9 feet that gives the deep fade mentioned above. The plots, provided in

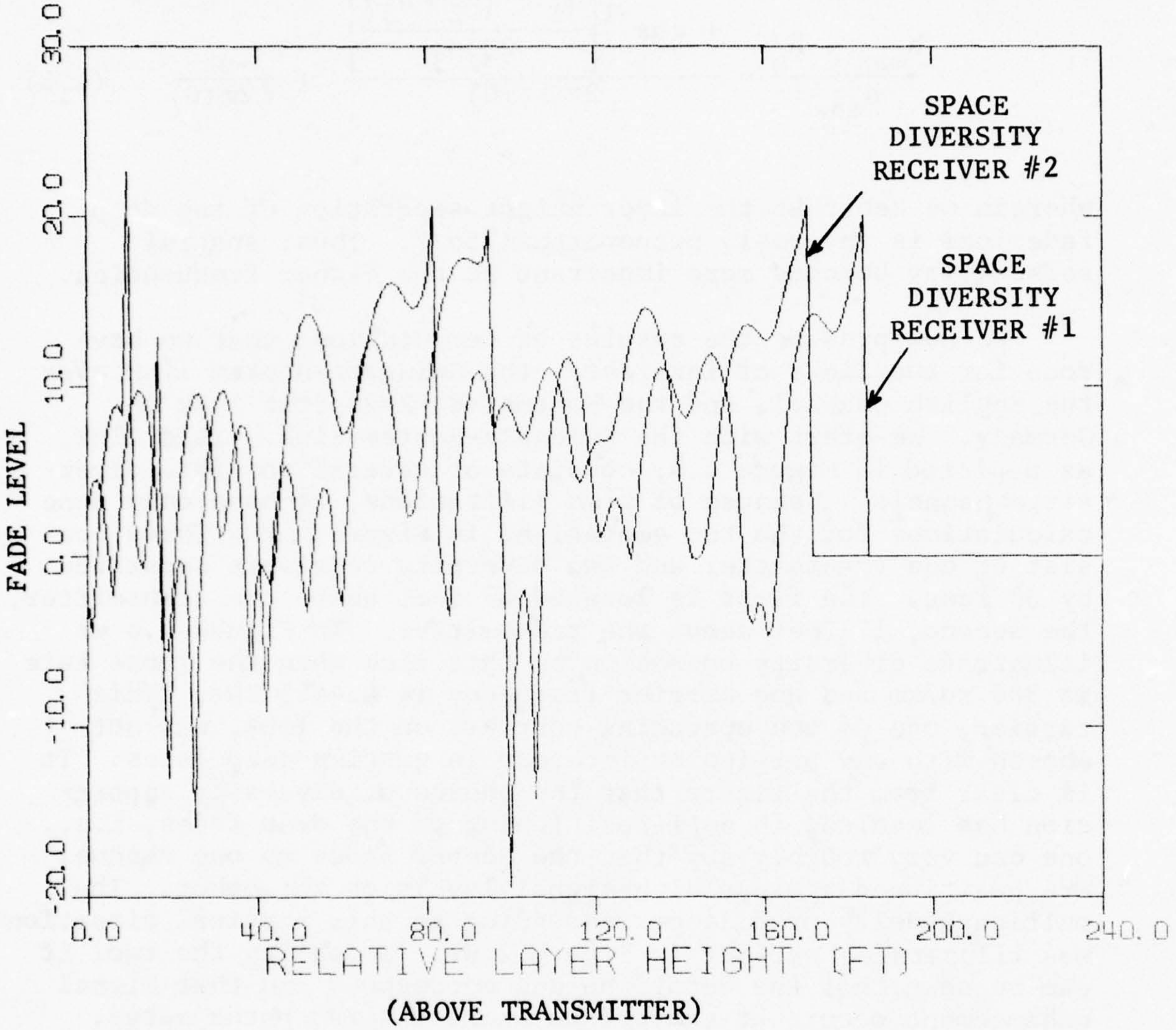

LAPSE RATE = 300 Nu/km

CARRIER FREQUENCY = 4.4465 GHz

Figure 4.6 Diversity Fade Levels vs. Layer Height on Swingate-Houtem Link (horizontal layer)

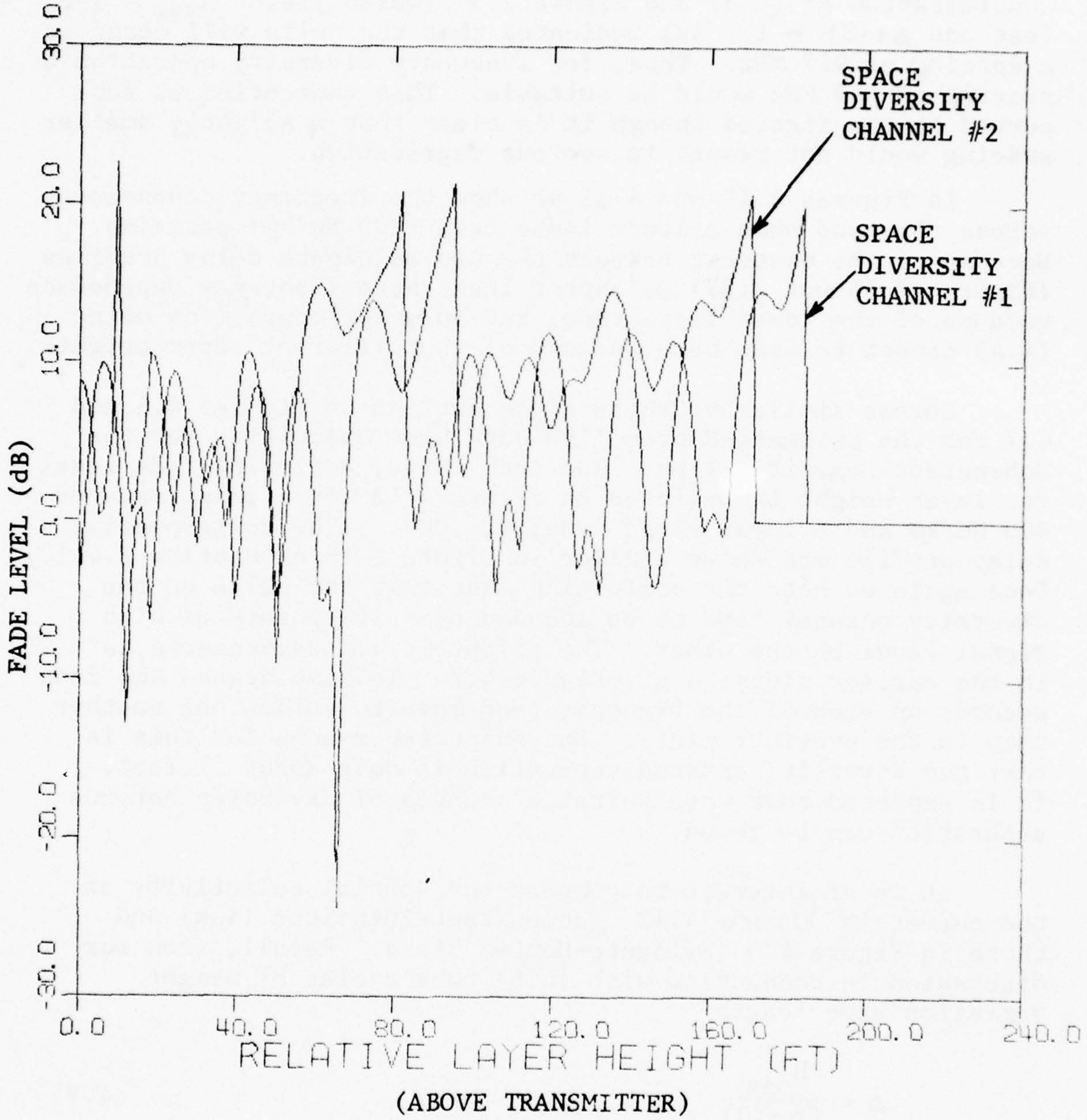

LAPSE RATE = 300 Nu/km
CARRIER FREQUENCY = 4.808 GHz

Figure 4.7 Diversity Fade Levels Vs. Layer Height on Swingate-Houtem Link

Figures 4.8 and 4.9 cover the whole band of operating frequencies. Consideration of (4.3) and Figure 2.37, (which yields $h_{max} = 180$ feet and $\Delta\tau(0) \approx 1.7$ ns) indicates that the nulls will occur at a spacing of 927 MHz. Thus, for frequency diversity operation a spacing of 460 MHz would be suitable. This contention is supported by the figures though it is clear that a slightly smaller spacing would not result in serious degradation.

In Figures 4.10 and 4.11 we show the frequency dependence across the band when a lower lapse rate (200 Nu/km) pertains. Because of the contrast between the two multipath delay profiles (Figures 2.36 and 2.37) we expect less sharp frequency dependence because of the lower lapse rate, but an exact comparison using (4.4) cannot be made here because of the different layer heights.

Curves similar to those given earlier in Figures 4.6 and 4.7 for the Swingate-Houtem link have been calculated for the Hohenstadt-Zugspitze link. One such curve, depicting fade level vs. layer height is depicted in Figure 4.12 for a lapse rate of 400 Nu/km and a layer slope equal to .009. (The corresponding delay profile was shown earlier in Figure 2.18 of Section 2.4.1.) Once again we note the comforting fact that the nulls on one diversity channel tend to be located opposite points of high signal level on the other. The effect is not as dramatic as in the earlier plots, e.g., Figure 4.7. To some degree the fade records on each of the branches tend more to follow one another than in the previous plots. The suspected reason for this is that the diversity antenna separation is only about 17 feet. It is expected that more suitable choices of diversity antenna separation can be found.

It is of interest to compare the spatial selectivity of the curves in Figure 4.12 (Hohenstadt-Zugspitze link) and those in Figure 4.6 (Swingate-Houtem link). Recall, from our discussion in connection with (4.6) that cycles of height variation have length

$$\Delta = \frac{h_{max}}{f\Delta\tau(0)} \tag{4.7}$$

In this expression the frequencies have already been specified. The quantities h_{max} and $\Delta\tau(0)$ can be determined from the respective multipath profiles; these are Figure 2.18 for the Hohenstadt-Zugspitze link, and Figure 2.37 for the Swingate-Houtem link. When this is done we find

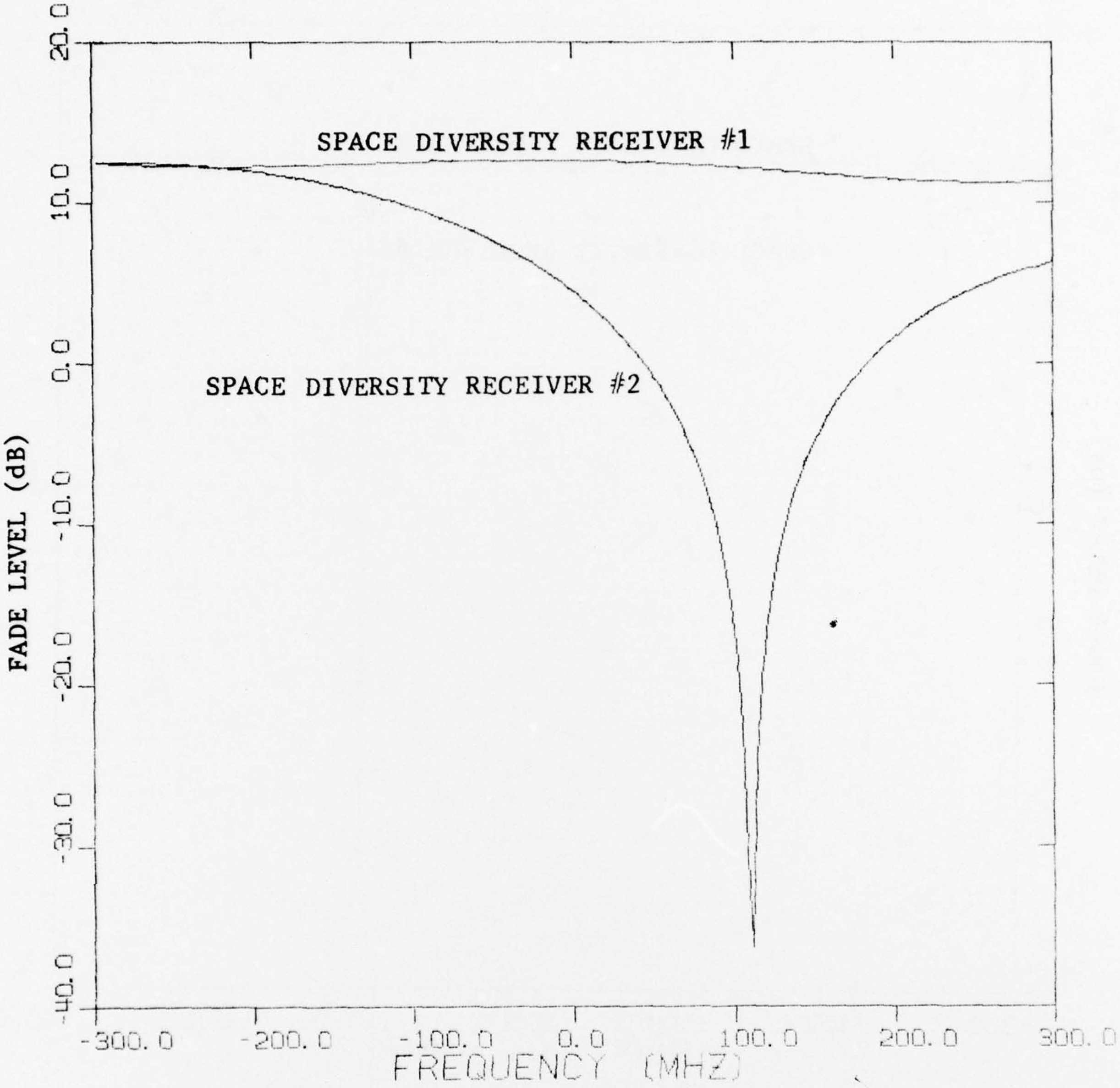

LAPSE RATE = 300 Nu/km
CENTER FREQUENCY = 4.7 GHz
LAYER HEIGHT = 65.9 FEET

Figure 4.8 Fade Level Vs. Frequency Over Total Band for Horizontal Layer on Swingate-Houtem Link

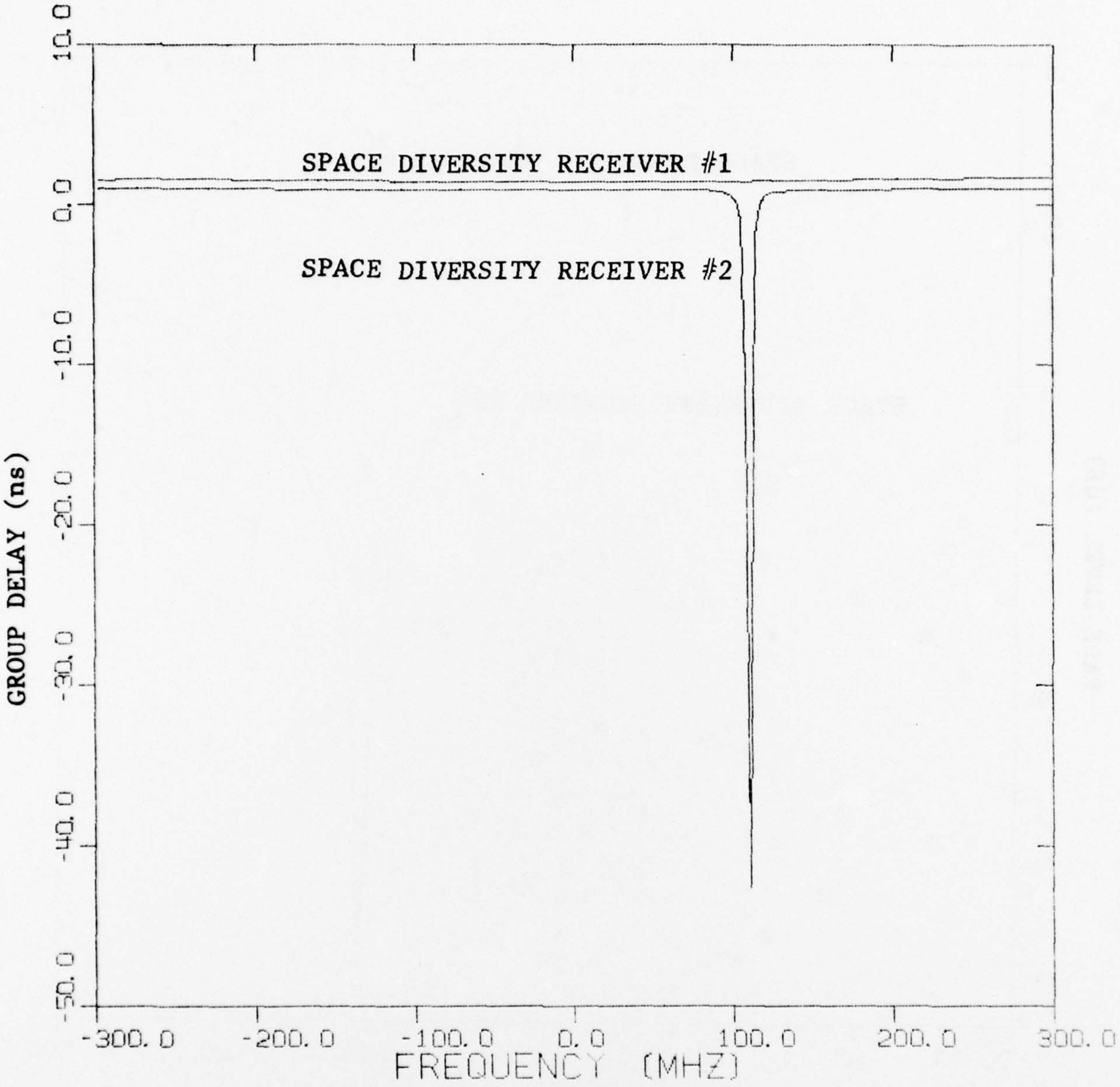

LAPSE RATE = 300 Nu/km
CENTER FREQUENCY = 4.7 GHz
LAYER HEIGHT = 65.9 FEET

Figure 4.9 Group Delay Vs. Frequency Over Total Band for Horizontal Layer on Swingate-Houtem Link

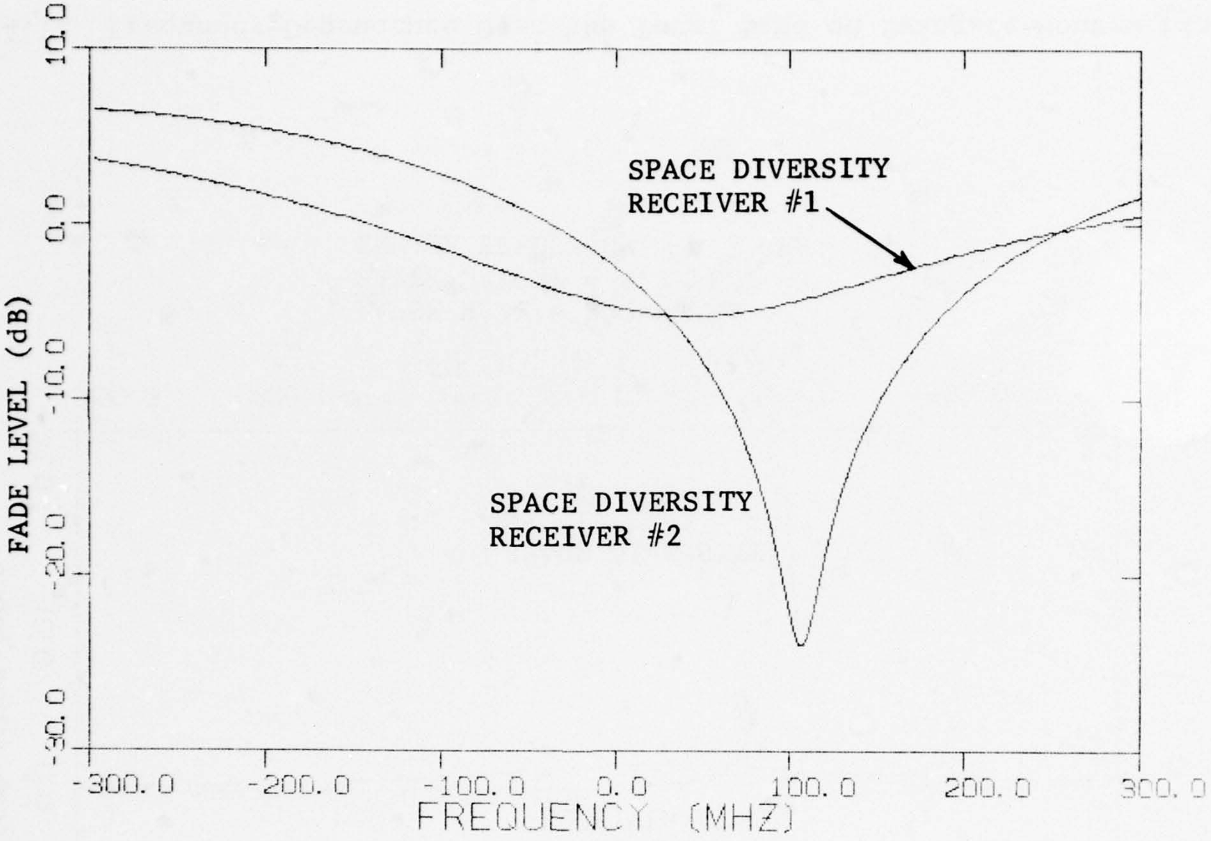

LAPSE RATE = 200 Nu/km
LAYER HEIGHT = 5.2 FEET
CENTER FREQUENCY = 4.7 GHz

Figure 4.10 Frequency-Dependence Over the Total Band on Swingate-Houtem Link

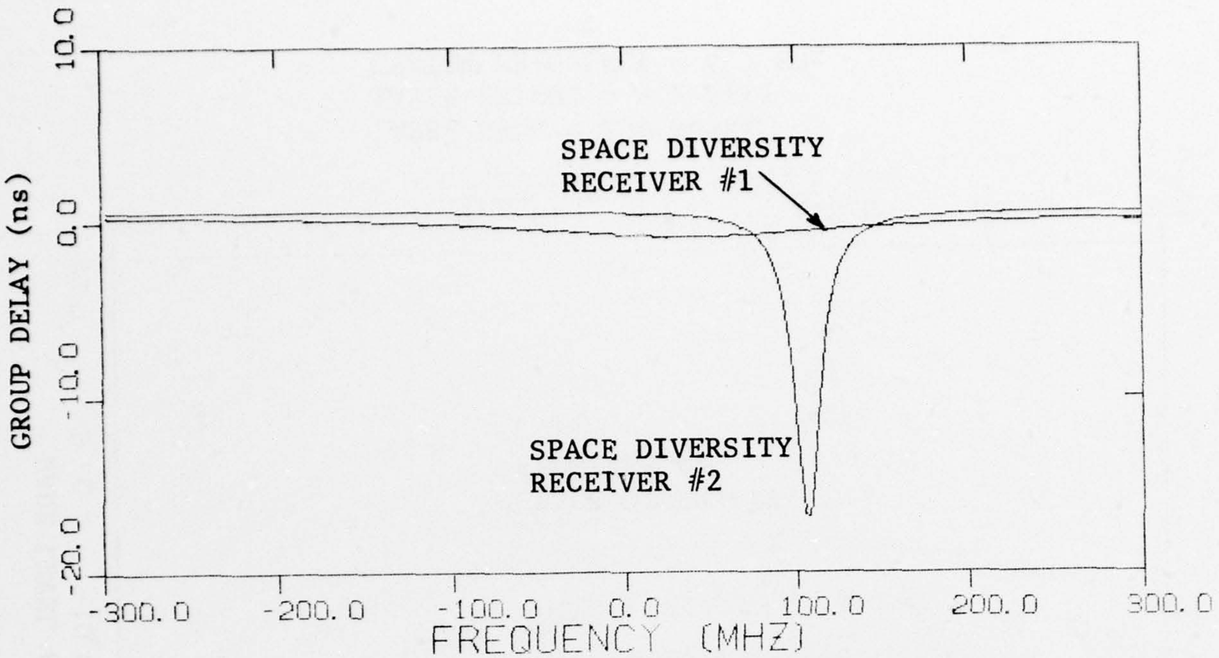

LAPSE RATE = 200 Nu/km
LAYER HEIGHT = 5.2 FEET
CENTER FREQUENCY = 4.7 GHz

Figure 4.11 Frequency-Dependence Over the Total Band on Swingate-Houtem Link

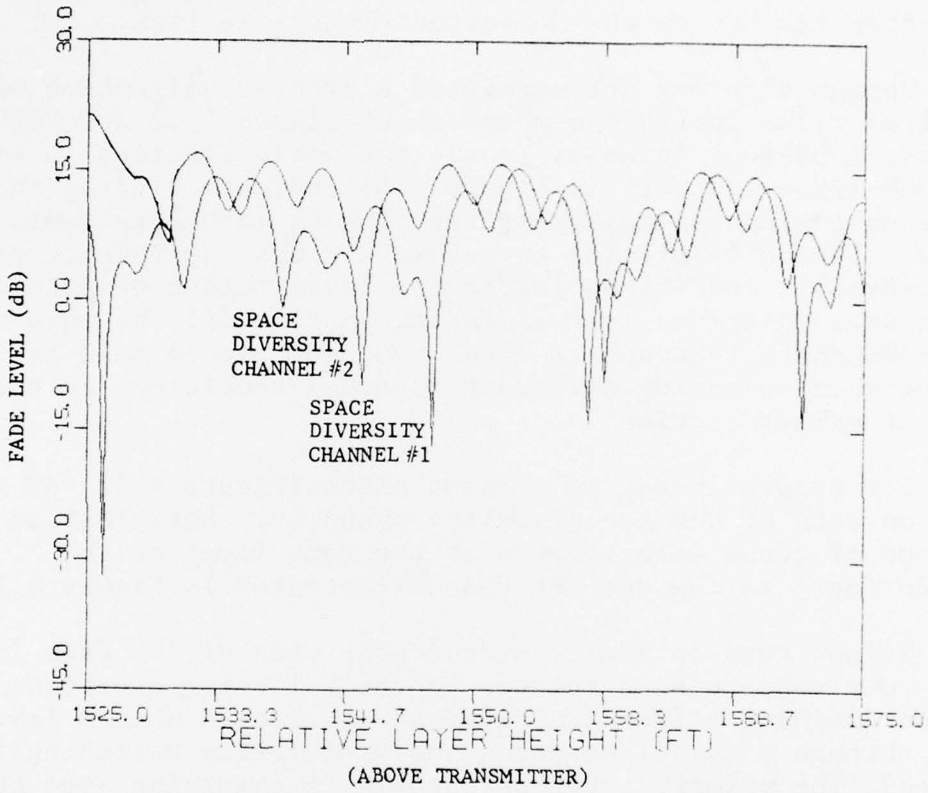

LAPSE RATE = 400 Nu/km
LAYER SLOPE = .009
CARRIER FREQUENCY = 8.591 GHz

Figure 4.12 Diversity Fade Levels Vs. Layer Height on Hohenstadt-Zugspitze Link

$$\frac{\Delta_{SH}}{\Delta_{ZH}} = 4.1 \qquad (4.8)$$

i.e., the spatial variation on the Hohenstadt-Zugspitze link is approximately four times as rapid as it is on the Swingate-Houten link. This is due primarily to the increased value of the factor $f\Delta\tau(0)$ on the Hohenstadt-Zugspitze link.

Though time has not permitted a precise validation of the numerical value in (4.8) comparison of Figure 4.12 and Figure 4.6 over a 50-foot interval (e.g., the whole abscissa in Figure 4.12 and 120 - 170 feet in Figure 4.6) indicate clearly that fading on the Hohenstadt-Zugspitze link is much more rapid spatially. If one is willing to assume a rough equivalence of the thermo-dynamic conditions leading to layer motion on each link, the natural inference is that fading <u>in time</u> will be more rapid on the Hohenstadt-Zugspitze link. No equivalence need be assumed when comparing different physical conditions on the <u>same</u> link; it exists a-priori.

For completeness, we present plots (Figure 4.13) of group delay on each of the two diversity channels. Note that an extremum of group delay occurs at the same layer height (≈ 1526 feet) as the deepest fade illustrated in Figure 4.12.

We now turn to a more microscopic view of the deep fade loci. Our concern here relates to the following question; what are the dominant effects on diversity operation when a layer moves through a deep fade locus and a diversity switching rule is used? The primary interest here is in examining some physical mechanisms that may result in loss of bit count integrity.

We consider three simple diversity rules:

1. Switch to other channel if current channel fades to depth greater than 30 dB and other channel is stronger.
2. Switch to other channel if current channel fades to depth greater than 20 dB and other channel is stronger.
3. Switch to other channel if stronger than current channel.

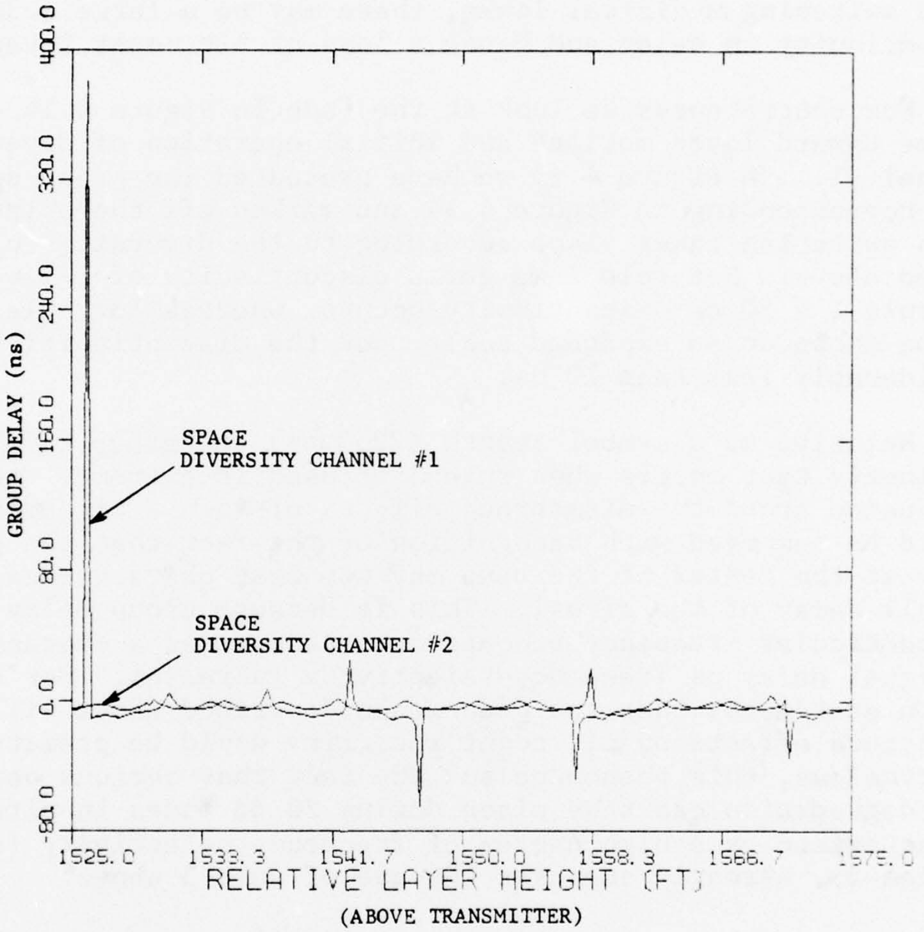

Lapse Rate = 400 Nu/km
Layer Slope = .009
Carrier Frequency = 8.591 GHz

Figure 4.13 Diversity Group Delays Vs. Layer Height on Hohenstadt-Zugspitze Link

Recall from our discussion of Section 2.3.3 that the largest excursions of group delay tend to occur during the deepest fades. This implies that diversity switching from a diversity channel with a deep fade on it to another channel with little or no fade is equivalent to switching from a channel with a large group delay to a channel with very small group delay. Because of the rapid switching on digital links, there may be a large sudden discontinuity in delay and hence a loss of bit count integrity.

For concreteness we look at the fade in Figure 4.14 and assume upward layer motion* and initial operation of diversity channel #1. In Figure 4.15 we have presented the group delay plot corresponding to Figure 4.14 and marked off the points at which switching takes place according to the diversity rules listed above. For rule 1 we get a discontinuity of 177 ns. For rule 2 a 50 ns discontinuity occurs, whereas for rule 3 it can be shown on an expanded scale that the discontinuities are considerably less than 10 ns.

Relative to a symbol length (72.3 ns) the group Delay discontinutiy that occurs when rule 3 is used is extreme. Any conclusion about the disastrous effects of such a circumstance should be tempered with recognition of the fact that the group delay at the center of the band may not best characterize the overall delay of the signal. This is because group delay at any one particular frequency becomes more tenuous as a characterizer of signal delay as frequency-selectivity increases. For this reason statements that the phenomenon described above will have disastrous effects on bit count integrity would be premature. Nevertheless, this phenomena and the fact that serious performance degradation can take place during 20 dB fades in situations characterized by a high degree of frequency selectivity (see Section 3), strongly suggests the use of rule 3 above.

---

*Note that regularity of layer motion need not be assumed over a large range. In fact, to think of the abscissa in Figure 4.14 as a time axis, we need only visualize layer motion as being regular over a very small range, e.g., .3 feet.

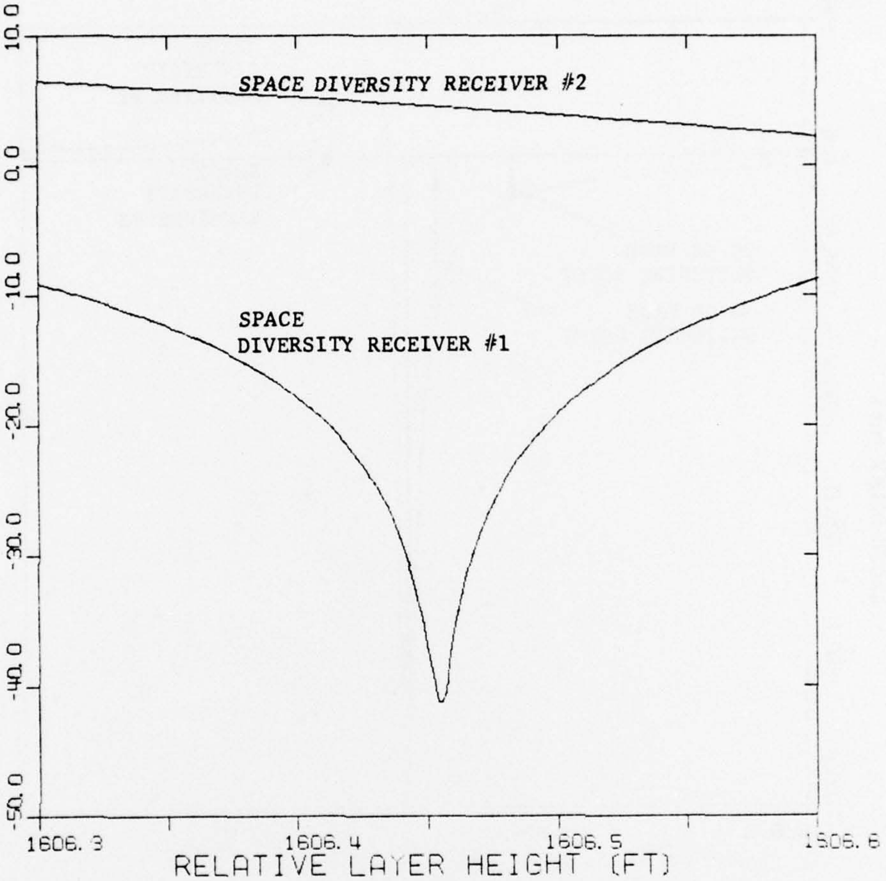

(ABOVE TRANSMITTER)

LAPSE RATE = 400 Nu/km
LAYER SLOPE = .009
CARRIER FREQUENCY = 8.301 GHz

Figure 4.14 **Fade Depth Vs. Layer Height on Hohenstadt-Zugspitze Link**

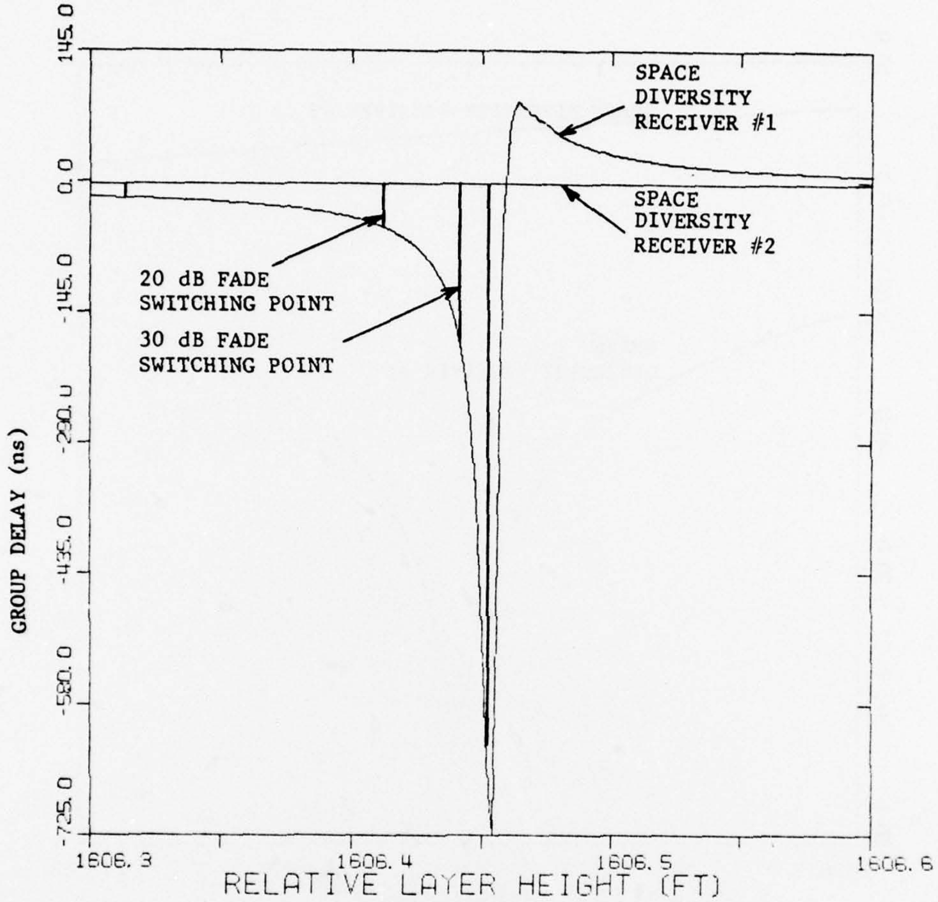

(ABOVE TRANSMITTER)

LAPSE RATE = 400 Nu/km
LAYER SLOPE = .009
CARRIER FREQUENCY = 8.301 GHz

Figure 4.15 Group Delay Vs. Layer Height On Hohenstadt-Zugspitze Link

4.2 Tracking Performance of Modems

The modem performance calculations presented in Section 3 required exact evaluation of modem tracking behavior under a variety of multipath conditions. In general, these results show that modem timing closely follows the group delay of the channel at the carrier frequency except under conditions of extreme degradation. This is particularly true of the baseband modem. For this modem no significant deviation between center-of-band group delay and modem tracking was found for any of the channels which did not cause complete degradation. For channels with an irreducible error rate, large tracking deviations (as much as a few tenths of a bit) were calculated. This is not surprising since irreducible error rates arise from eye closure, and eye closure for some data sequences will shift the position of the mean zero crossing which is used by the tracking loop.

IF modem tracking also follows the center-of-band group delay, although small deviations occur. Figure 4.16 shows both group delay and modem tracking as the angle of T_0 is varied over 360^o. (A discussion of the significance of this procedure may be found in Section 3.2.1.) These results are for the channel conditions of curve #1 of Fig. 3.16, although similar results were seen for all of the channels analyzed.

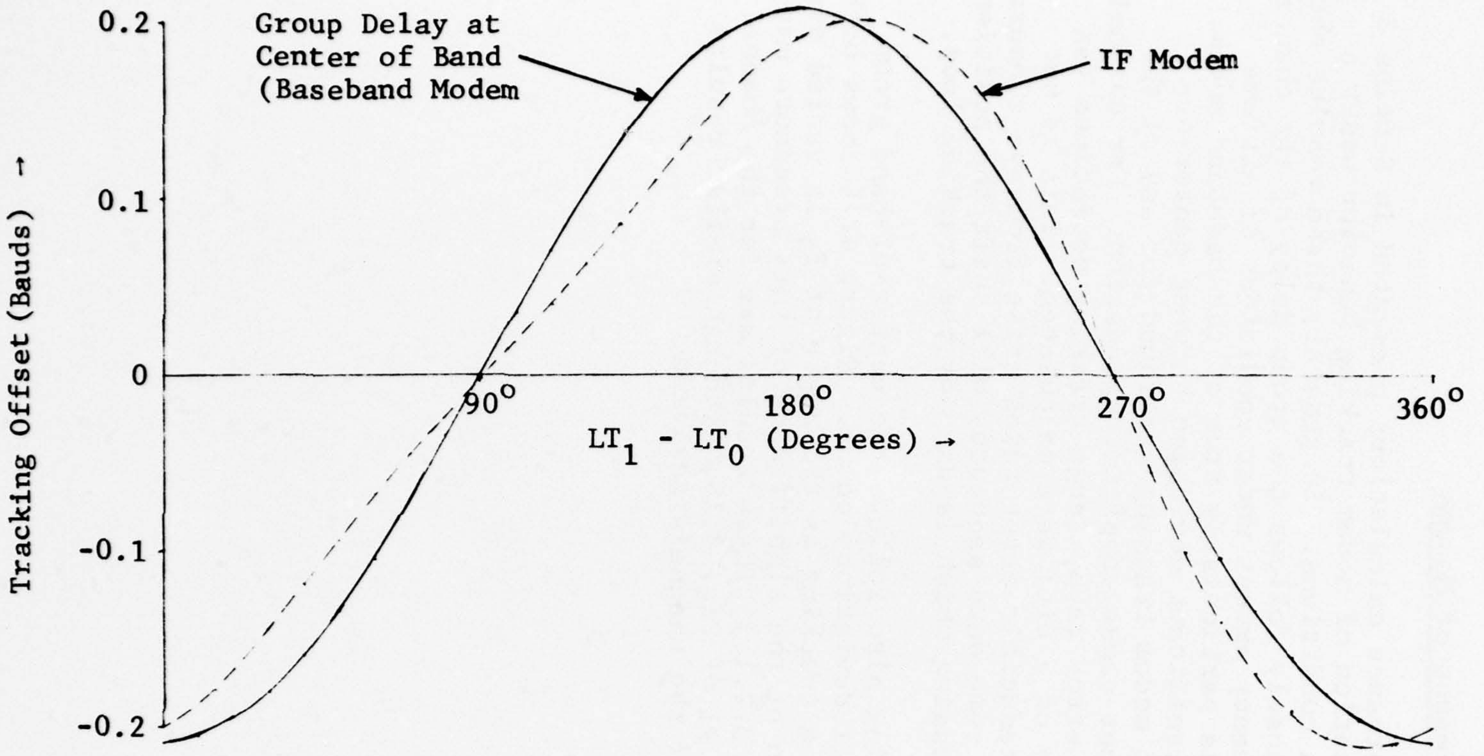

Refractive Index Gradient = -400 Nu/km
Layer Tilt Slope = 0.007
Fade Depth = 30 dB
Layer Height = 2270 Feet

Figure 4.16 Modem Tracking Behavior on Hohenstadt-Zugspitze Link

SECTION 4

REFERENCE

[4.1] R. L. Kaylor, "A Statistical Study of Selective Fading of Super-High Frequency Radio Signals," The Bell System Technical Journal, September 1953.

MISSION
of
Rome Air Development Center

RADC plans and conducts research, exploratory and advanced development programs in command, control, and communications (C^3) activities, and in the C^3 areas of information sciences and intelligence. The principal technical mission areas are communications, electromagnetic guidance and control, surveillance of ground and aerospace objects, intelligence data collection and handling, information system technology, ionospheric propagation, solid state sciences, microwave physics and electronic reliability, maintainability and compatibility.

AMERICAN REVOLUTION BICENTENNIAL
1776-1976

AD-A048 175 CNR INC NEEDHAM MA F/G 17/2.1
MULTIPATH OVER LOS CHANNELS STUDY.(U)
NOV 77 P A BELLO, L PICKERING, C BOARDMAN F30602-76-C-0419
UNCLASSIFIED RADC-TR-77-355 NL

2 OF 3
ADA
048175

The group delay has the classical definition

$$\tau_g(f,t) = \frac{-\theta'(f,t)}{2\pi} \tag{2.97}$$

where the prime denotes differentiation with respect to f. It will be helpful for us to consider the above expression in some alternate forms. Some elementary manipulation of (2.94) gives

$$\tau_g(f,t) = -\frac{1}{2\pi} \operatorname{Im}\left\{\frac{T'(f,t)}{T(f,t)}\right\} \tag{2.98}$$

which, by writing T(f,t) in terms of its real and imaginary parts,

$$T(f,t) = X(f,t) + j\,Y(f,t) \tag{2.99}$$

yields

$$\tau_g(f,t) = \frac{X'(f,t)Y(f,t) - X(f,t)Y'(f,t)}{2\pi L^2(f,t)} \tag{2.100}$$

The above expressions constitute the definitions and formalism that shall be used in much of the remainder of this report. Some specialization of these results is in order, however. This is because of the fact that refractive multipath links are known to support a finite number of discrete paths, as discussed in Section 2.1. This allows us to use the special form

$$T(f,t) = \sum_{i=1}^{N} \alpha_i(t)\, e^{-j2\pi f\tau_i(t)} \tag{2.101}$$

where there are N paths, $\alpha_i(t)$ being the time-varying amplitude of the i^{th} path and $\tau_i(t)$ being its delay. As in much of our following work, we shall keep in mind that we are dealing with a channel snapshot and no longer carry along an explicit dependence on t in our notation. Thus, we have

$$T(f) = \sum_{i=1}^{N} \alpha_i e^{-j2\pi f\tau_i} \tag{2.102}$$

The expression in (2.102) is worth considering in some slightly altered forms. We shall have occasion to refer back to these in later sections of this report.

One form derives from considering the frequency relative to the carrier frequency, i.e., by considering dependence on a relative frequency

$$f' = f - f_c \tag{2.103}$$

This has the effect of replacing the real amplitude in (2.102) with a complex amplitude. Substituting (2.103) in (2.102) we get

$$T(f') = \sum_{i=1}^{N} \beta_i e^{-j2\pi f'\tau_i} \tag{2.104}$$

where

$$\beta_i = \alpha_i e^{-j2\pi f_c\tau_i} \tag{2.105}$$

It will also be of interest to consider the effects of adding a fixed delay offset to each of the ray path delays. Replacing τ with $\tau+\tau_0$, we get

$$T(f') = e^{-j2\pi f_c\tau_0} \sum_{i=1}^{N} \left(\alpha_i e^{-j2\pi f_c\tau_i}\right) e^{-j2\pi f'(\tau_0+\tau_i)} \tag{2.106}$$

In our use of these expressions later on, we will not carry along the prime on f; the meaning will be clear from the context.

Expressions for fade level and group delay in terms of the ray path delays and amplitudes can be easily derived using (2.102). From (2.102) and (2.95) we get

$$L^2 = \sum_{i=1}^{N} \sum_{j=1}^{N} \alpha_i \alpha_j \cos 2\pi f(\tau_i - \tau_j) \tag{2.107}$$

for the fade level. To determine an expression for group delay, we use (2.102) and (2.98) and obtain

$$\tau_g = \mathrm{Im}\left\{ \frac{\sum_{i=1}^{N} j\,\alpha_i \tau_i\, e^{-j2\pi f\tau_i}}{\sum_{i=1}^{N} \alpha_i\, e^{-j2\pi f\tau_i}} \right\} \tag{2.108}$$

which, after some manipulating, gives

$$\tau_g = \frac{1}{L^2} \sum_{i=1}^{N} \sum_{j=1}^{N} \alpha_i \alpha_j \tau_i \cos 2\pi f(\tau_i - \tau_j) \tag{2.109}$$

This completes our summary of the analytical results for fade level and group delay.

Some insight into the behavior of the parameters discussed in this section can be gleaned by considering the illustration of phasor geometry in Figure 2.12. The figure represents a graphical depiction of the way in which the contributing terms in (2.104) link together to form the resultant phasor (bold-face arrow). The magnitude of this phasor is the fade level, and it is seen in the figure to vary substantially across the 2Δ band, decreasing at $f_c - \Delta$ to half the value it had at $f_c + \Delta$. In conjunction with this variation, the resultant traces a phasor trajectory in the xy plane and, in so doing, rotates. It is the variation of the central angle θ with respect to frequency that results in the occurrence of group delay, as is clear from (2.97).

It is interesting to note that insights into the statistical behavior of fading can be garnered from Figure 2.12. Consider a situation wherein the x and y components of the resultant phasor in Figure 2.12 are random variables with a

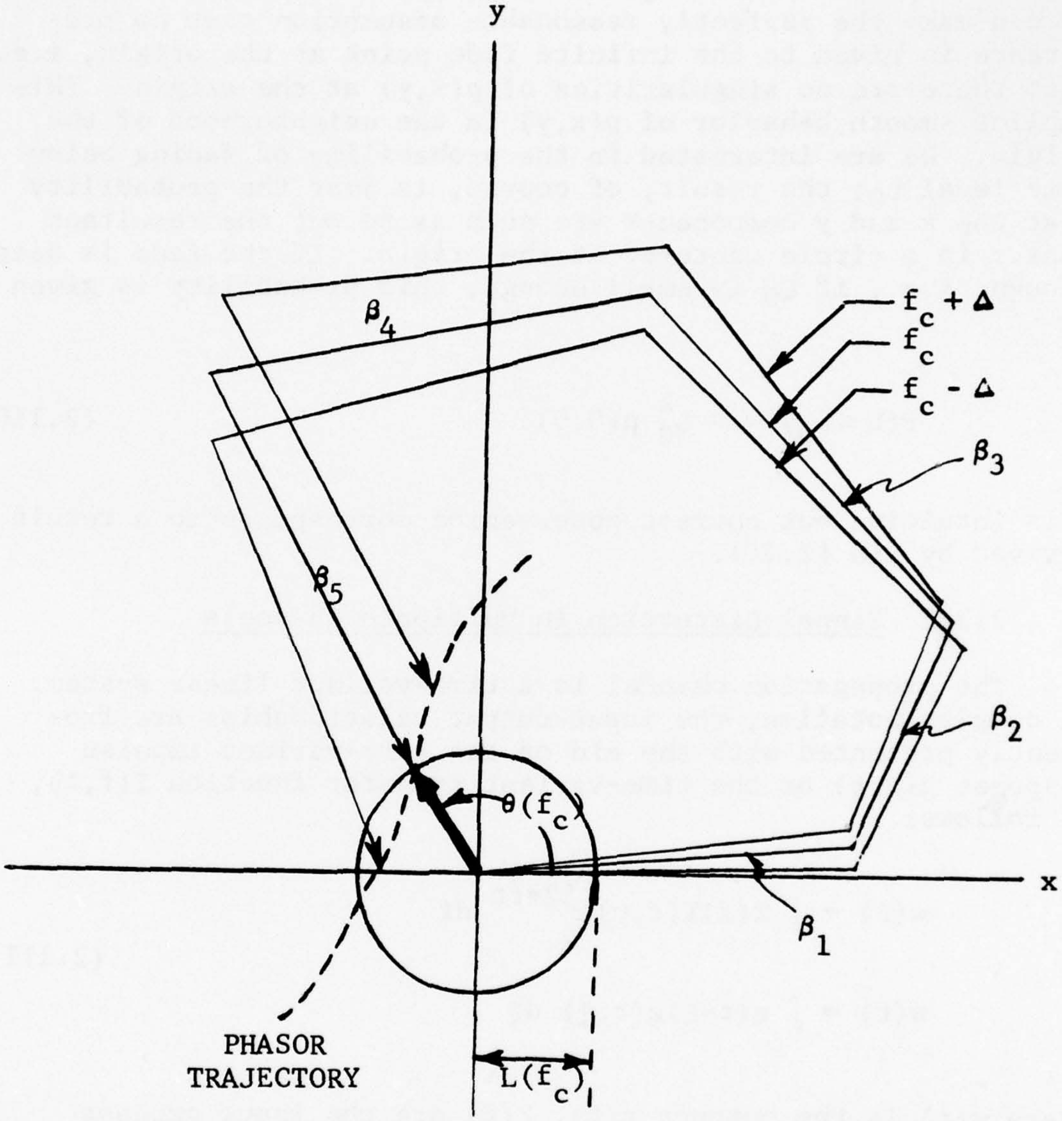

Figure 2.12 Phasor Components of Channel Transfer Function

probability distribution given by $p(x,y)$. About this situation we can make the perfectly reasonable assumption that no preference is given to the infinite fade point at the origin, i.e., that there are no singularities of $p(x,y)$ at the origin. This implies smooth behavior of $p(x,y)$ in the neighborhood of the origin. We are interested in the probability of fading below some level L_0; the result, of course, is just the probability that the x and y components are such as to put the resultant phasor in a circle centered at the origin. If the fade is deep enough, i.e., if L_0 is small enough, this probability is given by

$$P(L \leq L_0) \approx \pi L_0^2 \, p(0,0) \tag{2.110}$$

This intuitive but correct observation corresponds to a result derived by Lin [2.20].

2.3.2 Signal Distortion in Multipath Channels

The propagation channel is a time-variant linear system. In complex notation, the input-output relationships are frequently presented with the aid of the time-variant impulse response $g(t,\xi)$ or the time-variant transfer function $T(f,t)$, as follows:

$$\begin{aligned} w(t) &= \int Z(f)T(f,t)e^{j2\pi ft}\, df \\ w(t) &= \int z(t-\xi)g(t,\xi)\, d\xi \end{aligned} \tag{2.111}$$

where $w(t)$ is the output; $z(t)$, $Z(f)$ are the input process and its spectrum; and $T(f,t)$, $g(t,\xi)$ are related by Fourier transformation

$$\begin{aligned} T(f,t) &= \int g(t,\xi)e^{-j2\pi f\xi}\, d\xi \\ g(t,\xi) &= \int T(f,t)e^{j2\pi ft}\, df \end{aligned} \tag{2.112}$$

In calculating modem performance we are generally interested in situations where the degree of frequency selectivity displayed by the channel over the bandwidth of the data signal is moderate. This is particularly true for the two high packing density modems to be considered later, since high packing density is achieved at the expense of sensitivity to noise and intersymbol interference. Consequently, a few, or frequently only the first three terms in a power series expansion of the transfer function suffice to characterize the frequency selectivity. The utility of such a power series to model a time-variant dispersive channel by a chain of differentiations has been studied by Bello [2.19]. Formally,

$$T(f,t) = \sum_{n=0}^{\infty} T_n(t)(2\pi jf)^n \tag{2.113}$$

which represents the channel by a sum of the outputs of successively higher orders of (bandpass) differentiators, with the nth-order differentiator being multiplied by the complex function

$$T_n(t) = \begin{cases} \dfrac{1}{n!(2\pi j)^n}\left[\dfrac{\partial^n T(f,t)}{\partial f^n}\right]_{f=0} \\ \\ \dfrac{1}{n!}\int (-\xi)^n g(t,\xi)\, d\xi \end{cases} \tag{2.114}$$

Bello [2.21] has shown that the power series representation (2.113) will be most rapidly convergent when the expansion is taken for a channel in which a "mean" path delay has been removed. Assuming this mean path delay is ξ_0, the input-output representation corresponding to (2.113) (including the mean path delay) is given by

$$w(t) = \sum_{n=0}^{\infty} T_n(t) \frac{d^n z(t - \xi_0)}{dt^n} \qquad (2.115)$$

This parametric model is shown in Fig. 2.13. (This chain-differentiator model is called the f-power series model in [2.21].

When the frequency-selective fading in the channel is sufficiently small, only the first term in the series (2.115) will be sufficient to characterize the channel output, i.e.,

$$w(t) = T_0(t)z(t - \xi_0) \qquad (2.116)$$

where z(t), w(t), are the complex envelopes of the channel input and output, respectively. Equation (2.116) may be recognized as a "flat fading" or nonfrequency-selective channel model. If the first two terms are used,

$$w(t) = T_0(t)z(t - \xi_0) + T_1(t)\dot{z}(t - \xi_0) \qquad (2.117)$$

which is called a "linearly frequency-selective fading" channel [2.22] since it corresponds to approximating T(f,t) by a complex linear term in the frequency variable. One may continue and define a "quadratically frequency-selective fading" channel:

$$w(t) = T_0(t)z(t - \xi_0) + T_1(t)\dot{z}(t - \xi_0) + T_2\ddot{z}(t - \xi_0) \qquad (2.118)$$

This is the representation which will be used for performance modeling.

Given any channel impulse response structure one may compute the parameters $\{T_n(t)\}$ of the chain differentiator model. We are particularly concerned with an N-path channel for which the time-varying channel transfer function is given by

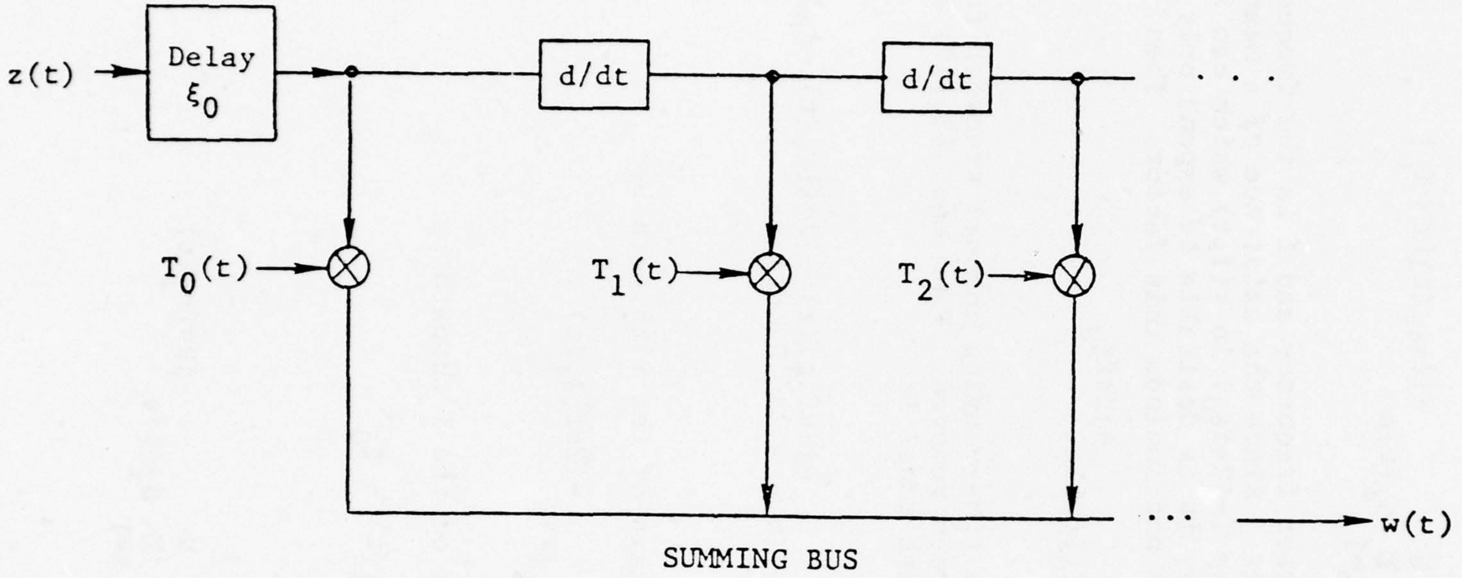

Figure 2.13 Chain-Differentiator Model of Propagation Channel

$$T(f,t) = \sum_{i=1}^{N} \alpha_i(t) e^{-j2\pi\xi_i(t)[f+f_c]} \tag{2.119}$$

where f_c is the carrier frequency and f is the frequency deviation from the carrier. Since the existence of a mean delay ξ_0 produces a factor exp $(-j2\pi f\xi_0)$ in T(f,t) which can fluctuate with f quite rapidly, it is desirable to expand only the portion of T(f,t) which does not include this factor. Then

$$T(f,t) = T_0(f,t) e^{-j2\pi f\xi_0} \tag{2.120}$$

where $T_0(f,t)$ is the time-varying channel transfer function after the mean delay has been removed. From Eqs. (2.119) and (2.120) $T_0(f,t)$ for the N-path model is

$$T_0(f,t) = \sum_{i=1}^{N} \alpha_i(t) e^{-j2\pi f_c\xi_i(t) - j2\pi f[\xi_i(t) - \xi_0]} \tag{2.121}$$

Defining a complex gain of the i'th path by

$$\beta_i(t) = \alpha_i(t) e^{-j2\pi f_c \xi_i(t)} \tag{2.122}$$

and a relative delay of the i'th path by

$$\eta_i(t) = \xi_i(t) - \xi_0 \tag{2.123}$$

then

$$T_0(f,t) = \sum_{i=1}^{N} \beta_i(t) e^{-j2\pi f\eta_i(t)} \tag{2.124}$$

It can be easily shown from Eq. (2.121) that the parameters of the model are given by

$$T_n(t) = \frac{(-1)^n}{n!} \sum_{i=1}^{N} \beta_i(t)[\eta_i(t)]^n \tag{2.125}$$

We have shown above how distortion of the complex envelope z(t) is related to the coefficients of the chain differentiator model $\{T_n(t)\}$ and how these coefficients may be calculated for an N-path channel. We now find expressions for the corresponding distortion of the modulating waveform when z(t) is either phase of frequency modulated. In either case we may write

$$z(t) = e^{j\varphi(t)} \tag{2.126}$$

In the case of phase modulation, the modulating waveform is given directly by $\varphi(t)$; in the case of frequency modulation it is given by

$$x(t) = \frac{1}{2\pi} \dot{\varphi}(t) \tag{2.127}$$

Using (2.127) and the quadratic channel model [Eq. (2.118)] we find that the complex envelope of the channel output is given by

$$w(t) = e^{j\varphi(t - \xi_0)} \Big\{ T_0(t) + jT_1(t)\dot{\varphi}(t - \xi_0) + T_2(t)\left[j\ddot{\varphi}(t - \xi_0) - \dot{\varphi}^2(t - \xi_0)\right] \Big\} \tag{2.128}$$

For the LOS channel of interest, time variations of the channel are much slower than time variations of $\varphi(t)$ and its derivatives. Thus, one may regard the channel as fixed when finding the discriminator output. Writing w(t) in the form

$$w(t) = A(t)T_0(t)e^{j[\varphi(t - \xi_0) + B(t)]} \tag{2.129}$$

the desired results for output angle and frequency are

$$\theta(t) = \varphi(t - \xi_0) + B(t) \tag{2.130}$$

and

$$y(t) = \frac{1}{2\pi}\dot{\theta}(t) = x(t - \xi_0) + \frac{1}{2\pi}\dot{B}(t) \tag{2.131}$$

By a simple calculation it may be shown that for small distortion B(t) is given by

$$B(t) = p_1\dot{\varphi}(t - \xi_0) + p_2\ddot{\varphi}(t - \xi_0) + \frac{1}{2}p_3\dot{\varphi}^2(t - \xi_0) \tag{2.132}$$

where the p parameters are defined by

$$\begin{aligned} p_1 &= \mathrm{Re}\left\{\frac{T_1(t)}{T_0(t)}\right\} \\ p_2 &= \mathrm{Re}\left\{\frac{T_2(t)}{T_0(t)}\right\} \\ p_3 &= 2\left[\mathrm{Re}\left\{\frac{T_1(t)}{T_0(t)}\right\}\mathrm{Im}\left\{\frac{T_1(t)}{T_0(t)}\right\} - \mathrm{Im}\left\{\frac{T_2(t)}{T_0(t)}\right\}\right] \end{aligned} \tag{2.133}$$

In this result derivatives (and their products) of order higher than 2 have been discarded, maintaining accuracy consistent with the quadratic channel model. Substituting (2.133) into (2.130) gives the phase modulation model directly:

$$\theta(t) = \varphi(t - \xi_0) + p_1\dot{\varphi}(t - \xi_0) + p_2\ddot{\varphi}(t - \xi_0) + \frac{1}{2}p_3\dot{\varphi}^2(t - \xi_0) \tag{2.134}$$

and substituting into (2.131) with the help of (2.132) gives the frequency modulation model

$$y(t) = x(t - \xi_0) + p_1\dot{x}(t - \xi_0) + p_2\ddot{x}(t - \xi_0) + p_3x(t - \xi_0)\dot{x}(t - \xi_0) \tag{2.135}$$

These models will be the basis for the modem performance analyses presented in Section 3.

2.3.3 Fade Depth and Group Delay Extrema

In this section we explore and answer some important questions relating to the frequency dependence of fade depth and group delay. Two questions are of utmost importance:

(1) Given a fixed set of channel parameters, at what frequencies do the deep fades occur?

(2) What is the joint behavior of fade level and group delay? Do large excursions of group delay usually occur during deep fades?

The first question is of importance because of the fact that the nonfading situations are of little interest to us. Because of the improbability of deep fades, it is helpful to have analytical results that can aid one in locating the deep fade loci. These are presented in this section.

The importance of the second question relates to loss of bit count integrity during diversity switching. Since many diversity schemes involve switching during deep fades, a large group delay excursion, occurring simultaneously with the deep fade, could result in a large rapid discontinuity occurring when the system is switched to the other channel. In this section we develop a bound on the group delay which indicates that the largest group delay excursion will <u>only</u> occur during deep fades. The importance of this phenomenon will be discussed later in Section 4.1.

Some interesting insights into the problem at hand are gained by considering the geometrical picture in Figure 2.14. Here the transfer function at $f - f_1$ is depicted as the sum of its component phasors, $\alpha_1 \exp(-j2\pi f_1\tau_1)$, $\alpha_2 \exp(-j2\pi f_2\tau_2)$, etc.

Clearly, as the frequency changes, the resultant phasor T(f) traces out a trajectory in the XY plane. This trajectory is illustrated by the dotted line in Figure 2.14. It is of use to define a "velocity" vector that describes the "motion" of the resultant phasor along the trajectory. We use these words in quotation marks (to be discarded in future discussion) because we are not dealing with true velocity and motion in the sense of kinematics. Dependence here is on frequency rather than time; nevertheless, the concept of velocity developed here is a useful one. In terms of the transfer function which we here separate into its component parts and write as a vector,

$$\vec{T}(f) = X\,\hat{x} + Y\,\hat{y} \tag{2.136}$$

where $\hat{x}$ and $\hat{y}$ are the unit vectors in the X and Y directions as illustrated in the figure, the velocity vector is defined simply as

$$\begin{aligned} \vec{v} &\equiv v_x\,\hat{x} + v_y\,\hat{y} \\ v_x &\equiv X'(f) \qquad v_y \equiv Y'(f) \end{aligned} \tag{2.137}$$

where the primes denote differentiation with respect to f.

It is also of interest to refer to the absolute speed along the trajectory. This is simply

$$v = \left(v_x^2 + v_y^2\right)^{\frac{1}{2}} \tag{2.138}$$

The velocity vector at $f = f_2$ is illustrated in Figure 2.14. The angle θ appearing in the figure is the same as that referred to in Eq. (2.94).

A simple examination of the geometry in Figure 2.14 and comparison with (2.97) reveals that the absolute value of the group delay at any frequency is inversely proportional to $2\pi L$

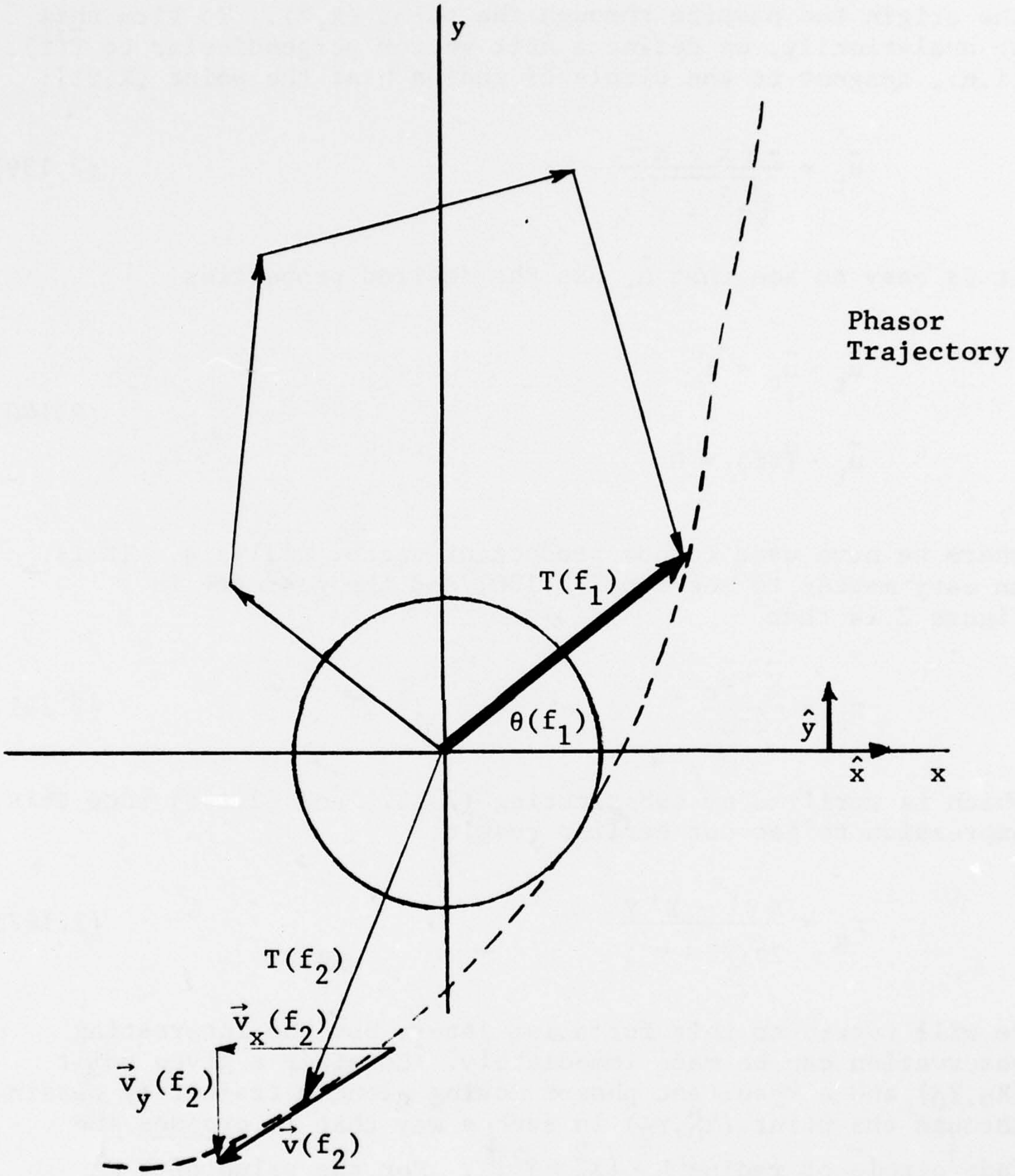

Figure 2.14 Phasor Geometry

and directly proportional to the absolute value of that component of the velocity vector tangent to a circle centered at the origin and passing through the point (X,Y). To firm this up analytically, we define a unit vector perpendicular to $\vec{T}(f)$, [i.e., tangent to the circle of radius L at the point (X,Y)]:

$$\hat{u}_t = \frac{-Y\hat{x} + X\hat{y}}{\sqrt{X^2 + Y^2}} \tag{2.139}$$

It is easy to see that $\hat{u}_t$ has the desired properties

$$\begin{aligned} \hat{u}_t \cdot \hat{u}_t &= 1 \\ \hat{u}_t \cdot \vec{T}(f) &= 0 \end{aligned} \tag{2.140}$$

where we have used to dot product of vector analysis. It is an easy matter to see from (2.100) and the geometry in Figure 2.14 that

$$\tau_g = \frac{\vec{v} \cdot \hat{u}_t}{2\pi L} \tag{2.141}$$

which is verified by substituting (2.137) and (2.138) into this expression to get our earlier result

$$\tau_g = \frac{XY' - X'Y}{2\pi(X^2 + Y^2)} \tag{2.142}$$

We will return to this formalism later, but one interesting observation can be made immediately. Consider a given point (X_0,Y_0) and a resultant phasor moving along a trajectory passing through the point (X_0,Y_0) in such a way that it crosses the fade circle of radius $L = \left(X_0^2 + Y_0^2\right)^{\frac{1}{2}}$. For the value of f at which the trajectory crosses the fade circle, the magnitude of the group delay is always less than the value it would have if the resultant phasor were moving (at the same speed) along a trajectory tangent to the fade circle. This is a simple consequence of the inequality

$$|\vec{v} \cdot \hat{u}_t| \leq v \tag{2.143}$$

and we shall make use of it later.

We now address question (1) mentioned at the beginning of this section, and determine those frequencies at which the deepest fades occur. From (2.102) it is easy to see that two necessary conditions for the occurrence of fades as deep as, or deeper than, that corresponding to some magnitude squared value L^2 are:

$$\sum_{i=1}^{N} \alpha_i \cos 2\pi f\tau_i \leq L \tag{2.144}$$

and

$$\sum_{i=1}^{N} \alpha_i \sin 2\pi f\tau_i \leq L \tag{2.145}$$

Thus, assigning a small value to L places a constraint on the values of f (for a given set of α_i and τ_i) allowing deep fades.

It is of interest to examine the constraints on f when $L = 0$. This is done by solving the system of equations

$$\sum_{i=1}^{N} \alpha_i \cos 2\pi f\tau_i = 0 \tag{2.146}$$

$$\sum_{i=1}^{N} \alpha_i \sin 2\pi f\tau_i = 0 \tag{2.147}$$

This, of course, is the constraint condition resulting from directly setting T(f) in (2.102) equal to 0. Generally, it is difficult to solve. For the case $N = 3$, some specific conclusions can be made.

Since this problem is by no means one of the major goals of this program, we concentrate then on a three path model. To find the infinite fade points, we set

$$\sum_{i=1}^{3} \alpha_i e^{-j2\pi f\tau_i} = 0 \qquad (2.148)$$

Manipulation of this expression is facilitated if we factor out the first term. Since α_1 is never 0, the constraint (2.148) becomes

$$1 + \alpha_2' e^{-j2\pi f\tau_2'} + \alpha_3' e^{-j2\pi f\tau_3'} = 0 \qquad (2.149)$$

where, for $j = 2,3$

$$\alpha_j' = \alpha_j/\alpha_1 \qquad (2.150)$$

and

$$\tau_j' = \tau_j - \tau_1 \qquad (2.151)$$

Separating the real and imaginary parts of (2.149), we obtain

$$1 + \alpha_2' \cos 2\pi f\tau_2' + \alpha_3' \cos 2\pi f\tau_3' = 0 \qquad (2.152)$$

and

$$\alpha_2' \sin 2\pi f\tau_2' + \alpha_3' \sin 2\pi f\tau_3' = 0 \qquad (2.153)$$

Squaring and adding both of these equations, we obtain

$$\cos 2\pi f(\tau_2' - \tau_3') = \frac{1 - \left(\alpha_2'^2 + \alpha_3'^2\right)}{2\,\alpha_2'\,\alpha_3'} \qquad (2.154)$$

or

$$\cos 2\pi f(\tau_2 - \tau_3) = \frac{\alpha_1^2 - \left(\alpha_2^2 + \alpha_3^2\right)}{2\,\alpha_2\,\alpha_3} \tag{2.155}$$

From (2.155) we have

$$f = \frac{\pm \cos^{-1}\left[\dfrac{\alpha_1^2 - \left(\alpha_2^2 + \alpha_3^2\right)}{2\,\alpha_2\,\alpha_3}\right]}{2\pi(\tau_3 - \tau_2)} + \frac{n}{(\tau_3 - \tau_2)} \tag{2.156}$$

where

$$n = 0, \pm 1, \pm 2, \ldots \tag{2.157}$$

Thus, it is clear for the model under consideration that two deep fades may occur every $(\tau_3 - \tau_2)^{-1}$ Hz in frequency, e.g., for a delay difference on the order of one nanosecond there can at most be two nulls across a 1-GHz band. We point out, however, that a simple examination of (2.155) and/or the phasor geometry indicates that the constraint on f can never be satisfied unless the conditions

$$\alpha_2 + \alpha_3 \geq \alpha_1 \tag{2.158}$$

and

$$|\alpha_2 - \alpha_3| \leq \alpha_1 \tag{2.159}$$

are met.

It should be pointed out that the use of (2.156) to locate a deep fade does not guarantee that a deep fade will actually occur at that frequency; it only means that deep fades, should they occur, will occur at the given frequencies.

We now turn from a determination of the deep fade loci to an examination of the joint behavior of the fade level and group delay. This is in response to question (2) at the beginning of this section; our analytical goal is to determine bounds on the group delay.

From (2.98) we see that

$$|\tau_g|^2 = \frac{1}{4\pi^2 L^4} \, |\mathrm{Im}[T'(f)T^*(f)|^2 \qquad (2.160)$$

Using (2.99), we obtain

$$|T'(f)T^*(f)|^2 = L^2\left[(x')^2 + (y')^2\right] \qquad (2.161)$$

With the definitions for v_x and v_y given in (2.137) and the additional definition

$$v = \sqrt{v_x^2 + v_y^2} \qquad (2.162)$$

which can be thought of as the "speed" of the resultant along the phase trajectory in Figure 2.14, we obtain the simple inequality

$$|\tau_g|^2 \leq \frac{v^2}{4\pi^2 L^2} \qquad (2.163)$$

Evaluation of v_x and v_y according to (2.137) gives

$$v_x = -\,2\pi \sum_{i=1}^{N} \alpha_i \, \tau_i \sin 2\pi f \tau_i \qquad (2.164)$$

$$v_y = -\,2\pi \sum_{i=1}^{N} \alpha_i \, \tau_i \cos 2\pi f \tau_i \qquad (2.165)$$

Application of Lagrange's identity

$$\left(\sum_{j=1}^{n} a_j b_j\right)^2 = \left(\sum_{j=1}^{n} a_j^2\right)\left(\sum_{k=1}^{n} b_k^2\right) - \frac{1}{2}\sum_{j=1}^{n}\sum_{k=1}^{n}\left(a_j b_k - a_k b_j\right)^2 \tag{2.166}$$

gives

$$v_x^2 = (2\pi)^2\left(\sum_{j=1}^{N} \alpha_j^2\right)\left(\sum_{j=1}^{N} \tau_j^2 \sin^2 2\pi f\tau_j\right)$$

$$- 2\pi^2 \sum_{j=1}^{N}\sum_{k=1}^{N}\left(\alpha_j\tau_k \sin 2\pi f\tau_k - \alpha_k\tau_j \sin 2\pi f\tau_j\right)^2 \tag{2.167}$$

with a similar expression for v_y^2. Adding the two expressions gives

$$v^2 = (2\pi)^2\left(\sum_{j=1}^{N} \alpha_j^2\right)\left(\sum_{j=1}^{N} \tau_j^2\right) - \frac{1}{2}Q \tag{2.168}$$

where

$$Q = (2\pi)^2 \sum_{j=1}^{N}\sum_{k=1}^{N}\Big[\left(\alpha_j\tau_k \sin 2\pi f\tau_k - \alpha_k\tau_j \sin 2\pi f\tau_j\right)^2$$

$$+ \left(\alpha_j\tau_k \cos 2\pi f\tau_k - \alpha_k\tau_j \cos 2\pi f\tau_j\right)^2\Big] \tag{2.169}$$

By doing the indicated squaring in (2.169), comining terms, and substituting back into (2.168), it is a simple matter to see that

$$v^2 = (2\pi)^2 \sum_{i=1}^{N}\sum_{j=1}^{N} \alpha_i\alpha_j\,\tau_i\tau_j \cos\left[2\pi f(\tau_i - \tau_j)\right]$$

$$\le (2\pi)^2\left(\sum \alpha_i\,|\tau_i|\right)^2 \tag{2.170}$$

Thus, from (2.163) the group delay is bounded according to the following inequality:

$$\tau_g \le \frac{\sum_{i=1}^{N} \alpha_i |\tau_i|}{L} \tag{2.171}$$

We have derived inequalities by other means than that used here (e.g., by applying the Schwarz inequality to each of the terms in $v^2 = v_x^2 + v_y^2$) but in all cases these inequalities have been found to be weaker than (2.171).

Examination of the steps leading to (2.171) indicate that the bound, if it is to be achieved, can only be achieved at the fade depth minimum.

As a numerical example we have taken some computed values of amplitudes and delays (typical for the shorter links). These are:

$$\begin{array}{lll} \alpha_1 = 1 & \alpha_2 = 1.184 & \alpha_3 = 1.196 \\ \tau_1 = 0 & \tau_2 = 1.266 & \tau_3 = 1.740 \end{array} \tag{2.172}$$

Across a 30-MHz band centered on a carrier frequency of 4.9888 GHz, the selected set of amplitudes and delays above gives rise to a minimum fade level given by

$$D = -43.457 \text{ dB} \tag{2.173}$$

Using

$$\left|\tau_g\right|_{\max} = 10^{\frac{D}{20}} \left(\sum_{i=1}^{3} \alpha_i |\tau_i| \right)^{\frac{1}{2}} \tag{2.174}$$

we get

$$\left|\tau_g\right|_{\max} = 281.7 \text{ ns} \tag{2.175}$$

as the maximum group delay excursion corresponding to the set of parameters in (2.172). This compares favorably with a computed value of 240 ns.

The example leading to (2.175) is a worst-case situation, of course; we have calculated the bound at the frequency which gives rise to the deepest fade. The bound in (2.171) is useful in other respects; e.g., it indicates the relative unimportance of group delay excursions during shallower fades. As a case in point, the group delay upper bounds for 10 dB, 20 dB, and 30 dB fades are 5.983 ns, 18.920 ns, and 59.83 ns, respectively.

2.4 Two Specific Communication Channels of Interest

Using the analytical results described in Section 2.2 we have computed delays and amplitudes on two specific links of interest, the Hohenstadt-Zugspitze link in Germany and the Swingate-Houten link which crosses the English Channel at a point near Dover. Additionally we have calculated the dependence of fade depth and group delay on frequency and layer height for these two links.

Because modem performance on the Hohenstadt-Zugspitze link will be evaluated at a later point in this report we have emphasized calculation of the multipath delays and amplitudes on that link. It will be recalled that the set of multipath amplitudes and delays provides a complete characterization of the link from which all other quantities of interest can be calculated, e.g., fade depth, group delay, and distortion parameters. Most significantly, the delays and amplitudes can be used to calculate error probability and, hence, determine the SNR degradation of the frequency-selective channel relative to a flat-fading channel. The results of calculations of the SNR degradation are provided in Section 3.

2.4.1 Hohenstadt-Zugspitze Link

The Hohenstadt-to-Zugspitze (H → Z) and Zugspitze-to-Hohenstadt (Z → H) link are of interest because of their rather extreme geometries relative to typical earth-based LOS microwave links. As illustrated in Fig. 2.15 the two terminals are separated by approximately 100 miles with the terminal at Zugspitze elevated over a mile relative to that at Hohenstadt. (It should be noted that all heights are referred to the height of the primary antenna at Hohenstadt.*) The intuitive motion that such an extreme geometry can lead to extreme fading is supported by the program of measurements described in [2.8]. It is reported there that fading over the H → Z path is greater than over any other tested in the DEB Stage I system. Therefore, it was not surprising for us to encounter more extreme values of multipath than we have encountered on shorter links that we have investigated.

---

*The "primary" antenna is the one antenna at either location that is enabled to both transmit and receive.

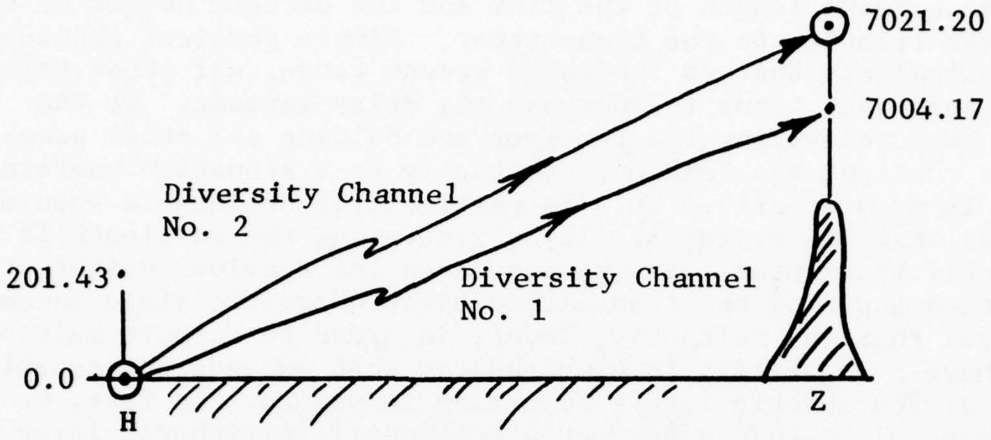

(a) Hohenstadt-to-Zugspitze Link

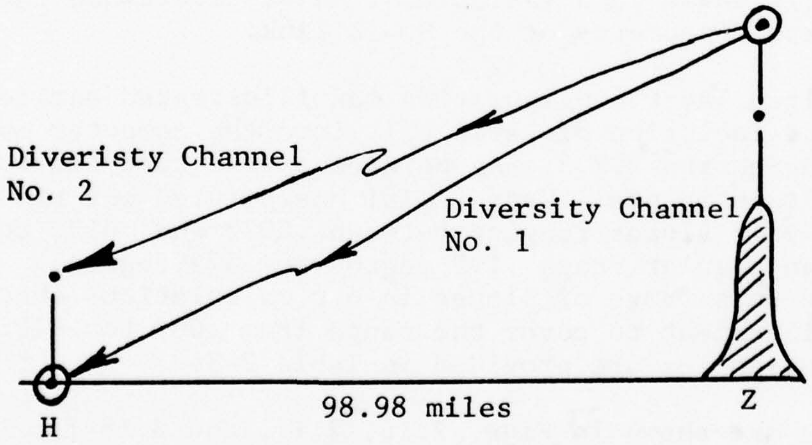

(b) Zugspitze-to-Hohenstadt Link

Figure 2.15 Link Geometry for Hohenstadt-Zugspitze Link

Before describing the results of the calculations we should point out that there are two features of the H → Z link which, in one important sense, tend to balance one another out. These are the extreme length of the link and the extreme height of the receiver relative to the transmitter. Simple physical considerations indicate that an increased ground range, all other things being constant, tends to increase the delay spreads. On the other hand, elevating the receiver and holding all other parameters constant can lead one eventually to a situation wherein there is no multipath. This is particularly noticeable when one assumes that the refractive layer generating the multipath is perfectly horizontal. As one increases the receiver height, the elevation angle of the transmitted electromagnetic field becomes so great that the refractive layer, in order to support multipath, must have a capability to bend the ray that exceeds the capabilities of atmospheric layers occurring in nature. In fact, we have determined that a perfectly horizontal atmospheric layer will not support multipath on the H → Z link unless its lapse rate* exceeds 800 Nu/km. For virtually all of the useful quantitative data that has come into our hands (e.g., [2.5], [2.6], and [2.7]) this value is considerably off scale.

Were it not for the fact that layers tilt [2.17], [2.18] the fading on the H → Z path would be unexplainable via the mechanism of refractive multipath in atmospheric layers. As it happens, the layer tilt angle is a variable of major importance for links with the extreme geometry of the H → Z link.

The tilted layer configuration was illustrated earlier in Fig. 2.10 and inclusion of layer tilt into the computer model was discussed in Section 2.2.3. As pointed out in that section data on layer tilt is meagre. Kerr [2.18] has pointed out that warm fronts have tilt slopes ranging between .0033 and .010, corresponding to an angular range .190 degree to .573 degree. We have used this range of slopes in our calculations choosing a .001 slope increment to cover the range from .003 to .010. The corresponding angles are provided in Table 2-3.

Results are shown in Figs. 2.16, 2.17, and 2.18 for three different values of the lapse rate of refractive index gradient, 300, 350, and 400 Nu/km. The curves in these figures are the

---

*By lapse rate we are referring to the lapse rate of refractive index gradient. Algebraically this quantity is just the negative of the refractive index gradient.

TABLE 2-3

VALUES OF LAYER SLOPE USED IN CALCULATIONS AND CORRESPONDING LAYER TILT ANGLES

Layer Slopes	Layer Tilt Angle (Degrees)
.003	.172
.004	.229
.005	.286
.006	.344
.007	.401
.008	.458
.009	.5156
.010	.573

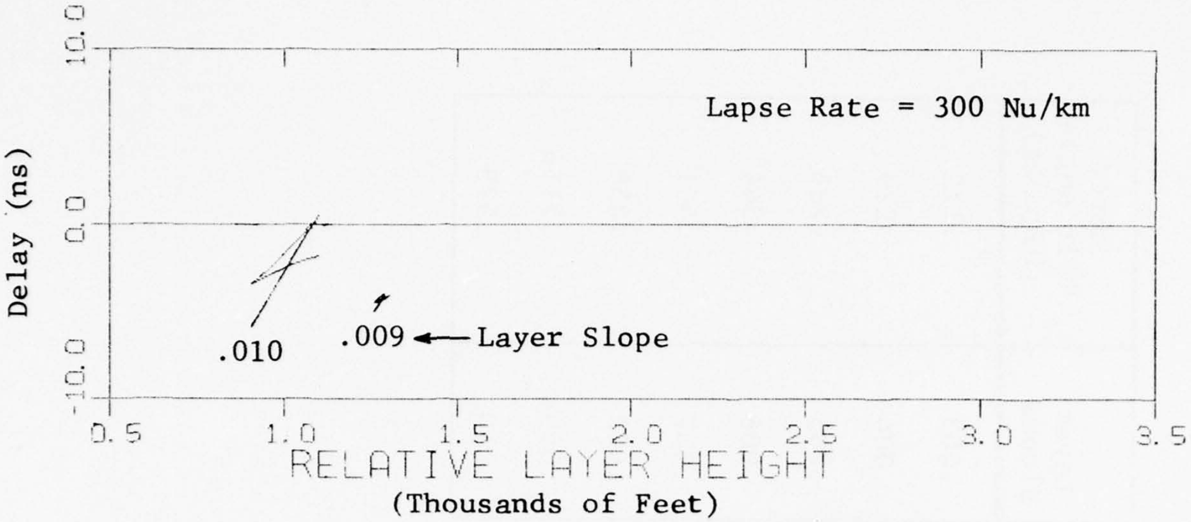

Figure 2.16 Multipath Delay Profile of Diversity Channel No. 1 on the Hohenstadt-to-Zugspitze Link for a Lapse Rate of 300 Nu/km

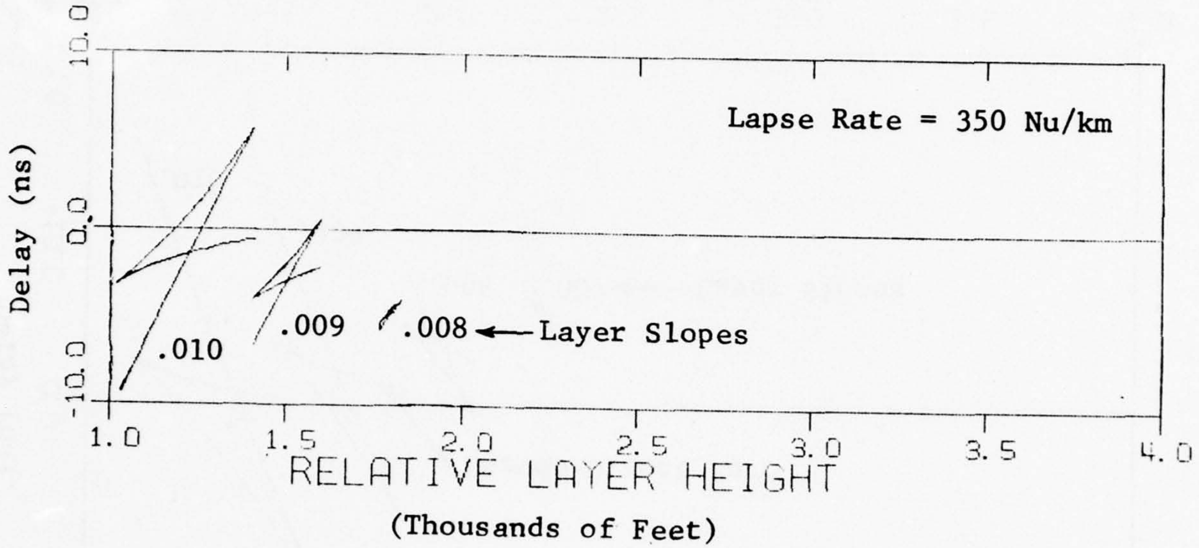

Figure 2.17 Multipath Delay Profile of Diversity Channel No. 1 on the Hohenstadt-to-Zugspitze Link for a Lapse Rate of 350 Nu/km

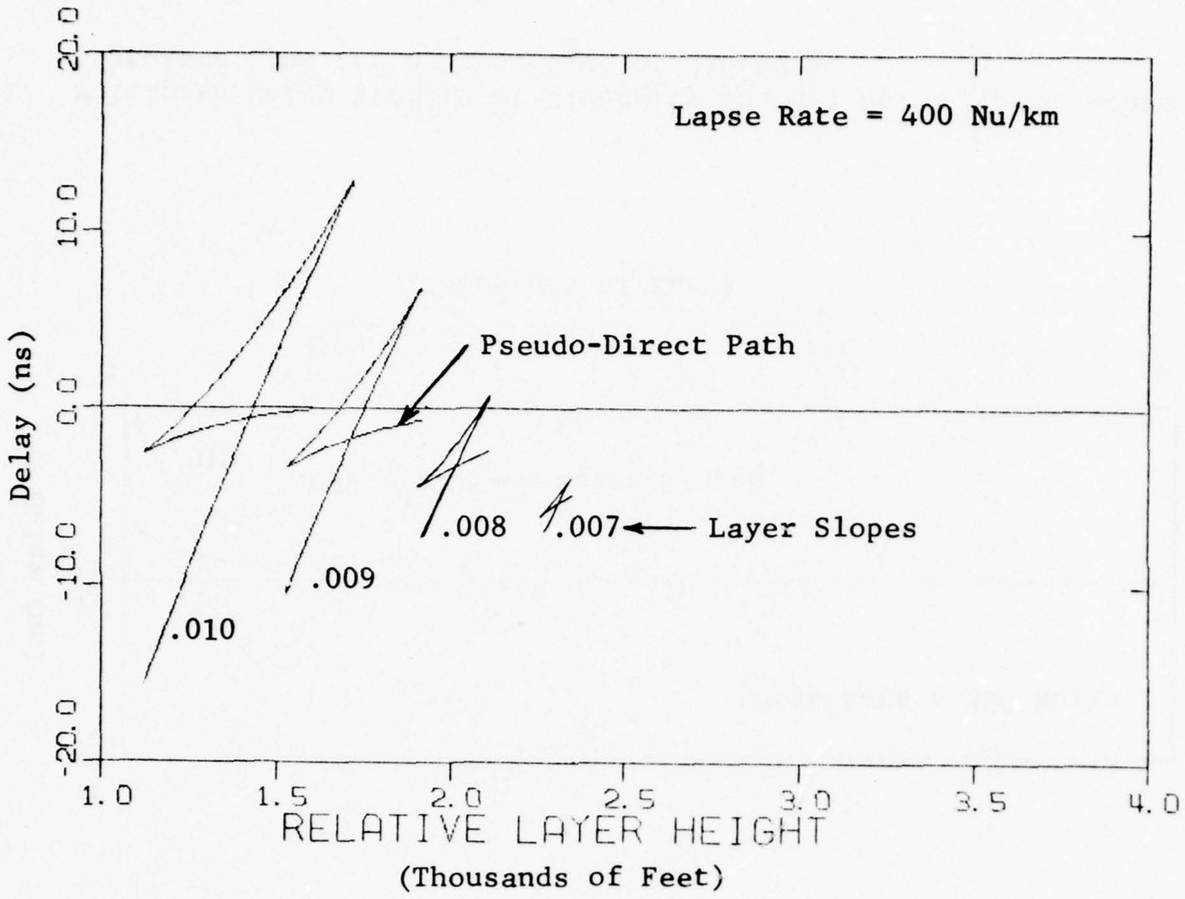

Figure 2.18 Multipath Delay Profile of Diversity Channel No. 1 on the Hohenstadt-to-Zugspitze Link for a Lapse Rate of 400 Nu/km

multipath delay profiles; they represent the delay of each ray path supported by the propagation channel. The delays are plotted vs. layer height and are measured relative to the delay of the direct path channel. As an example, note from Fig. 2.18 that a layer with slope .010 supports three ray paths when it is at a height of 1500 feet. For two of these paths there are delay lags; one is at 3 ns, the others at 6 ns. For the other path there is a delay advance of about -1 ns. As the layer moves up this path delay converges on zero, reaching that point when the layer rises above the receiver and, by so doing, allows a direct path to exist between transmitter and receiver. For this reason we refer to it as the pseudo-direct path. As the layer rises it is also clear from the figure that the upper two ray paths converge; it should be emphasized that the point of convergence is by no means the same as the point of convergence between the direct and pseudo-direct path. Another point that should be emphasized is that the delay profiles presented in this report, for economy of presentation, only show the delays that exist in a multipath situation, i.e., when there is more than one delay.

One interesting feature of each of these curves, e.g., Fig. 2.17, is that the multipath profiles tend to open up or spread as the slope of the layer increases. This is because the layer is approaching the position of maximal multipath which occurs when the layer and the straight line connecting the transmitter and the receiver are perfectly parallel. This position is never quite reached here since the straight line slope, at a value of .013, is slightly in excess of .010, the largest layer slope of interest.

Another feature of Figs. 2.16 to 2.18 is that increases in lapse rate allow for the occurrence of multipath at smaller tilt angles. This is not surprising in view of our knowledge of the general fact that the large lapse rates tend to be more amenable to support of multipath than the smaller ones. An extreme case is shown in Fig. 2.19 where we have used a lapse rate value of 500 Nu/km. It can be seen that multipath support exists over layer slopes ranging from .005 to .010 with delay spreads sometimes in excess of 20 ns. Fortunately, this lapse rate is not within the range expected for the H → Z link. (See comments in [2.8] and data on page 107 of [2.6].)

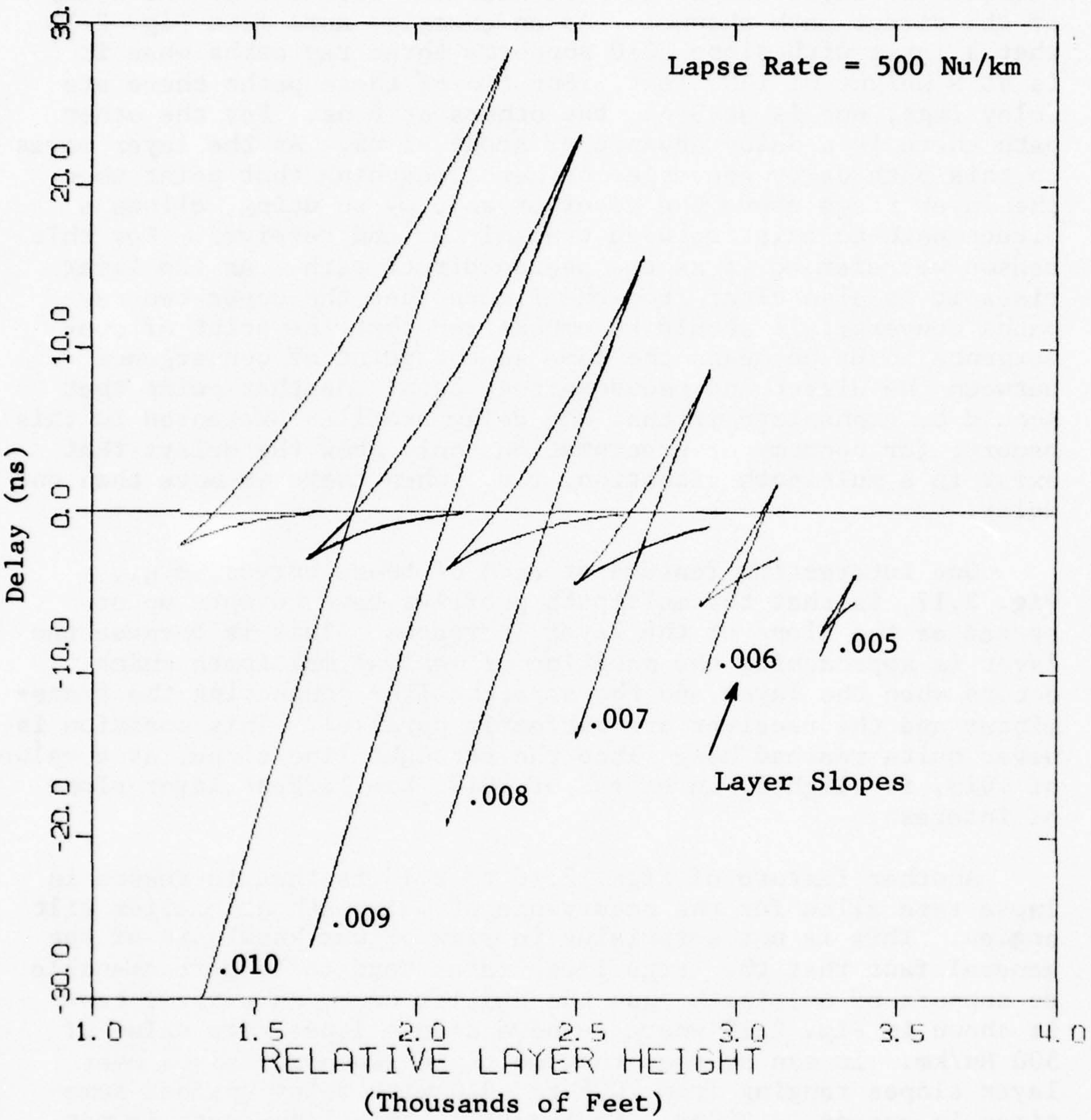

Figure 2.19 Multipath Delay Profile of Diversity Channel No. 1 on the Hohenstadt-to-Zugspitze Link for a Lapse Rate of 500 Nu/km

The dependence on lapse rate is more clearly demonstrated in Fig. 2.20 below where we show how the multipath delay profile changes as the lapse rate is increased. From an extremely small profile when the lapse rate is 350 Nu/km the profile is seen to evolve to a condition wherein there are multipath delay separations in excess of 20 ns when the lapse rate is 550 Nu/km. For the curves in Fig. 2.20 the layer slope is kept fixed at a value of .008.

For Figs. 2.16 through 2.20 it should be pointed out that each profile in each of the figures is plotted only over the range of layer heights supporting multipath. In actuality the single negative path extends indefinitely to the left whereas the pseudo-direct path (see Fig. 2.18) extends beyond the profile and steadily increases until it becomes zero. This is the point, of course, at which the layer rises above the receiving terminal and direct path propagation becomes possible. This observation coupled with examination of Figs. 2.16 through 2.20 indicates that the refractive multipath model would have been totally inadequate for the extreme geometry situation encountered on the H → Z link were it not for the model up-date described in Section 2.2.2.2 and illustrated in Fig. 2.5(b).

When the delay calculations are complemented with amplitude calculations the LOS refractive channel characterization is complete. The plots of amplitude vs. layer height do not have as great an effect as their delay counterparts do, and we have restricted the presentation to the amplitudes for a lapse rate of 400 Nu/km as shown in Fig. 2.21. The layer slopes range from .007 to .010 as in Fig. 2.18. As the tilt increases the same horizontal spreading that was observed in the delay profiles is observed here. It should be noted, however, that the amplitude increases for the smaller tilt angles. This is because the delay profiles are "tighter" at the smaller tilt angles, as pointed out earlier. This means as the layer height passes through that range of values that allows the existence of multipath, the delays and amplitudes of each of the ray paths are closer in value. In the geometrical sense this means that the rays are closer to one another in space. This latter is a focussing condition and makes for higher signal amplitudes on each path.

Figure 2.21 is rather densely packed. The nature of the amplitude dependence on layer height is more clearly displayed in Fig. 2.22. This figure shows both the amplitude and delay profile for a lapse rate of 400 Nu/km. We can easily identify the pseudo-direct path as the one that converges on zero (layer

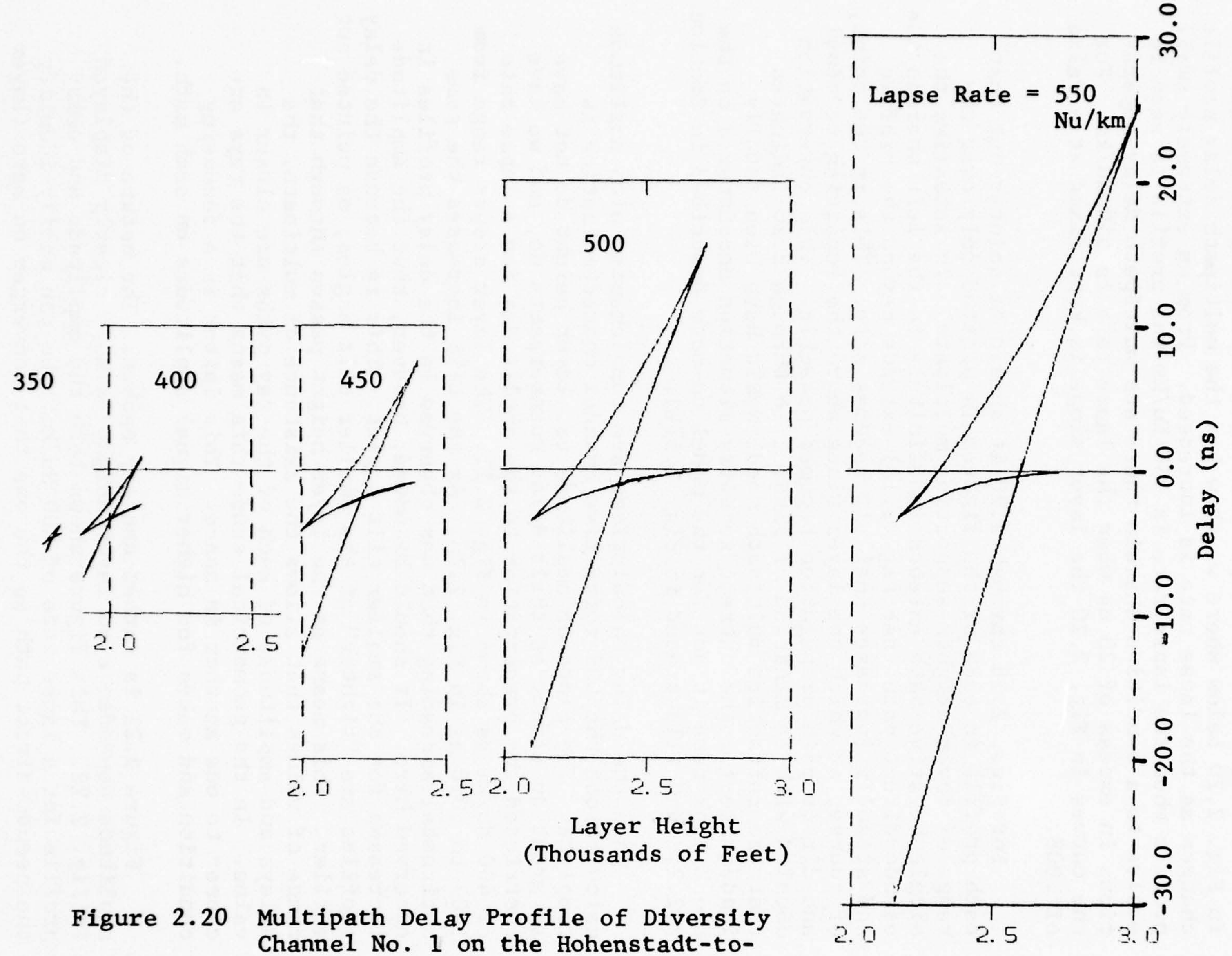

Figure 2.20 Multipath Delay Profile of Diversity Channel No. 1 on the Hohenstadt-to-Zugspitze Link. Layer slope is .008.

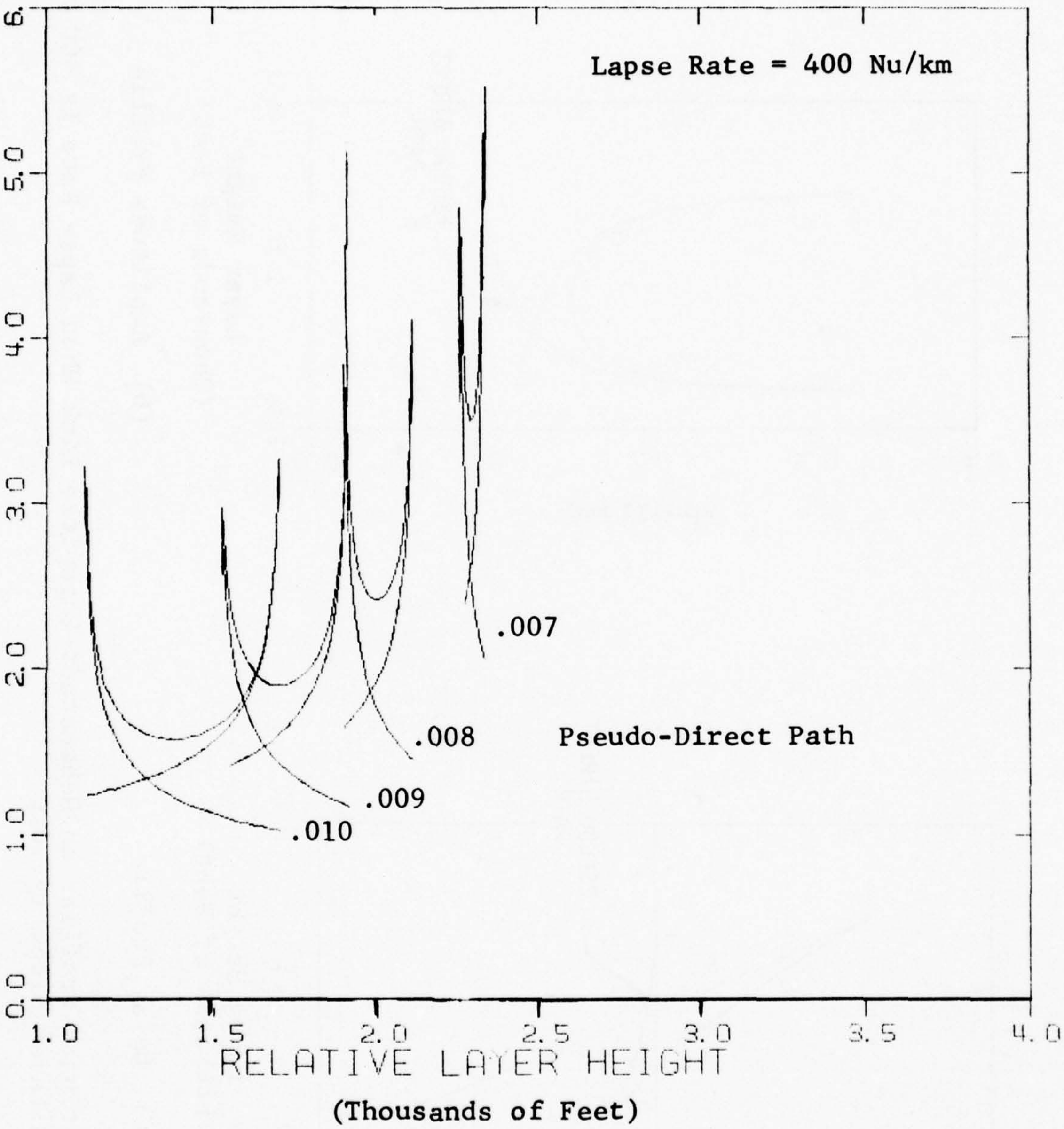

Figure 2.21 Multipath Amplitude Profile of Diversity Channel No. 1 on the Hohenstadt-to-Zugspitze Link for a Lapse Rate of 400 Nu/km

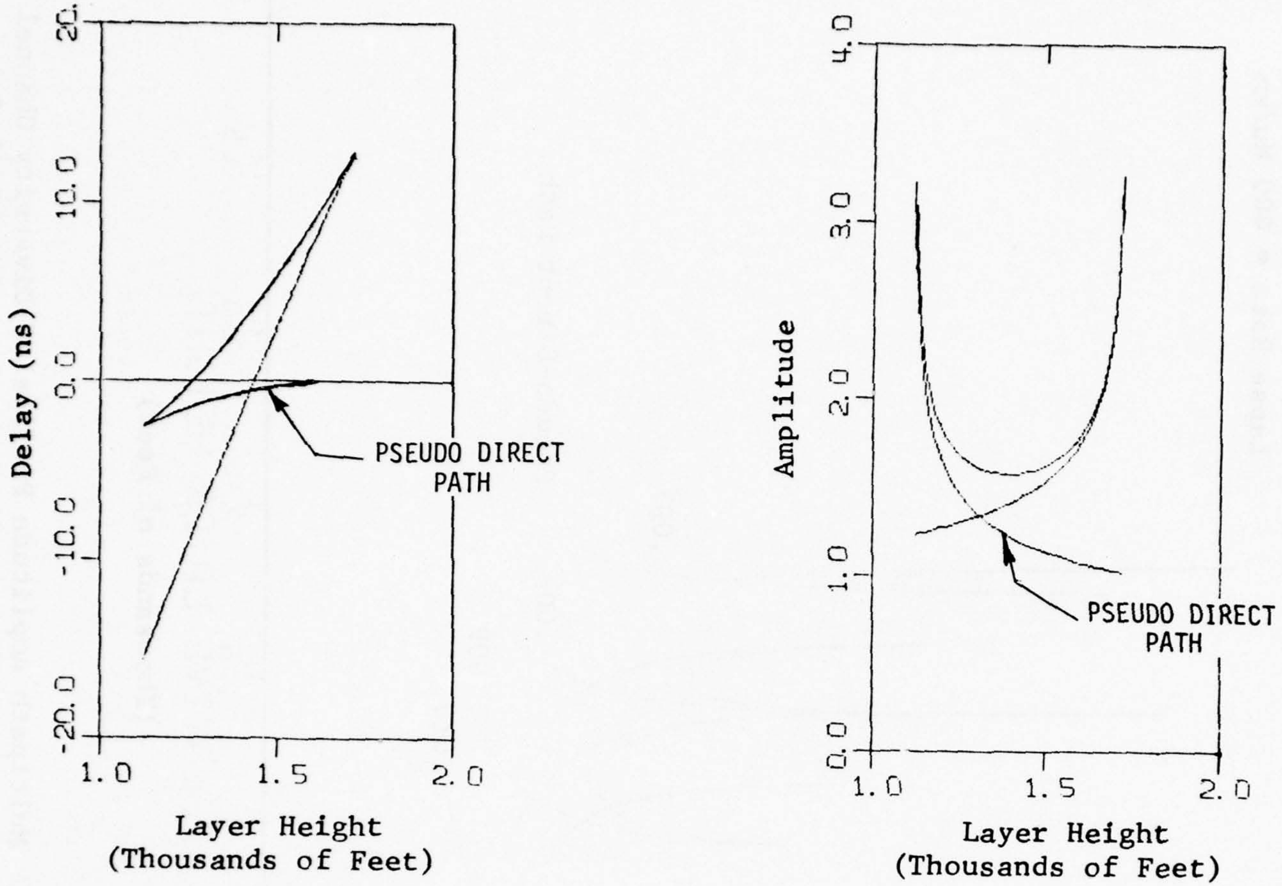

(a) Delay Profile

(b) Amplitude Profile

Figure 2.22 Multipath Profiles on Hohenstadt-Zugspitze Link When Lapse Rate is 400 Nu/km and Layer Slope is .010

height increasing) in the delay profile and converges on unity in the amplitude profile.

The data described above has been used as input parameters for the modem performance evaluations discussed in Section 3. For easy reference the method of choosing the parameters and the parameter choices are provided with a separate section (Section 2.4.3).

With the delays and amplitudes described above we have calculated (in addition to the performance calculations presented in Section 3) two basic fading parameters, the fade level and the group delay. We now turn to the presentation of several curves that illustrate the basic nature of the fading.

One such curve is presented in Fig. 2.23. This plot illustrates the dependence of fade level on layer height for an arbitrarily chosen carrier frequency of 8.2 GHz. This figure should be examined in connection with the .009 multipath delay profile of Fig. 2.18. Comparing the two we see that the fading occurs over the same interval of layer height that is characterized by a multiplicity of rays in Fig. 2.18. This range extends from approximately 1520 feet to 1920 feet. At the higher end of the range there is the focussing condition (enhanced amplitude) that we have mentioned before. In the middle of the range there are three fades that go down to about -10 dB. The fact that deeper fades do not occur is not surprising in view of the dearth of deep fade loci evident in Fig. 1.1 and our arbitrary choice of carrier frequency.

From the figure it can be seen that the signal level is not zero dB outside the fading interval. The reason for this is that the one remaining propagation path still intersects the layer, i.e., the highest terminal is still immersed in the layer. Thus there is still some signal enhancement; at the higher layer locations propagation takes place via the "quasi-direct" path of Fig. 2.5(b). The amplitude decreases at the higher levels until finally the layer rises above the highest receiver, direct path propagation is allowed to take place and the signal amplitude (always measured relative to the direct path) becomes 0 dB.

Since refractive layers are thought to move vertically [2.12], Fig. 2.23 can, to some extent, be viewed as a dynamic plot. This is true also of subsequent plots (depicting fading behavior as a function of layer height) to be presented in this report. In fact, it is of interest to temporarily assume some

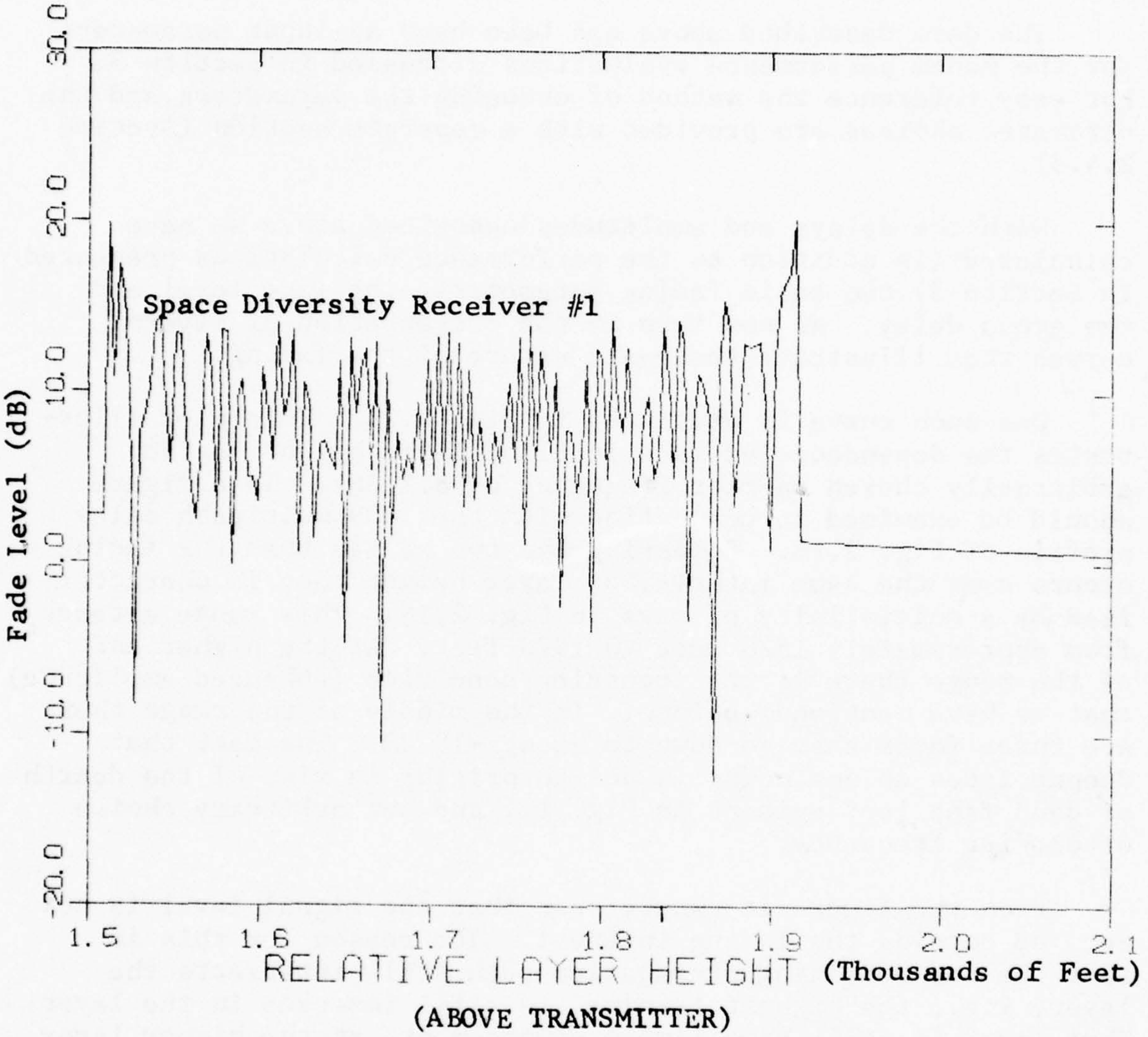

Lapse Rate = -400

Carrier Frequency = 8.2 GHz

Layer Slope = .009

Figure 2.23 Fade Level Vs. Layer Height on Hohenstadt-to-Zugspitze Link

constancy of speed and direction for the layer and view the figures as plots depicting dependence on time. Viewed in this light Fig. 2.23 and later plots bear more than a superficial resemblance to fading records of various channel parameters.

The computer plot of Fig. 2.23 is limited in resolution because of the fact that it was generated from only 200 points. Magnification of the plot reveals that a fade deeper than any one of those depicted in Fig. 2.23 occurs near 1900 feet. The magnification of this fade is shown in Fig. 2.24. It can be seen that the fade extends slightly deeper than -20 dB.

We recall from the discussion of Section 2. that the largest group delay excursions are allowed to take place during deep fades. For this reason it is of interest to examine the dependence of group delay over the same interval of layer height shown in Fig. 2.24. This illustration is provided in Fig. 2.25. We see that the extrema of group delay (about 100 ns) and fade level coincide.

As we discuss in Section 4 the group delay in Fig. 2.25 does not apply to all the frequency components of a signal traversing the refractive channel. Such a consideration raises questions that are best addressed by Figs. 2.26 and 2.27. There we depict the frequency dependence of the fade level and group delay across a 30 MHz band centered on the 8.2 GHz carrier. There we see that some frequency components of the signal are hardly attenuated at all, whereas others are down 20 dB; some frequency components are hardly time shifted at all whereas others arrive with a 100 ns time shift. It is comforting to note, however, that the frequency components most delayed are also those that are most attenuated. Thus, neglect of the distortion effects of frequency components 10 dB down at the receiver is equivalent to neglect of frequency components delayed by more than about 10 ns. Though such considerations are of interest they are probably best addressed through the T and P parameter formalism developed in Section 2.3.2 and applied extensively in Section 3.

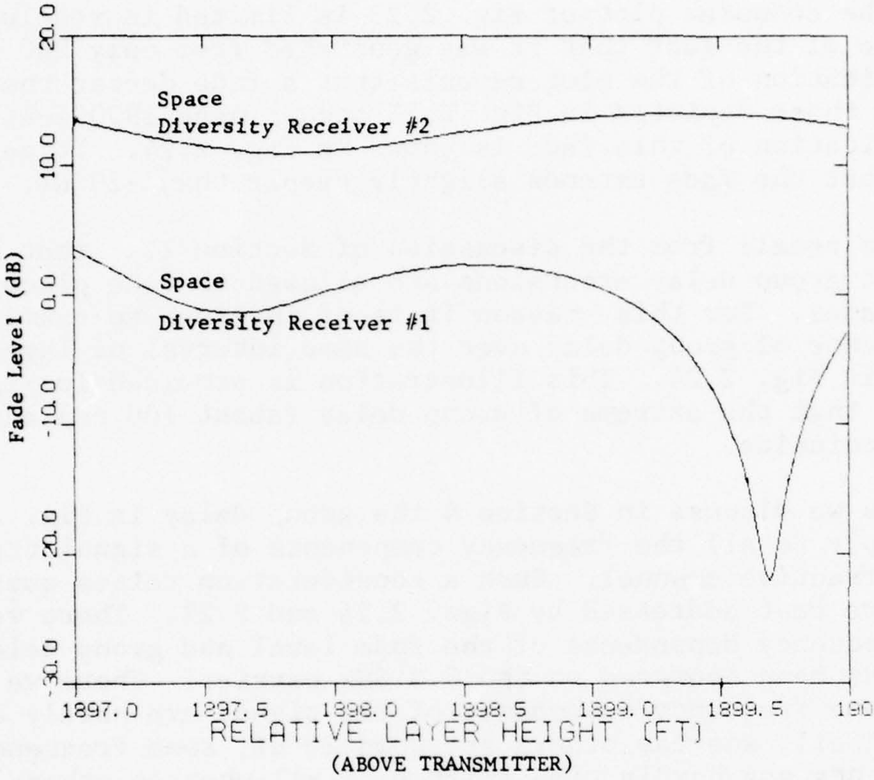

Lapse Rate = -400

Carrier Frequency = 8.2 GHz

Layer Slope = .009

Figure 2.24 Fade Level Vs. Layer Height on Hohenstadt-to-Zugspitze Link

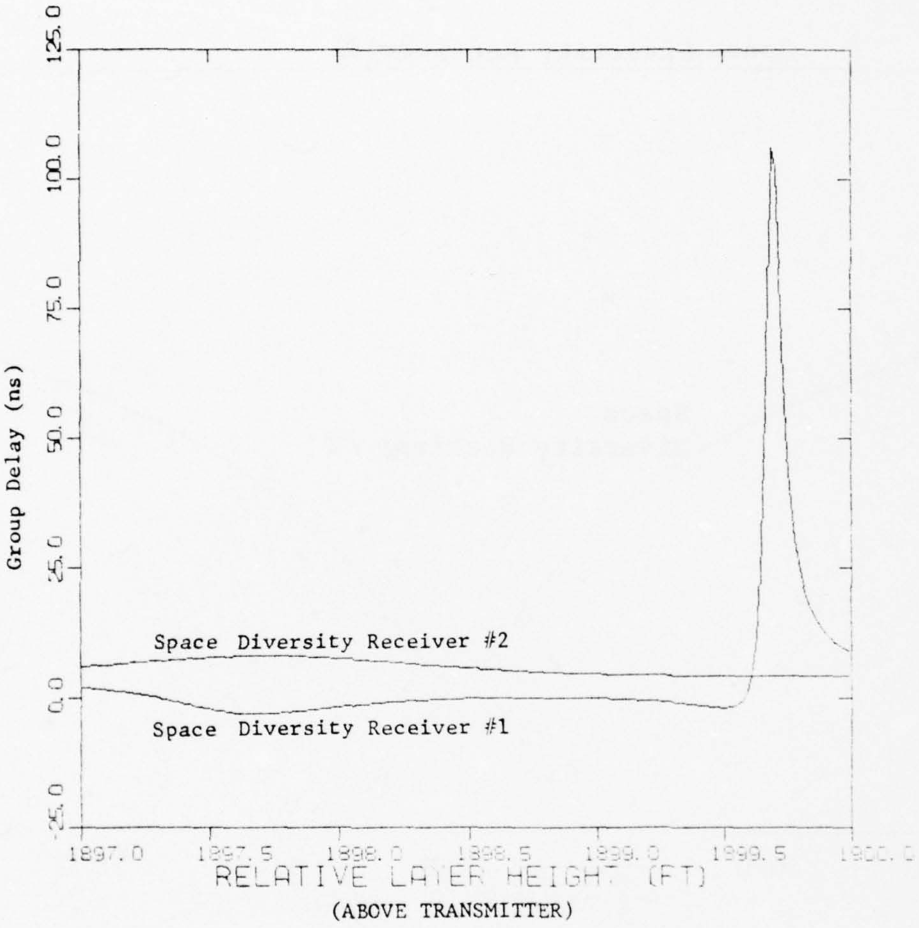

Lapse Rate = -400

Carrier Frequency = 8.2 GHz

Layer Slope = .009

Figure 2.25 Group Delay Vs. Layer Height on Hohenstadt-to-Zugspitze Link

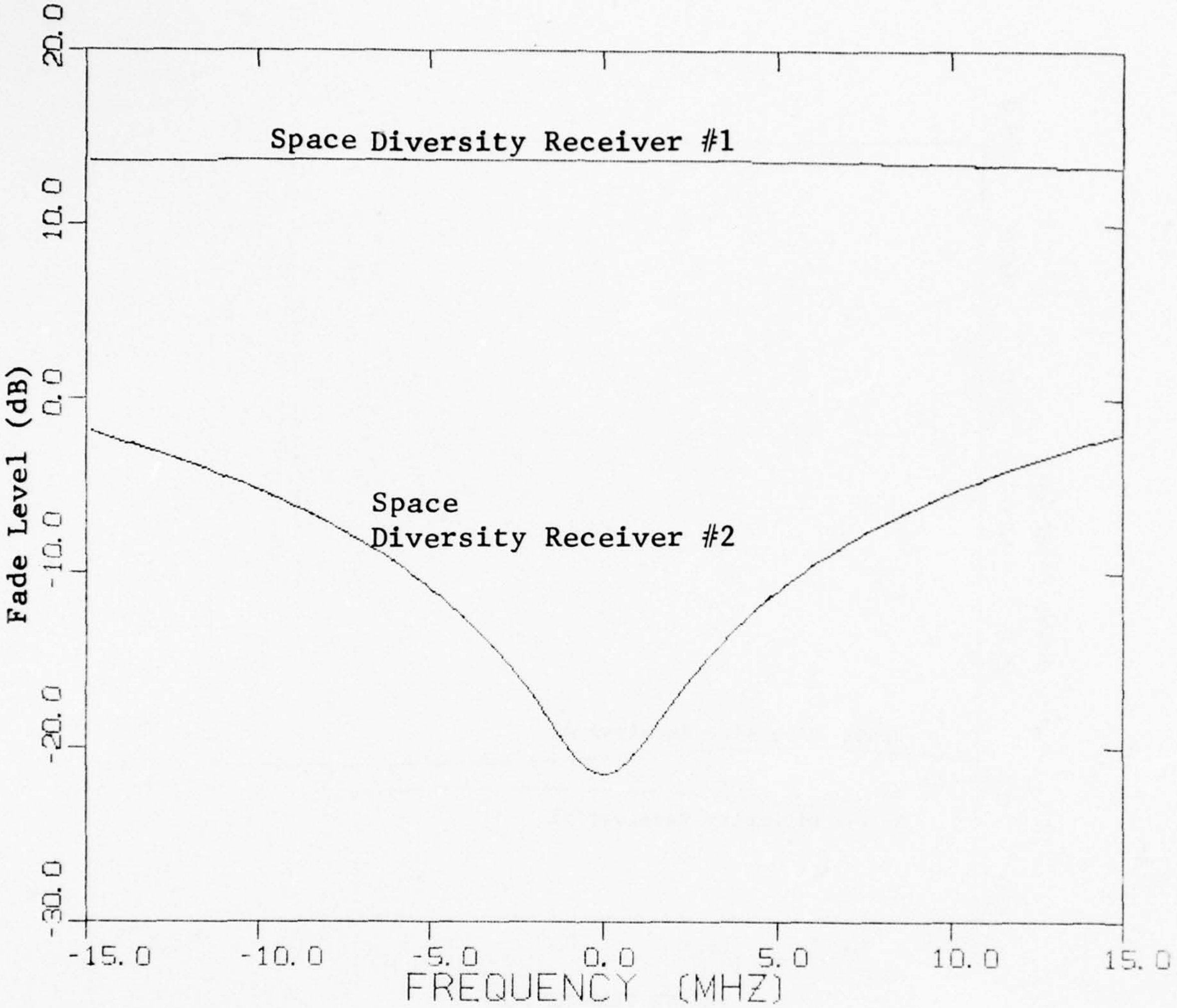

Lapse Rate = -400

Carrier Frequency = 8.2 GHz

Layer Slope = .009

Layer Height = 1899.7

Figure 2.26 Fade Level Vs. Frequency on Hohenstadt-to-Zugspitze Link

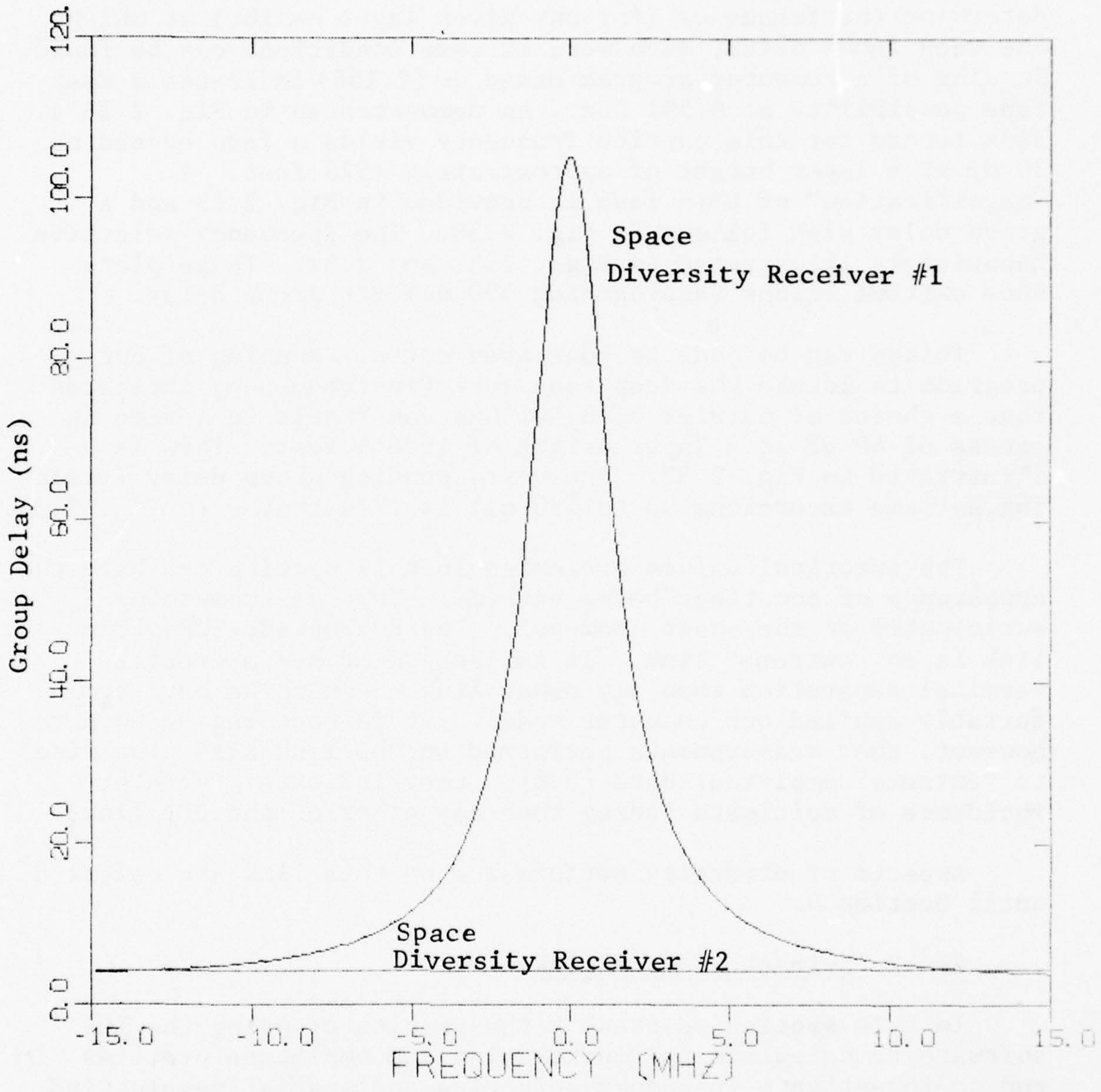

Lapse Rate = -400

Carrier Frequency = 8.2 GHz

Layer Slope = .009

Layer Height = 1899.7

Figure 2.27 Group Delay Vs. Frequency on Hohenstadt-to-Zugspitze Link

When the analytical results of Section 3 are applied to determine the frequency (for any given layer height) at which the deep fades occur, much more extreme conditions can be found. Running of a computer program based on (2.156) indicates a deep fade possibility at 8.591 GHz. As demonstrated in Fig. 2.28 a fade record for this carrier frequency yields a fade exceeding 30 dB at a layer height of approximately 1526 feet. A "magnification" of this fade is provided in Fig. 2.29 and a group delay plot follows in Fig. 2.30. The frequency-selective behavior is illustrated in Figs. 2.31 and 2.32. These plots show extreme values (approaching 400 ns) for group delay.

Things can be made to look even worse. Running of our programs to locate the deep fade loci (in frequency) indicates that a choice of carrier of 8.301 GHz can result in a fade in excess of 40 dB at a layer height of 1606.5 feet. This is illustrated in Fig. 2.33. The corresponding group delay (yielding extreme excursions up to 750 ns) is illustrated in Fig. 2.34.

The numerical values presented in this section can have the appearance of sometimes being extreme. This was something anticipated at the onset, however. The Hohenstadt-Zugspitze link is an "extreme" link. It is longer and has a greater terminal separation than any other link to which we have comfortably applied our computer model. It is encouraging to note, however, that measurements performed on the link also give rise to "extreme" empirical data [2.8]; they indicate a greater incidence of multipath fading than any other of the DEB links.

Aspects of diversity performance on this link are deferred until Section 4.

2.4.2 Swingate-Houtem Link

In this section we present the results of using the LOS software to calculate multipath delay and amplitude profiles and to investigate frequency-selective and spatially-selective fading characteristics of the Swingate-Houtem link. This link consists of a very long (55 mile) line-of-sight microwave path across the English Channel from Swingate near Dover, England to a site near Houten, Belgium.

Some refractivity data for this link has been presented in [2.23]. The data was taken at Shoeburyness which is located approximately 50 km northwest of Dover along the English coast and indicates that the choice of refractivity gradient -300 Nu/km that we have used in many of our calculations below is entirely reasonable.

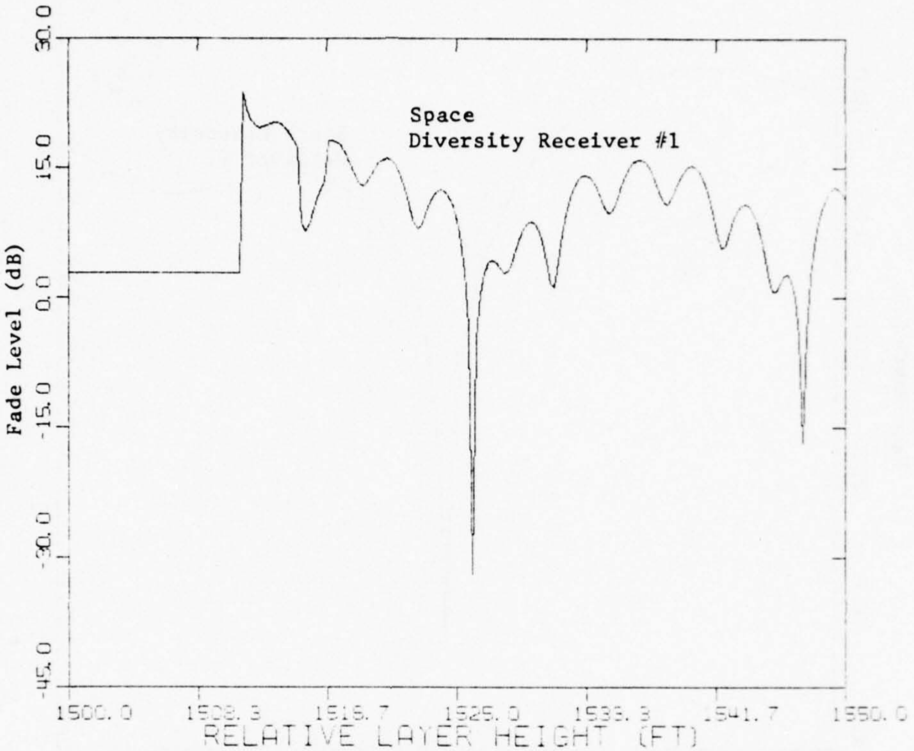

(ABOVE TRANSMITTER)

Lapse Rate = -400

Carrier Frequency = 8.591 GHz

Layer Slope = .009

Figure 2.28 Fade Level Vs. Layer Height on Hohenstadt-to-Zugspitze Link

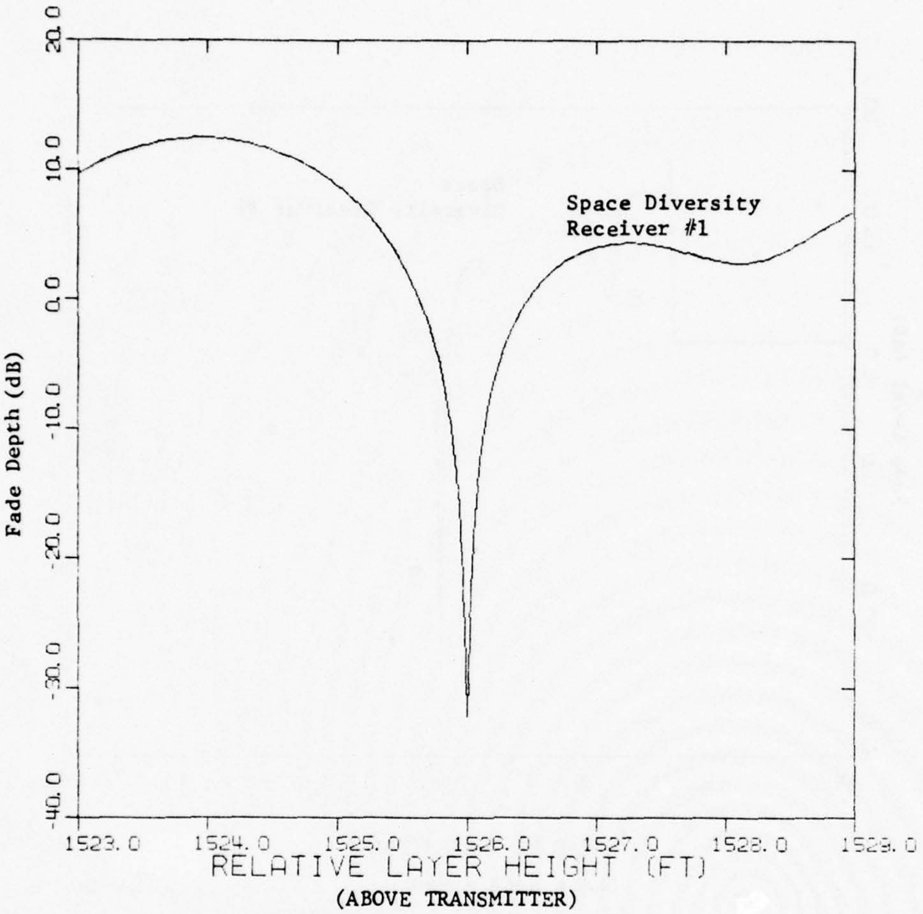

Lapse Rate = -400

Carrier Frequency = 8.591 GHz

Layer Slope = .009

Figure 2.29 Fade Depth Vs. Layer Height (Expanded View) on Hohenstadt-Zugspitze Link

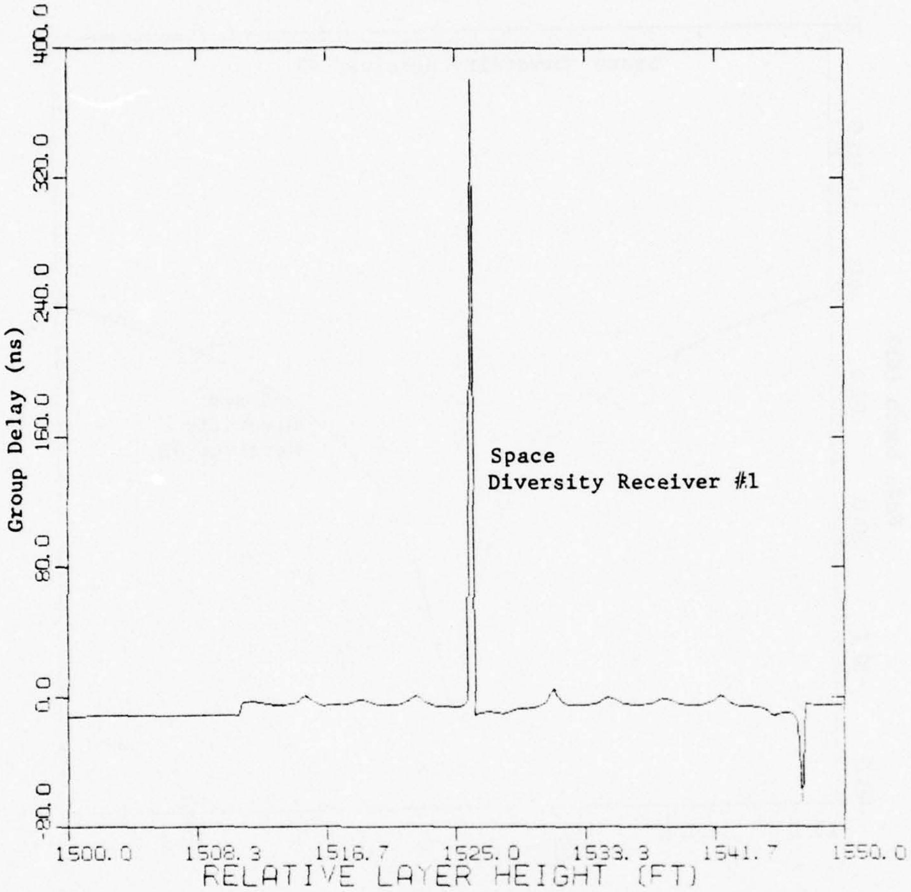

(ABOVE TRANSMITTER)

Lapse Rate = -400

Carrier Frequency = 8.591 GHz

Layer Slope = .009

Figure 2.30 Group Delay Vs. Layer Height on Hohenstadt-to-Zugspitze Link

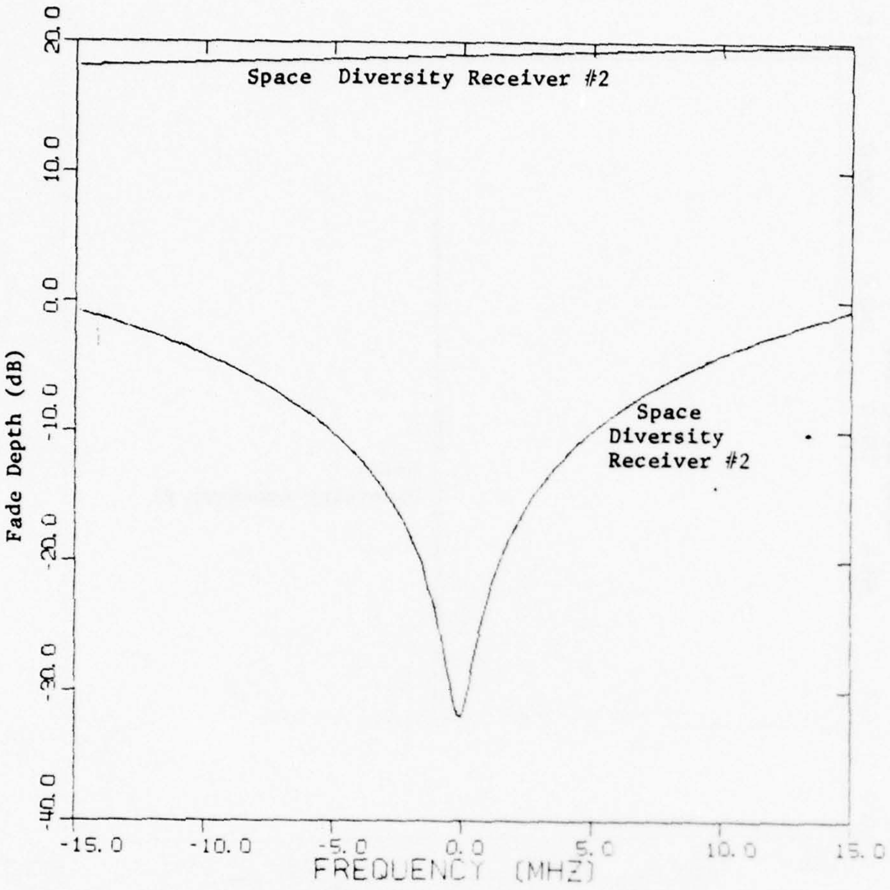

Lapse Rate = -400
Carrier Frequency = 8.591 GHz
Layer Slope = .009
Layer Height = 1526 Feet

Figure 2.31 Fade Depth Vs. Frequency on Hohenstadt-to-Zugspitze Link

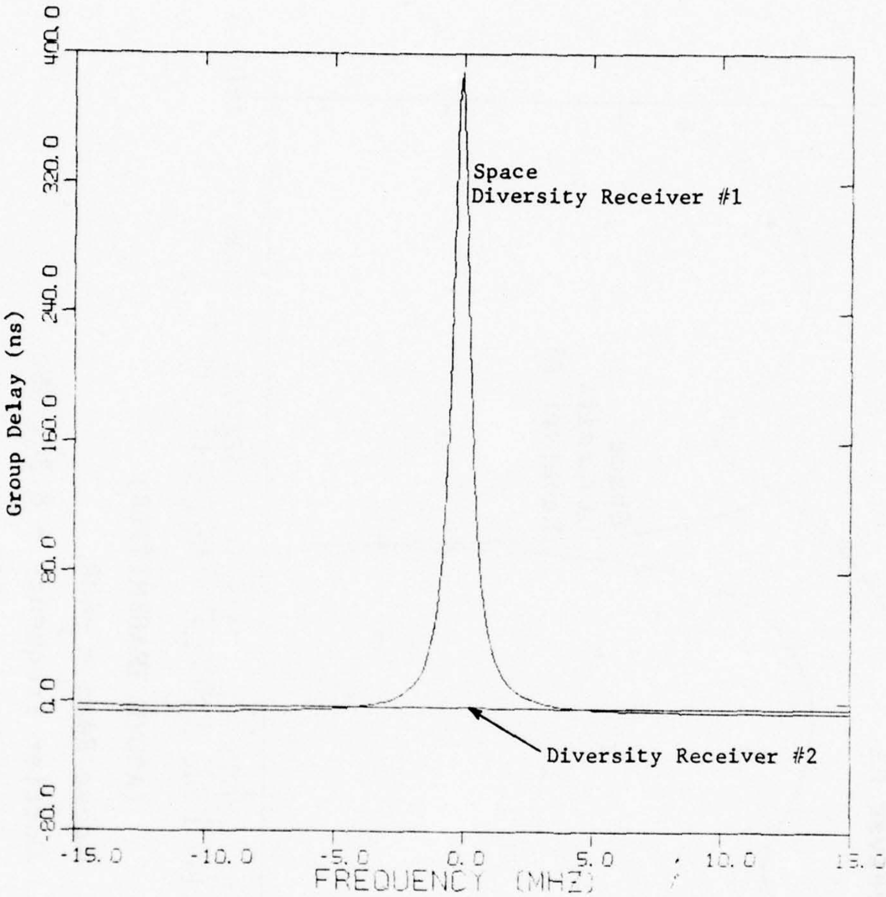

Lapse Rate = -400

Carrier Frequency = 8.591 GHz

Layer Slope = .009

Layer Height = 1526 Feet

Figure 2.32 Group Delay Vs. Frequency on Hohenstadt-to-Zugspitze Link

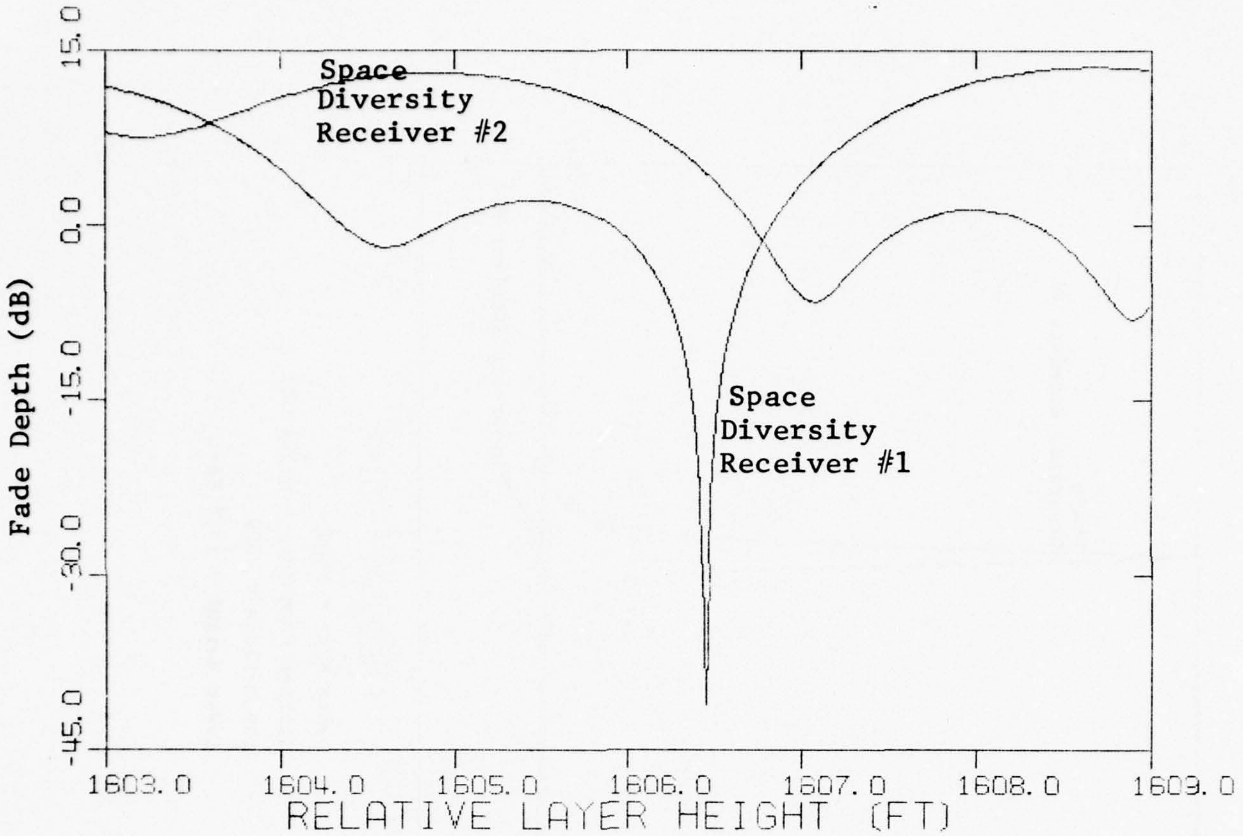

(ABOVE TRANSMITTER)

Lapse Rate = -400

Carrier Frequency = 8.301 GHz

Layer Slope = .009

Figure 2.33 Fade Level Vs. Layer Height on Hohenstadt-to-Zugspitze Link

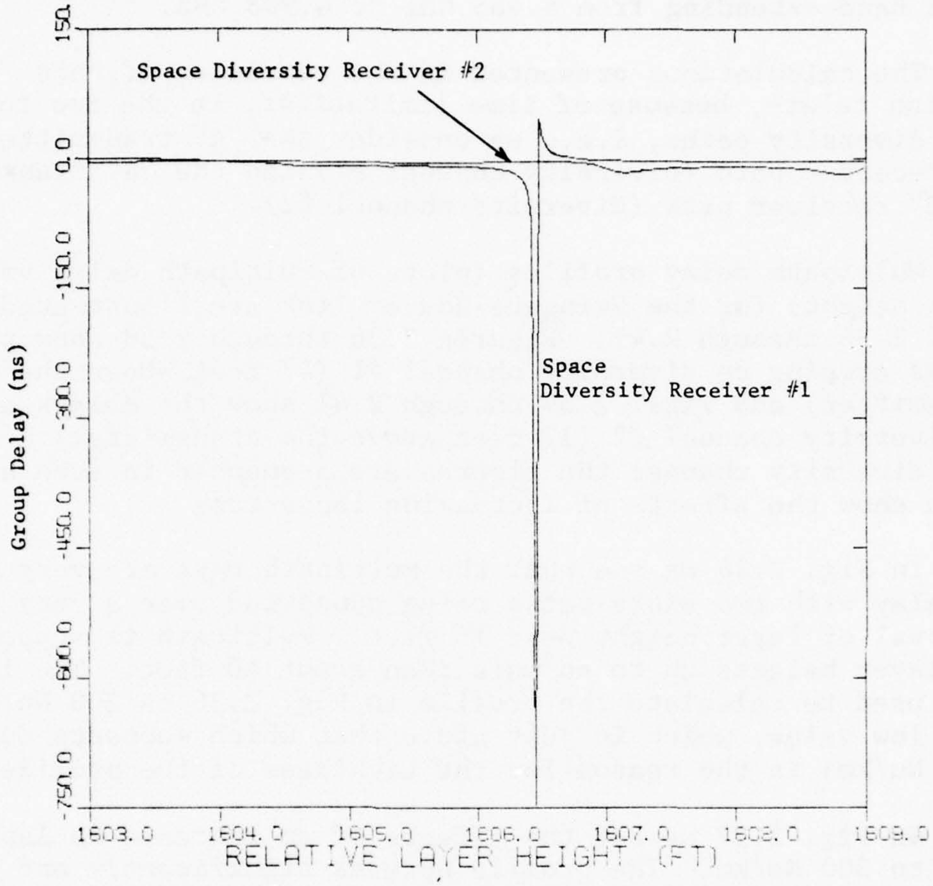

(ABOVE TRANSMITTER)

Lapse Rate = -400

Carrier Frequency = 8.301 GHz

Layer Slope = .009

Figure 2.34 Group Delay Vs. Layer Height on Hohenstadt-to-Zugspitze Link

The geometry of the Swingate-Houtem link is illustrated in Fig. 2.35. The two terminals are separated by 55 miles. The positions of the two top-most receiving terminals relative to the "A" transmitting terminal are 47 feet (receiver "A") and 17 feet (receiver "B").* The operating frequencies are in the 4 GHz band extending from 4.465 GHz to 4.908 GHz.

The calculations presented in the remainder of this section relate, because of time limitations, to the two top-most diversity paths, i.e., we consider the "A" transmitter to "A" receiver path (diversity channel #1) and the "A" transmitter to "B" receiver path (diversity channel #2).

Multipath delay profiles (plots of multipath delay vs. layer height) for the Swingate-Houtem link are illustrated in Figs. 2.36 through 2.41. Figures 2.36 through 2.38 show the delays arising on diversity channel #1 (47 feet above the transmitter) and Figs. 2.39 through 2.41 show the delays arising on diversity channel #2 (17 feet above the transmitter). For each diversity channel the figures are sequenced in such a way as to show the effects of increasing lapse rate.

In Fig. 2.36 we see that the multipath rays are very close in delay with two extra paths being supported over a very small interval of layer height near 15 feet. Multipath is supported for layer heights up to no more than about 40 feet. The lapse rate used to calculate the profile in Fig. 2.36 is 200 Nu/km. This low value, which is just above that which supports ducting (157 Nu/km) is the reason for the tightness of the profile.

In Fig. 2.37 we see the effects of an increase in lapse rate to 300 Nu/km. The profile spreads significantly and support of multipath propagation continues to a layer height in excess of 180 feet.

The effects of a further increase in lapse rate are illustrated in Fig. 2.38. The trends already discussed are evident here to an even greater degree. Significantly, a lapse rate of 400 Nu/km here supports multipath up to 340 feet.

---

*The zero reference level is at sea level. The elevations of the two antenna sites, not given in Fig. 2.35, are provided in [2.23].

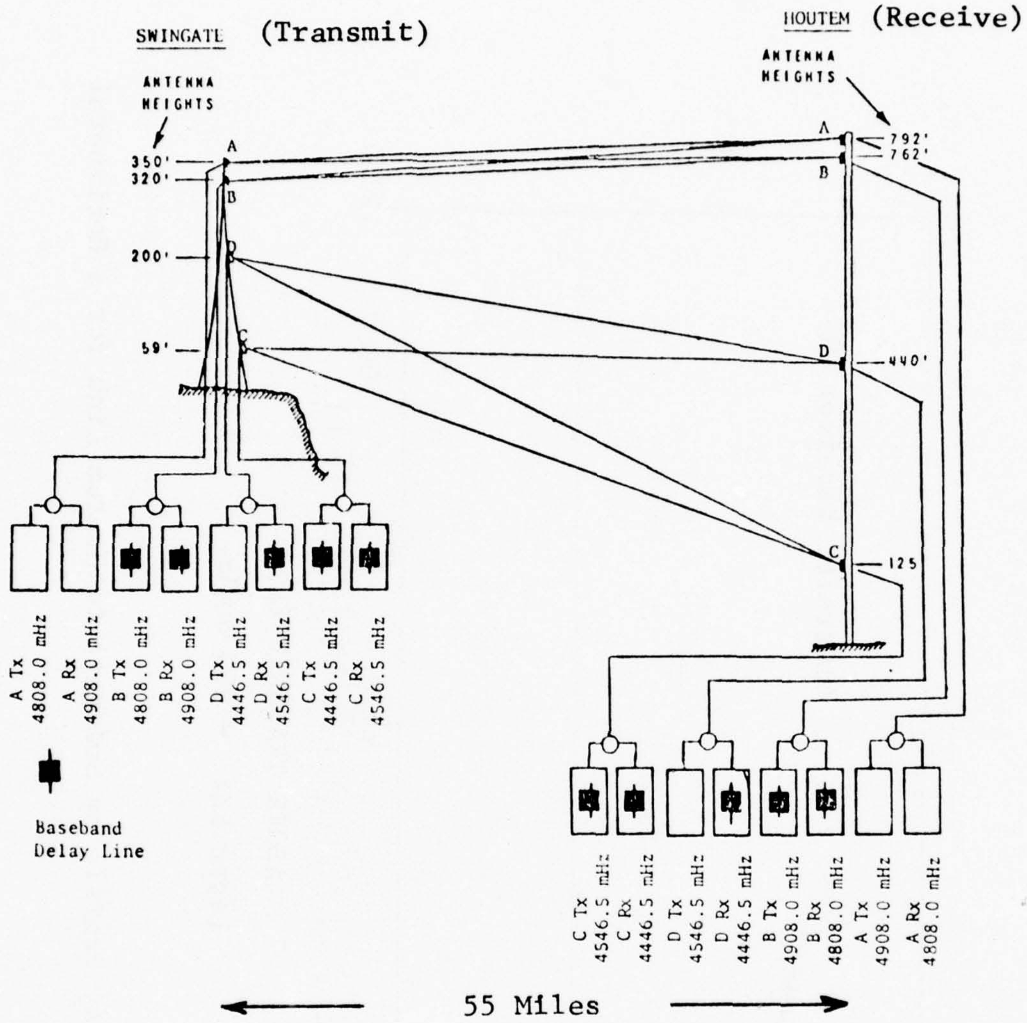

Diversity Channel #1 ...... A → A

Diversity Channel #2 ...... A → B

Figure 2.35 Swingate-Houtem Configuration (From [2.24])

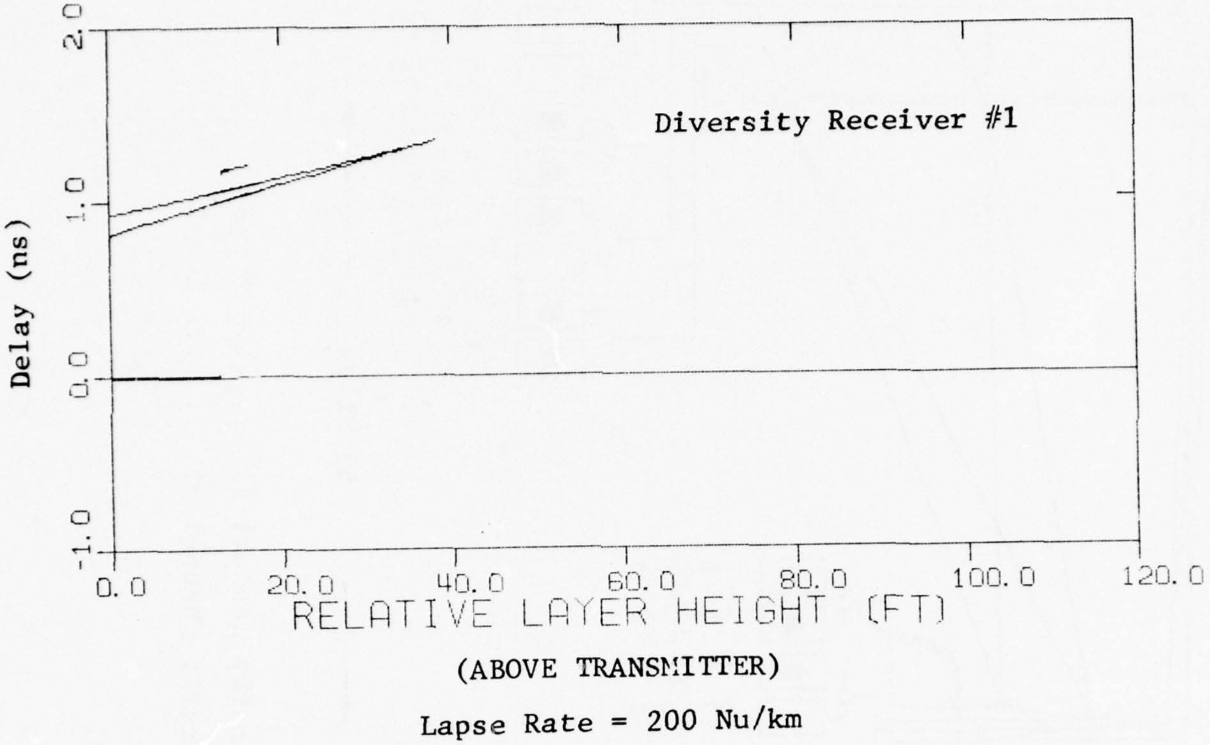

Figure 2.36 Multipath Delay Profile on Swingate-to-Houtem Link for a Horizontal Layer

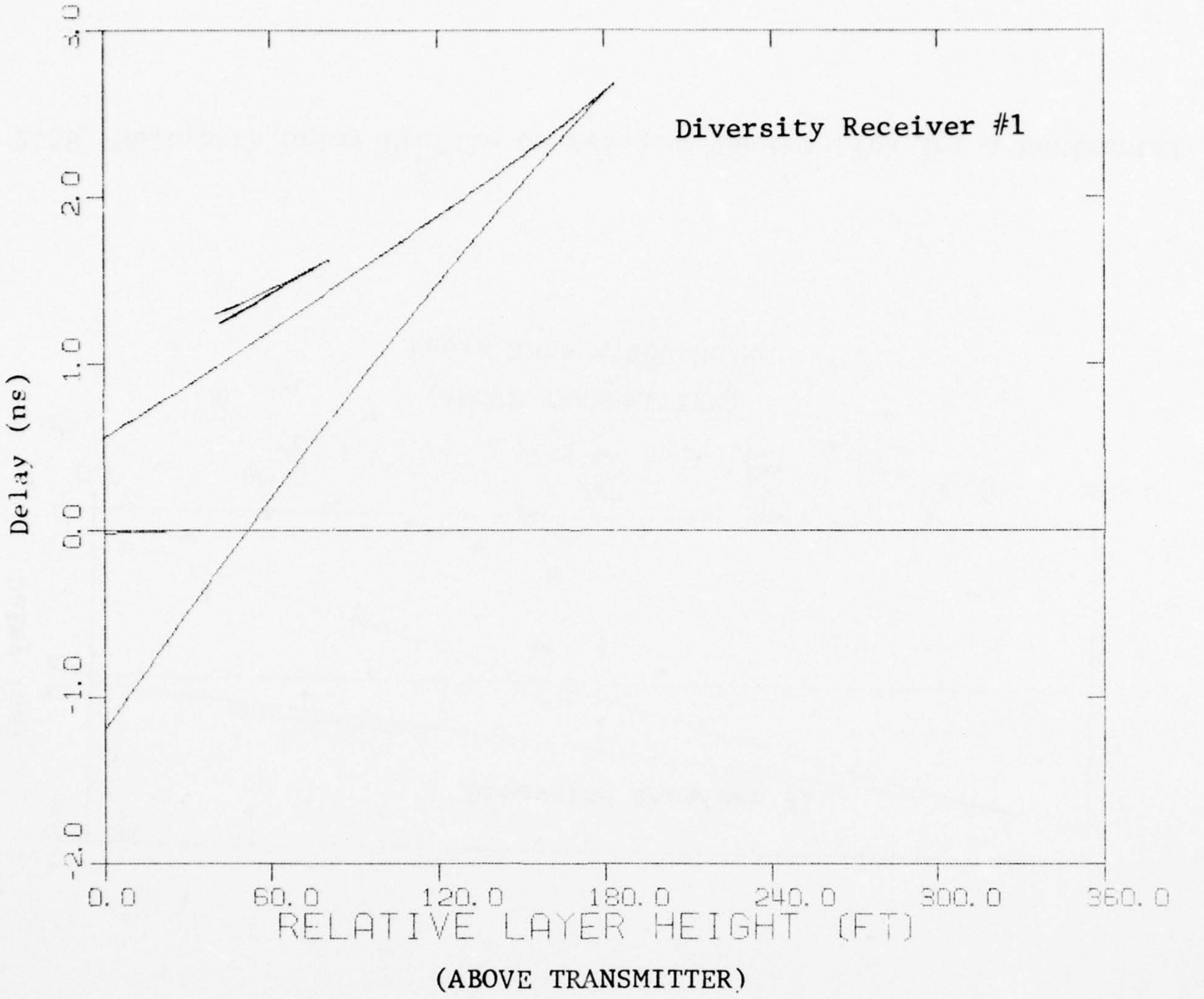

Lapse Rate = 300 Nu/km

Figure 2.37 Multipath Delay Profile on Swingate-to-Houtem Link for a Horizontal Layer

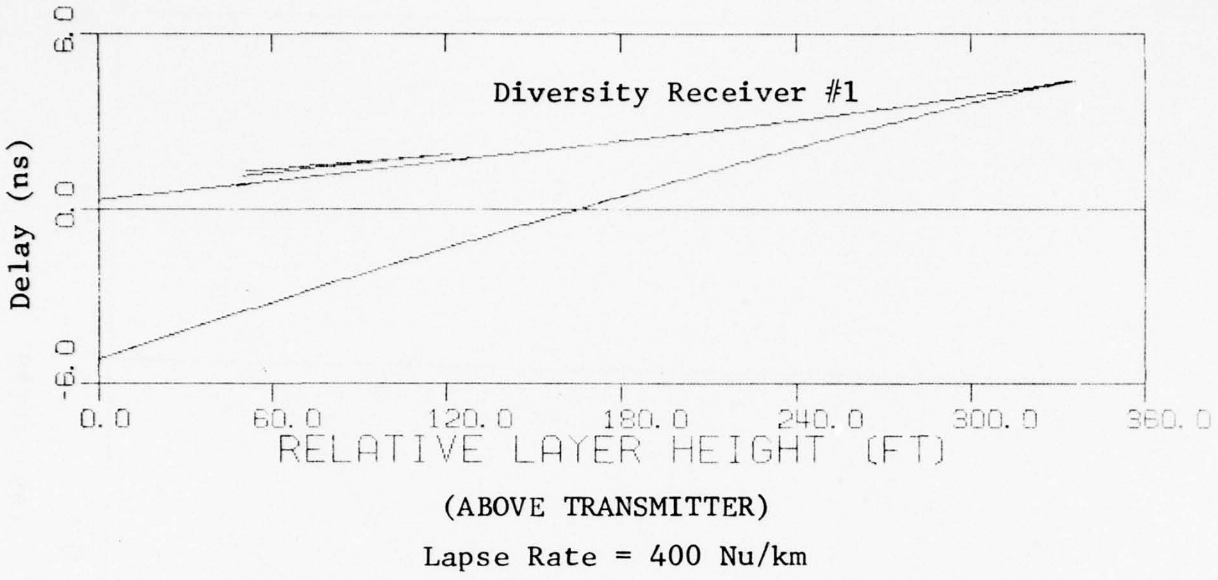

Figure 2.38 Multipath Delay Profile on Swingate-Houtem Link for a Horizontal Layer

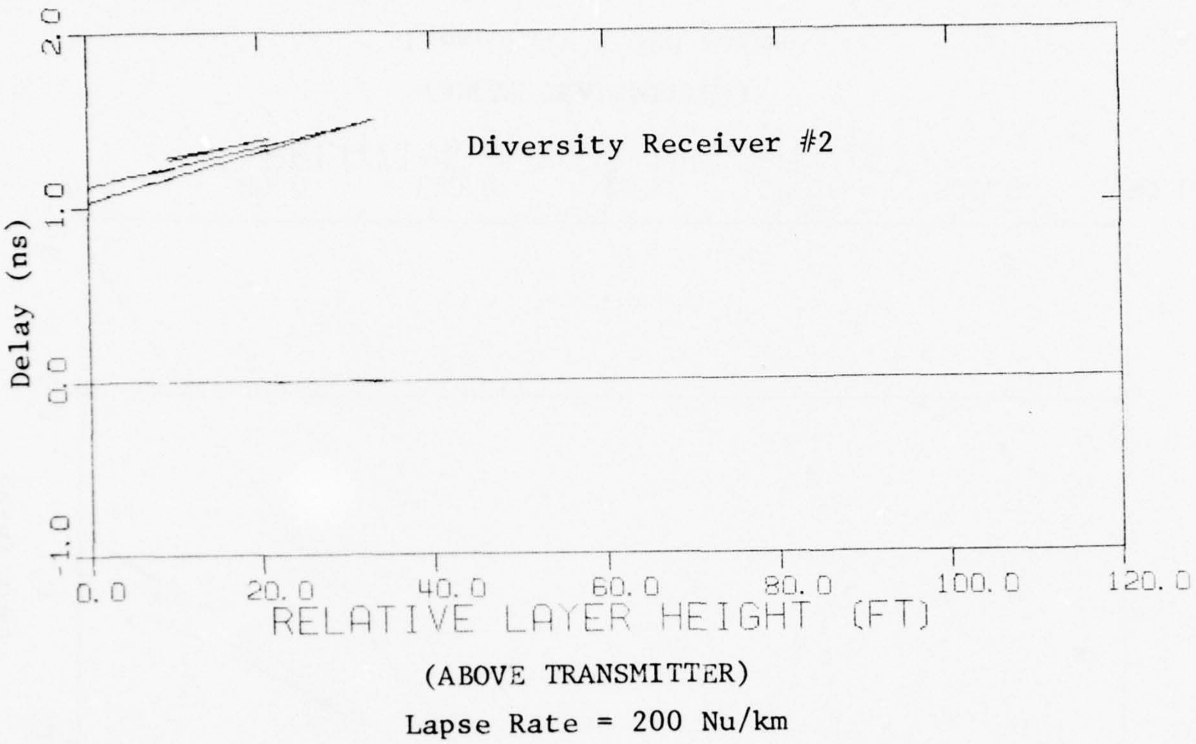

Figure 2.39 Multipath Delay Profile on Swingate-to-Houtem Link for a Horizontal Layer

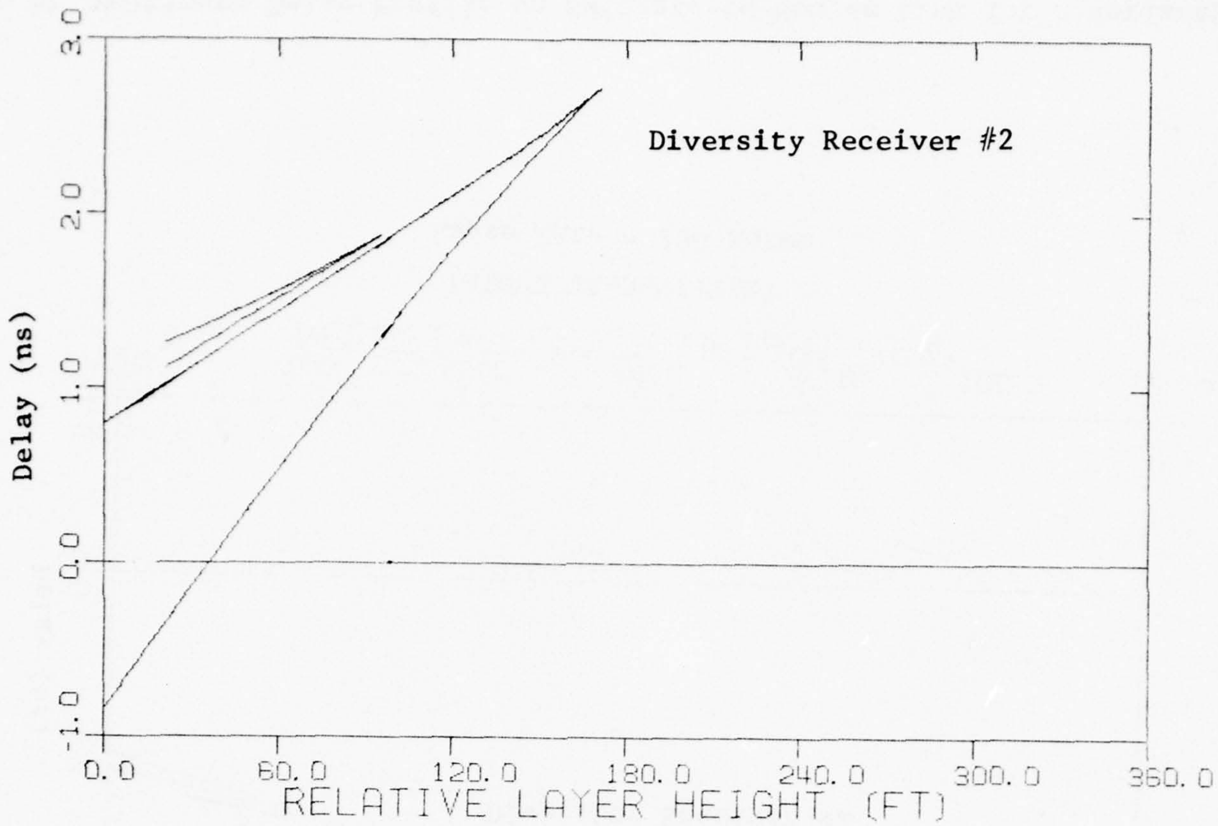

(ABCVE TRANSMITTER)

Lapse Rate = 300 Nu/km

Figure 2.40 Multipath Delay Profile on Swingate-to-Houtem Link for a Horizontal Layer

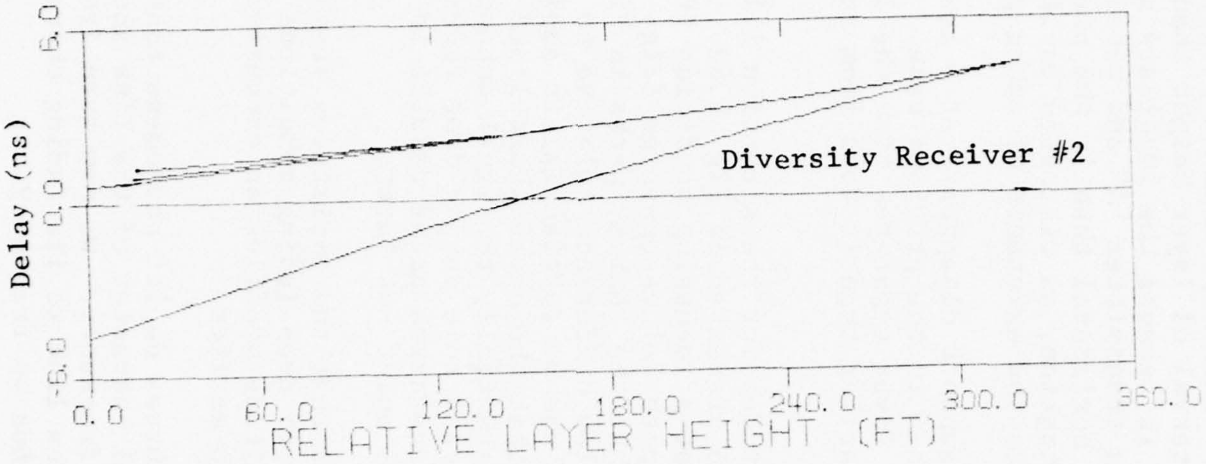

(ABOVE TRANSMITTER)

Lapse Rate = 400 Nu/km

Figure 2.41 Multipath Delay Profile on Swingate-to-Houtem Link for a Horizontal Layer

Similar trends are evident in Figs. 2.39 - 2.41 which show the effects on diversity channel #2 (receiver at relative height of 17 feet) which is closer to the transmitter height. Two basic differences are observable, however. These are:

1) The "extra" multipath rays exist over a more substantial interval of layer height than previously. This is because the imaginary straight line connecting transmitter "A" and receiver "B" is more nearly horizontal than in the previous case. This situation, as discussed earlier, is more amenable to the existence of extra paths.

2) The multipath support disappears at a lower layer height than in the previous case. This is because the layer separates from the lower receiver "B" earlier than it does from receiver "A".

The ray path amplitudes for the situation illustrated earlier in Fig. 2.37 are presented in Fig. 2.42. Comparing the two figures, we note that a focussing condition (Fig. 2.42) takes place as the ray path delays converge (Fig. 2.37). Additionally, we note that the "extra" paths in Fig. 2.37, though negligible in delay difference relative to the more enduring multipath rays can be substantial in amplitude. The implication of this is that the extra short-lined multipath rays can contribute substantially to signal enhancement but only rarely play any significant role during deep fades. In fact, the disappearance of these extra paths results in discontinuities of fade level as we will point out later.

Because of the fact that the amplitudes seem to play less of a role as indicators of deep fading conditions we have chosen not to display the amplitude profiles as extensively as the delay profiles presented earlier.

All of the above curves depict phenomena that depend strictly on the physical character of the link and its geometry. None of them depend on frequency. We now turn from the physical character of the link to its fading character. This latter, of course, depends on frequency.

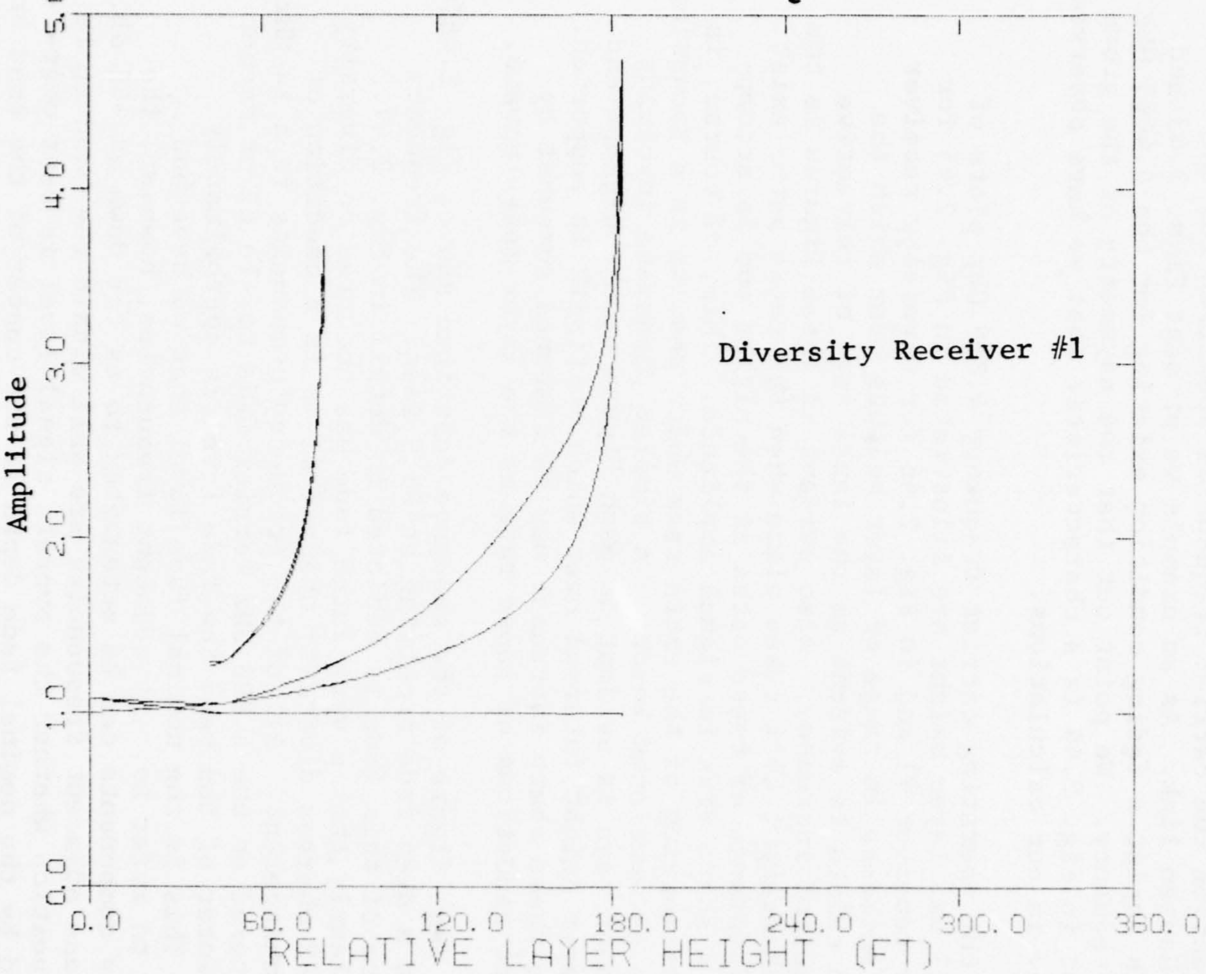

(ABOVE TRANSMITTER)

Lapse Rate = 300 Nu/km

Figure 2.42 Amplitude Profile on Swingate-Houtem Link for a Horizontal Layer

In order to be fair and not over-emphasize the most serious cases of signal degradation [obtained by using (2.156) to locate the frequencies at which the deepest fades occur] we have assumed for most of the calculations presented in the remainder of this section the carrier frequencies specified for the Swingate-Houten link. As an example we present Figs. 2.43 and 2.44 which depict a fading condition existing for the 4.4465 GHz carrier frequency. We point out that the asymmetry of the group delay plot in Fig. 2.44 is a characteristic that we have observed repeatedly in our calculations.

For the operating carrier frequency 4.808 GHz plots of fade level vs. layer height are illustrated in Fig. 2.45 for diversity receiver #1 and in Fig. 2.46 for diversity receiver #2. The increase in range of layer heights over which the multipath exists is evident as the lapse rate of refractive index gradient increases. Also evident in these figures is the signal enhancement that takes place when the extra paths exist. The disappearance of these paths at the higher end is accompanied by a sharp rise in signal amplitude. This, of course, is due to the merging of the extra rays which results in a focussing condition as mentioned before. A similar phenomena involving the dominant rays is evident in each figure at the highest end of the layer height interval over which multipath is supported. In nature these sharp increases may be dampened somewhat by concurrent reductions of lapse rate as the layer moves upward.

The last figure of the sequence described above, Fig. 2.46(c) indicates a deep fade occurring at 65.9 feet. The frequency dependence of this fade is depicted in detail in Fig. 2.47. We see clearly that a very large fade has occurred on diversity channel #2 whereas diversity channel #1 is in a condition of signal enhancement. All of the frequency components in a 14 MHz band centered on the 4.808 GHz carrier fade to -16 dB or deeper. At the center of the band the fade level is approximately -30 dB. This is the nominal fade level that we have had occasion to refer to. At adjacent frequencies, however, the frequency components can be attenuated to as far down as -45 dB. Since these adjacent frequencies are well within the band it is a moot question whether the overall signal level is best characterized by the nominal fade depth at the center of the band or by the behavior at some adjacent frequency. In any event the fading is characterized by a higher degree of frequency selectivity.

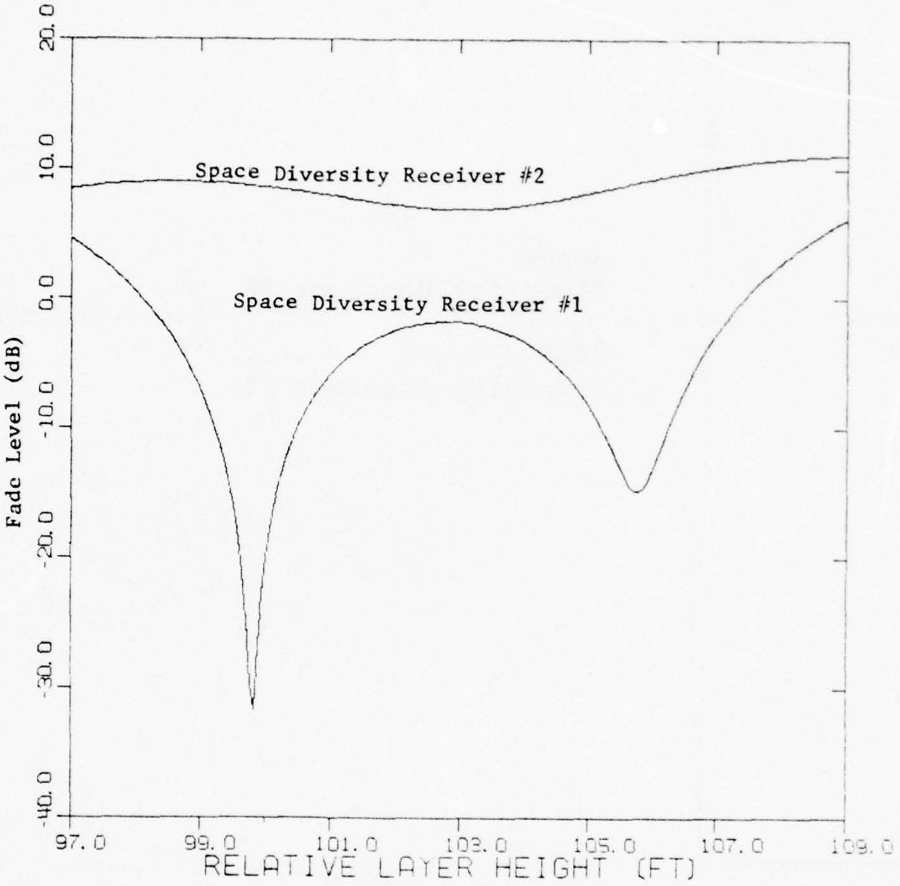

(ABOVE TRANSMITTER)

Lapse Rate = 300 Nu/km

Carrier Frequency = 4.4465

Figure 2.43 Fade Level Vs. Layer Height for Swingate-Houtem Link (Horizontal Layer)

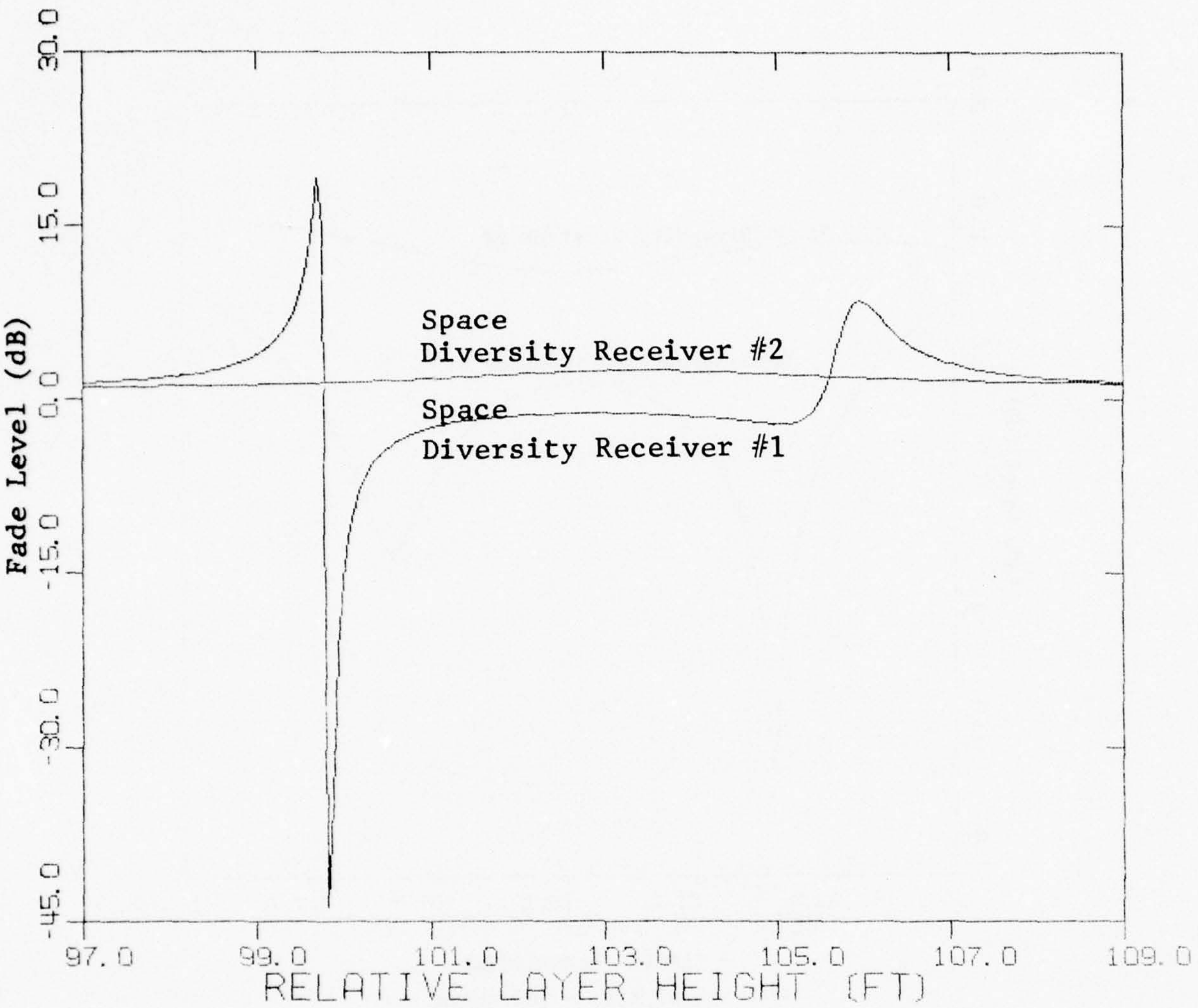

(ABOVE TRANSMITTER)

Lapse Rate = 300 Nu/km

Carrier Frequency = 4.4465

Figure 2.44 Fade Level Vs. Layer Height for Swingate-Houtem Link (Horizontal Layer)

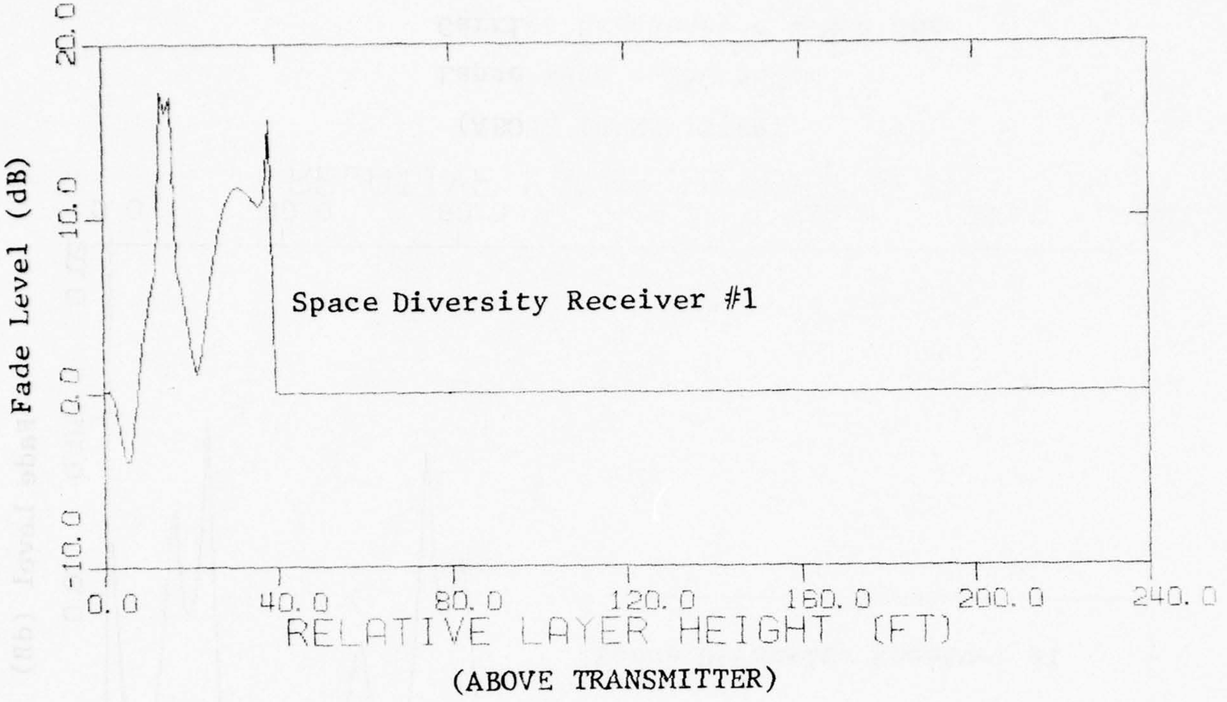

Lapse Rate = 200 Nu/km

Carrier Frequency = 4.808 GHz

Figure 2.45(a) Fade Level Vs. Layer Height for Swingate-Houtem Link (Horizontal Layer)

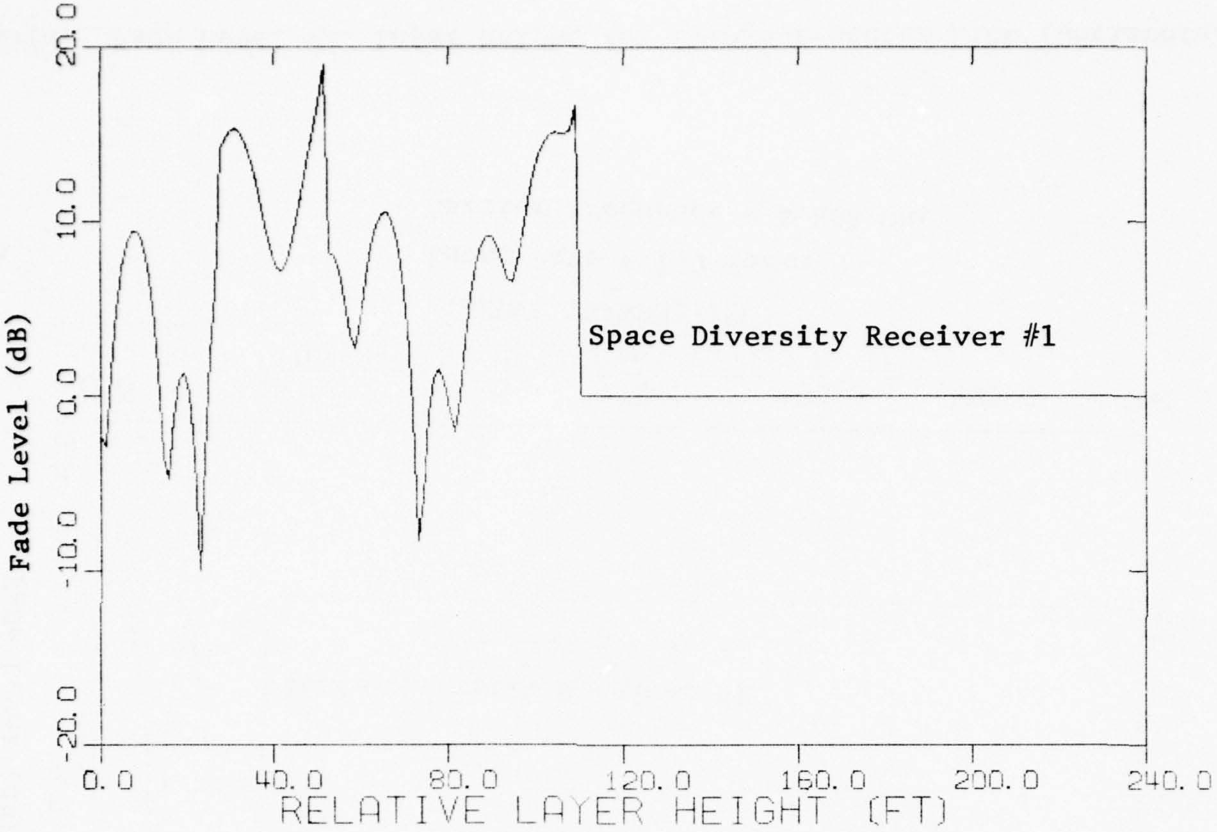

(ABOVE TRANSMITTER)

Lapse Rate = 250 Nu/km

Carrier Frequency = 4.808 GHz

Figure 2.45(b) Fade Level Vs. Layer Height for Swingate-Houtem Link (Horizontal Layer)

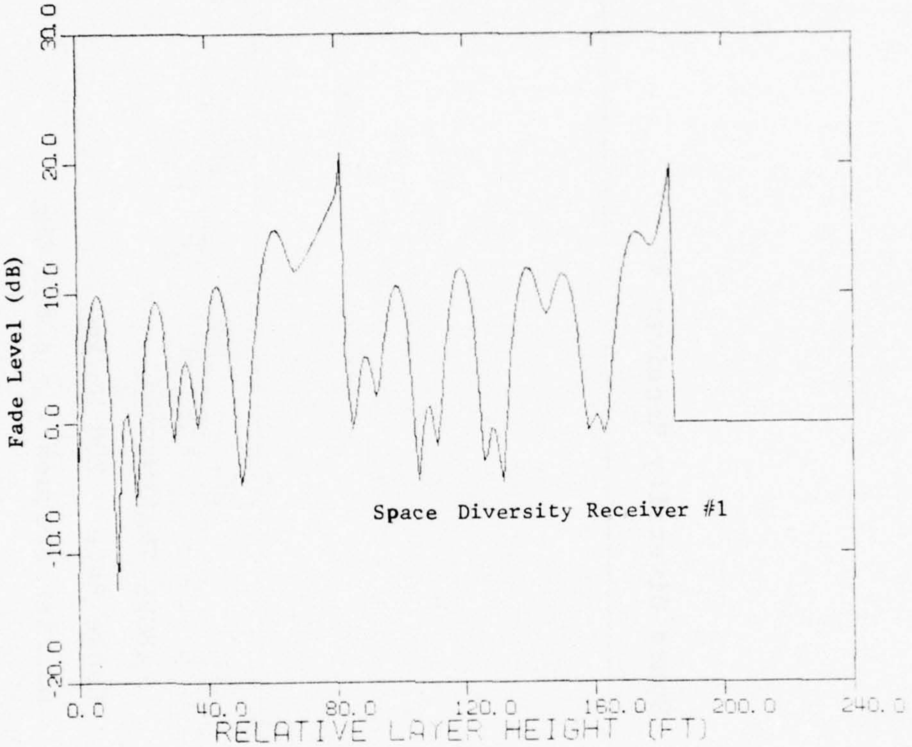

(ABOVE TRANSMITTER)

Lapse Rate = 300 Nu/km

Carrier Frequency = 4.808 GHz

Figure 2.45 (c) Fade Level Vs. Layer Height for Swingate-Houtem Link (Horizontal Layer)

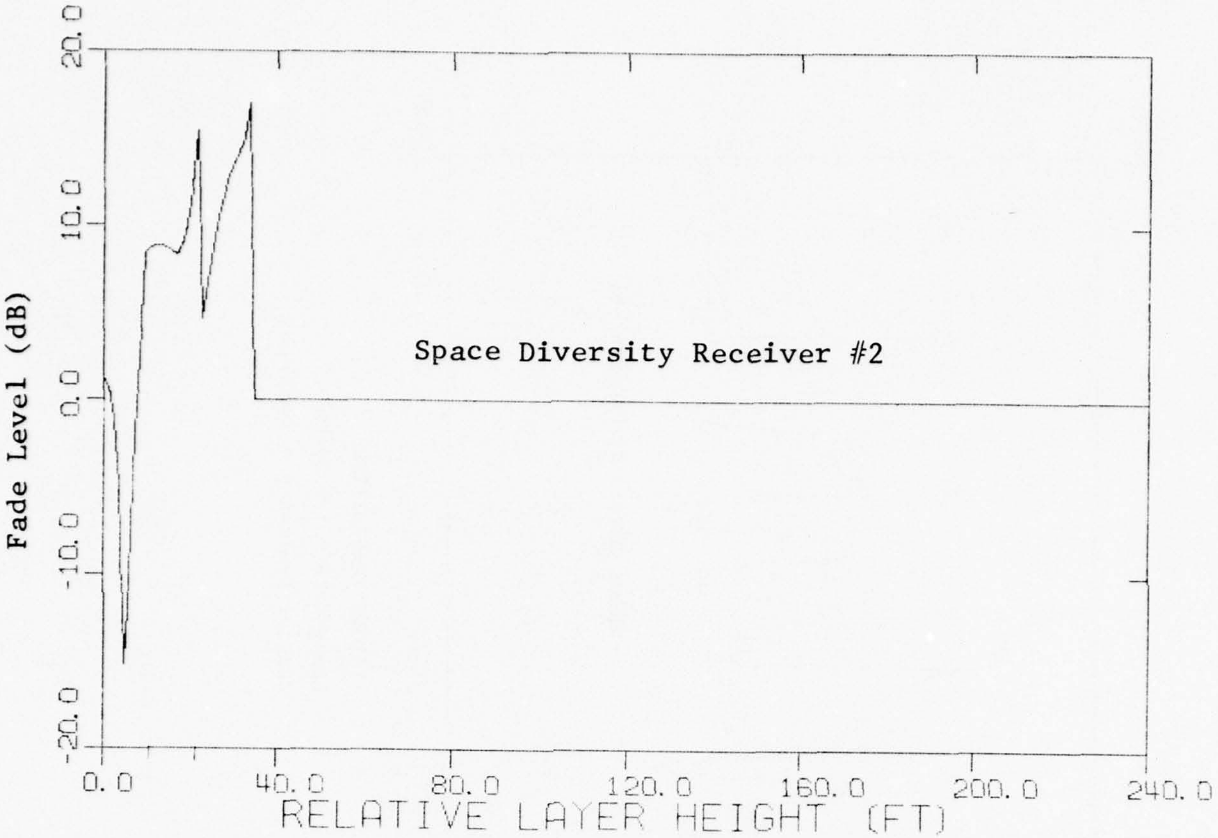

(ABOVE TRANSMITTER)

Lapse Rate = 200 Nu/km

Carrier Frequency = 4.808 GHz

Figure 2.46(a) Fade Level Vs. Layer Height for Swingate-Houtem Link (Horizontal Layer)

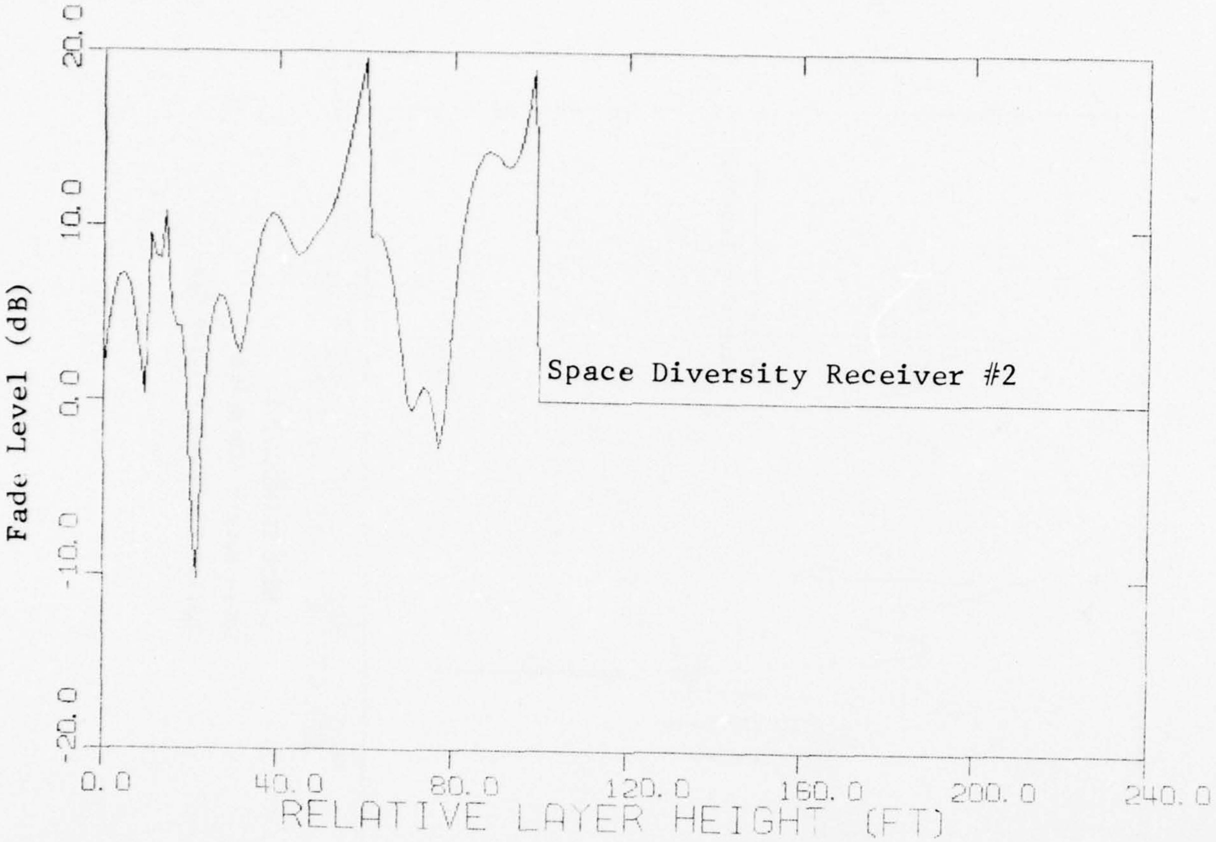

(Above Transmitter)

Lapse Rate = 250 Nu/km

Carrier Frequency = 4.808 GHz

Figure 2.46(b) Fade Level Vs. Layer Height for Swingate-Houtem Link (Horizontal Layer)

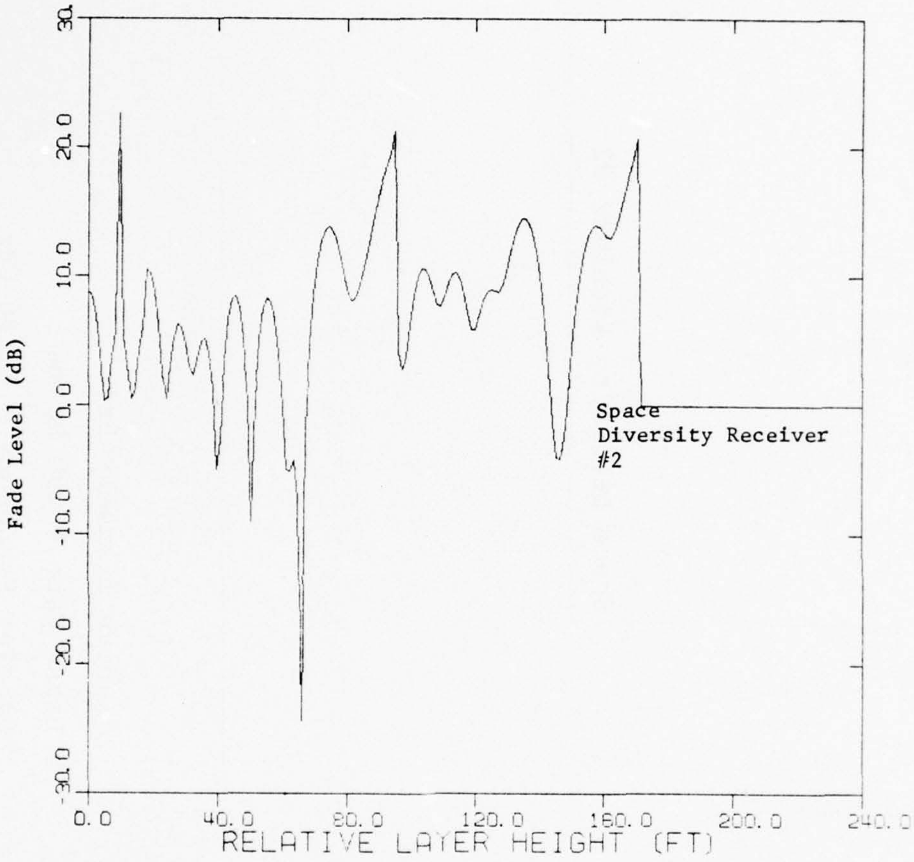

(ABOVE TRANSMITTER)

Lapse Rate = 300 Nu/km

Carrier Frequency = 4.808 GHz

Figure 2.46 (c) Fade Level Vs. Layer Height for Swingate-Houtem Link (Horizontal Layer)

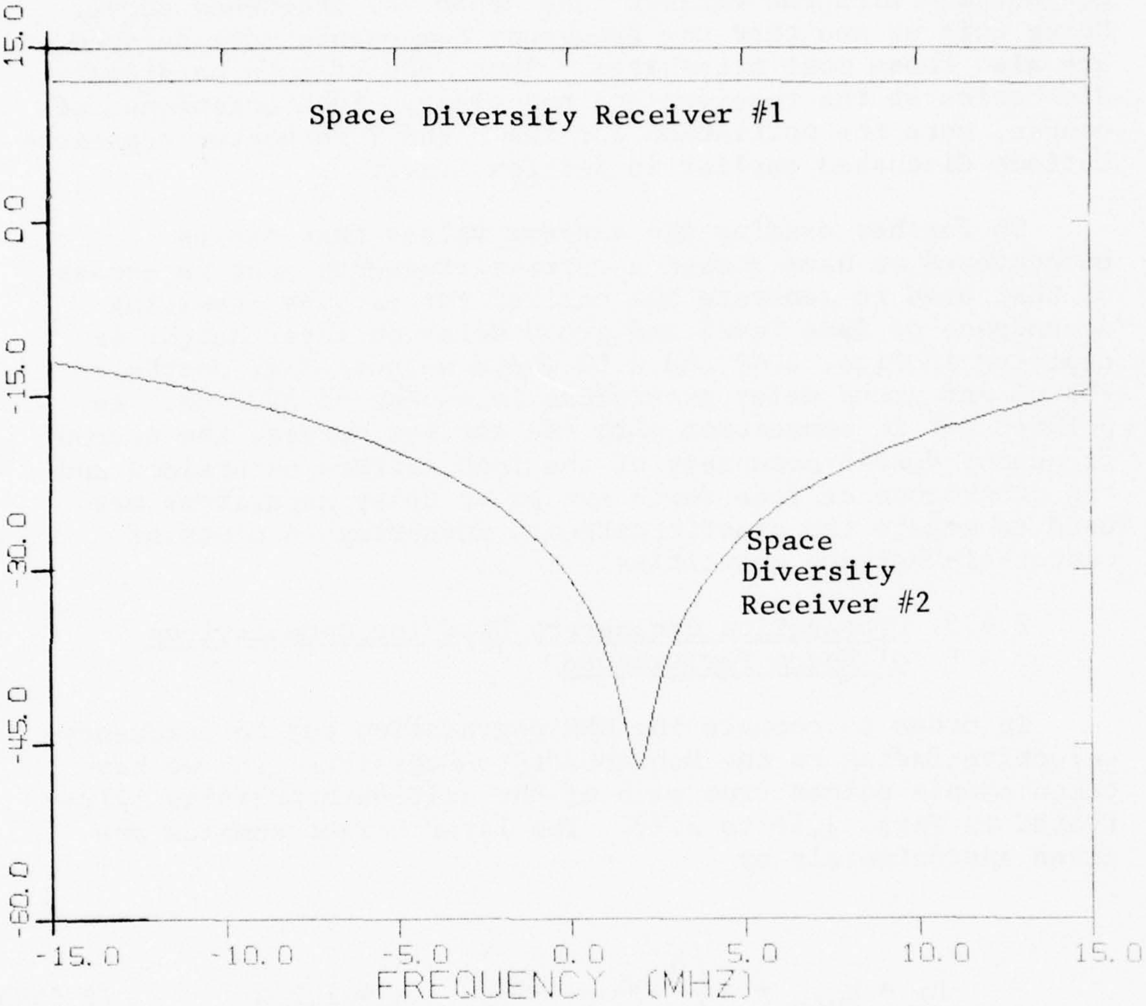

Lapse Rate = 300 Nu/km

Carrier Frequency = 4.808 GHz

Layer Height = 65.9 Feet

Figure 2.47 Fade Level Vs. Frequency for Swingate-Houtem Link (Horizontal Layer)

The forementioned frequency selectivity is also apparent in the plot of group delay vs. frequency in Fig. 2.48. We see that extreme excursions are possible within the band. The extremely large group delay excursions must be considered in conjunction with the earlier fade depth vs. frequency curve. Doing this we see that the frequency components most delayed are also those most attenuated. Thus, the effects on signal distortion at the receiver are not clear. Such questions, of course, were the motivation for the P and T parameter representations discussed earlier in Section 2.3.2.

To further examine the extreme values that can be encountered we have chosen a carrier frequency just in excess of that used to generate the earlier curves. The resulting dependence of fade level and group delay on layer height is depicted in Figs. 2.49 and 2.50 where we note fade depths to -63 dB and group delay excursions in excess of 2000 ns. As pointed out in connection with the earlier curves, the narrow frequency domain occupancy of the most extreme excursions and the congruence of fade depth and group delay excursions may tend to negate the drastic extremes appearing in plots of center-of-the-band quantities.

2.4.3 Propagation Parameters Used for Computations of Modem Performance

In order to compute the SNR degradation due to frequency-selective fading on the Hohenstadt-to-Zugspitze link we have taken sample points from each of the multipath profiles illustrated in Figs. 2.16 to 2.18. The layer height samples are given approximately by

$$h_L = h_{min} + n\left(\frac{h_{max} - h_{min}}{4}\right) \qquad n = 1,2,3 \qquad (2.177)$$

where h_{min} is the smallest layer height resulting in multipath for a given layer tilt and h_{max} is the largest. This scheme is illustrated in Fig. 2.51 where we have numbered the cuts according to the value of n in (2.177). This numbering, accompanied by the exact layer heights involved, also appears on the error rate curves to be presented later in this report.

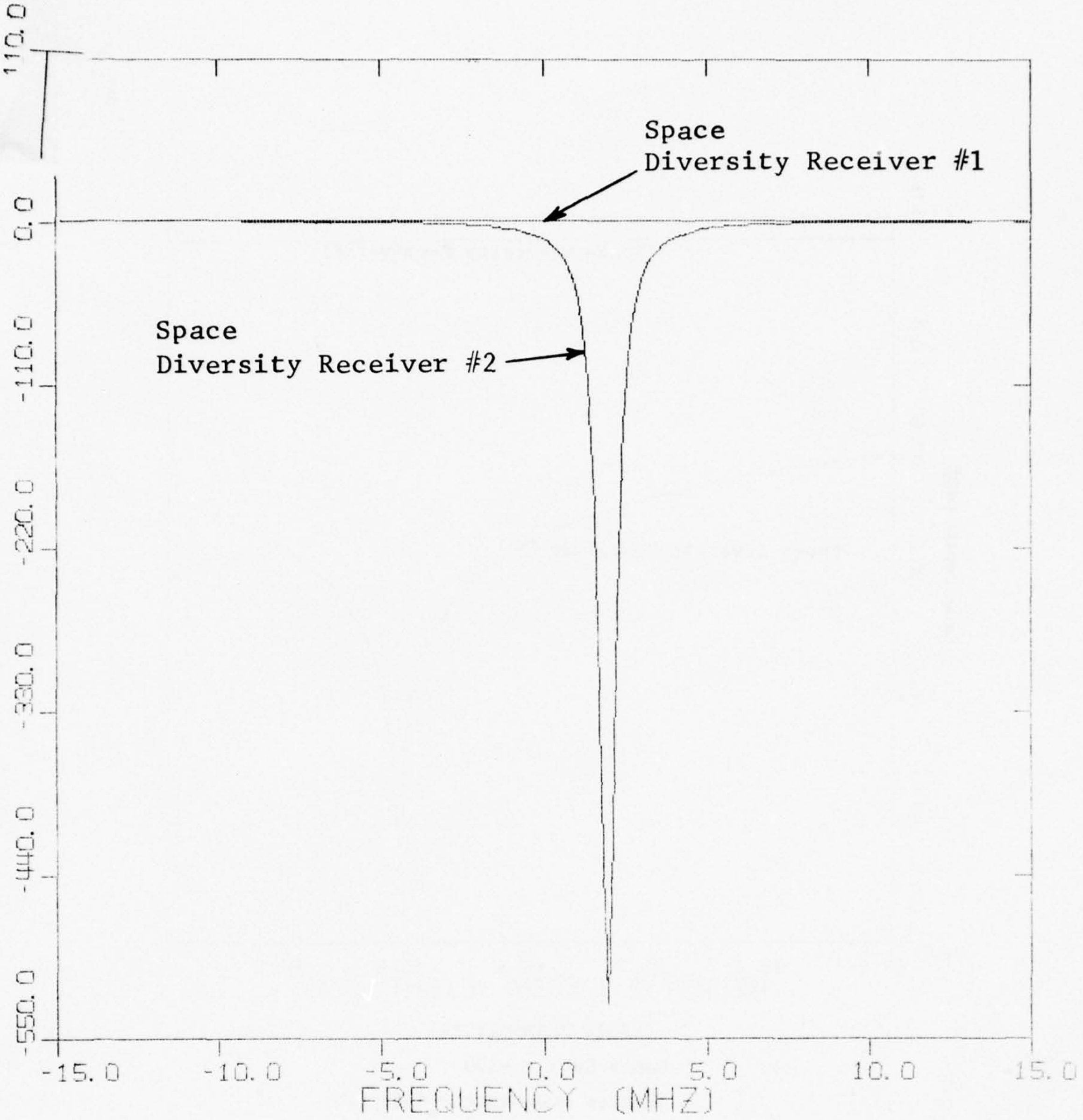

Lapse Rate = 300 Nu/km

Carrier Frequency = 4.808 GHz

Layer Height = 65.9 Feet

Figure 2.48 Group Delay Vs. Frequency for Swingate-Houtem Link (Horizontal Layer)

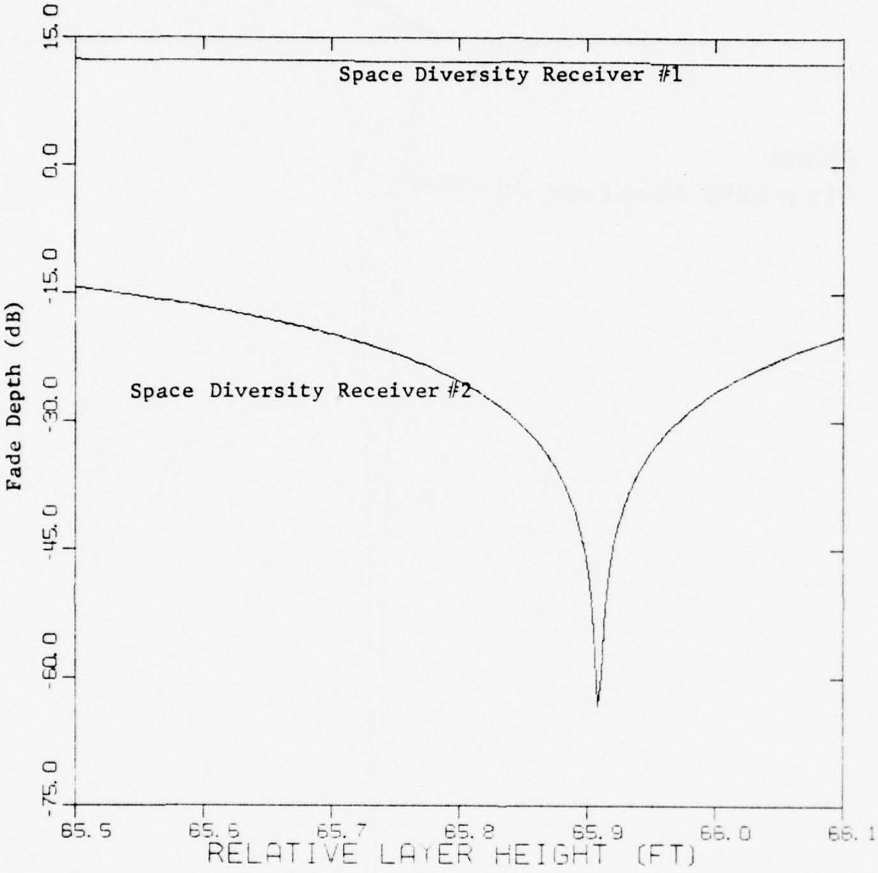

(ABOVE TRANSMITTER)

Lapse Rate = -300

Carrier Frequency = 4.81 GHz

Figure 2.49 Fade Depth Vs. Layer Height on Swingate-Houtem Link (Horizontal Layer)

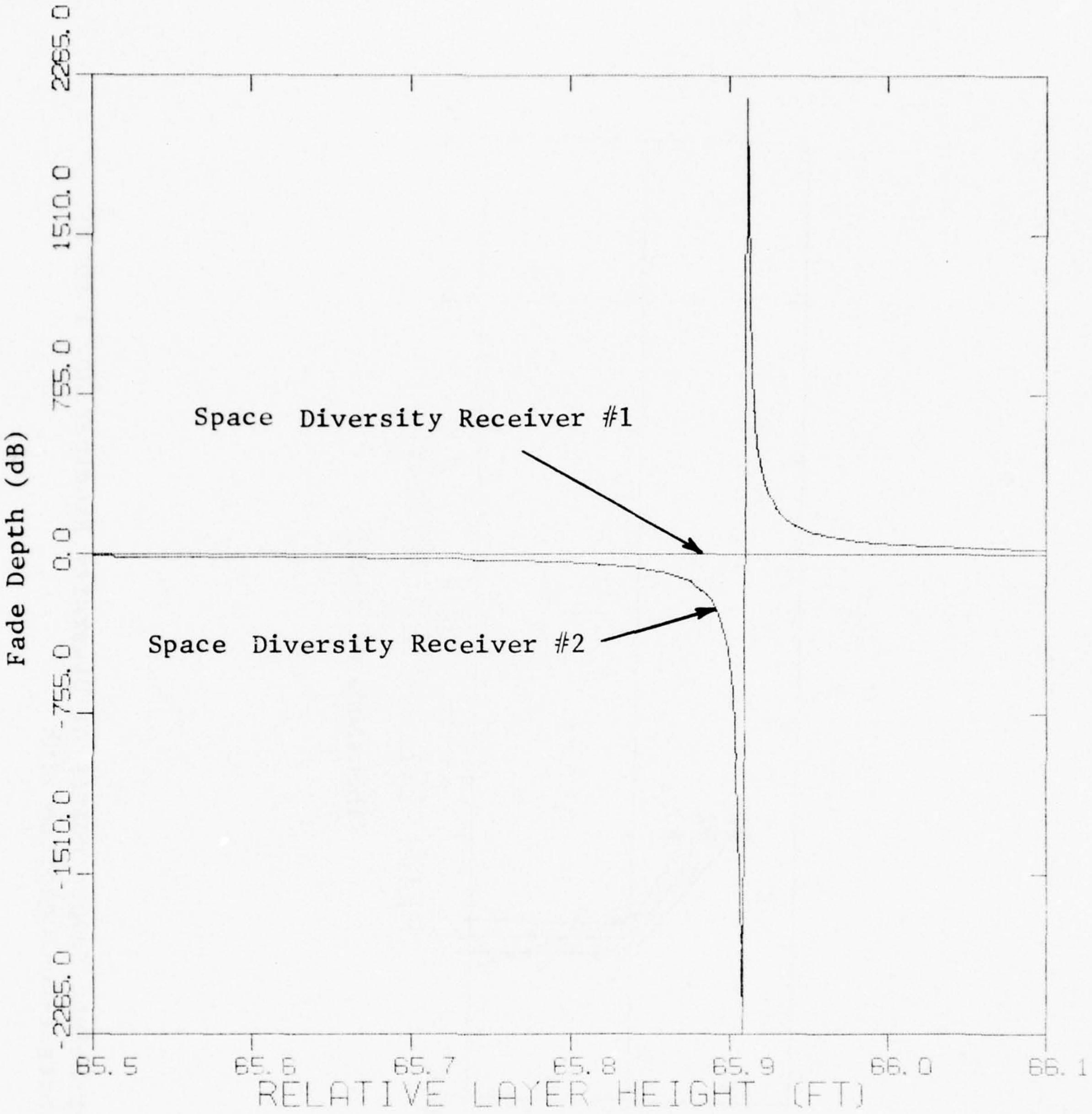

(ABOVE TRANSMITTER)

Lapse Rate = -300

Carrier Frequency = 4.81 GHz

Figure 2.50 Fade Depth Vs. Layer Height on Swingate-Houtem Link (Horizontal Layer)

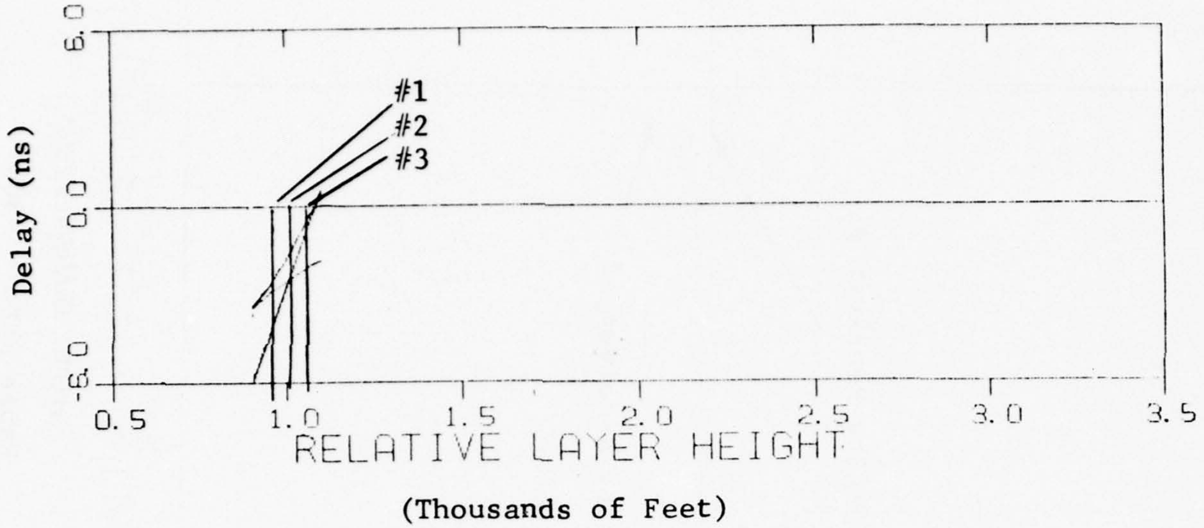

Figure 2.51 Layer Height Sample Points of Diversity Receiver No. 1 on the Hohenstadt-to-Zugspitze Link

Extensive computer simulations of the DAU modem and IF modem operating over the channel described above have been carried out using the simulation software developed under this contract. This software is based upon the frequency power series model of the multipath channel and uses the distortion parameters p_1, p_2, and p_3 (see Section 2.3.2) to characterize the distortion in the discriminator output. The SNR degradation due to frequency-selective fading is the topic of Section 3.

Before presenting performance results we briefly summarize the process of identifying channel parameters for simulation. First, for the geometrical parameters we utilize the Hohenstadt-to-Zugspitze specifications described earlier. For the refractive index gradient the values -400, -350, and -300 Nu/km are used; these are in reasonable accord with relevant data [2.6]. For each value of refractive index gradient the layer slopes given in Table 2-3 have been used in the calculations. This results in consideration of 27 distinct channel conditions. Not all combinations of refractive index gradient and layer slope result in multipath, however. All of the multipath profiles resulting from those combinations that do support multipath have been illustrated earlier in this report and have been sampled in the manner illustrated in Fig. 2.51. This approach via the propagation software provides us with the discrete set of amplitudes and delays that have been used in the simulations described in Section 3.

2.5 Comparisons With Experiment

In this section we briefly compare our computed results with experimental data and theoretical conclusions of other workers in the field. Most of our comparisons relate to work done by investigators of the Bell Telephone Company.

Our comparisons with the available literature reveal no significant differences between our computed results and experimental measurements—in fact, the overwhelming impression imparted in such a comparison is that our results show the same physical dependencies as the experimental data.

As an example of the above noted correspondence between experimental results and our computed results we point out that measurements reported by Babler [2.25] show no disagreement, in terms of fundamental numerical values with our computed quantities. In fact, his measured plots of amplitude vs. frequency, bear a striking resemblance to the ones we have calculated. Babler reports on statistical measurements of linear and quadratic distortions of amplitude. The quantities he deals with derive strictly from consideration of signal amplitude and do not include any information on the important frequency variation of phase. Similar limitations apply to the diversity data in [2.26]. As a continuation of the forementioned program, however, the limitations were removed in the work of Subramanian, et al. [2.27] who present fade records in conjunction with records of phase difference. These records (Figures 5 and 6 in [2.27]) bear a close resemblance to the plots of fade level and group delay that we have calculated for links of comparable length, and yield similarly close numerical values.*

The authors of [2.27] conclude their paper with the statement:

> "Although simple two-ray models can be made to account for both amplitude and phase dispersion, the complex temporal behavior indicated in our results along with that reported by Babler lead us to believe that the multi-ray (more than two rays) phenomenon is the cause of these deep fades."

(A two-ray model, of course, would yield a simple sinusoidal dependence on frequency.) The above "belief," in our model, is a direct consequence—one direct path and two layer paths being the most probable situation for condition "A" of Fig. 2.5, (see demonstration of this at the end of Section 2.2.4), and one pseudo-direct path and two layer paths being the standard case for condition "B", [see discussion in connection with the cubic equation (2.65)].

Relative to the importance of frequency-selectivity on microwave LOS links we note that Babler, as previously pointed out by Kaylor [2.28], points out the increased importance of frequency-selectivity during deep fades. This is something that has stood out clearly in the analysis (see Section 2.3.3), and in virtually all of the computations in this report.

---

*By "phase difference" is meant the difference in phase between two tones .55 MHz apart. Though this resolution is suitable for estimates of group delay (frequency derivative of phase) on the link measured in [2.27] the group delay curves shown there are not as sharp as our computed ones.

Another example of the appropriateness of our model relates to the occurrence of signal enhancement. This seems not to have been a major concern (justifiably so) of the BTL workers. Naturally, for a phenomena that doesn't result in signal degradation, there is no profound interest. Nevertheless, the secondary results of a useful propagation model, though of little interest, should correspond with real world results. As pointed out in [2.29] microwave paths that support the formation of ground based atmospheric layers may cause signal enhancement up to 30 dB. We have observed signal enhancements up to 24 dB in the calculation from our model (see Fig. 2.46) and were it not for the limited resolution of these plots (there was no practical motivation for looking at a finer resolution) the enhancements would be slightly larger. Relative to occurrence of fades we point out that Barnett's conclusion [2.30] that the probability of deep multipath fading is linear in frequency is in keeping with ours that the spatial rate of fading is linear in frequency (see discussion in Section 4.1 following), i.e., that the higher frequencies will yield proportionately higher a number of layer heights at which deep fading will occur.

We now turn to the work of Ruthroff [2.31] whose attempt to analyze refractive multipath was the forerunner of our own. It is easy to point out the limitations of pioneering work. As an example, we point out that some simplifying assumptions about link geometry were made (e.g., transmitter and receiver antenna heights were assumed to be equal). Additionally, and perhaps more importantly, a determination of ray path amplitudes was not attempted [an absolute requirement of system function modeling as evident from Eq. (2.119)]. It is, no doubt, because of this last limitation that the author makes the following erroneous supposition:

> "In the present model the amplitudes of the signals received via the refracted rays are nominally equal to the amplitude of the signal received in the absence of the refracting layer."

This is equivalent to assuming the α_i in (2.119) are all of value unity. We have found this not to be the case and have uncovered substantial physical reasons why it should not be the case. Our analysis indicates that, with high probability, a total of three interfering rays are supported—two within the layer—a third beneath the layer. The very existence of the layer multipath rays indicates that the layer is in a focussing condition (i.e., there is an intersection of ray paths at the terminals). This strongly indicates a signal amplitude above unity. Our calculations reveal invariably that this is the case in a multipath fading situation.

Ruthroff goes on to say:

> "Since the probability of three rays of equal amplitude combining to form a deep fade is much less than the probability of two rays of equal amplitude combining to form a deep fade, we conclude that the distribution of attenuation is dominated by two-ray interference."

This contradicts the conclusion (cited above) of other workers who felt that the complexity of their data could not be explained in two-ray terms, and our detailed analysis which indicates the probable existence of three paths (or more).

SECTION 2

REFERENCES

[2.1] P. Beckmann and A. Spizzichino, The Scattering of Electromagnetic Waves From Rough Surfaces, Pergamon Press, 1963.

[2.2] B. R. Bean and E. J. Dutton, Radio Meteorology, National Bureau of Standards Monograph 92, 1 March 1966.

[2.3] P. A. Bello, J. K. DeRosa, and C. J. Boardman, Line-of-Sight Wideband Propagation, Final Report, Contract No. F30602-73-C-0013, RADC, CNR, Inc., Newton, Mass., May 1973.

[2.4] D. E. Kerr, Propagation of Short Radio Waves, Dover Publications, Inc., New York, 1965.

[2.5] B. R. Bean, et al., "A World Atlas of Atmospheric Radio Refractivity," Essa Monograph No. 1, U.S. Government Printing Office, Washington, D.C., 1966.

[2.6] C. A. Samson, "Refractivity Gradients in the Northern Hemisphere," OT Report 75-59, U.S. Department of Commerce, April 1975.

[2.7] C. A. Samson, "Refractivity and Rainfall Data for Radio Systems Engineering," OT Report 76-105, U.S. Department of Commerce, September 1976.

[2.8] R. W. Hubbard and R. F. Linfield, "Wideband Channel Probe Measurements for the DEB (Stage I) Path Test Program," ITS Report, Boulder, Colorado, April 1976.

[2.9] D. E. Kerr, Ed., Propagation of Short Radio Waves, Dover, 1965, page 203.

[2.10] D. E. Kerr, Ed., Propagation of Short Radio Waves, Dover, 1965, page 220.

[2.11] D. E. Kerr, Ed., Propagation of Short Radio Waves, Dover, 1965, page 260.

[2.12] K. Bullington, "Phase and Amplitude Variations in Multipath Fading of Microwave Signals," BSTJ, Vol. 50, No. 6, July - August 1971, pp. 2039 - 2053.

[2.13] "Line-of-Sight Techniques Investigation," Final Report by CNR, Inc., on RADC Contract No. F30602-73-C-0244, (AD006104).

[2.14] M. S. Wong, "Refraction Anomalies in Airborne Propagation," Proc. of the IEEE, Vol. 46, September 1958, pp. 1628 - 1638.

[2.15] L. H. Doherty, "Geometric Optics and the Field at a Caustic," Ph.D. Dissertation, Department of Electrical Engineering, Cornell University, Ithaca, New York, 1952.

[2.16] G. A. Deschamps, "Ray Techniques in Electromagnetics," Proc. of the IEEE, Vol. 60, No. 9, September 1972, pp. 1022 - 1035.

[2.17] E. E. Gossard, "The Reflection of Microwaves by a Refractive Layer Perturbed by Waves," IEEE Trans. on Antennas and Propagation, May 1962, pp. 317 - 325.

[2.18] D. E. Kerr, Propagation of Short Radio Waves, Dover, 1965, page 263.

[2.19] P. A. Bello, "Characterization of Random Time-Variant Linear Channels," IRE Trans. on Communication Systems, Vol. CS-11, December 1963, pp. 360 - 393.

[2.20] S. H. Lin, "Statistical Behavior of a Fading Signal," BSTJ, December 1971, pp. 3211 - 3270.

[2.21] P. A. Bello and B. D. Nelin, "The Effect of Frequency-Selective Fading on Intermodulation Distortion and Subcarrier Phase Stability in FM Systems," IEEE Trans. on Communication Systems, Vol. CS-12, No. 1, March 1964, pp. 87 - 101.

[2.22] P. A. Bello, et al., "Adaptive Channel Measurement Study," Final Report by CNR, Inc., Prepared for Rome Air Development Center, Under Contract F30602-74-C-0283, March 1975.

[2.23] S. Zebrowitz, "The Use of Multiple Diversity to Minimize the Effects of Ducting on a Long Microwave Path," Aeronautic Ford Corp., Willow Grove, Pennsylvania.

[2.24] K. H. Lewis, "Delay Line Requirements for Houtem-Swingate Link (Scope Communications)," Radio System Branch, 1842 Electronics Engineering Group, 15 August 1976, AD A030416.

[2.25] G. M. Babler, "A Study of Frequency-Selective Fading for a Microwave Line-of-Sight Narrowband Radio Channel," BSTJ, Vol. 51, No. 3, March 1972.

[2.26] G. M. Babler, "Selectivity Faded Nondiversity and Space Diversity Narrowband Microwave Radio Channels," BSTJ, Vol. 52, No. 2, February 1973.

[2.27] M. Subramanian, et al., "Phase Dispersion Characteristics During Fade in a Microwave Line-of-Sight Radio Channel," BSTJ, December 1973.

[2.28] R. L. Kaylor, "A Statistical Study of Selective Fading of Super-High Frequency Radio Signals," BSTJ, September 1953.

[2.29] "Experimental Analysis of Cross-Polarized Signals at 8 GHz," RADC Report, November 1975.

[2.30] W. T. Barnett, "Multipath Propagation at 4, 6, and 11 GHz," BSTJ, February 1972.

[2.31] C. L. Ruthroff, "Multiple-Path Fading on Line-of-Sight Microwave Radio Systems as a Function of Path Length and Frequency," BSTJ, Vol. 50, No. 7, pp. 2375 - 2398, September 1971.

SECTION 3

SNR DEGRADATION DUE TO FADING

3.1 Receiver Modeling for Performance Evaluation

3.1.1 Introduction

In Section 2.3 we presented the frequency power series (T parameters) model for the propagation channel. From this we derived the p-parameter representation for receiver output waveforms. This representation may be expressed in terms of either frequency or phase. In the first case it takes the form

$$\dot{\theta}(t) = \dot{\varphi}(t) + p_1\ddot{\varphi}(t) + p_2\dddot{\varphi}(t) + p_3\dot{\varphi}(t)\ddot{\varphi}(t) \qquad (3.1)$$

where $\dot{\varphi}(t)$ is proportional to the input frequency and $\dot{\theta}(t)$ to the output frequency. In the second case we have

$$\theta(t) = \varphi(t) + p_1\dot{\varphi}(t) + p_2\ddot{\varphi}(t) + \frac{1}{2}\, p_3\dot{\varphi}^2(t) \qquad (3.2)$$

where $\varphi(t)$ is the input phase and $\theta(t)$ the output phase. In this section we will use the p-series model to calculate performance of two modems. The first is a baseband modem operating with conventional FM radios; for this application the form of Eq. (3.1) will be used. The second is a narrow band phase-continuous FSK modem; detection in this modem is based on phase measurement so the form of Eq. (3.2) will be used.

Before proceeding to discuss the two modems, it is appropriate to indicate the approach which will be used to evaluate performance in the presence of distortion. In essence, we will consider a sequence of symbols consisting of the symbol to be detected plus any adjoining symbols which contribute to intersymbol interference. For each of the many possible sequences, the error probability will be evaluated numerically. The final step will be to average these results to find the true average error probability. This procedure is, of course, different from a true simulation in which samples of the actual waveform are generated, processed through a mathematical model of the channel and receiver, and errors counted. The disadvantage of the latter approach is that only high error rates may be obtained, since inordinately long runs would be required to observe low error rates. Thus, the approach to be used will facilitate calculation of low error rates which could not be obtained with a true simulation. This is a valuable property in the analysis of line-of-sight modems where the performance goal is a bit error rate of 5×10^{-9}.

3.1.2 Baseband Modem

3.1.2.1 Operation in the Absence of Distortion

The DAU modem supplies a quaternary baseband waveform for an FM transmitter. This waveform consists of a sequence of band-limited pulses modulated by quaternary symbols. Referring to Fig. 3.1, we may write the baseband waveform as

$$x(t) = \sum_{-\infty}^{\infty} a_k h_X(t - kT) \qquad a_k \epsilon \left\{\pm \frac{a}{3}, \pm a\right\} \tag{3.3}$$

In terms of the transmitted energy per bit E_b and symbol duration T, the FM modulated signal in complex notation may be written

$$2\sqrt{\frac{E_b}{T}}\; e^{j2\pi\delta \int^{t} x(\tau)\, d\tau} \tag{3.4}$$

The basic pulse waveform used in this modem is:

$$h_X(t) = \frac{1}{2\pi} \frac{\frac{1}{2}\sin\left(\frac{\pi t}{2T}\right) + \frac{t}{T}\cos\left(\frac{3\pi t}{2T}\right)}{\left(\frac{t}{T}\right)\left[\frac{1}{4} - \left(\frac{t}{T}\right)^2\right]} \tag{3.5}$$

with transform

$$H_X(\omega) = \begin{cases} T & |\omega| \leq \frac{\pi}{2T} \\ \frac{T}{\sqrt{2}}\sqrt{1 + \sin |\omega|\, T} & \frac{\pi}{2T} \leq |\omega| \leq \frac{3\pi}{2T} \\ 0 & |\omega| \geq \frac{3\pi}{2T} \end{cases} \tag{3.6}$$

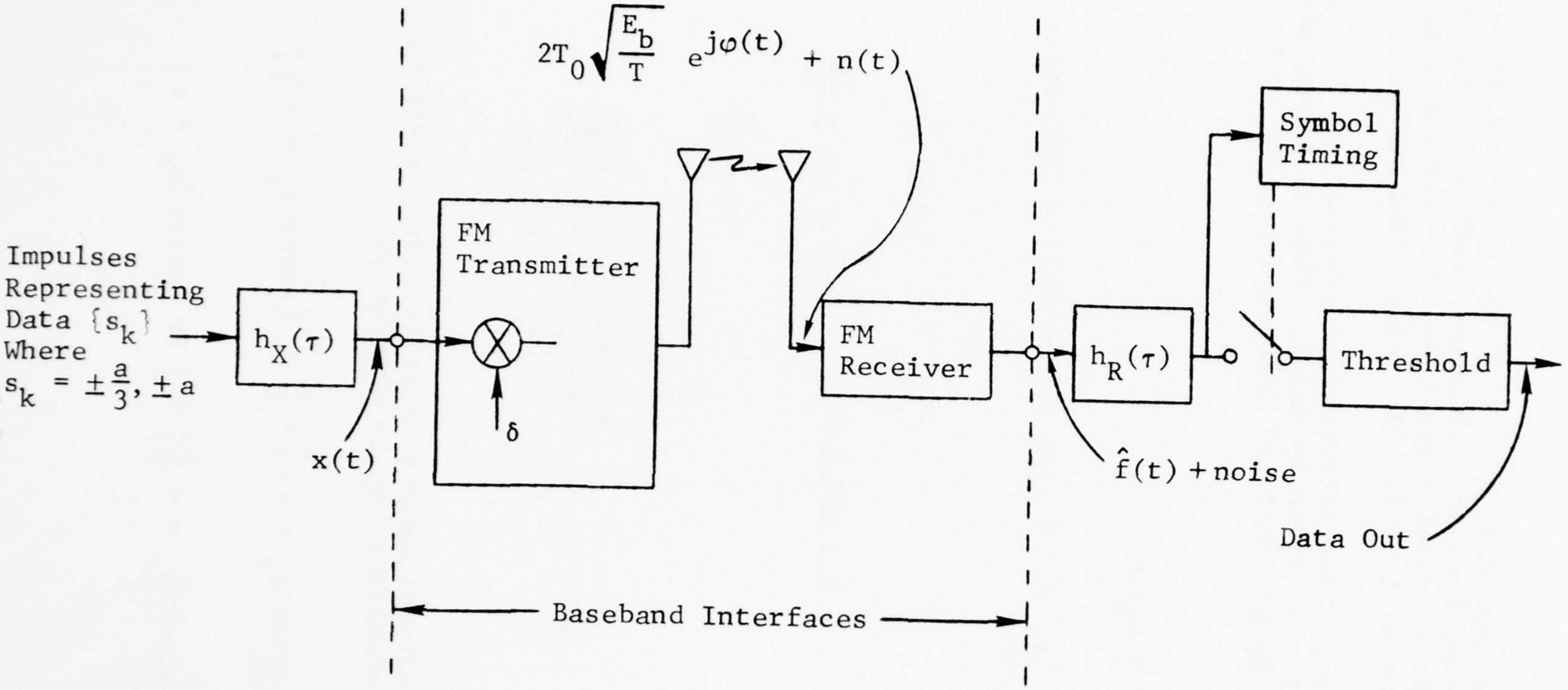

Figure 3.1 Block Diagram of DAU Modem Signal Processing Operations

We will adjust the amplitude a so that the peak instantaneous value of x(t) (taking into account pulse overlap for the worst-case symbol sequence) is unity and hence the peak instantaneous frequency deviation will be δ; this value turns out to be $a = 0.685$.

At the receiver, the instantaneous frequency at the output of the discriminator is given by $\delta x(t)$. This is passed through a receiver filter $H_R(\omega)$ identical (except for gain) to the transmit filter:

$$H_R(\omega) = \frac{1}{T} H_X(\omega) \tag{3.7}$$

In cascade, $H_X(\omega)$ and $H_R(\omega)$ give the so-called "50% roll-off" bandlimited waveform:

$$G(\omega) = H_X(\omega) H_R(\omega) = \begin{cases} T & |\omega| \le \frac{\pi}{2T} \\ \frac{1 + \sin |\omega| T}{2} & \frac{\pi}{2T} \le |\omega| \le \frac{3\pi}{2T} \\ 0 & |\omega| \le \frac{3\pi}{2T} \end{cases} \tag{3.8}$$

$$g(t) = h_X(t) * h_R(t) = \frac{\sin \pi \left(\frac{t}{T}\right)}{\pi \left(\frac{t}{T}\right)} \; \frac{\cos \left(\frac{\pi t}{2T}\right)}{1 - \left(\frac{t}{T}\right)^2} \tag{3.9}$$

In a quaternary modem with equally likely symbols, the average error probability may be written as

$$P_e = \frac{1}{4} \Pr \left\{ \text{error} \,|\, s_k = -a \right\} + \frac{1}{4} \Pr \left\{ \text{error} \,|\, s_k = -\frac{a}{3} \right\}$$

$$+ \frac{1}{4} \Pr \left\{ \text{error} \,|\, s_k = +\frac{1}{3} \right\} + \frac{1}{4} \Pr \left\{ \text{error} \,|\, s_k = a \right\} \tag{3.10}$$

Taking into account the modulation index δ, the proper decision thresholds for the receiver are 0 and $\pm\, 2\delta a/3$. Thus, if y_k is the sampled receive filter output due to signal and n_k the noise component, the probabilities appearing in (3.10) are given by

$$\Pr\left\{\text{error} \mid s_k = -a\right\} = \Pr\left\{y_k + n_k > -\frac{2\delta a}{3} \mid s_k = -a\right\} \tag{3.11}$$

$$\begin{aligned}\Pr\left\{\text{error} \mid s_k = -\frac{a}{3}\right\} &= \Pr\left\{y_k + n_k < -\frac{2\delta a}{3} \mid s_k = -\frac{a}{3}\right\} \\ &\quad + \Pr\left\{y_k + n_k > 0 \mid s_k = -\frac{a}{3}\right\}\end{aligned} \tag{3.12}$$

$$\begin{aligned}\Pr\left\{\text{error} \mid s_k = \frac{a}{3}\right\} &= \Pr\left\{y_k + n_k < 0 \mid s_k = \frac{a}{3}\right\} \\ &\quad + \Pr\left\{y_k + n_k > \frac{2\delta a}{3} \mid s_k = \frac{a}{3}\right\}\end{aligned} \tag{3.13}$$

and

$$\Pr\left\{\text{error} \mid s_k = a\right\} \Pr\left\{y_k + n_k < \frac{2\delta a}{3} \mid s_k = a\right\} \tag{3.14}$$

Recognizing that the noise will be zero-mean and Gaussian, we may combine these equations as

$$\begin{aligned}P_e = \frac{1}{4}\Bigg\{ & Q\left[\frac{-y_k(-a) - \frac{2\delta a}{3}}{\sigma}\right] + Q\left[\frac{y_k\left(-\frac{a}{3}\right) + \frac{2\delta a}{3}}{\sigma}\right] \\ & + Q\left[\frac{-y_k\left(-\frac{a}{3}\right)}{\sigma}\right] + Q\left[\frac{y_k\left(\frac{a}{3}\right)}{\sigma}\right] \\ & + Q\left[\frac{-y_k\left(\frac{a}{3}\right) + \frac{2\delta a}{3}}{\sigma}\right] + Q\left[\frac{y_k(a) - \frac{2\delta a}{3}}{\sigma}\right]\Bigg\}\end{aligned} \tag{3.15}$$

where $Q(x)$ is the probability of a Gaussian exceeding x times the variance:

$$Q(x) = \frac{1}{\sqrt{2\pi}} \int_x^\infty e^{-\frac{t^2}{2}} dt \qquad (3.16)$$

Note also that the argument of y denotes the transmitted symbol s_k.

The response of Eq. (3.9) has the Nyquist property of no intersymbol interference when sampled correctly; that is,

$$g(kT) = \begin{cases} 1 & k = 0 \\ 0 & k \neq 0 \end{cases} \qquad (3.17)$$

Thus, in the absence of channel distortion, the signal component in the receiver output is given simply by

$$y(s_k) = \delta s_k \qquad (3.18)$$

When this is true Eq. (3.15) may be simplified greatly; noting that all the arguments on the right-hand side are identical, it becomes

$$P_e = \frac{3}{2} Q \left(\frac{\delta a}{3\sigma}\right) \qquad (3.19)$$

In calculating the noise variance at the receiver filter output we will use the quadrature approximation. Thus, if n(t) is the complex envelope of the noise in the receiver front-end, the phase noise is given by

$$\frac{\text{Im}\,\{n(t)\}}{2T_0\sqrt{\frac{E_b}{T}}} \qquad (3.20)$$

For a two-sided spectral density of $N_0/2$ watts/Hz, the spectral density of the complex low-pass waveform n(t) is $2N_0$ and that of Im {n(t)} is N_0 so that the density of the phase noise is

$$\frac{N_0 T}{4\,|T_0|^2 E_b} \qquad (3.21)$$

The discriminator output is proportional to instantaneous frequency:

$$\frac{1}{2\pi}\ \frac{d}{dt}\ \frac{\mathrm{Im}\ \{n(t)\}}{2T_0\sqrt{\frac{E_b}{T}}} \tag{3.22}$$

and will have spectral density given by

$$\frac{\omega^2}{(2\pi)^2}\ \frac{N_0 T}{4|T_0|^2\ E_b} \tag{3.23}$$

Thus, the noise variance in the filter output is given by

$$\sigma^2 = \frac{N_0 T}{4(2\pi)^2 |T_0|^2 E_b} \int_{-\infty}^{\infty} \omega^2 |H_R(\omega)|^2 \frac{d\omega}{2\pi} \tag{3.24}$$

Evaluation of this integral using the transfer function of Eq. (3.7) gives the following result

$$\sigma^2 = \frac{N_0}{4(2\pi T)^2 |T_0|^2 E_b} \left(\frac{7\pi^2 - 24}{12}\right) \tag{3.25}$$

Substituting this result into Eq. (3.19) gives the result:

$$P_e = \frac{3}{2} Q \left\{ \left[\frac{0.0555\ (2\pi\delta T)^2\ |T_0|^2\ E_b}{N_0} \right]^{1/2} \right\} \tag{3.26}$$

In evaluating performance, a value of δ must be selected to approximate the value used in the actual modem. This value, which was selected to produce a 99% bandwidth equal to half the bit rate, is somewhat unclear. In making the calculations we have assumed a transmitted bit rate of 27.648 M bit/sec (the highest rate of which the modem is capable) and a peak-to-peak deviation of 8.1 MHz. With this value $2\pi\delta T = 1.85$ and Eq. (3.26) becomes

$$P_e = \frac{3}{2} Q \left\{ \sqrt{\frac{0.190 |T_0|^2 E_b}{N_0}} \right\} \tag{3.27}$$

This gives an error probability of 5×10^{-9} at $|T_0|^2 E_b/N_0 \approx 22.5$ dB (where $|T_0|^2 E_b/N_0$ is the value of E_b/N_0 in a flat fade), which corresponds well with both other predictions and measured results (cf. Fig. 19 of [3.1]).

3.1.2.2 Performance in the Presence of Multipath

We will now consider the process by which performance is calculated in the presence of multipath. Our basic p-parameter model relates the time derivations of input and output phase:

$$\dot{\theta}(t) = \dot{\varphi}(t) + p_1\ddot{\varphi}(t) + p_2\dddot{\varphi}(t) + p_3\dot{\varphi}\,\ddot{\varphi} \tag{3.28}$$

We let $\hat{f}(t)$ denote the signal component of the discriminator output, or $\theta(t)/2\pi$. Making use of the transmitted phase definition of Eq. (3.4), the p-parameter model becomes

$$\hat{f}(t) = \delta[x(t) + p_1\dot{x}(t) + p_2\ddot{x}(t) + 2\pi\delta p_3 x(t)\dot{x}(t)] \tag{3.29}$$

Note that x(t) is given by Eq. (3.3); consequently the derivatives appearing in (3.29) are given by

$$\dot{x}(t) = \Sigma\, a_k \dot{h}_x(t - kT) \tag{3.30}$$

and

$$\ddot{x}(t) = \Sigma\, a_k \ddot{h}_x(t - kT) \tag{3.31}$$

Referring to Fig. 3.1, the waveform at the sampling point is the result of passing $\hat{f}(t)$ through the receive filter, or

$$y(t) = \hat{f}(t) * h_R(t) \tag{3.32}$$

Using Eqs. (3.29), (3.3), (3.30), (3.31), and (3.9) this becomes

$$\begin{aligned} y(t) = {} & \delta \Sigma a_k[g(t - kT) + p_1\dot{g}(t - kT) + p_2\ddot{g}(t - kT)] \\ & + \delta(2\pi\delta)p_3[(\Sigma a_k h_x(t - kT))(\Sigma a_\ell \dot{h}_x(t - \ell T))] * h_R(t) \end{aligned} \tag{3.33}$$

The first term in this expression may be readily calculated since g(t) and its derivatives are known. Since g(t) falls off rapidly, only a few symbols influence y(t). In the computer evaluation of performance two symbols preceding and two symbols following the one being detected were considered, giving $4^4 = 256$ individual cases. On the other hand, the second term must be calculated by numerical convolution. For each of the 256 cases (representing distinct sequences of adjacent symbols) the error probability may be calculated from Eq. (3.13); the average error probability is found by averaging over these cases. However, before making this calculation we must specify the instant of time $kT + t_s$ at which y(t) is sampled to detect a_k. This problem is considered below.

In calculating receiver timing we assume a tracking loop which responds to the mean zero crossing point of the waveform y(t). Consider the T second interval between t = kT and t = (k + 1)T. (We are neglecting delay in order to simplify the discussion.) If a_k and a_{k+1} are of opposite polarity the undistorted waveform x(t) will have a zero crossing in this interval. Although the position of this zero crossing will depend on the data sequence, its mean value (averaged over all data sequences) will be exactly at the mid-point of the interval. The distorted waveform y(t) will also have a zero crossing in this interval as long as the "eye" of the waveform has not closed. Since eye closure will result in catastrophic performance degradation, we will not seriously restrict the analysis by assuming the eye is open. In finding the mean-zero crossing two preceding and two following symbols are considered. Of these 256 cases only 128 will have a zero crossing in view of the requirement on the polarity of a_k and a_{k+1}. For each of these cases, the zero crossing of y(t) [as given by Eq. (3.33)] is found and the results are averaged.

3.1.3 IF Modem

3.1.3.1 Principles of Operation

The modulation technique used in the Harris IF modem is phase-continuous FSK. The only unconventional feature of the modulator is that the deviation is set to the unusually low value of 1/8 to achieve a packing density of 2 bits/sec/Hz. In the receiver portion of the modem, however, a very unconventional structure has been implemented to achieve high performance. In order to provide background necessary to understand the model used for performance evaluation, we must briefly describe the principle of operation of this receiver. For a more complete description, as well as for details of implementation, the reader should consult reference [3.2].

For a modulation index of 1/8, the separation between adjacent tone frequencies is 1/8T, where T is the symbol duration. Thus, the set of four frequencies (referenced to the lowest) are

$$f_i = \frac{i}{8T} \qquad i = 0,1,2,3 \qquad (3.34)$$

Considering a single baud, the transmitted phase waveform assuming a transmitted frequency f_i will be

$$\varphi_0 + i\,\frac{\pi}{4}\left(\frac{t}{T}\right) \qquad 0 < t < T \qquad (3.35)$$

where we have assumed a starting phase φ_0 and are again referencing to the lowest frequency f_0. It is clear from (3.35) that the phase increment over a baud will be a multiple of $\pi/4$ and hence the allowable phase at any symbol boundary will be one of eight possible values spaced at intervals of $\pi/4$ around a circle.

Assuming the signal structure described above, if one could measure the phase at each symbol boundary with a reference at frequency f_0 one could demodulate the transmitted frequencies by comparing adjacent phase measurements. In essence, this is the approach used in the demodulator in question. However, the presence of a bandpass filter at the receiver input (Fig. 3.2) introduces variations in the received phase which depend on adjacent frequencies. This filter is a fourth-order Bessel filter with noise bandwidth equal to the symbol rate, so that (in the

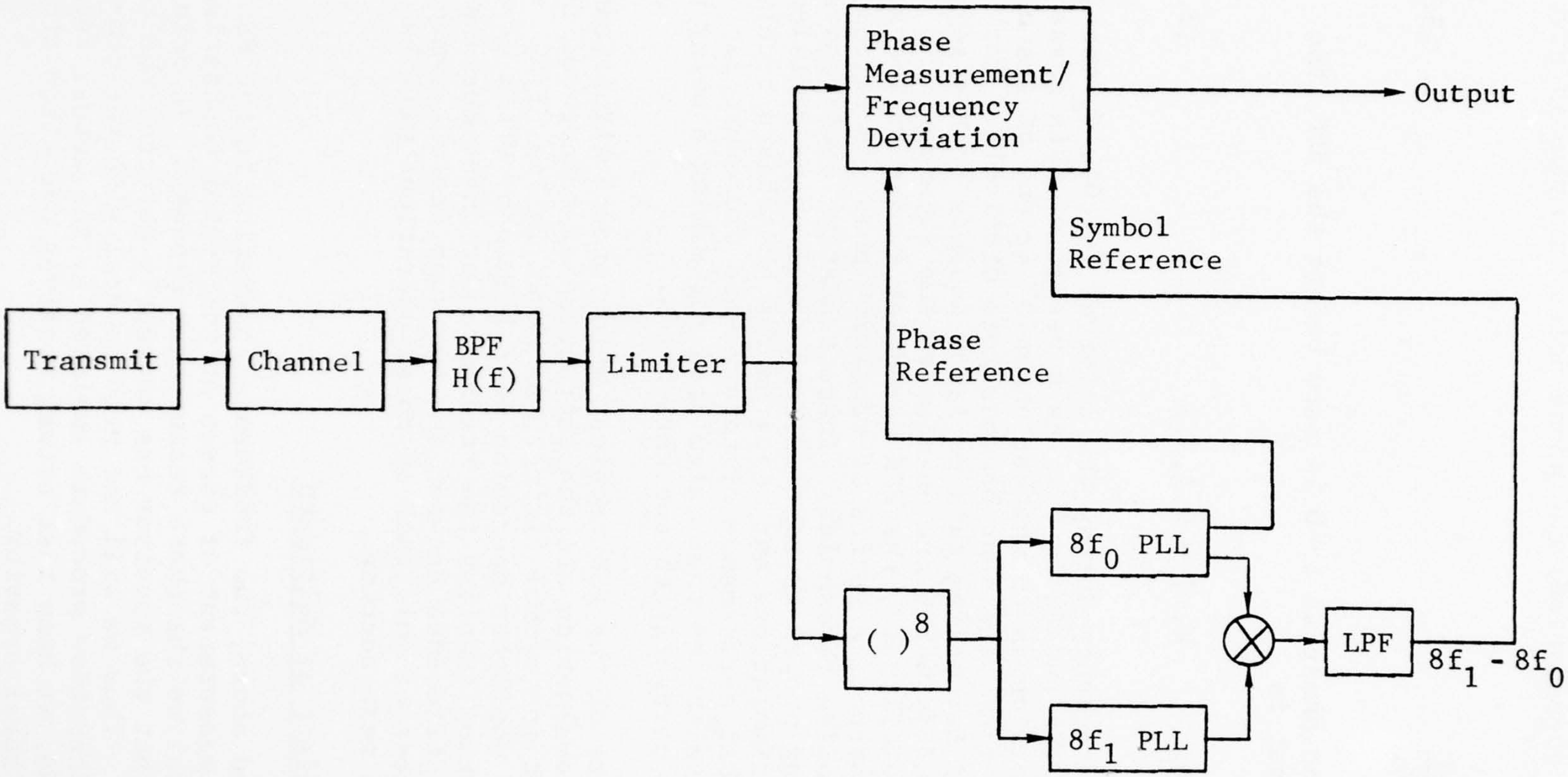

Figure 3.2 Simplified Modem Block Diagram

absence of other degradation) the phase noise variance is given by

$$\sigma^2 = \frac{N_0}{4E_b} \tag{3.36}$$

In summary, if the phase at $t = 0$ is zero before the BPF, the phase at its output is

$$(k - j)\theta_0 \qquad k, j = 0,1,2,3 \tag{3.37}$$

where f_j is the frequency during the interval $(-T,0)$, f_k the frequency during $(0,T)$ and θ_0 is 5°. As a result of this phase distortion, a decision as to whether phase 0° or one of its nearest neighbors at $\pm 45^\circ$ was sent becomes more difficult. The correct threshold for making this decision depends on the adjacent frequencies f_j and f_k which are unknown to the receiver. To circumvent this difficulty, the FSK demodulator uses an iterative procedure. In essence, a series of tentative phase decisions are made using compromise thresholds. These tentative decisions are used for selecting proper thresholds, and final phase decisions are made. Both simulations and tests on the breadboard receiver [3.2] indicate that performance of this ad-hoc procedure is essentially equivalent to that calculated for making a noisy phase measurement with correctly chosen thresholds.

Other aspects of the FSK receiver which are of significance for performance evaluation are the extraction of references for phase measurement and symbol timing. As shown in Fig. 3.2, an eighth-order nonlinear operation is followed by PLL's at $8f_0$ and $8f_1$. The former supplies the reference for phase measurement, while the difference between the two supplies the symbol timing. The effect of multipath on these operations will be discussed in the next section.

3.1.3.2 Effect of Multipath

As described above, the fundamental operation in the FSK receiver is the measurement of phases at the symbol boundaries. Thus, we will analyze the phase measurement process. In doing so, we will assume that the receiver has correctly detected the two adjacent phases. Thus we will not need to deal with the complexity of the iterative procedure employed by the actual receiver. On the other hand, we know that actual receiver operation closely approaches this ideal behavior.

Consider the following situation: the receiver has correctly detected the transmitted phases $\varphi(-T)$ and $\varphi(T)$. With no loss of generality, we may assume that the true phase at $t = 0$ is 0. Thus two error events are of significance:

Event A: Receiver decides $\varphi(0) = \frac{\pi}{4}$

Event B: Receiver decides $\varphi(0) = -\frac{\pi}{4}$

In the absence of multipath the actual phase γ at the bandpass filter output depends in a simple manner on the preceding and succeeding frequencies f_j and f_k:

$$\gamma(0) = (k - j)\theta_0 \tag{3.38}$$

For $\varphi(0) = \frac{\pi}{4}$ the preceding and succeeding frequencies would have to be f_{j+1} and f_{k-1}, giving an actual phase

$$\gamma(0)\big|_A = \frac{\pi}{4} + (k - j - 2)\theta_0 \tag{3.39}$$

So that the correct threshold to be
$\varphi(0) = 0$ and $\varphi(0) = \pi/4$ is

$$\frac{1}{2}\left[\gamma(0) + \gamma(0)\big|_A\right] = \frac{\pi}{8} + (k - j - 1)\theta_0 \tag{3.40}$$

Thus the probability of event A is

$$\begin{aligned} P_A(j,k) &= \Pr\left\{\gamma(0) + n > \frac{\pi}{8} + (k - j - 1)\theta_0\right\} \\ &= 1 - \Phi\left[\frac{\frac{\pi}{8} + (k - j - 1)\theta_0 - \gamma(0)}{\sigma}\right] \end{aligned} \tag{3.41}$$

where the noise variance σ^2 has been defined above. Similarly, event B requires that the adjacent frequencies be f_{j-1} and f_{k+1}, so that in the absence of distortion

$$\gamma(0)\,\Big|_B = -\frac{\pi}{4} + (k - j + 2)\theta_0 \tag{3.42}$$

Thus, for the decision between $\varphi(0) = 0$ and $\varphi(0) = -\pi/4$ the correct threshold is

$$\frac{1}{2}\left[\gamma(0) + \gamma(0)\,\Big|_B\right] = -\frac{\pi}{8} + (k - j + 1)\theta_0 \tag{3.43}$$

and the probability of event B is

$$\begin{aligned} P_B(j,k) &= \Pr\left\{\gamma(0) + n < -\frac{\pi}{8} + (k - j - 1)\varphi_0\right\} \\ &= 1 - \Phi\left[\frac{\gamma(0) + \frac{\pi}{8} - (k - j + 1)\varphi_0}{\sigma}\right] \end{aligned} \tag{3.44}$$

To obtain average error rates these expressions must be averaged over j and k, taking into account the fact that frequencies outside the range (0,3) are not allowed. Thus we have

$$\Pr\,\{\text{phase error}\} = \frac{1}{16}\sum_{j=0}^{2}\sum_{k-1}^{3} P_A(j,k) + \frac{1}{16}\sum_{j=1}^{3}\sum_{k=0}^{2} P_B(j,k) \tag{3.45}$$

Since each phase error will result in two frequency errors, the symbol error rate (and the bit error rate, if grey coding is used) will be twice this quantity.

In the presence of multipath, the simple expression for $\gamma(0)$ given above [Eq. (3.38)] cannot be used in evaluating $P_A(j,k)$ and $P_B(j,k)$. First of all, the actual sampling time will not be zero; but will be determined by the operation of the receiver reference extraction as will be described later. Secondly, the calculation of the received phase $\gamma(t_{samp})$ must take into account the multipath distortion. Referring to Fig. 3.3, we observe that since the receiver BPF and channel model are linear operations, we may interchange them. Although we have previously discussed $\varphi(t)$ as the phase relative to a carrier at f_0, it will be convenient in what follows to refer phases to a hypothetical center frequency. With this reference, the transmitted phases are